Diffusive processes in mineral processing

by

Kirsten Ingrid Louw

M.Sc. in Computational and Applied Mathematics

B.Sc. Honours in Computational and Applied Mathematics

B.Sc. in Computational and Applied Mathematics, Mathematics and Economic Sciences

A thesis submitted for the degree of

Doctor of Philosophy in Applied Mathematics

UniSA STEM



University of South Australia

May 2023

Table of contents

List of Figures vii

List of Tables x

Abstract xii

Declaration xiv

Acknowledgments xv

List of Publications xvi

1 INTRODUCTION 1

1.1 Industrial motivation 1

1.2 Overview of metal organic frameworks 4

1.2.1 Physical chemistry of the MOF thin film 4

1.3 Parameters and geometry of system 5

1.3.1 Physical attributes of the MOF 6

1.3.2 Physical attributes of a hydrated ferric ion 8

1.3.3 Physical attributes of polymer 10

1.3.4 Testing device 11

1.4 Mathematical methods 12

1.5 Aims and structure of thesis 13

I Microenvironment 16

2 THEORY OF CALCULATING THE INTERACTION ENERGY AND FORCE 19

2.1 Lennard-Jones potential 19

2.2 Interaction energies and force between two particles 22

2.2.1 Interaction energy 22

2.2.2 Interaction force 22

2.2.3 Acceptance and kinetic energy 23

2.3 Effects of temperature on Lennard-Jones potential 25

3 INTERACTIONS BETWEEN A HYDRATED FERRIC ION AND A SEMI-INFINITE CYLINDRICAL MOF PORE 27

3.1 Interaction energies . . . 28

3.1.1 Ferric ion point to MOF pore . . . 28

3.1.2 Oxygen and hydrogen spheres to MOF pore . . . 29

3.2 Interaction forces . . . 32

3.2.1 Ferric ion point to MOF pore . . . 32

3.2.2 Ferric ion point's attraction limit . . . 33

3.2.3 Oxygen and hydrogen spheres to MOF pore . . . 35

3.2.4 Oxygen and hydrogen sphere's attraction limit . . . 37

3.3 Acceptance and kinetic energy . . . 38

3.3.1 Ferric ion point to MOF pore . . . 38

3.3.2 Oxygen and hydrogen spheres to MOF pore . . . 40

3.4 Discussion . . . 42

4 INTERACTIONS BETWEEN A HYDRATED FERRIC ION AND A FINITE CYLINDRICAL MOF PORE 46

4.1 Interaction energies . . . 46

4.1.1 Ferric ion point to MOF pore . . . 46

4.1.2 Oxygen and hydrogen spheres to MOF pore . . . 47

4.2 Interaction forces . . . 49

4.2.1 Ferric ion point to MOF pore . . . 49

4.2.2 Ferric ion point's attraction limit . . . 50

4.2.3 Oxygen and hydrogen spheres to MOF pore . . . 53

4.2.4 Oxygen and hydrogen sphere's attraction limit . . . 54

4.3 Acceptance and kinetic energy . . . 57

4.3.1 Ferric ion point to MOF pore . . . 57

4.3.2 Oxygen and hydrogen spheres to MOF pore . . . 58

4.4 Discussion . . . 61

5 CHANGES IN MODELLING ASSUMPTIONS 65

5.1 Interactions between other metal ions and a semi-infinite cylindrical MOF pore . . . 65

5.2 Interactions between a ferric ion and a semi-infinite rectangular prism MOF pore . . . 68

5.2.1 Parameters and geometry of the remodelled system 69
5.2.2 Interaction energy 71
5.2.3 Interaction forces 74
5.3 Prism versus cylinder MOF pore approximation 77
5.4 Implications of a pore blockage 82
5.5 Interactions between a hydrated ferric ion and multiple MOF pores 84
5.6 Implications of change in temperature 85
5.7 Discussion 89

6 CONCLUDING REMARKS FOR PART I **92**
6.1 Summary 92
6.2 Experimental consideration 94

II Macroenvironment **96**

7 FERRIC ION DIFFUSION IN SOLUTION AND POLYMER: A MOF CRYSTAL AT THE SOLUTION-POLYMER BOUNDARY **98**
7.1 Mathematical modelling and assumptions 98
7.1.1 Nondimensional two-dimensional model 101
7.1.2 One-dimensional model 102
7.1.3 Nondimensional one-dimensional model 103
7.2 Variation of nondimensional parameters in one-dimensional model 104
7.2.1 Varying the nondimensional diffusion coefficient, s_1 105
7.2.2 Varying the effective association parameter, s_2 105
7.2.3 Varying the effective dissociation parameter, s_3 106
7.2.4 Varying the effective flux parameter, s_4 107
7.3 Variation of nondimensional parameters in two-dimensional model 108
7.3.1 Varying the nondimensional diffusion coefficient, s_1 110
7.3.2 Varying the effective association parameter, s_2 110
7.3.3 Varying the effective dissociation parameter, s_3 111
7.3.4 Varying the effective flux parameter, s_4 112
7.3.5 Varying the relative diffusion coefficient, D 112
7.4 Discussion 113

8 FERRIC ION DIFFUSION IN THE POLYMER: MOF CRYSTALS DISTRIBUTED THROUGHOUT THE POLYMER **115**

8.1 Mathematical modelling and assumptions 115

8.1.1 Nondimensional model 118

8.2 Solution for ferric ion concentration 119

8.3 Variation of nondimensional parameters 122

8.3.1 Varying the modified diffusion coefficient, $\mathcal{D}$ 123

8.3.2 Varying the effective dissociation parameter, s_3 123

8.3.3 Varying the effective bath reservoir, C_0/B_0 125

8.3.4 Varying MOF density, ρ 126

8.4 Discussion 127

9 CONCLUDING REMARKS FOR PART II **129**

9.1 Summary 129

9.2 Experimental consideration 130

III Mathematical Exploration **132**

10 PERTURBATION METHODS FOR SOLVING A MODIFIED DIFFUSION EQUATION **134**

10.1 Unperturbed ferric ion concentration 135

10.2 Perturbed ferric ion concentration 136

10.3 Discussion 139

11 LIE GROUP METHODS FOR SOLVING MODEL EQUATIONS **140**

11.1 Exact solution to modified diffusion equation 141

11.2 Exact solutions to a system of partial differential equations 143

11.2.1 Ferric ion diffusion and MOF occupancy where s_3 is non-zero 144

11.2.2 Ferric ion diffusion and MOF occupancy when $s_3 = 0$ 145

11.3 Discussion 147

12 FINAL REMARKS AND FUTURE WORK **148**

REFERENCES **151**

Appendix A CALCULATION OF THE INTERACTION ENERGY AND FORCE BETWEEN EITHER A POINT OR A SPHERE AND A SEMI-INFINITE CYLINDER 157

A.1 Step-by-step calculations for interaction energy 157

A.1.1 Point to semi-infinite cylinder 157

A.1.2 Sphere to semi-infinite cylinder 158

A.2 Step-by-step calculations for interaction forces 160

A.2.1 Point atom to semi-infinite cylinder 160

A.2.2 Sphere to semi-infinite cylinder 160

A.3 Step-by-step calculations for kinetic energy 161

A.3.1 Point atom to semi-infinite cylinder 161

A.3.2 Sphere to semi-infinite cylinder 162

Appendix B CALCULATION OF THE INTERACTION ENERGY AND FORCE BETWEEN EITHER A POINT OR A SPHERE AND A FINITE CYLINDER 164

B.1 Step-by-step calculations for interaction energy 164

B.1.1 Point to finite cylinder 164

B.1.2 Sphere to finite cylinder 165

B.2 Step-by-step calculations for interaction force 167

B.2.1 Point to finite cylinder 167

B.2.2 Sphere to finite cylinder 167

B.3 Step-by-step calculations for kinetic energy 168

B.3.1 Point to finite cylinder 168

B.3.2 Sphere to finite cylinder 169

Appendix C CALCULATION OF THE INTERACTION ENERGY AND FORCE BETWEEN A POINT AND A SEMI-INFINITE RECTANGULAR PRISM 171

C.1 Step-by-step calculations for interaction energy 171

C.1.1 Point to semi-infinite line 171

C.1.2 Point to perpendicular semi-infinite plane 172

C.2 Step-by-step calculations for interaction forces 181

C.2.1 Point to semi-infinite straight line 181

C.2.2 Point to perpendicular semi-infinite plane 181

Appendix D EXPANSION OF AND DEFINITION FOR THE INDEFINITE INTEGRAL $\cos^{2n}\theta$, I_n **184**

D.1 Definite integral evaluated at $\frac{\pi}{2}$ and ψ, J_n 187

D.2 Definite integral evaluated at ψ_1 and ψ_2, H_n 190

Appendix E EXPANSION OF AND DEFINITION FOR THE INDEFINITE INTEGRAL $\sin^{2m}\theta\cos^2\theta$ **192**

Appendix F NUMERICAL ALGORITHM FOR DIMENSIONLESS ONE-DIMENSIONAL MODEL **194**

Appendix G NUMERICAL ALGORITHM FOR DIMENSIONLESS TWO-DIMENSIONAL MODEL **198**

Appendix H CODE **203**

H.1 Part I 203

H.1.1 Plots for interaction potential energy, force and kinetic energy: semi-infinite case 203

H.1.2 Lennard-Jones parameters and surface densities 221

H.1.3 Interaction potential energy, force and kinetic energy functions 226

H.1.4 Calculating interaction potential energy, force and kinetic energy 231

H.2 Part II 241

H.2.1 Numerical scheme for nondimensional two-dimensional system 241

H.3 Part III 259

H.3.1 Calculating admitted Lie point symmetries for system of PDEs 259

Appendix I STATEMENTS OF AUTHORSHIP **260**

List of Figures

1.1 Typical mining and processing flowsheet [7]. 2
1.2 Schematic of proposed device for ferric ion detection [39]. 3
1.3 2D representation of molecular structure of organic and metallic compounds used as reagents to make MOF crystals. 5
1.4 Molecular configuration ligands in MOF and MOF structural composition. 6
1.5 MOF configuration with basis vectors to identify unit cell. 7
1.6 Unit cell cylindrical geometry. 7
1.7 Continuum approximation of hydrated ferric ion. 9
1.8 2D representation of molecular structure of crosslinker and monomer used to create thin film to hold MOF crystals. 11
1.9 (a) Sensor in cast with analyte solution containing ferric ions being dispensed. (b) Ferric ion sensor design [39]. 12

2.1 Schematic showing how van der Waals potential depends on separation distance, as calculated using Lennard-Jones potential. 20
2.2 Lennard-Jones potentials 21
2.3 van der Waals force and interaction forces between atom and cylindrical pore. 23

3.1 Geometrical approximations of hydrated ferric ion and MOF pore approximated by semi-infinite cylinder. 27
3.2 Interaction energy between ferric ion and semi-infinite cylindrical MOF pore. 29
3.3 Interaction energy between oxygen (and hydrogen) sphere and semi-infinite cylindrical MOF pore. 32
3.4 Interaction force between ferric ion and semi-infinite cylindrical MOF pore. 33
3.5 Attraction limit X_0 for ferric ion point. 35
3.6 Interaction force between oxygen (and hydrogen) sphere and semi-infinite cylindrical MOF pore. 36
3.7 Attraction limits X_0 for oxygen sphere and hydrogen sphere. 37
3.8 Total acceptance energy and maximum kinetic energy of ferric ion. 40
3.9 Total acceptance energy and maximum kinetic energy of oxygen and hydrogen sphere. 42
3.10 Interaction energy between (hydrated) ferric ion and semi-infinite cylindrical MOF pore. 43

3.11 Interaction force between (hydrated) ferric ion and semi-infinite cylindrical MOF pore, and attraction limits X_0. 44
3.12 Total acceptance energy and maximum kinetic energy of (hydrated) ferric ion. 45

4.1 Interaction energy between ferric ion and finite cylindrical MOF pore. 47
4.2 Interaction energy between oxygen (and hydrogen) sphere and finite cylindrical MOF pore. 49
4.3 Interaction force between ferric ion and finite cylindrical MOF pore. 50
4.4 Interaction force between ferric ion and finite cylindrical MOF pore, with varying MOF radius. 51
4.5 Attraction limit X_0 for ferric ion point. 52
4.6 Interaction force between oxygen (and hydrogen) sphere and semi-infinite cylindrical MOF pore. 54
4.7 Attraction limit X_0 for oxygen sphere sphere. 55
4.8 Interaction force between oxygen sphere and finite cylindrical MOF pore, with varying MOF radius. 55
4.9 Attraction limits X_0 for oxygen sphere and hydrogen sphere. 56
4.10 Total acceptance energy and maximum kinetic energy of ferric ion. 58
4.11 Total acceptance energy and maximum kinetic energy of oxygen and hydrogen sphere. 60
4.12 Interaction energy between (hydrated) ferric ion and finite cylindrical MOF pore. . . 61
4.13 Interaction force between (hydrated) ferric ion and finite cylindrical MOF pore. . . . 62
4.14 Interaction force between ferric ion and finite cylindrical MOF pore, with varying MOF depth. 63
4.15 Attraction limits X_0 for (hydrated) ferric ion. 63
4.16 Total acceptance energy and maximum kinetic energy of (hydrated) ferric ion. 64

5.1 Interaction energy and force between different metal ions and a semi-infinite cylindrical MOF pore. 66
5.2 Attraction limit X_0 for different metal ions. 67
5.3 Schematic of ferric ion and MOF pore as approximated by semi-infinite rectangular prism. 70
5.4 Visual justification of parameters used for prism approximation. 70
5.5 Interaction energy between ferric ion and semi-infinite prism MOF pore. 74

5.6 Interaction force between ferric ion and semi-infinite prism MOF pore. 76
5.7 Prismatic and two cylindrical approximations of EuBDC-OMe MOF pore. 77
5.8 Interaction energy between ferric ion and various MOF pore approximations. 78
5.9 Interaction energy between ferric ion and europium (and carbon) in various MOF pore approximations. 79
5.10 Interaction force between ferric ion and various MOF pore approximations. 80
5.11 Interaction force between ferric ion and europium (and carbon) in various MOF pore approximations. 81
5.12 Interaction energy and force between ferric ion and blocked semi-infinite prism MOF pore. 84
5.13 Simplified graphic of multiple MOF pores using basis vectors. 84
5.14 Lennard-Jones potentials for carbon atoms and benzene molecules, with varying temperature for benzene molecules. 87
5.15 Lennard-Jones potentials for carbon atoms, with varying temperature. 87
5.16 Interaction energy between ferric ion and semi-infinite prismatic MOF pore, with varying temperature. 88
5.17 Interaction force between ferric ion and semi-infinite prismatic MOF pore, with varying temperature. 89

7.1 Two-dimensional cross section of optic fibre with MOF-polymer thin film. 98
7.2 Modelled two-dimensional system in Cartesian co-ordinate frame. 99
7.3 One-dimensional representation of ferric ions diffusing through column of solution with MOF crystal at left boundary. 103
7.4 Nondimensional concentration of ferric ions in solution and MOF occupancy. 104
7.5 Nondimensional concentration of ferric ions in solution and MOF occupancy, with varying nondimensional diffusion. 105
7.6 Nondimensional concentration of ferric ions in solution and MOF occupancy, with varying effective association. 106
7.7 Nondimensional concentration of ferric ions in solution and MOF occupancy, with varying effective dissociation. 107
7.8 Nondimensional concentration of ferric ions in solution and MOF occupancy, with varying effective flux. 108
7.9 Nondimensional concentration of ferric ions across two media, with varying time. . . 109

7.10 Nondimensional concentration of ferric ions across two media and MOF occupancy. . 109
7.11 Nondimensional concentration of ferric ions across two media and MOF occupancy, with varying nondimensional diffusion. 110
7.12 Nondimensional concentration of ferric ions across two media and MOF occupancy, with varying effective association. 111
7.13 Nondimensional concentration of ferric ions across two media and MOF occupancy, with varying effective dissociation. 111
7.14 Nondimensional concentration of ferric ions across two media and MOF occupancy, with varying effective flux. 112
7.15 Nondimensional concentration of ferric ions across two media and MOF occupancy, with varying relative diffusion coefficient. 113

8.1 Small section of two-dimensional cross-section of optic fibre. 116
8.2 One-dimensional representation of ferric ions diffusing through column of polymer composite with uniformly distributed MOF crystals represented by red dots. 116
8.3 Nondimensional concentration of ferric ions in solution, with varying time. 122
8.4 Nondimensional concentration of ferric ions in solution, with varying modified diffusion. 123
8.5 Nondimensional concentration of ferric ions in solution, with varying effective dissociation. 124
8.6 Nondimensional concentration of ferric ions in solution, with bounded regions for effective dissociation. 125
8.7 Nondimensional concentration of ferric ions in solution, with varying effective bath reservoir. 126
8.8 Nondimensional concentration of ferric ions in solution, with varying MOF density. . 126

12.1 Schematic of MOF pore as approximated by semi-infinite parallelogram prism. . . . 149
12.2 Two hydrated ferric ions approximated by points and two concentric spheres, distance δ apart. 150

List of Tables

1.1 Physical attributes of EuBDC-OMe [41]. 7

1.2 Counting MOF atoms in unit cell. 8

1.3 Mean density for each atom type for approximated cylindrical MOF unit cell. 8

1.4 Experimental bonds distances and angles [26] using B3LYP/6-31G. 10

1.5 Mean density for hydrogen and oxygen in approximate concentric spheres. 10

2.1 Lennard-Jones parameters [37]. 21

5.1 Lennard-Jones parameters for copper(II) and magnesium(II) [37]. 66

5.2 Number of atoms located at ligand and node, and split by atom type [41]. 69

5.3 Mean density for each atom type for approximated prismatic MOF unit cell. 71

5.4 Parameter values used incorporating physical attributes for cylindrical and fitted cylindrical MOF pore. 78

F.1 Numerical values for one-dimensional simulation. 197

G.1 Numerical values for two-dimensional simulation. 202

Abstract

Increased copper demand and decreasing ore grades, necessitates closer scrutiny and optimisation of all beneficiation and extraction processes. Sensors monitoring key controlling physical and chemical variables are a critical tool for ensuring process performance and minimising variability. This thesis focuses on modelling the process of detection of ferric (Fe^{3+}) ions in controlling the ferrous-ferric redox potential in hydrometallurgical processes.

This theoretical project studies a new sensor that consists of an optic fibre with a thin film coating. The thin film is a polymer composite with embedded crystals called metal organic frameworks (MOFs), known for their porosity. In application, ferric ions diffuse through the polymer composite to associate with the MOF crystals. When a light is pulsed through the optic fibre, changes in fluorescence are indicative of the concentration of ferric ions in the analyte solution.

This project applies mathematics to model the behaviour of a submerged sensor in solution containing ferric ions and investigates this behaviour with two different length scales, referred to as the microenvironment and macroenvironment.

In the microenvironment, van der Waals interactions between a hydrated ferric ion and a single MOF pore are investigated. The Lennard-Jones potential with a continuum approach is used to study these interactions, where the hydrated ferric ion is approximated by a point with two concentric spheres and the MOF pore as a semi-infinite cylinder. Results show that the hydrated ferric ion is indeed attracted to the MOF pore and experiences the greatest attraction at the pore's entrance. However, consideration of the ionic radii of the hydrated ferric ion and the MOF pore reveals that the hydrated ferric ion is geometrically too large to fit inside the available MOF pore space. Consequently, the sensor can be "washed" and re-used leading to cost savings.

Whilst using a semi-infinite pore may seem idealistic, this approximation gives a good approximation for a finite pore of depth 70 angstroms or more, while MOF crystals within the sensor are of the order of 100 nanometres. Building onto the established framework, further investigations are done to be more inclusive of the sensing environment.

In the macroenvironment, ferric ion diffusion in the solution and the polymer composite, and ferric ion association with MOF crystals are investigated. First, diffusion in mixed media together with a Robin boundary condition representing a MOF crystal sink is used to study ferric ion concentration in the sensor. Results show how the ions, the MOF crystal and the media characteristics can influence sensing time. Second, the dissolved ferric ion concentration and the density of ions

associated with the MOF crystals is studied to determine how MOF crystal density impacts sensing time. For solutions with high ferric ion concentrations, a lower MOF crystal density is more appropriate.

Finally, a mathematical exploration of the model equations is provided using perturbation methods, Lie point symmetry methods, Laplace transformations and Fourier transformations.

All physical insights regarding the newly developed sensor are new and will assist material scientists in making informed decisions regarding sensor synthesis and use.

Declaration

This thesis presents work carried out by myself and does not incorporate without acknowledgment any material previously submitted for a degree or diploma in any university; to the best of my knowledge it does not contain any materials previously published or written by another person except where due reference is made in the text; and all substantive contributions by others to the work presented, including jointly authored publications, are clearly acknowledged.

Signed



Kirsten Ingrid Louw 29 May 2023

Acknowledgments

First and foremost, I would like to say a big thank you to Associate Professor Bronwyn Hajek for travelling to South Africa which lead me the opportunity to do my PhD with her. Thank you for all the support and guidance you have given me. Not only in a professional capacity but also in a personal capacity like stepping in as my next of kin when the need arose. I have great admiration for you.

Thank you to Linda Rozenberga for being such a wonderful experimental PhD sister. Thank you for always making time to take me on tours of your lab and showing me all the different processes needed to design and synthesize the novel ferric ion sensor, and for answering all my questions.

I'm extremely thankful to my co-supervisors Professor Jim Hill, Professor Marta Krasowska and Professor Bill Skinner. Thank you for all the contributions you made to my work and for increasing my knowledge set. Your individual contributions have allowed me to have a deeper understanding of how this project contributes to the mathematics, chemistry and mining fields.

Thanks to Professor Phil Broadbridge. You have been instrumental with regards to the work surrounding the modified total ferric ion concentration. Thank you for being so patient and freely offering your time. It was an honour to meet you and to work with my academic "grandfather".

I would also like to extend my thanks to Doctor Witold Bloch for always responding to my chemistry related questions in a way that I could understand, and to Pearl Louw, Kristina Dakin and Professor Joe Grotowski for their support by proof-reading chapters of my thesis.

Thank you to the members of the PRIF Consortium, postdocs and PhD students. It has been a memorable experience to be exposed to and to learn from researchers so far removed from my field. Thank you for the workshops that guided me on how to properly address different audiences, especially in the mining sector.

Thank you to the South Australian Government through the PRIF RCP Mining Consortium "Unlocking Complex Resources through Lean Processing" for sponsoring my stipend and University of South Australia through the International Research Tuition Scholarship.

My sincerest thanks to my family, friends and "acquired" Australian families for all the love, support and encouragement that I could not have done without during my PhD journey.

List of publications

1. K. I. Louw and B. H. Bradshaw-Hajek and J. M. Hill. Interaction of ferric ions with europium metal organic framework and application to mineral processing sensing. *Philosophical Magazine*, 102(13): 1231–1246, 2022

   Relating to Sections 3.1, 3.2 and 5.1

2. K. I. Louw and B. H. Bradshaw-Hajek and J. M. Hill. Ferric Ion Diffusion for MOF-Polymer Composite with Internal Boundary Sinks. *Nanomaterials*, 12(5): 887, 2022

   Relating to Chapter 7

3. K. I. Louw and B. H. Bradshaw-Hajek and J. M. Hill. van der Waals interaction energies for ferric ion sensors using prismatic and cylindrical pore approximations for a MOF pore. *Royal Society Open Science*, 10(5):230232, 2023

   Relating to Sections 5.2, 5.3 and 5.4

CHAPTER 1

INTRODUCTION

The quality of mined copper ore has been steadily decreasing over the last few decades. In particular, those properties affecting beneficiation (i.e. copper grade, mineralogical associations, fine grain size and problematic waste minerals) have made processing more difficult and costly. Nevertheless, copper is a critical mineral as it is the enabler for the transition to renewable energy generation and supply, and for the resources sector, in electrification of the industry. The Premier's Research and Infrastructure Fund (PRIF) initiative, "Unlocking Complex Resources through Lean Processing", is a research consortium involving technology and mining companies with the objective of developing sensors, data analytics and data fusion along the mine-to-metal value chain resulting in strategies contributing to the digitalisation of mining through sophisticated and robust sensors, data farming, and machine learning. This project is part of this consortium.

Sensors in particular play a critical role, as performance variation is a major mechanism by which valuable metal-hosting minerals are lost, and energy and water wasted. In this project, a mathematical modelling approach has been adopted to examine the factors governing metal ion interaction with sensor materials and the diffusion processes of ions in a new sensor. A particular class of sensor material, metal organic frameworks (MOFs) is the focus, and the theoretical investigations herein comprise a parallel investigation to experimental sensor development for the measurement of ferric ions in processing solutions.

The research presented in this thesis has broader relevance in metal ion sensing in situ and may be universally applied to sensor design as mathematical modelling is a powerful tool. Modelling often provides insight into the behaviour of a system or process that can be difficult to unlock with experimental measurements alone, and allows for a more efficient exploration of the relevant parameter space. The following sections provide some context for this project and state the aims and structure of this thesis.

1.1. INDUSTRIAL MOTIVATION

Mined copper ore is hauled to the production facilities to be crushed and then taken to the surface to be transported to the mill. There are two main types of ore that can be mined: (i) high quality copper ore, which is rare and hard, and can damage the grinding machinery at the mill, and (ii) softer, lower quality ore, with a chemical composition that makes it more chemically reactive in the

grinding process.

Once the ore is delivered, there are three main ore treatment phases, namely: grinding, flotation, and tails leaching. Copper concentrate is made by grinding the raw material and using a flotation process to separate the copper from unwanted rock. In the flotation circuit, the fine particles (crushed ore) are suspended in an aqueous solution by exploiting the differences in the ability of specific mineral surfaces to adhere to the air/water interface. The hydrophobic particles attach to the bubbles and the consequent froth is separated. These extracted particles are then smelted and refined. The hydrophilic particles fall to the base and are separated and sent to the tailings circuit. Finally, the tails leaching process is used to extract more copper and any other precious metals such as gold and silver from the tails. Tailings (tails) are the waste products from initial copper extraction, such as rock, water and trace amounts of metals.



Figure 1.1: Typical mining and processing flowsheet [7].

The steps involved in the mining and processing of copper ore are summarised in Figure 1.1.

The leaching process involves a chemical reaction whereby metals are extracted from the surrounding ore in an acidic water solution or other suitable solvents. The solution is further processed to obtain the metal in its metallic state or as a chemical compound. There are a few key factors that contribute to the leaching process: formation of inert obstructive layers, the acidic media or solvent, pH level, solution redox potential, temperature, and the concentration of ions, in particular, ferrous (Fe(II) or iron(II)) and ferric ions (Fe(III) or iron(III)).

The ferrous-ferric ion redox couple in the hydrometallurgical extraction of copper and uranium is especially important, further highlighting the need for, and the application of, an additional (ferric ion) sensor in the flotation circuit to measure the impact of ferrous-ferric ion redox potential on output. Flotation circuits need to optimally modify and respond to changing concentrations of

ferric and ferrous ions in the solution [49] for successful acid leaching. This can often control the redox potential in process waters. Additionally, the redox potential needs to be above a certain value for collectors to work effectively. Collectors are substances that form a hydrophobic layer on the fine particles and aid the minerals of interest to attach to the air bubbles so they can be recovered in the froth product.

As a consequence, it is essential to monitor ferrous and ferric ion concentrations, and much attention has focused on the development of reliable and efficient ferric ion detection methods. While reliable tests exist for determining ferrous ion concentrations, there are no similar, simple and cost-effective tests to determine the concentration of ferric ions [36, 42]. This current lack of a suitable testing option spearheads the research and development of a ferric ion sensor.

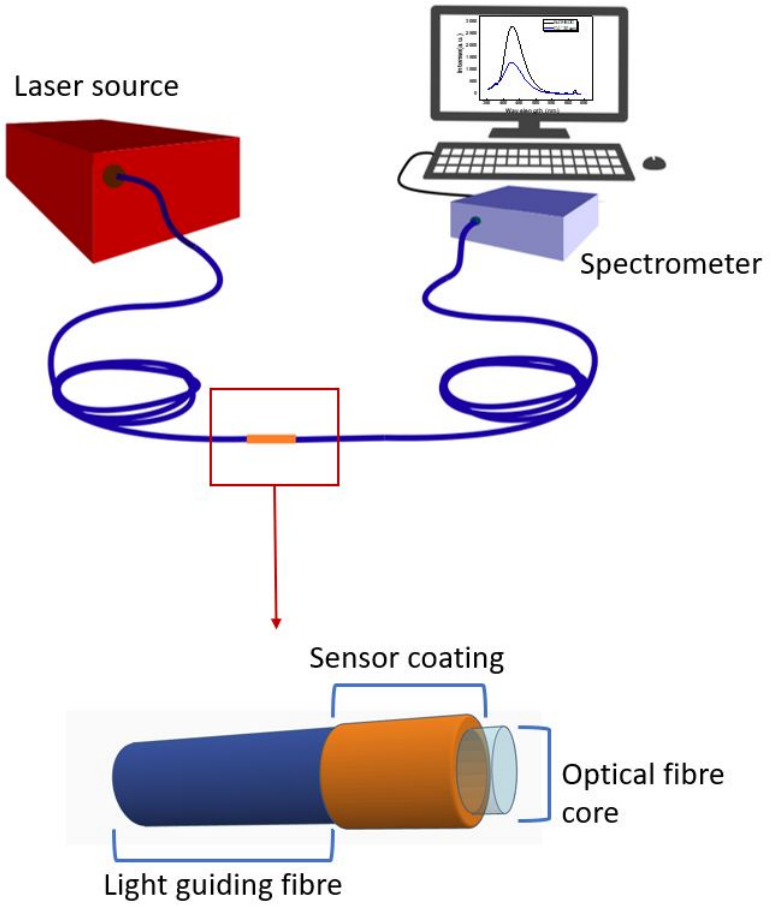


Figure 1.2: Schematic of proposed device for ferric ion detection [39].

The proposed method of detecting ferric ions is to synthesise a fluorescent sensor, as depicted in Figure 1.2. This theoretical PhD dovetails with an experimental one, where physical chemist Linda Rozenberga optimised and refined the process of creating MOF crystals, and the subsequent

development of a thin film comprised of a polymer matrix with embedded MOF crystals. The thin film is then placed on a section of an optic fibre. The coated optic fibre is submerged into the analyte solution containing ferric ions, where the ferric ions associate with the MOF crystals. A light pulse is sent through the MOF-coated optic fibre and a spectrometer detects changes in luminosity. The diminished luminosity is indicative of the concentration of ferric ions in the analyte solution.

This current PhD project specifically focusses on the interaction of ferric ions with the MOF crystals in the polymer matrix, and the diffusion of ferric ions through the polymer to associate with the MOF crystals.

1.2. OVERVIEW OF METAL ORGANIC FRAMEWORKS

MOFs are porous medium structures with metallic nodes and organic linkers. They are ordered structures with a large surface area to volume ratio. One common use of MOFs is in the storage of hydrogen gas to use as a power source for vehicles [19].

MOF pore sizes can be tailored to accommodate specific goals. MOFs can be used to collect, separate or store gases, liquids, and particles for various applications including drug delivery, wastewater treatment, separating gases, and fuel storage [24]. In this project, the MOF will collect ferric ions that are present in the analyte solution. The crystalline MOF crystal used in this study is called EuBDC-OMe [41]. Although MOFs are known for their porous characteristics, this property is not the most important feature for the sensor investigated here. The primary feature is it's ability to fluoresce in the presence of ferric ions (later discussed in Subsection 1.3.4).

1.2.1. Physical chemistry of the MOF thin film

The MOF particulates synthesised in the parallel experimental program use the techniques described by Xu *et al.* [59] as the basis for creating the MOF crystals, where 2-methoxyterephthalic acid is the organic linker and europium nitrate forms the metallic node. Figure 1.3 shows the two-dimensional structural view of 2-methoxyterephthalic acid and europium nitrate, where O is oxygen, H is hydrogen, N is nitrogen and Eu is europium.

There are three techniques used to confirm that the MOFs have the structural composition expected from theory. Firstly, powder X-ray diffraction (XRD) is used to study the crystal structure and composition of the MOF. XRD looks at the atoms in the crystal and how they are placed and

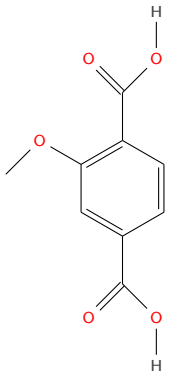
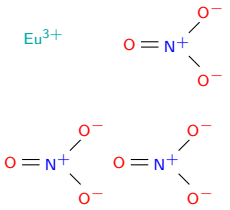
Organic Linker	Metallic Node
2-Methoxyterephthalic acid	Europium nitrate
	

Figure 1.3: 2D representation of molecular structure of organic and metallic compounds used as reagents to make MOF crystals.

connected to each other. Secondly, fluorescence spectroscopy makes use of a beam of light to cause the tested material to emit light. The wavelength of the emitted light is measured and molecules are identified. XRD and fluorescence spectroscopy are key techniques used in the corresponding experimental PhD project in the consortium [39]. Thirdly, Fourier-transform infrared spectroscopy (FTIR) with attenuated total reflectance (ATR) is used to study the chemical structure of the MOF crystals. FTIR identifies the chemical bonds present between the atoms.

Xu *et al.* [59] reported that in the synthesising of the europium MOF crystal, the organic linker's methoxy ($O-CH_3$) group was replaced with a hydroxy (OH) group and further attributed the "turn-off" sensing (when luminosity decreases) to ferric ions binding to a hydroxy groups within the MOF pores. However, Rozenberga *et al.* [41] discovered the previously reported MOF structure was incorrect and the benzene ring in the organic linker does not change its configuration. Figure 1.4 shows there is a methoxy ($O-CH_3$) group that protrudes into the MOF pore, reducing the available pore space for ferric ions to diffuse into the pore [41]. As a consequence, ferric ions do not diffuse into the pore and associate to an OH-group; rather they associate to the surface of the MOF crystal, consequently driving the changes in luminescence.

1.3. PARAMETERS AND GEOMETRY OF SYSTEM

The first step towards developing a mathematical model is to understand the physical environment. This section examines the geometry and other physical attributes of the interacting components, that is, a europium-based MOF and a hydrated ferric ion, hexa-aqua iron(III).

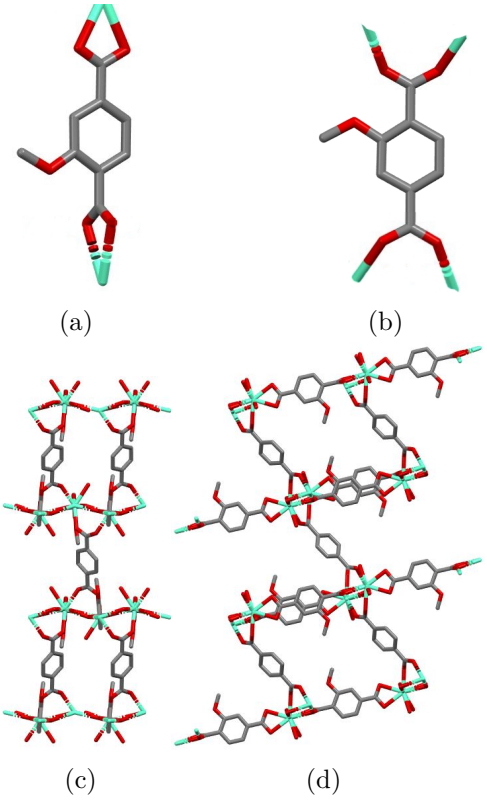


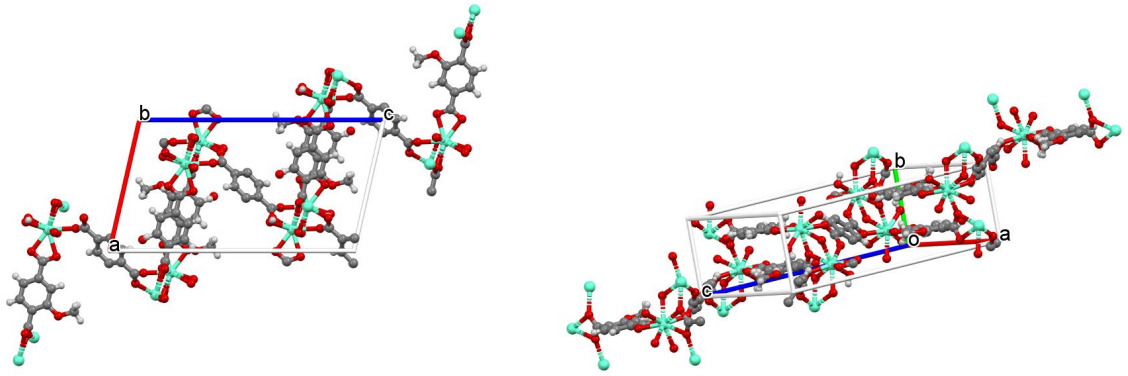
Figure 1.4: (a-b) Two possible configurations of ligands with europium(III) ion (turquoise) [41]. (c-d) Structural composition of MOF at a-axis and b-axis (axis of symmetry) [41].

This project takes a continuum approach to investigating the behaviour of the sensor. Part I investigates the interaction of ferric ions with the MOF crystals; Sections 1.3.1 and 1.3.2 describe the physical attributes of the MOF crystals and the hydrated ferric ions, and outline a continuum approximation for these structure. Sections 1.3.3 and 1.3.4 describe the polymer in which the MOF crystals are embedded, and the sensor itself.

1.3.1. Physical attributes of the MOF

Figure 1.5 depicts the atomic structure of the MOF where europium(III) atoms are shown as turquoise spheres, oxygen are red, hydrogen are white and carbon are grey. Figure 1.5 also shows the a-, b- and c-axes of symmetry. These axes of symmetry are the base vectors that describe the orientation of the unit cell. Figure 1.5(a) shows the structure down the b-axis of symmetry. This shows a portion what is described as the MOF pore in this thesis, which arises as the unit structure is duplicated or tessellated through space.

In this project, the MOF pore is approximated with a cylinder (both semi-infinite and finite) and a rectangular prism; the atoms of the pore are assumed to be uniformly distributed (or smoothed)



(a) (b)

Figure 1.5: (a) Unit cell structure with europium(III) nodes and organic linkers viewed along b-axis of symmetry [41]. (b) Unit cell structure with europium(III) nodes and organic linkers [41].

across the surface of the cylinder or prism. The cylindrical approximation has been used previously to approximate a carbon nanotube (see Cox *et al.* [13]). The first approximation used for the MOF pore is a cylinder, shown in Figure 1.6. The b-axis in Figure 1.5 is orientated in the same direction as the x-axis in the Cartesian coordinate frame of the symmetrical cylinder approximation in Figure 1.6.

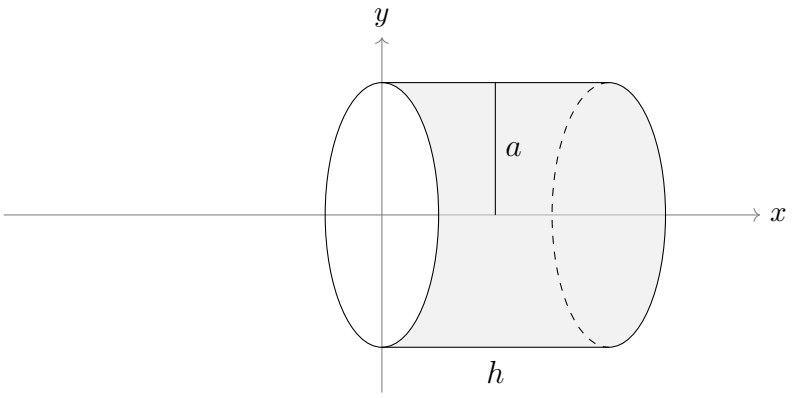


Figure 1.6: Unit cell cylindrical geometry.

The length of each base vector of a unit cell is listed in Table 1.1 [41].

Geometric parameters	
a-axis basis vector	11.513Å
b-axis basis vector	6.829Å
c-axis basis vector	20.976Å
a-axis and c-axis intersection angle	$\theta = 102.8°$

Table 1.1: Physical attributes of EuBDC-OMe [41].

As a first approximation, the data in Table 1.1 is used to approximate the pore by a cylinder of radius, $a = 5.7565\,\text{Å}$ ($= 11.513/2$ Å). One unit cell has depth, $h = 6.8290\,\text{Å}$ (b-axis basis vector), so that the surface area of a unit cell is approximately $246.9992\,\text{Å}^2$.

It is important to know how many atoms of each type are in a unit cell to calculate the mean surface density of each atom in the MOF. Using the molecular formula and additional information in [41], the number of each atom type can be deduced. Table 1.2 shows the logic used to count atom types.

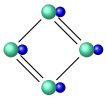
Diagram	Molecular formula	Explanation
	$Eu_2(C_9H_6O_5)_3$	The simplest chemical structure is ligands connected to an europium node.
	$2\,Eu_2(C_9H_6O_5)_3$	An additional simple chemical structure to create a pore.
	$2\,Eu_2(C_9H_6O_5)_3 + 2\,Eu_2$	The simple structures are joined with two europium nodes.
	$2\,Eu_2(C_9H_6O_5)_3 + 2\,Eu_2 + 8\,H_2O$	Each europium atom has a water molecule attached to it.

Table 1.2: Counting atoms where one black line represents one ligand, one turquoise circle represents two europium atoms, and one blue circle two water molecules.

The molecular formula for the MOF crystals is $Eu_2(C_9H_6O_5)_3 \cdot 2\,H_2O$ and each repeating unit in the pore consists of two of these molecular units with four linking europium atoms and water molecules [41]; in this PhD project this europium-based MOF will be referred to as EuMOF. Finally, mean surface densities for each atom type can be calculated, shown in Table 1.3.

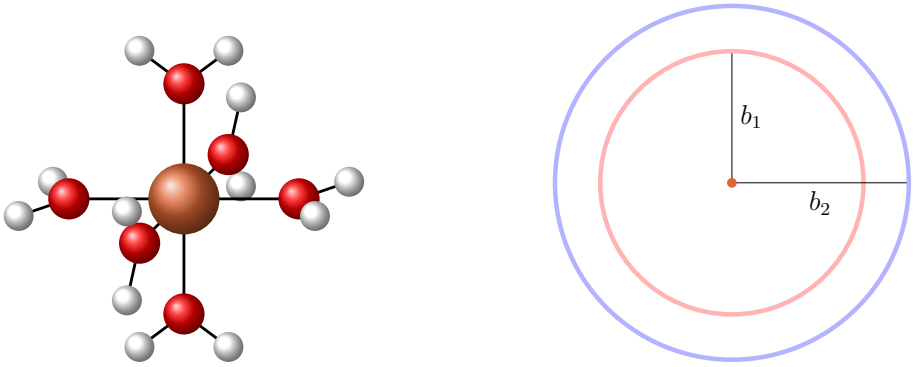
Atom type	Number of atoms	Mean surface density, Å^{-2}
Europium(III), Eu^{3+}	8	$n_{Eu} = 0.0324$
Hydrogen, H	52	$n_H = 0.2105$
Oxygen, O	38	$n_O = 0.1538$
Carbon, C	54	$n_C = 0.2186$

Table 1.3: Mean density for each atom type for approximated cylindrical MOF unit cell.

1.3.2. Physical attributes of a hydrated ferric ion

In their stable state, ferric ions in solution are bonded with six water molecules. Jarzecki *et al.* [26] studied the geometric structure of these hexa-aqua iron(III) clusters: a graphical representation is

given in Figure 1.7(a). In a similar manner to the MOF pore, a continuum approach is taken to approximate the hydrated ferric ion with a point surrounded by an oxygen sphere, which is in turn surrounded by a hydrogen sphere, Figure 1.7(b).



(a) (b)

Figure 1.7: (a) Atomic structure of ferric ion (rusty red centre sphere) with 6 water molecules, where oxygen atoms are red spheres and hydrogen white [26]. (b) Ferric ion is approximated by point, with inner oxygen sphere and outer hydrogen sphere.

Adisa *et al.* [1] used a similar geometric approximation to calculate the interaction energies between a methane molecule and a carbon nanotube, while Baowan *et al.* [5] considered an adamantane molecule interacting with a carbon nanotube. In the case of the adamantane molecule, the spherical approximation produces results comparable to density-functional theory (DFT) calculations, even when the hydrogen atoms are ignored, and even though this molecule has an irregular shape. In other words, the spherical approximation gives reliable insight and results, even though the adamantane molecule has an irregular shape. The model's predicted equilibrium distances (i.e. a distance with respect to the carbon nanotube where no interaction force acts on the molecule) are within a 10% range of the DFT calculated equilibrium distances. Although there was a large discrepancy in binding energy between the adamantane molecule and a carbon nanotube, this was due to the model only accounting for the van der Waals energies and not the entirety of the DFT calculations.

The bond length and angles between the ferric ion, oxygen and hydrogen atoms were measured by Jarzecki *et al.* [26] using B3LYP/6-31G (a fully optimised polarisable continuum model (PCM) structure) and Ahlrichs' VTZ level of theory (in vacuum) and are shown in Table 1.4.

The radius of the oxygen (and hydrogen) sphere is taken as the distance from the centre of the ferric ion to the centre of an oxygen atom (and hydrogen atom). From the dimensions provided in Table 1.4, the radii of the oxygen and hydrogen sphere is given by $b_1 = 2.039\,\text{Å}$ and $b_2 = 2.741\,\text{Å}$ (

Bond length, Å		Angles, degrees	
Fe-O	2.039	O-Fe-O	90.000°
O-H	0.982	H-O-H	106.760°

Table 1.4: Experimental bonds distances and angles [26] using B3LYP/6-31G.

$= [2.039^2 + 0.982^2 - 2 \times 2.039 \times 0.982 \times \cos(\frac{360-106.76}{2})]^{1/2})$. The radius of the hydrogen sphere is calculated using the cosine rule to find the centre-to-centre distance between the ferric ion and the hydrogen atom, where the distances Fe-O and O-H are known and the angle Fe-O-H can be easily calculated since the H-O-H angle is known. The resulting surface area of the oxygen and hydrogen spheres are $52.245\,\text{Å}^2$ and $94.381\,\text{Å}^2$, respectively.

The mean atom densities of the approximate spheres are shown in Table 1.5.

Atom type	Number of atoms	Mean surface density, Å^{-2}
Hydrogen, H	12	$n_{\text{HS}} = 0.1271$
Oxygen, O	6	$n_{\text{OS}} = 0.1148$
Iron(III), Fe^{3+}	1	

Table 1.5: Mean density for hydrogen and oxygen in approximate concentric spheres.

Finally, the atomic mass of a ferric ion is $55.845\,00\,\text{g mol}^{-1}$, an oxygen atom is $15.999\,40\,\text{g mol}^{-1}$ and a hydrogen atom is $1.007\,94\,\text{g mol}^{-1}$ [53].

1.3.3. Physical attributes of polymer

Polymers are large molecules (macromolecules) created by the polymerization of monomers [28]. In the fabrication of the thin film coating, 2-hydroxyethyl methacrylate monomer (HEMA) was used [40]. When MOF crystals are embedded into the polymer thin film, the crystals do not form covalent or ionic bonds to the polymer chains. For the MOF crystals to remain within the polymer thin film, the use of crosslinkers is required. Crosslinkers are used to link together two or more molecules by covalent bonding, increasing rigidity but retaining binding sites (for the MOF crystals) [3]. Rozenberga *et al.* [40] used crosslinker ethylene glycol dimethacrylate (EGDMA). The molecular representations of the crosslinker and monomer are shown in Figure 1.8. The thin film polymer composite is fabricated using HEMA and EGDMA and is called polyHEMA [40].

The monomers, crosslinkers and MOF crystals are suspended together in solution and processed to synthesise the MOF-polymer thin film. Therefore, the process of embedding the MOF crystals and the crosslinking occur simultaneously.

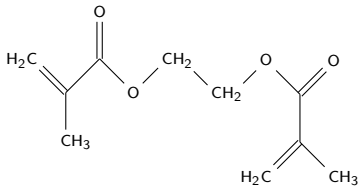
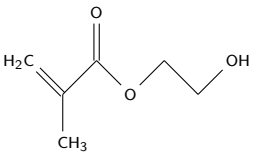
Crosslinker	Monomer
Ethylene glycol dimethacrylate	2-Hydroxyethyl methacrylate
	

Figure 1.8: 2D representation of molecular structure of crosslinker and monomer used to create thin film to hold MOF crystals.

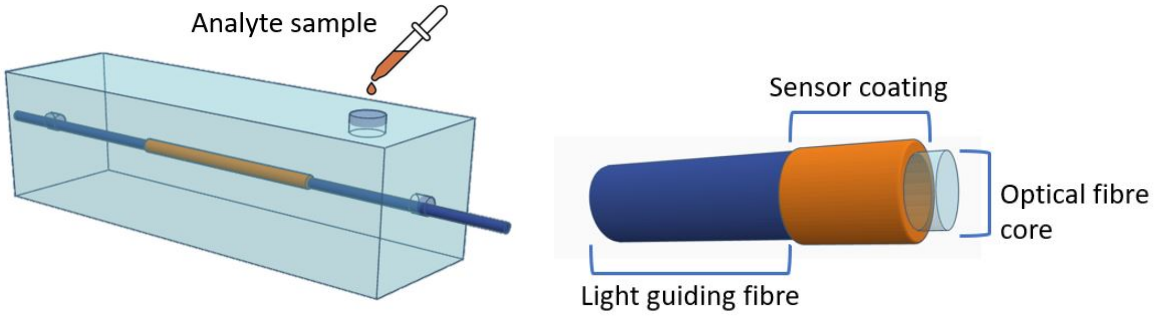
The sensor is intended for ferric ion detection, and consequently, it is important that ferric ions can diffuse into and through the polymer composite to interact with the embedded MOF crystals. There are two aspects that needs to be considered in terms of ferric ion diffusion: the "branchiness" of the crosslinker and the degree of crosslinking [27]. A non-branched crosslinker is a straight singular chain. Figure 1.8 shows that EGDMA is branched. The more branched the crosslinker is, the more porous the polymer composite is, since ferric ions require the water medium to transport them through the polymer composite to associate with MOF crystals away from the polymer composite surface.

When the degree of crosslinking is increased, the volume ratio of crosslinker to polymer increases, implying that more (but smaller) pores are formed and more MOF crystals can be embedded in the polymer composite. However, the increase in degree of crosslinking decreases the permeability for diffusion. If diffusion through the polymer composite is reduced, the sensor would require a longer exposure time for ferric ions to interact with embedded MOF crystals. This is particularly important for MOF crystals farthest from the polymer composite's exposed surface. Therefore, the degree of crosslinking needs to be robust enough to retain MOF crystals in the polymer composite while at the same time retain water permeability of the coating.

The final composition of the thin film is PolyHEMA with 8% cross-linker and 0.5% MOF [40].

1.3.4. Testing device

Figure 1.9(a) depicts one of the iterations of the proposed sensor design by Rozenberga. Since the optic fibres are fragile, the fibre is placed in a cast to reduce the probability of breakage. The EuMOF crystals are embedded in a polymer composite to create a thin film coating over a section of the optic fibre, Figure 1.9(b).



(a) (b)

Figure 1.9: (a) Sensor in cast with analyte solution containing ferric ions being dispensed. (b) Ferric ion sensor design [39].

When the sensor is submerged in an analyte solution containing ferric ions, ferric ions will associate with the MOF crystals. A light pulse sent through the optic fibre from a light source, Figure 1.2, will illuminate the sensor and florescence readings are recorded by the spectrometer, and processed by the computer to determine ferric ion concentration. MOF crystals illuminate because of the light source and when ferric ions associate to the MOF crystals, the ferric ions quench the emitted light.

In [40], the florescence sensitivity of the EuMOF is tested against multiple cations (for example Na(II), Mg(II), Zn(II) and Fe(II)) and Fe(III), where the "turn-off" sensing was greatest in the presence of ferric ions and little effect was shown for the other tested cations.

1.4. MATHEMATICAL METHODS

Various mathematical tools are used to investigate the behaviour between ferric ions and the sensor. In this environment, the length scale has two distinct orders of magnitude: atomic, 10^{-10}, and colloidal, 10^{-6}. These two environments are later referred to as the microenvironment and macroenvironment, respectively.

The microenvironment aims to understand how ferric ions interact with MOF crystals. There are two basic approaches to calculate the interaction energies and forces between two atoms or between two molecules [46, 47]. Either a discrete method where many discrete methods use molecular dynamics to calculate forces between each interacting non-bonded pair of atoms, or a continuum method to approximate the non-bonded atoms (or molecules) as geometric shapes, followed by a calculation of the interaction energy between each interacting body [1, 2]. In this thesis, the second

approach is used. The hydrated ferric ion and MOF pore geometry are parametrised by a point with two concentric spheres and a semi-infinite cylinder (or finite cylinder or semi-infinite prism), respectively. Following this parametrisation, the Lennard-Jones potential is used to calculate the van der Waals energies and forces between a hydrated ferric ion and a MOF pore.

The macroenvironment aims to understand the diffusion of ferric ions through solution (and the polymer) to associate with MOF crystals. Regions of the Cartesian coordinate frame are defined to represent the solution, the polymer composite, and a single MOF crystal at the solution polymer boundary. The movement of ferric ions is assumed to be governed by Brownian motion. Therefore, ferric ion movement through the solution and polymer is governed by the conventional diffusion equation, and the MOF pore occupancy is governed by a pseudo ordinary differential equation (ODE). Numerical techniques are used to solve the system of equations and understand what physical properties affect ferric ion diffusion. An explicit Runga-Kutta 4 is used to discretise the pseudo ODE since it is more accurate and reliable than the Euler method. In one-dimension, ferric ion diffusion is solved using Crank-Nicolson forwards-time, centred-space because this scheme is unconditionally stable. In two-dimensions, ferric ion diffusion is solved using a forwards-time, two-dimensional centred-space finite difference scheme and step sizes are chosen such that the scheme is stable.

To study the effects of MOF crystals uniformly distributed in the polymer composite, the property that the total density of ferric ions is conserved (that is, the total of the dissolved ions in the polymer and those associated with the MOF crystals is conserved), is exploited. Algebraic methods are used to find a solution such that ferric ion density in the system is conserved and to find an analytical solution for dissolved ferric ion concentration.

Perturbation methods, in conjunction with Laplace and Fourier transforms, and Lie point symmetries are used as alternative methods to solve for one-dimensional differential equations found in the macroenvironment.

1.5. AIMS AND STRUCTURE OF THESIS

This project aims to develop a theoretical understanding of the processes governing the diffusion of ferric ions through solution and the polymer media, and the interaction of ferric ions with MOF crystals embedded in the polymer composite. This research is split into three main parts,

I. Microenvironment: Analyse the interaction forces and energies between the hydrated ferric

ion and a MOF pore, while considering different MOF pore approximations.

II. Macroenvironment: Model the diffusion of ferric ions through solution and the polymer composite media with the MOF crystals acting as a sink. First, consider a MOF crystal at the solution-polymer boundary, and then consider MOF crystals distributed throughout the polymer composite.

III. Mathematical exploration: Use perturbations and symmetry techniques to investigate the equations describing ferric ion diffusion in the polymer composite and MOF occupancy.

Part I, the microenvironment, investigates the environment at the atomic scale to understand how the hexa-hydrated ferric ions interact with the EuMOF crystals in the sensor. Chapter 2 provides the theory behind the Lennard-Jones potential and the justification of its use to calculate the interaction energies and forces. This chapter also acknowledges the effect of temperature on the system and on the resulting calculations. The Lennard-Jones theory is applied to the approximated hydrated ferric ion and semi-infinite (and finite) cylindrical MOF pore in Chapter 3 (and 4). In Chapter 5, changes in the modelling environment are considered, such as other metal ions interacting with the MOF pore, approximating the MOF pore using a prism, implications of blocked pore, a discussion considering multiple pore interactions, and the implication of a change in temperature.

Some physical insights obtained in Part I are: (i) Ferric ions cannot fit inside the MOF pore, therefore ferric ions have surface level association to MOF crystals. The consequence of this results is that the sensor can be re-used and double detection of ferric ions is avoided. (ii) The water molecules of the hydrated ferric ion contribute the most to the interaction between the MOF pores and the hydrated ferric ions. (iii) Changes in temperature do not have a qualitative impact on the interaction. (iv) Other metals ions are attracted to the MOF pore, however they do not impact fluorescence sensing.

Part II, the macroenvironment, seeks to understand how the hydrated ferric ions diffuse through the solution and into MOF-polymer sensor coating. Chapter 7 provides insight into which physical attributes of the system affect the time taken for the MOF crystals to reach steady state in terms of the number of ferric ions associated to the crystal surface. In Chapter 8, the effects of MOF crystal density in the polymer composite are investigated.

Some physical insights obtained in Part II are: (i) The important ferric ion and MOF characteristics, and their impact on sensing time are identified. (ii) There are two different time-scales that are important for modelling the sensing device, implying that MOF crystal saturation will occur faster

than ferric ion diffusion through the polymer composite. (iii) Fewer MOF crystals are required in the polymer composite for solutions with known high ferric ion concentrations. (iv) Polymer composites with more MOF crystals require a longer exposure time.

Part III, mathematical exploration, is more mathematically focused and seeks to establish analytical solutions for the differential equations describing diffusion of ferric ions in the MOF crystal-embedded polymer composite using perturbation methods and Lie point symmetries.

Part I

Microenvironment

Part I studies the environment at an atomic scale to investigate how a ferric ion interacts with a MOF pore. In situ, it is problematic to directly observe how ferric ions and MOF crystals interact. Therefore, Part I applies established theory to investigate the energetically favourable behaviour of the ferric ion with respect to the MOF pore, and uses the Lennard-Jones potential to calculate the interaction energies and forces between the hydrated ferric ion and the MOF pore.

Unlike in molecular dynamics simulations, where atom-to-atom interactions are considered, Part I uses the continuum approach when determining the interactions. As described in the Introduction, this means that atoms are smoothed over surfaces using the geometric shapes of the relevant structures to calculate the interaction energies and forces. A hydrated ferric ion is approximated as a point and two concentric spheres. The MOF pore is initially approximated using two different cylinders: semi-infinite and finite. This way, the dependence of interaction energies and forces on different pore depths is investigated.

The above model is then expanded to incorporate additional aspects of the sensing environment. Firstly, the interactions between other metal ions and the MOF pore are investigated since there are other metals in the analyte solution, which may interfere with ferric ion sensing. Secondly, the MOF pore parametrisation is changed to a semi-infinite prism to obtain a "truer" representation of the interactions. Thirdly, the interaction between a second ferric ion and a blocked pore are studied, followed by a discussion regarding the impact of a ferric ion interacting with multiple MOF pores. Lastly, the effects of temperature on the interaction energies and forces are considered.

The original contributions contained in Part I broadly fall in three categories: (i) insights, (ii) impact of geometry and atom type, and (iii) mathematical contributions.

First, there is currently no theoretical insight available regarding ferric ion-EuMOF interactions at an atomic scale for the new ferric ion sensor. For example, independent of and prior to experimental testing, this research leads to the understanding that the hydrated ferric ion would be attracted to the MOF pore but does not fit into the pores. A previous study stated that hydrated ferric ions associate to methoxy groups *inside* the MOF pore [59]. However, the calculations in this part show that hydrated ferric ions only associate to the surface of the MOF pore.

Second, the geometric and atom-specific considerations of an ion interacting with a pore are new. The literature contains examples of a point atom interacting with a pore (sphere, cylinder, prism, or cone) where the pore has more than one atom type, and a structured molecule (point and sphere, or torus) interacting with a cylindrical pore with one atom type. This research considers

a structured molecule (point and two concentric spheres) interacting with a cylindrical pore where the pore has more than one atom type, and the interaction between a structured molecule and structured prismatic pore (with planar and linear components) where the pore has more than one atom type. Note that the structured molecule (hydrated ferric ion) also considers multiple atom-specific locations.

Third, Part I applies the methodology developed by Cox *et al.* [13] as the foundation for the research framework. Their methodology provides analytical expressions for the interaction force between a point and a semi-infinite/finite cylinder (also, sphere and cylinder), and expresses them in closed form. In subsequent work [6], they constructed the relevant integral expressions for the interaction energy for other geometric shapes including a point/sphere and a finite cylindrical pore, and a point/sphere and a finite square prismatic pore. In these cases, the interaction energy was expressed as integrals, rather than in closed form. Here, these integral expressions are evaluated in the case of a semi-infinite rectangular prism, and the interaction energies and forces are expressed in closed form. Evaluation of the integrals resulted in an extremely complicated expression, so a simple rule-of-thumb is introduced to approximate the prismatic pore expressions with simpler expressions using an approximate cylindrical pore. This is achieved by matching the cross-sectional areas of the openings of the two different pore shapes.

CHAPTER 2

THEORY OF CALCULATING THE INTERACTION ENERGY AND FORCE

This chapter focuses on the theory of calculating the interaction energy and forces between non-bonded atoms and the application of this theory assuming a continuum approach. Finally, the effect of temperature on the interaction energy between non-bonded atoms is discussed.

2.1. LENNARD-JONES POTENTIAL

There are two main types of forces that might exist: van der Waals forces or Lennard-Jones, and electrostatic or Coulombic forces [14, 31, 48]. The tails leaching process typically occurs in a highly acidic environment and at high salt concentrations, so that the double layers surrounding particles are extremely small, since the Debye length is inversely proportional to the square root of the salt concentration. The higher the ion concentration (and ionic strength), the shorter the Debye length and the smaller the electric double layers. In practice, the analyte solution will have an ionic strength of $0.1 - 0.5$ M, so that the Debye length will be less than 1 nm. In comparison to the MOF crystal particle size (200 ± 150 nm), the double layers will be small so that electrostatic interactions can be ignored [40]. Consequently, the electrostatic or Coulombic forces are expected to be small and over very short distances, so that the Lennard-Jones or van der Waals forces dominate. For this reason, only the van der Waals atomic interaction forces existing between the ferric ions and the EuMOF pores are considered here.

The van der Waals force is weakest amongst the bonding types that atoms/molecules experience when interacting with one another. The strongest kind of van der Waals force is a consequence of dipole-dipole interactions where the presence of polar molecules (such as H_2O) means that the positive end of one molecule is attracted to the negative end of another. Here, the van der Waals interaction between two atoms/molecules separated by a distance, ρ, is described using the Lennard-Jones potential [29], given by

$$U(\rho) = -\frac{A}{\rho^6} + \frac{B}{\rho^{12}}, \tag{2.1}$$

where A and B are the attractive and repulsive constants. This can also be written as

$$U(\rho) = 4\,\epsilon \left[-\left(\frac{\sigma}{\rho}\right)^{6} + \left(\frac{\sigma}{\rho}\right)^{12} \right], \tag{2.2}$$

where $\sigma = (B/A)^{1/6}$ is the van der Waals diameter and $\epsilon = A^2/(4B)$ is the well depth. Alternatively, the Lennard-Jones potential can be written in terms of the equilibrium separation [37],

$$U(\rho) = -2\,\epsilon \left(\frac{\rho_0}{\rho}\right)^{6} + \epsilon \left(\frac{\rho_0}{\rho}\right)^{12},$$

where $\rho_0 = 2^{1/6}\,\sigma$ is the equilibrium separation and represents the separation distance at which the particle(s) experience no force. In Figure 2.1, the profile of the Lennard-Jones potential is depicted with an illustration of the above mentioned parameters.

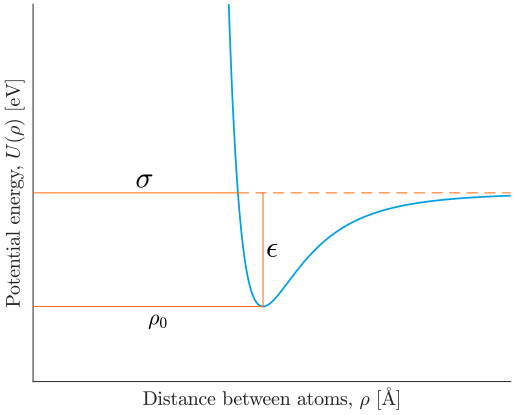


Figure 2.1: Schematic showing how van der Waals potential depends on separation distance, as calculated using Lennard-Jones potential.

Rappé *et al* [37] developed the Universal Force Field table providing rules to estimate elemental properties and parameters for molecules of complex geometry. The Lennard-Jones pair potential parameters for all atom types of relevance to this thesis are taken from [37] and are given in Table 2.1.

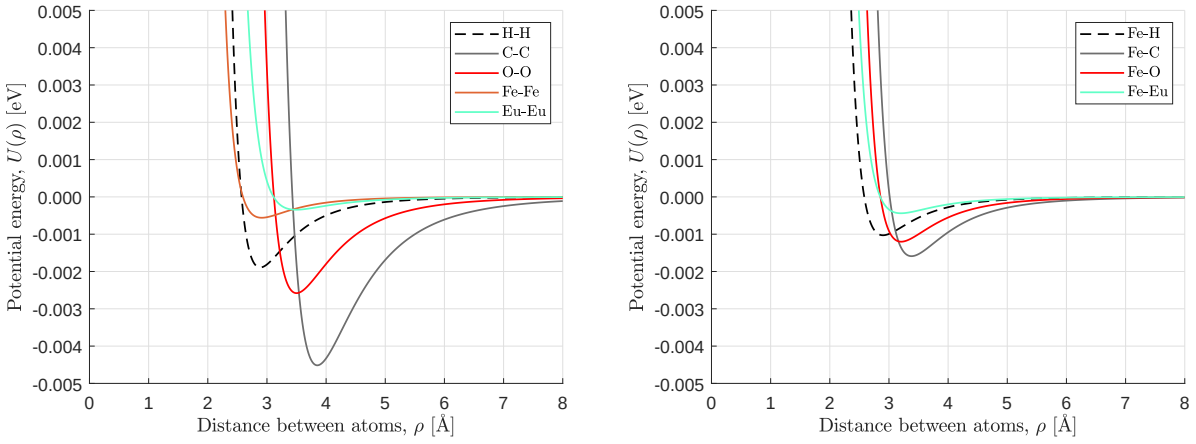
In [37], the Lennard-Jones pair potential parameters are the same for atoms with different valencies. Values for the ferrous ion are provided in [37], therefore it is assumed that the pair potential parameters for ferric ions are the same as for ferrous ions. Using the values in Table 2.1, the potential energies for interactions between atoms of the same type can be calculated using Equation (2.2); Figure 2.2(a) shows the results. Note that these potential energy profiles are specifically for

Atom type	van der Waals diameter, σ (Å)	Well-depth, ϵ (eV)
Europium(III), Eu^{3+}	3.1119	0.0003
Hydrogen, H	2.5711	0.0019
Oxygen, O	3.1181	0.0026
Carbon, C	3.4309	0.0045
Iron(III), Fe^{3+}	2.5943	0.0006

Table 2.1: Lennard-Jones parameters [37].

interactions between atoms of the same type. To investigate interactions between atoms of different types, the geometric and arithmetic mean for the well depth and van der Waals diameter are taken respectively, that is $\epsilon_{ij} = \sqrt{\epsilon_i \epsilon_j}$ and $\sigma_{ij} = (\sigma_i + \sigma_j)/2$ [4]. The interactions of a ferric ion (alone) with a hydrogen, carbon, oxygen and europium atom are shown in Figure 2.2(b).

The well-depth for iron(III)-europium(III) interactions is greater than for the europium-europium interactions, however for all other atoms shown here the reverse is true. That is, the well-depth for interactions with iron(III) is less than for the interactions with atoms of the same type. This implies that less energy is needed to move a hydrogen, a carbon and an oxygen atom away from an iron(III) ion than from an atom of the same type. In the case of iron(III)-europium(III), marginally more energy is needed.



(a) (b)

Figure 2.2: (a) Lennard-Jones potential for interactions between like atom types (electron volts, eV). (b) Lennard-Jones potential between ferric ion and various atom types in MOF pore (eV).

Figure 2.2(b) shows that the van der Waals diameter for all atom types except hydrogen decreases when interacting with iron(III) (in comparison to a like-atom interaction), and subsequently the equilibrium distance at which there is zero net force is smaller. This means that the repulsive energy at a particular separation distance decreases when the ferric ion interacts with carbon, oxygen and

europium. This is because the parameter B in Equation (2.1) becomes smaller. The opposite is true for hydrogen.

2.2. INTERACTION ENERGIES AND FORCE BETWEEN TWO PARTICLES

This section provides the equations required to model the van der Waals interaction energy and force between objects of various geometries of relevance to this project. Whilst applying these functions to the established geometries, Part I of this thesis assumes that the MOF pore is static (i.e. does not move or distort).

2.2.1. Interaction energy

To calculate the total interaction energy between a hydrated ferric ion and a MOF pore, the contributions of all possible combinations of interacting atoms are added,

$$E = \sum_i \sum_j U(\rho),$$

where $U(\rho)$ is the Lennard-Jones potential between atoms i (in the hydrated ferric ion) and j (in the MOF pore) that are distance ρ apart. As described in Section 1.3.1, a continuum approximation is taken for both the MOF pore and the hydrated ferric ion, smoothing the atoms over the surface of a cylinder and two spheres respectively (see Figures 1.6 and 1.7). As a consequence, when investigating the interaction potential between two geometric shapes (e.g. a cylinder and a sphere), the double summation above can be replaced with an integral over the two surfaces, S_i

$$E = n_1\, n_2 \int_{S_1} \int_{S_2} U(\rho)\, \mathrm{d}S_2\, \mathrm{d}S_1, \tag{2.3}$$

where n_i is the mean surface density of atoms on the two interacting objects.

2.2.2. Interaction force

The van der Waals force is a distance-dependent force between atoms and/or molecules, which in most cases is relatively weaker than ionic bonds and always weaker than covalent bonds. The Lennard-Jones potential is used to model the interaction potential between a point object representing the hydrated ferric ion and the MOF pore.

The van der Waals force experienced by a point object outside the pore and located on the pore's axis of symmetry can be calculated by differentiating the Lennard-Jones potential. The force acts in the direction of the atoms on the cylindrical surface (see Figure 2.3) so that the force in the axial direction may be calculated using similar triangles,

$$F(x) = F_{\text{vdW}} \frac{(X-x)}{\rho} = \frac{\mathrm{d}\,E}{\mathrm{d}\rho} \frac{(x-X)}{\rho}, \tag{2.4}$$

where $\rho^2 = a^2 + (x-X)^2$, a is the radius of the cylinder, and X is the horizontal distance of the point object from the pore's entrance. The interaction energy E, is given by Equation (2.3).

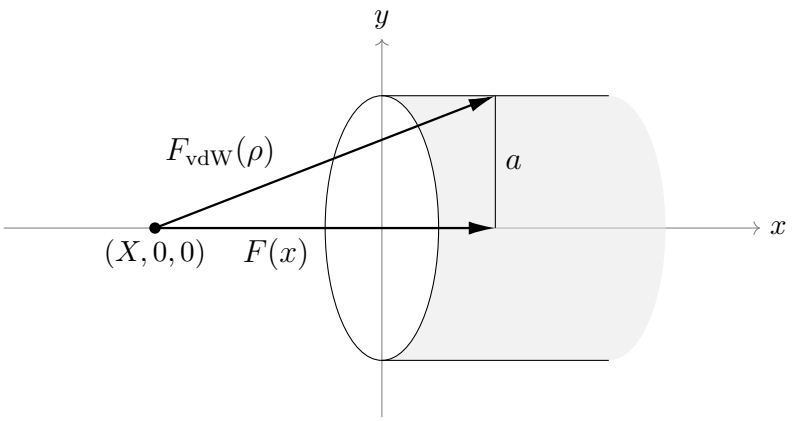


Figure 2.3: van der Waals force, F_{vdW}, between point object located on axis of symmetry and atoms on cylindrical surface, and interaction forces in axial direction between atom and cylindrical pore.

2.2.3. Acceptance and kinetic energy

Whether an object is sucked into any pore or cavity is both a mechanical and geometrical problem. It is mechanical in the sense that there are certain forces at play but is it also geometrical in the sense that the object must be small enough to enter the pore.

Assuming energy is conserved, then the kinetic energy gained by an object when acted upon by a force which causes it to move, is calculated by integrating the force over an interval of space,

$$Ek = \int F\,dx.$$

Here, the van der Waals force is that between the MOF pore and the hydrated ferric ion, and the hydrated ferric ion moves towards or away from the MOF pore. More specifically, the amount of kinetic energy gained by the hydrated ferric ion as a consequence of the van der Waals force when

it is moved from an infinitely large distance away to the location X may be calculated using

$$Ek = \int_{-\infty}^{X} F dx,$$

where $F(x)$ is given by Equation (2.4).

Depending on the radius of the pore, the direction of the van der Waals force experienced by the object may depend on its location relative to the pore's entrance. That is, for some values of X the force may be directed to the left in Figure 2.3, while at other locations it may be directed to the right. This section focuses on atoms/molecules initially located outside the MOF pore entrance, and calculates whether the kinetic energy gained by the object will be sufficient for it to enter the pore. In order for the energy to be sufficient, the kinetic energy gain as a consequence of the force to the right must be greater than the kinetic energy lost as a consequence of the force to the left. The acceptance energy, Ea, is defined to be the amount of kinetic energy gained by the object when it starts far away and moves to a specific location within the pore. If the acceptance energy is positive, then the object will gain enough energy to enter the pore and will not exit from the entrance. Assuming the object starts at rest and far away from the pore, if the acceptance energy is negative, then either the object will be attracted towards the MOF pore but will not gain enough energy to enter the pore and remain there (it may not reach the entrance, or it may enter and then exit again), or perhaps the object will be repelled away from the pore. In this case, the object must be initially moving in the direction of the pore to enter and remain in the pore.

For a pore with a radius such that the interaction force is positive regardless of the location of the object (that is, force is always directed to the right), the acceptance energy will be positive, while for a pore with a radius such that the interaction force is negative regardless of the location of the object (that is, always directed to the left), the acceptance energy will be negative. Section 1.3.1 introduces two MOF pore depths studies in the microenvironment: semi-infinite and finite. These two different depths affect how acceptance and kinetic energies are calculated, and each calculation is described below.

Semi-infinite pores with a radius such that the direction of the interaction force depends on the object's relative location to the pore's entrance requires careful consideration. Consider a pore of semi-infinite depth which has an interaction force function that is even about the entrance to the pore. An object will be accepted into the semi-infinite pore if the kinetic energy required to move

the object from the far (left) field ($X \to -\infty$) to the location $X_0 \geq 0$,

$$Ea = \int_{-\infty}^{X_0} F dx, \tag{2.5}$$

is positive, where X_0 is the attraction limit of the interaction force (a detailed definition of the attraction limit is provided in Subsection 3.2.2). If the van der Waals interaction force is positive everywhere, then the attraction limit is at the pore entrance ($X_0 = 0$). Otherwise, the attraction limit is a specific point near the right-side of the pore entrance ($X_0 > 0$).

The maximum kinetic energy gain by an object due to the van der Waals forces can also be calculated. For a semi-infinite pore depth, the maximum kinetic energy gained as a consequence of the van der Waals forces on an object to move it from the far (left) field to far (right) into the pore is,

$$Ek = \int_{-\infty}^{\infty} F dx. \tag{2.6}$$

A pore with a finite depth d has an odd interaction force function centred about the centre of the pore at $d/2$. Section 4.2.2 provides an algebraic proof that there is a root of the interaction force for a point object at the mid-depth of the pore, i.e. $F(d/2) = 0$; numerical calculations show that this also holds true for concentric spheres. Therefore, the upper bound for the right-side attraction limit is $d/2$ and is excluded from the integral when calculating the acceptance energy of an object into the MOF pore (Equation (2.5)), where $X_0 \in [0, d/2)$. This is because acceptance energy is evaluated for an object from the far (left) field to near right-side (or at) the entrance of the pore to determine if the object will have enough energy to enter and remain inside the pore.

Since the interaction force function for a finite pore is odd centred at the pore mid-depth, the kinetic energy is only a maximum at pore depth $d/2$, i.e. the upper bound of Equation (2.6) is $d/2$. For a finite pore depth, the maximum kinetic energy gain as a consequence of the van der Waals forces on an object to move it from the far (left) field to the pore mid-depth is,

$$Ek = \int_{-\infty}^{d/2} F dx. \tag{2.7}$$

2.3. EFFECTS OF TEMPERATURE ON LENNARD-JONES POTENTIAL

The Lennard-Jones parameters provided in Table 2.1 are from the Universal Force Field (UFF) table [37], which provides force field parameters for elements in the periodic table in order to simulate

molecular mechanics and molecular dynamics. There is no specific mention of temperature and therefore this project assumes that the values are accurate at room temperature, that is, 20 °C (293 K).

Temperature has an impact on the magnitude of the Lennard-Jones pair potential parameters, i.e. the well-depth ϵ and the van der Waals diameter, σ. Nasehzadeh et al. [33] applies the Chandler-Weeks-Andersen perturbation theory as modified by Verlet and Wies [51, 52] to express the pair potential parameters as linear functions of temperature. The van der Waals diameter increases with an increase in temperature, whereas the well-depth decreases with an increase in temperature. In addition, the well-depth ϵ has a greater sensitivity to changes in temperature.

Zarkova and Hohm [61] uses a temperature dependent Lennard-Jones potential to calculate virial coefficients, viscosity and diffusion coefficients of alkenes and cyclealkanes C_mH_{2m} for a temperature range of 200 K to 1000 K and pressures 0.1 MPa and less. Unlike in [33], the Lennard-Jones pair potential parameters are non-linear. The equilibrium separation, $\rho_0 = 2^{1/6}\sigma$, was assumed to be a function of temperature that included the non-linear vibrational partition function.

Online sensing of the ferric ion concentration, where the sensor is placed directly in the leaching circuit to measure iron concentration in the solution, is preferable to offline sensing where a sample solution is taken to the laboratory for testing. The leaching temperature onsite can range from 50 °C (323 K) to 100 °C (373 K). Generally, the temperature at the mining site at Roxy Downs ranges from 0 °C (273 K) to 50 °C (323 K). It is not economical to regulate the temperature of the tailings circuit. The majority of calculations in this thesis are performed using values of the Lennard-Jones parameters suitable for 293 K.

Section 5.6 investigates changes in temperature and its impact on the interaction energy and force. While the temperature range in the leaching circuit affects the magnitude of the interactions, the qualitative nature of the interaction does not change. Further discussion appears in Section 5.6.

CHAPTER 3

INTERACTIONS BETWEEN A HYDRATED FERRIC ION AND A SEMI-INFINITE CYLINDRICAL MOF PORE

This chapter focuses on the interactions between a hydrated ferric ion and a MOF pore. Using the continuum approach, the hydrated ferric ion is approximated by a charged point mass and the water molecules by concentric oxygen and hydrogen spheres centred on the ferric ion, while the MOF pore is approximated by a semi-infinite cylinder, as shown in Figure 3.1. First, the interaction energies between the MOF pore and the ferric ion, oxygen and hydrogen spheres are calculated and results are discussed. Second, the interaction forces and the attraction limit of the interaction force are calculated. Third, the acceptance energy and the maximum kinetic energy is calculated to determine whether the ferric ion, the oxygen sphere and the hydrogen sphere are (un)conditionally accepted into the MOF pore and determine the maximum energy gain. Lastly, a discussion regarding the interactions between a hydrated ferric ion and a MOF pore is provided.

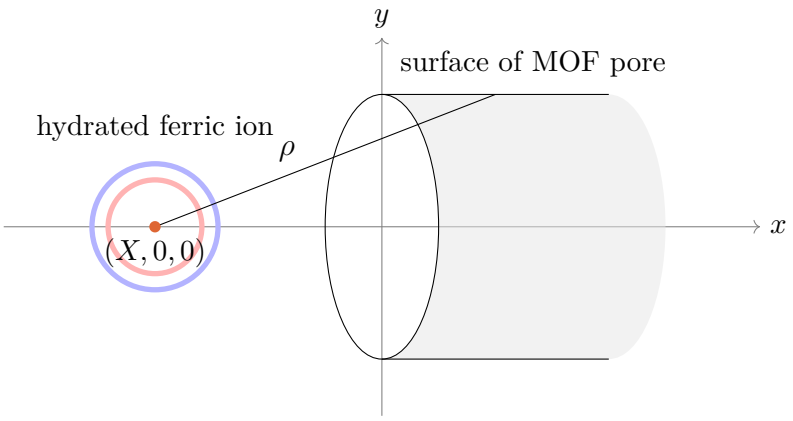


Figure 3.1: Geometrical approximations of hydrated ferric ion and MOF pore approximated by semi-infinite cylinder.

In Figure 3.1, the ferric ion is characterised by a point located on the axis of symmetry near the entrance of the pore and has Cartesian coordinates $(X, 0, 0)$, where $X < 0$. The oxygen sphere has a radius of b_1, the hydrogen sphere b_2, and both are centred at $(X, 0, 0)$. The surface of the pore is defined as $(x, a\sin\theta, a\cos\theta)$ characterised using Cartesian coordinates, where a is the pore radius, $\theta \in [0, 2\pi]$ and the entrance of the pore is located at $x = 0$, so that $x > 0$ is the distance into the pore.

Using the Pythagoras theorem, the distance between the point $(X, 0, 0)$ and a point $(x, a\sin\theta, a\cos\theta)$

on the surface of the semi-infinite cylinder is given by

$$\rho^2 = (x - X)^2 + a^2. \tag{3.1}$$

3.1. INTERACTION ENERGIES

Assuming the MOF pore is cylindrical and that the atoms are evenly spread (i.e. smoothed over the surface), the total interaction energy between the hydrated ferric ion and the MOF pore is given by

$$E_{\text{tot}} = E_{\text{Fe}} + E_{\text{OS}} + E_{\text{HS}}, \tag{3.2}$$

where E_{Fe} is the interaction energy between the ferric ion and the MOF pore, and E_{OS} and E_{HS} are the interaction energies between the MOF pore and the oxygen and hydrogen spheres, respectively. These quantities can be calculated using Equation (2.3). The following sections give details for the calculation of each of these energies.

3.1.1. Ferric ion point to MOF pore

The interaction energy between a ferric ion and the MOF pore will be the sum of the interaction energies between the ferric ion and each atom type in the MOF pore,

$$E_{\text{Fe}}(X) = E_{\text{Fe,Eu}} + E_{\text{Fe,H}} + E_{\text{Fe,O}} + E_{\text{Fe,C}} = \sum_k E_{\text{Fe},k}, \tag{3.3}$$

where $k \in \{\text{Eu}, \text{H}, \text{O}, \text{C}\}$ and $E_{\text{Fe},k}$ denotes the interaction energy of the ferric ion point with atom type k in the MOF pore. Each of these terms may be calculated using Equation (2.3). The ferric ion is treated as a point, thereby reducing the double integral to a single integral over the surface of the MOF pore only. The interaction energy between the point ferric ion and one atom type in the semi-infinite MOF pore is given by

$$\begin{aligned} E_{\text{Fe},k}(X) &= n_k \int_{S_1} U(\rho) \mathrm{d}S_1, \\ &= 2\pi\, a\, n_k \int_0^\infty \left[-\frac{A_{\text{Fe},k}}{\rho^6} + \frac{B_{\text{Fe},k}}{\rho^{12}} \right] \mathrm{d}x, \end{aligned} \tag{3.4}$$

where n_k is the mean surface density of atom type k, and $A_{\text{Fe},k}$ and $B_{\text{Fe},k}$ are the attractive and repulsive constants for an interaction between a ferric ion and atom k. By writing ρ in terms of x,

this integral may be written as

$$E_{\mathrm{Fe},k}(X) = \frac{2\pi\, n_k}{a^4}\left[-A_{\mathrm{Fe},k}\, J_2(a,-X) + \frac{1}{a^6} B_{\mathrm{Fe},k}\, J_5(a,-X)\right], \tag{3.5}$$

where the J_n are integrals of powers of cosine functions as defined in Equation (D.2) (see Appendix D for details). The total interaction energy can then be calculated using Equation (3.3),

$$E_{\mathrm{Fe}}(X) = \frac{2\pi}{a^4}\sum_k n_k\left[-A_{\mathrm{Fe},k}\, J_2(a,-X) + \frac{1}{a^6} B_{\mathrm{Fe},k}\, J_5(a,-X)\right].$$

The interaction energy profiles between the ferric ion and each of the four atom types in the MOF pore are shown in Figure 3.2. The interaction energy between the ferric ion and europium contributes the least to the total energy, whereas the interaction energy between the ferric ion and carbon has the highest contribution. This is partly due to the number of carbon atoms present in the MOF pore. It is energetically favourable for the ferric ion to enter and remain inside the MOF pore, since the global minimum of the total interaction energy E_{Fe} is located inside the MOF pore. The potential energy minimum for the ferric ion inside the MOF pore is approximately $-0.012\,\mathrm{eV}$.

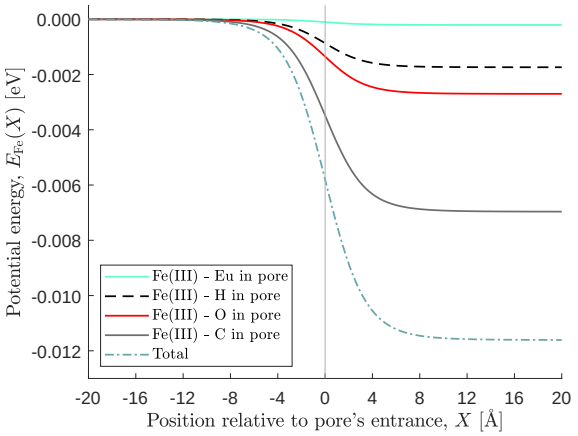


Figure 3.2: Interaction energy between ferric ion and semi-infinite cylindrical MOF pore, Equations (3.5) and (3.3). Vertical line marks location of pore opening.

3.1.2. Oxygen and hydrogen spheres to MOF pore

The total interaction energy between the oxygen sphere (OS) and the MOF pore is given by

$$E_{\mathrm{OS}}(X) = E_{\mathrm{OS,Eu}} + E_{\mathrm{OS,H}} + E_{\mathrm{OS,O}} + E_{\mathrm{OS,C}} = \sum_k E_{\mathrm{OS},k}, \tag{3.6}$$

where $k \in \{\mathrm{Eu}, \mathrm{H}, \mathrm{O}, \mathrm{C}\}$. Note that the subscript OS,O is the oxygen sphere interacting with the oxygen atoms in the MOF pore. Since the interaction is between like atom types, there are no adjustments made to the attractive and repulsive constants in the energetic profile for $E_{\mathrm{OS,O}}$ (see Section 2.1).

The interaction energy between the surface of the oxygen sphere and the cylindrical MOF pore, taking in consideration only atom type k, can be calculated using Equation (2.3), so that

$$E_{\mathrm{OS},k}(X) = n_k \, n_{\mathrm{OS}} \int_{S_1} \int_{S_2} U(\rho) \, \mathrm{d}S_2 \, \mathrm{d}S_1,$$

where S_1 is the surface of the MOF pore with a mean density of atoms n_k and S_2 is the surface of the oxygen sphere with a mean surface density of oxygen atoms n_{OS}.

The integral over the surface of the sphere can be evaluated to give [1, 13],

$$\begin{aligned} G(\rho) &= n_{\mathrm{OS}} \int_{S_2} U(\rho) \, \mathrm{d}S_2, \\ &= \frac{\pi \, b_1 \, n_{\mathrm{OS}}}{\rho} \left[\frac{A_{\mathrm{O},k}}{2} \left(\frac{1}{(\rho + b_1)^4} - \frac{1}{(\rho - b_1)^4} \right) - \frac{B_{\mathrm{O},k}}{5} \left(\frac{1}{(\rho + b_1)^{10}} - \frac{1}{(\rho - b_1)^{10}} \right) \right]. \end{aligned} \tag{3.7}$$

The interaction energy between the oxygen sphere and a representative atom type in the MOF pore is found by integrating $G(\rho)$ over the surface of the cylinder (details are shown in Appendix A),

$$\begin{aligned} E_{\mathrm{OS},k}(X) &= n_k \int_{S_1} G(\rho) \mathrm{d}S_1, \\ &= 2\pi \, a \, n_k \int_0^\infty G(\rho) \mathrm{d}x, \\ &= 8\pi^2 \, a \, b_1^2 \, n_k \, n_{\mathrm{OS}} \, \lambda_1^{-5} \left[-A_{\mathrm{O},k} \left(J_2(\lambda_1, -X) + 2 \, b_1^2 \, \lambda_1^{-2} \, J_3(\lambda_1, -X) \right) \right. \\ &\quad + \frac{1}{5} B_{\mathrm{O},k} \, \lambda_1^{-6} \left(5 \, J_5(\lambda_1, -X) + 80 \, b_1^2 \, \lambda_1^{-2} J_6(\lambda_1, -X) + 336 \, b_1^4 \, \lambda_1^{-4} J_7(\lambda_1, -X) \right. \\ &\quad \left. \left. + 512 \, b_1^6 \, \lambda_1^{-6} J_8(\lambda_1, -X) + 256 \, b_1^8 \, \lambda_1^{-8} J_9(\lambda_1, -X) \right) \right], \end{aligned} \tag{3.8}$$

where $\lambda_1^2 = a^2 - b_1^2$, a is the radius of the MOF pore, b_1 is the radius of the oxygen sphere, and the $J_n(\lambda_1, -X)$ are integrals of powers of cosine functions defined in Appendix D.

The total interaction energy between the oxygen sphere and the MOF pore can be calculated by

using Equation (3.6)

$$E_{\mathrm{OS}}(X) = 8\pi^2\, a\, b_1^2\, n_{\mathrm{OS}}\, \lambda_1^{-5} \sum_k n_k \left[-A_{\mathrm{O},k} \left(J_2(\lambda_1, -X) + 2\, b_1^2\, \lambda_1^{-2}\, J_3(\lambda_1, -X) \right) \right.$$
$$+ \frac{1}{5} B_{\mathrm{O},k}\, \lambda_1^{-6} \left(5\, J_5(\lambda_1, -X) + 80\, b_1^2\, \lambda_1^{-2} J_6(\lambda_1, -X) + 336\, b_1^4\, \lambda_1^{-4} J_7(\lambda_1, -X) \right.$$
$$\left. \left. + 512\, b_1^6\, \lambda_1^{-6} J_8(\lambda_1, -X) + 256\, b_1^8\, \lambda_1^{-8} J_9(\lambda_1, -X) \right) \right] . \tag{3.9}$$

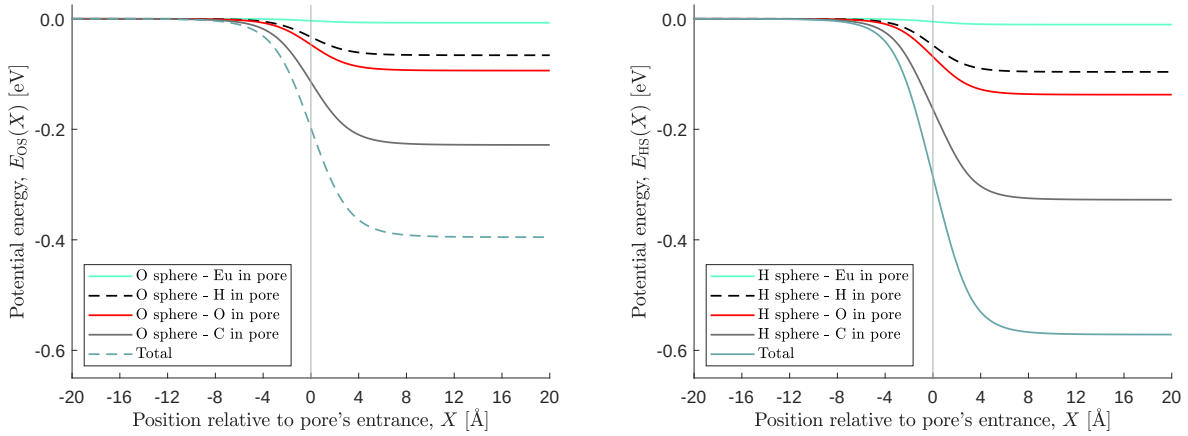
Similarly, the total interaction energy between the hydrogen sphere and the MOF pore is given by

$$E_{\mathrm{HS}}(X) = 8\pi^2\, a\, b_2^2\, n_{\mathrm{HS}}\, \lambda_2^{-5} \sum_k n_k \left[-A_{\mathrm{H},k} \left(J_2(\lambda_2, -X) + 2\, b_2^2\, \lambda_2^{-2}\, J_3(\lambda_2, -X) \right) \right.$$
$$+ \frac{1}{5} B_{\mathrm{H},k}\, \lambda_2^{-6} \left(5\, J_5(\lambda_2, -X) + 80\, b_2^2\, \lambda_2^{-2} J_6(\lambda_2, -X) + 336\, b_2^4\, \lambda_2^{-4} J_7(\lambda_2, -X) \right.$$
$$\left. \left. + 512\, b_2^6\, \lambda_2^{-6} J_8(\lambda_2, -X) + 256\, b_2^8\, \lambda_2^{-8} J_9(\lambda_2, -X) \right) \right] , \tag{3.10}$$

where $\lambda_2^2 = a^2 - b_2^2$, a is the radius of the pore, and b_2 is the radius of the hydrogen sphere.

Figure 3.3 shows the interaction energy between the (a) oxygen and (b) hydrogen spheres and each of the atoms in the MOF pore. The hydrogen sphere has a lower potential minimum inside the MOF pore in comparison to the oxygen sphere. This is partly because there are twice as many hydrogen atoms and more importantly, because the surface of the hydrogen sphere is always closer to the surface of the MOF pore. The van der Waals energy is very sensitive to distance, and so the radius of the hydrogen sphere greatly influences its potential energy minimum inside the MOF pore.

Comparing Figure 3.2 with Figure 3.3 shows that the qualitative behaviour of the interaction energy between the spheres and the MOF pore is similar to that of the ferric ion interacting with the MOF pore. That is, the carbon atoms make the largest contribution while the europium atoms make the smallest. The energy minimum is located inside the pore. While the profiles are similar, the magnitudes differ. The potential energy minimum for the oxygen sphere is approximately $-0.395\,\mathrm{eV}$ and the hydrogen sphere is approximately $-0.571\,\mathrm{eV}$ inside the MOF pore, whereas the minimum for the ferric ion is an order of magnitude smaller, $-0.012\,\mathrm{eV}$.



(a) (b)

Figure 3.3: Interaction energy between (a) oxygen sphere (Equation (3.9)), (b) hydrogen sphere (Equation (3.10)) and semi-infinite cylindrical MOF pore. Vertical line marks location of pore opening.

3.2. INTERACTION FORCES

The total interaction force between the hydrated ferric ion and the MOF pore is given by

$$F_{\text{tot}}(X) = F_{\text{Fe}} + F_{\text{OS}} + F_{\text{HS}}, \tag{3.11}$$

where F_{Fe} is the interaction force between the ferric ion and the MOF pore, and F_{OS} and F_{HS} are the interaction forces between the MOF pore and the oxygen and hydrogen spheres, respectively. The interaction forces are calculated using Equations (2.4).

3.2.1. Ferric ion point to MOF pore

The interaction force between a ferric ion and the MOF pore is the sum of the interaction forces between the ferric ion and each atom type in the MOF pore,

$$F_{\text{Fe}}(X) = F_{\text{Fe,Eu}} + F_{\text{Fe,H}} + F_{\text{Fe,O}} + F_{\text{Fe,C}} = \sum_{k} F_{\text{Fe},k}, \tag{3.12}$$

where $k \in \{\text{Eu}, \text{H}, \text{O}, \text{C}\}$. Using Equation (2.4), the van der Waals interaction force in the axial direction between a ferric ion and a representative atom type in the MOF is given by (see Appendix A.2 for details)

$$F_{\text{Fe},k}(X) = 2\,\pi\,a\,n_k \left[\frac{A_{\text{Fe},k}}{(X^2 + a^2)^3} - \frac{B_{\text{Fe},k}}{(X^2 + a^2)^6} \right], \tag{3.13}$$

so that the total interaction force between the ferric ion and the MOF pore is

$$F_{\mathrm{Fe}}(X) = 2\,\pi\,a \sum_k n_k \left[\frac{A_{\mathrm{Fe},k}}{(X^2+a^2)^3} - \frac{B_{\mathrm{Fe},k}}{(X^2+a^2)^6} \right]. \tag{3.14}$$

Note that the interaction force plots in this thesis depict the interaction force *in the axial direction*, where a positive value represents a force to the right, i.e., attraction between the ferric ion and the MOF pore entrance in the case when $X < 0$. A negative value represents a force to the left. This is in contrast to the standard van der Waals figures that represent *attraction* between two objects as a negative force, and *repulsion* as a positive force. An alternative figure is used here since there is the possibility that the ferric ion might enter the MOF pore and as a consequence it becomes important to clearly show the *direction* of the force rather than label it as attractive or repulsive.

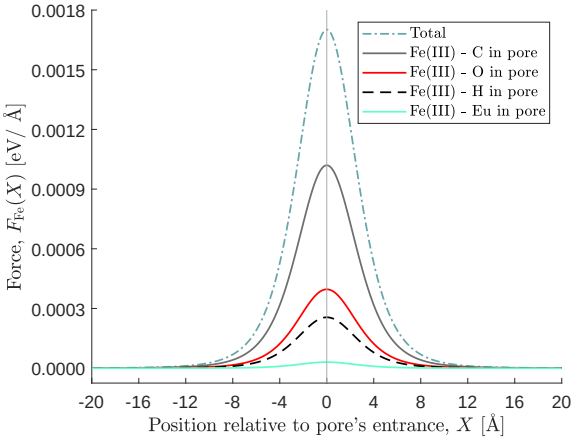


Figure 3.4: Interaction force between ferric ion and various atoms in semi-infinite cylindrical MOF pore (Equation (3.13), together with total interaction force (Equation (3.14)). Vertical line marks location of pore opening.

Figure 3.4 shows the interaction force between the ferric ion and the various atom types in the MOF pore. The interaction force is always positive, indicating that the ferric ion is attracted to the MOF pore entrance and likely enter to reach the location of minimum potential energy. At the entrance of the MOF pore, the ferric ion experiences the maximum interaction force, approximately $0.002\,\mathrm{eV\,Å^{-1}}$.

3.2.2. Ferric ion point's attraction limit

The expression for the interaction force (3.14) can be used to investigate what might be possible if a redesign of the MOF pore was feasible and the redesign is not beholden to a prescribed MOF

structure. First, this expression can be used to specify a minimum MOF pore radius such that a ferric ion will only experience an attraction to the entrance of the MOF pore (and no repulsion away from the pore). Second, if the ferric ion experiences repulsion near the entrance of the MOF pore, the expression can be used to find the farthest distance into a MOF pore for a ferric ion such that the ferric ion no longer experiences a negative force. This distance is the right-most zero of the interaction force and is defined as the attraction limit.

Any equilibrium points of the force function (i.e. where the force is neither attractive or repulsive) can be determined as a function of the MOF pore radius. The attraction limit is located where $F_{\mathrm{Fe}}(X_0) = 0$, that is

$$X_0(a) = \sqrt{\sigma_{\mathrm{tot_Fe}}^2 - a^2}, \tag{3.15}$$

where

$$\sigma_{\mathrm{tot_Fe}} = \left[\frac{\sum_k n_k \, B_{\mathrm{Fe,k}}}{\sum_k n_k \, A_{\mathrm{Fe,k}}} \right]^{1/6} . \tag{3.16}$$

The atom densities n_k are kept constant, regardless of the variation in the MOF pore radius. Note that the force is symmetric about the entrance, therefore only one root needs to be located (either positive or negative) and the other can be inferred. Here, the root to the right of the entrance ($X_0 \geq 0$) is chosen to be located.

For X_0 to be real, the radicand needs to be positive, therefore it is required that

$$\sigma_{\mathrm{tot_Fe}} \geq a. \tag{3.17}$$

Figure 3.5 shows the location where the ferric ion experiences a change in force direction as a function of the radius of a hypothetical MOF pore. For a pore with a radius greater than 2.594 Å, condition (3.17) fails, the interaction force is always positive, and the ferric ion will always experience a force towards the pore entrance. For a smaller MOF pore, a ferric ion located far from the pore entrance (above the dotted line) will experience a force towards the pore, while a ferric ion at a closer location will experience repulsion (below the dotted line). In the case of the true MOF pore (indicated by the asterisk on the figure), the radius is greater than 2.594 Å, so that the condition (3.17) fails (i.e. the interaction force has no real zeros), and the ferric ion is attracted to the pore entrance regardless of its initial location.

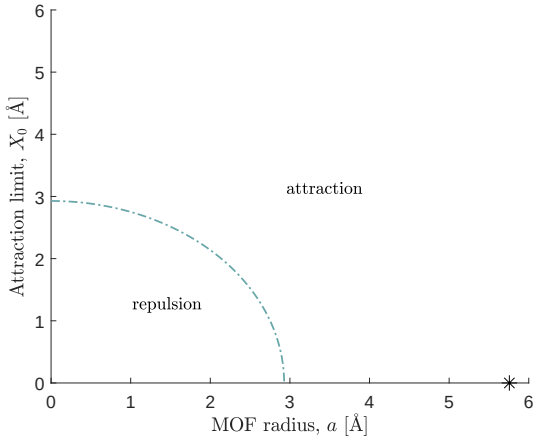


Figure 3.5: Attraction limit X_0 for ferric ion point as a function of radius of hypothetical semi-infinite cylinder. Asterisk indicates EuMOF pore's radius.

When the condition (3.17) fails, the attraction limit is considered to be at the entrance of the MOF pore, as there is no longer a negative interaction force to overcome. Therefore, the definition of the attraction limit is extended to be

$$X_0(a) = \begin{cases} \sqrt{\sigma_{\text{tot_Fe}}^2 - a^2}, & \text{for } \sigma_{\text{tot_Fe}} \geq a, \\ 0, & \text{otherwise.} \end{cases} \tag{3.18}$$

3.2.3. Oxygen and hydrogen spheres to MOF pore

Once again, the axial force between the oxygen sphere and the MOF pore will be the sum of the interaction forces between the sphere and each atom in the pore. By taking the derivative of the interaction energy (3.8), the axial force between the oxygen sphere and a particular atom type in the MOF pore is (see Appendix A.2.2 for details)

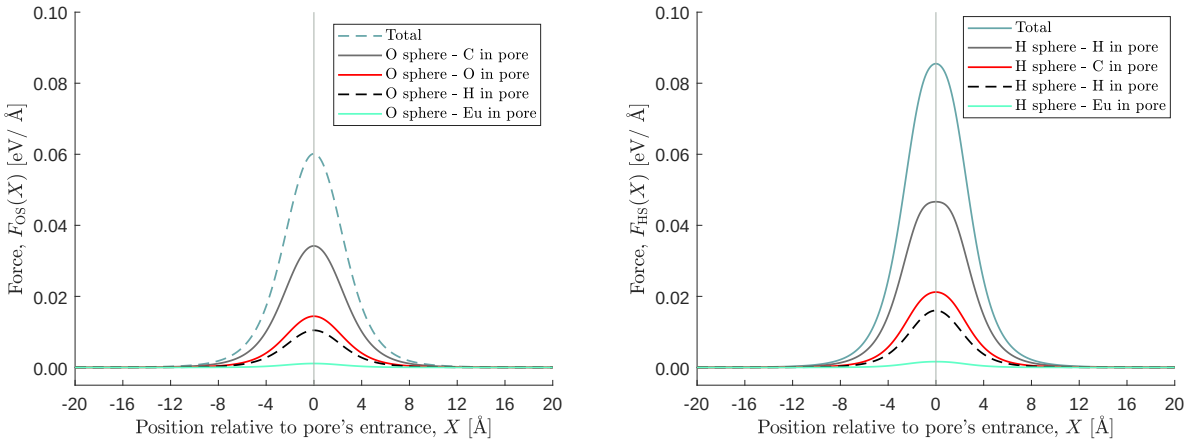
$$\begin{aligned} F_{\text{OS,k}}(X) = 8\pi^2\, a\, b_1^2\, n_k\, n_{\text{OS}} \Bigg[& A_{\text{O},k} \left(\frac{1}{(a^2 - b_1^2 + X^2)^3} + \frac{2\, b_1^2}{(a^2 - b_1^2 + X^2)^4} \right) \\ & - \frac{1}{5} B_{\text{O},k} \left(\frac{5}{(a^2 - b_1^2 + X^2)^6} + \frac{80\, b_1^2}{(a^2 - b_1^2 + X^2)^7} + \frac{336\, b_1^4}{(a^2 - b_1^2 + X^2)^8} \right. \\ & \left. + \frac{512\, b_1^6}{(a^2 - b_1^2 + X^2)^9} + \frac{256\, b_1^8}{(a^2 - b_1^2 + X^2)^{10}} \right) \Bigg]. \end{aligned} \tag{3.19}$$

The total interaction force between the oxygen sphere and the MOF pore is then given by

$$F_{\mathrm{OS}}(X) = 8\pi^2\, a\, b_1^2\, n_{\mathrm{OS}} \sum_k n_k \left[A_{\mathrm{O},k} \left(\frac{1}{(a^2 - b_1^2 + X^2)^3} + \frac{2\, b_1^2}{(a^2 - b_1^2 + X^2)^4} \right) - \frac{1}{5} B_{\mathrm{O},k} \left(\frac{5}{(a^2 - b_1^2 + X^2)^6} + \frac{80\, b_1^2}{(a^2 - b_1^2 + X^2)^7} + \frac{336\, b_1^4}{(a^2 - b_1^2 + X^2)^8} + \frac{512\, b_1^6}{(a^2 - b_1^2 + X^2)^9} + \frac{256\, b_1^8}{(a^2 - b_1^2 + X^2)^{10}} \right) \right]. \tag{3.20}$$

Similarly, the total interaction force between the hydrogen sphere and the MOF pore is

$$F_{\mathrm{HS}}(X) = 8\pi^2\, a\, b_2^2\, n_{\mathrm{HS}} \sum_k n_k \left[A_{\mathrm{H},k} \left(\frac{1}{(a^2 - b_2^2 + X^2)^3} + \frac{2\, b_2^2}{(a^2 - b_2^2 + X^2)^4} \right) - \frac{1}{5} B_{\mathrm{H},k} \left(\frac{5}{(a^2 - b_2^2 + X^2)^6} + \frac{80\, b_2^2}{(a^2 - b_2^2 + X^2)^7} + \frac{336\, b_2^4}{(a^2 - b_2^2 + X^2)^8} + \frac{512\, b_2^6}{(a^2 - b_2^2 + X^2)^9} + \frac{256\, b_2^8}{(a^2 - b_2^2 + X^2)^{10}} \right) \right]. \tag{3.21}$$



(a) (b)

Figure 3.6: Interaction force between (a) oxygen sphere (Equation (3.20)), (b) hydrogen sphere (Equation (3.21)) and various atoms in semi-infinite cylindrical MOF pore, together with total interaction force. Vertical line marks location of pore opening.

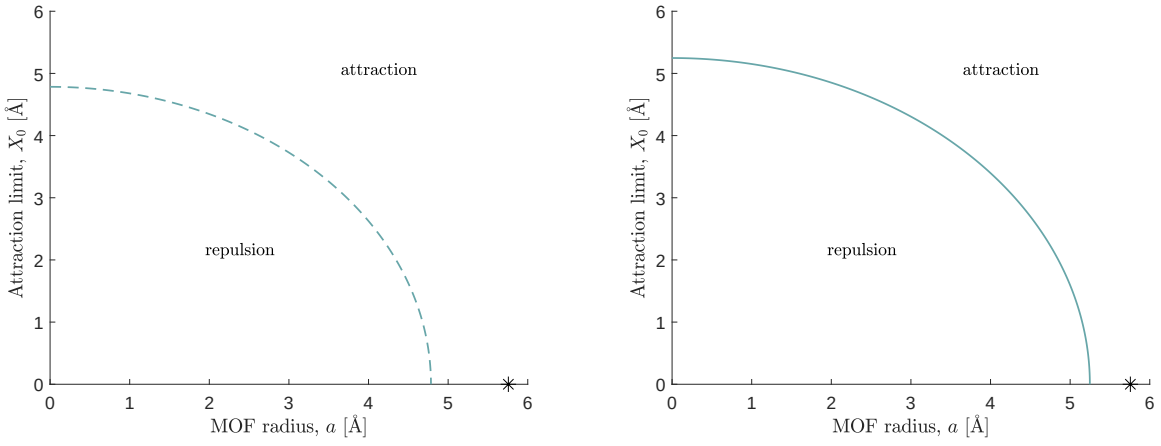
Figure 3.6 shows the interaction forces between the oxygen and hydrogen spheres and the MOF pore. The oxygen and hydrogen profiles behave in the same manner as the ferric ion profile, where the maximum interaction force is at the entrance of the MOF pore, $0.060\,\mathrm{eV\,\AA^{-1}}$ and $0.086\,\mathrm{eV\,\AA^{-1}}$ respectively. Europium, found in the MOF pore, contributes the least in terms of interaction forces and carbon contributes the most. The interaction forces between the oxygen and hydrogen spheres

and the MOF pore contribute significantly to the attraction of the hydrated ferric ion to the pore entrance.

3.2.4. Oxygen and hydrogen sphere's attraction limit

Again, consider a hypothetical MOF pore whereby a redesign of the MOF pore radius is possible while maintaining the same atom density of the true MOF pore. The right-most zero of the interaction force between the oxygen sphere and the hypothetical MOF pore is calculated by solving $F_{\mathrm{OS}}(X_0) = 0$. Solving for these equilibrium points analytically is difficult. The equilibrium points for the interaction force of the oxygen sphere are found numerically using MATLAB's inbuilt function `fzero`; the attraction limit is some function of the MOF pore radius a, denoted as $f(a)$. For MOF pore radii greater than the horizontal-intercept of $f(a)$, the attraction limit is set at the entrance of the MOF pore. Therefore, the attraction limit for the oxygen sphere is given by,

$$X_0(a) = \begin{cases} f(a), & \text{for } 0 \leq a \leq 4.784, \\ 0, & \text{otherwise.} \end{cases}$$



(a) (b)

Figure 3.7: Attraction limits X_0 for (a) oxygen sphere and (b) hydrogen sphere as a function of radius of hypothetical semi-infinite cylinder. Asterisks indicate EuMOF pore's radius.

A similar expression can be written for the attraction limit for the hydrogen sphere, where the horizontal-intercept is 5.248 Å. Figure 3.7 shows the attraction limits for the oxygen and hydrogen spheres. In the case of the true MOF pore radius (indicated in the figures with asterisks), both the oxygen and hydrogen spheres are always attracted to the MOF pore regardless of their initial

locations with respect to the MOF pore entrance.

3.3. ACCEPTANCE AND KINETIC ENERGY

The previous section highlighted that the hydrated ferric ion is attracted to the true MOF pore (that is, a MOF pore of the correct radius). This section calculates the hydrated ferric ion's gain in kinetic energy as a consequence of the interaction force, while maintaining the thought experiment of a hypothetical MOF where it is possible to vary the MOF pore radius a. Specifically, this section considers the energy gain of the hydrated ferric ion to move from the far (left) field either to a distance X_0 into the MOF pore, or to the far (right) into the MOF pore, given the MOF pore radius a.

The total acceptance energy of the hydrated ferric ion as consequence of the interaction forces to displace it from the far (left) field to the attraction limit, X_0, using Equation (2.5), is

$$Ea_{\text{tot}} = Ea_{\text{Fe}} + Ea_{\text{OS}} + Ea_{\text{HS}}. \tag{3.22}$$

The maximum kinetic energy gain of the hydrated ferric ion as consequence of the interaction forces, using Equation (2.6), is

$$Ek_{\text{tot}} = Ek_{\text{Fe}} + Ek_{\text{OS}} + Ek_{\text{HS}}. \tag{3.23}$$

3.3.1. Ferric ion point to MOF pore

The acceptance energy needed for the ferric ion to enter the MOF pore is,

$$Ea_{\text{Fe}} = Ea_{\text{Fe,Eu}} + Ea_{\text{Fe,H}} + Ea_{\text{Fe,O}} + Ea_{\text{Fe,C}} = \sum_{k} Ea_{\text{Fe},k}, \tag{3.24}$$

where $k \in \{\text{Eu}, \text{H}, \text{O}, \text{C}\}$ and $Ea_{\text{Fe},k}$ is the acceptance energy gain as a consequence of the interaction force between the ferric ion and atom type k in the MOF pore, that is, the energy required to displace the ferric ion from the far (left) field to a distance X_0 into the MOF pore. Using Equations (2.5) and (3.13) to calculate the acceptance energy for the ferric ion to enter the MOF's pore gives (see

Appendix A.3.1 for details),

$$\begin{aligned} Ea_{\mathrm{Fe},k} &= \int_{-\infty}^{X_0} F_{\mathrm{Fe},k}\, dx, \\ &= \frac{2\pi\, n_k}{a^4}\left[A_{\mathrm{Fe},k}\, J_2(a,-X_0) - \frac{1}{a^6} B_{\mathrm{Fe},k}\, J_5(a,-X_0)\right]. \end{aligned}$$

The total acceptance energy for the ferric ion to enter the MOF pore is

$$Ea_{\mathrm{Fe}} = \frac{2\pi}{a^4}\sum_k n_k\left[A_{\mathrm{Fe},k}\, J_2(a,-X_0) - \frac{1}{a^6} B_{\mathrm{Fe},k}\, J_5(a,-X_0)\right]. \tag{3.25}$$

The maximum kinetic energy gain as a consequence of the interaction force of atom type k to move the ferric ion from the far (left) field to far (right) into the pore is (see Appendix A.3.1 for details)

$$Ek_{\mathrm{Fe},k} = \frac{3\pi^2\, n_k}{128\, a^4}\left[32\, A_{\mathrm{Fe},k} - \frac{21}{a^6} B_{\mathrm{Fe},k}\right].$$

Therefore, the maximum energy gain as a consequence of the interaction force of the MOF pore to move the ferric ion from the far (left) field to far (right) into the pore is

$$Ek_{\mathrm{Fe}} = \frac{3\pi^2}{128\, a^4}\sum_k n_k\left[32\, A_{\mathrm{Fe},k} - \frac{21}{a^6} B_{\mathrm{Fe},k}\right]. \tag{3.26}$$

The total acceptance energy and the maximum kinetic energy gain of the ferric ion interacting with the true MOF pore is 0.006 eV and 0.012 eV, and indicated by an asterisk in Figure 3.8.

Figure 3.8 shows the energy profiles as functions of the pore radius for the acceptance energy (3.25) and the maximum kinetic energy (3.26) due to the interaction forces. In the region where the acceptance energy is negative and the maximum kinetic energy is positive (pore radii ranges $2.729\,\text{Å} < a < 2.785\,\text{Å}$), the ferric ion would need an initial velocity to the right to enter the MOF's pore to negate the effects of the negative acceptance energy. In the case of this project, the true MOF pore radius is greater than 5 Å, therefore the ferric ion will always be accepted into the MOF pore, reconfirming condition (3.17). Note that for a MOF pore radius a, the corresponding attraction limit was used as the upper bound of the integral as shown in Figure 3.5.

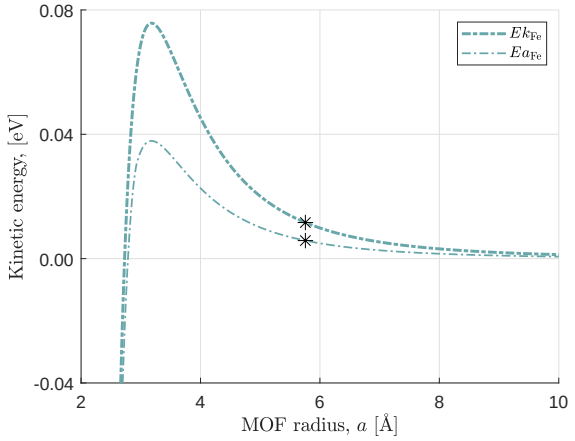


Figure 3.8: Total acceptance energy (Equation (3.25)) and maximum kinetic energy (Equation (3.26)) as consequence of interaction force of ferric ion. Asterisks indicate EuMOF pore's radius.

3.3.2. Oxygen and hydrogen spheres to MOF pore

As with the ferric ion, the energy gain due to the interaction forces of the water molecules can be calculated. In particular, the acceptance energy and the maximum kinetic energy. The acceptance energy needed for the oxygen sphere to enter the MOF pore is,

$$Ea_{\mathrm{OS}} = Ea_{\mathrm{OS,Eu}} + Ea_{\mathrm{OS,H}} + Ea_{\mathrm{OS,O}} + Ea_{\mathrm{OS,C}} = \sum_k Ea_{\mathrm{OS},k}. \tag{3.27}$$

The oxygen sphere will be accepted into the MOF pore provided that the kinetic energy gain due to the interaction force between the oxygen sphere and the MOF pore is positive. The contribution from atom type k using Equations (3.27) and (3.19) is (see Appendix A.3.2 for details),

$$\begin{aligned} Ea_{\mathrm{OS},k} = 8\pi^2\, a\, b_1^2\, n_k\, n_{\mathrm{OS}}\, \lambda_1^{-5} \big[& A_{\mathrm{O},k} \left(J_2(\lambda_1, -X_0) + 2\, b_1^2\, \lambda_1^{-2}\, J_3(\lambda_1, -X_0) \right) \\ & - \frac{1}{5} \lambda_1^{-6}\, B_{\mathrm{O},k} \left(5\, J_5(\lambda_1, -X_0) + 80\, b_1^2\, \lambda_1^{-2} J_6(\lambda_1, -X_0) + 336\, b_1^4\, \lambda_1^{-4} J_7(\lambda_1, -X_0) \right. \\ & \left. + 512\, b_1^6\, \lambda_1^{-6} J_8(\lambda_1, -X_0) + 256\, b_1^8\, \lambda_1^{-8} J_9(\lambda_1, -X_0) \right) \big] . \end{aligned}$$

The total acceptance energy for the oxygen sphere is

$$\begin{aligned} Ea_{\mathrm{OS}} = 8\pi^2\, a\, b_1^2\, n_{\mathrm{OS}}\, \lambda_1^{-5} \sum_k n_k \big[& A_{\mathrm{O},k} \left(J_2(\lambda_1, -X_0) + 2\, b_1^2\, \lambda_1^{-2}\, J_3(\lambda_1, -X_0) \right) \\ & - \frac{1}{5} \lambda_1^{-6}\, B_{\mathrm{O},k} \left(5\, J_5(\lambda_1, -X_0) + 80\, b_1^2\, \lambda_1^{-2} J_6(\lambda_1, -X_0) + 336\, b_1^4\, \lambda_1^{-4} J_7(\lambda_1, -X_0) \right. \end{aligned}$$

$$+512\,b_1^6\,\lambda_1^{-6}J_8(\lambda_1,-X_0)+256\,b_1^8\,\lambda_1^{-8}J_9(\lambda_1,-X_0))\big]\,.$$

The maximum kinetic energy gain of the oxygen sphere as it is moved from the far (left) field to far (right) into the pore, as a result of the interaction with atom k in the MOF pore is

$$Ek_{\mathrm{OS},k}=\pi^3\,a\,b_1^2\,n_k\,n_{\mathrm{OS}}\lambda_1^{-5}\left[A_{\mathrm{O},k}\left(3+5\,b_1^2\,\lambda_1^{-2}\right)-\frac{1}{80}\lambda_1^{-6}\,B_{\mathrm{O},k}\,\left(315+2310\,b_1^2\,\lambda_1^{-2}\right.\right.$$
$$\left.\left.+9009\,b_1^4\,\lambda_1^{-4}+12870\,b_1^6\,\lambda_1^{-6}+12155\,b_1^8\,\lambda_1^{-8}\right)\right]\,,$$

so that the maximum kinetic energy gain due to the interaction forces between the oxygen sphere and the MOF pore is

$$Ek_{\mathrm{OS}}=\pi^3\,a\,b_1^2\,n_{\mathrm{OS}}\lambda_1^{-5}\sum_k n_k\left[A_{\mathrm{O},k}\left(3+5\,b_1^2\,\lambda_1^{-2}\right)-\frac{1}{80}\lambda_1^{-6}\,B_{\mathrm{O},k}\,\left(315+2310\,b_1^2\,\lambda_1^{-2}\right.\right.$$
$$\left.\left.+9009\,b_1^4\,\lambda_1^{-4}+12870\,b_1^6\,\lambda_1^{-6}+12155\,b_1^8\,\lambda_1^{-8}\right)\right]\,.$$

The total acceptance energy and the maximum kinetic energy gain of the oxygen sphere interacting with the true MOF pore is 0.198 eV and 0.395 eV, and indicated by asterisks in Figure 3.9(a).

Similarly, the total acceptance energy for the hydrogen sphere entering the MOF pore is

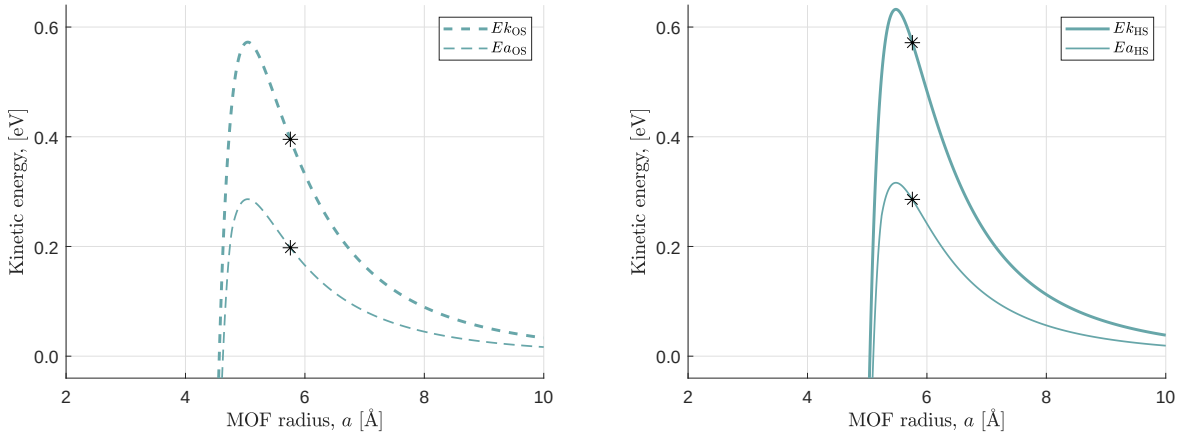
$$Ea_{\mathrm{HS}}=8\pi^2\,a\,b_2^2\,n_{\mathrm{HS}}\,\lambda_2^{-5}\sum_k n_k\left[A_{\mathrm{H},k}\left(J_2(\lambda_2,-X_0)+2\,b_2^2\,\lambda_2^{-2}\,J_3(\lambda_2,-X_0)\right)\right.$$
$$-\frac{1}{5}\lambda_2^{-6}\,B_{\mathrm{H},k}\,\left(5\,J_5(\lambda_2,-X_0)+80\,b_2^2\,\lambda_2^{-2}J_6(\lambda_2,-X_0)+336\,b_2^4\,\lambda_2^{-4}J_7(\lambda_2,-X_0)\right.$$
$$\left.\left.+512\,b_2^6\,\lambda_2^{-6}J_8(\lambda_2,-X_0)+256\,b_2^8\,\lambda_2^{-8}J_9(\lambda_2,-X_0)\right)\right]\,,$$

and the maximum kinetic energy of the hydrogen sphere is

$$Ek_{\mathrm{HS}}=\pi^3\,a\,b_2^2\,n_{\mathrm{HS}}\lambda_2^{-5}\sum_k n_k\left[A_{\mathrm{H},k}\left(3+5\,b_2^2\,\lambda_2^{-2}\right)-\frac{1}{80}\lambda_2^{-6}\,B_{\mathrm{H},k}\,\left(315+2310\,b_2^2\,\lambda_2^{-2}\right.\right.$$
$$\left.\left.+9009\,b_2^4\,\lambda_2^{-4}+12870\,b_2^6\,\lambda_2^{-6}+12155\,b_2^8\,\lambda_2^{-8}\right)\right]\,.$$

The total acceptance energy and the maximum kinetic energy gain of the hydrogen sphere interacting with the true MOF pore is 0.286 eV and 0.572 eV, and indicated by asterisks in Figure 3.9(b).

In comparison to the ferric ion, a larger MOF pore radius is required for the water molecules to be accepted into the pore without an initial (rightward) velocity. For MOF pore radii where 4.566 Å $< a <$ 4.628 Å (Figure 3.9(a)), the oxygen sphere will be attracted towards the MOF pore but an initial rightward velocity will not be enough to overcome the repulsive forces near the pore entrance and for the oxygen sphere to enter the MOF pore. In the case of the hydrogen sphere, the corresponding MOF pore radii is 5.046 Å $< a <$ 5.103 Å (Figure 3.9(b)).



(a) (b)

Figure 3.9: Total acceptance energy and maximum kinetic energy as consequence of interaction force of (a) oxygen and (b) hydrogen sphere. Asterisks indicate EuMOF pore's radius.

Note that Figure 3.9 plots the energies for a MOF pore radius greater than the interacting oxygen sphere radius and hydrogen sphere radius, i.e. $b_1 < a$ and $b_2 < a$. If the interacting sphere radii are greater than the MOF pore's radius, λ_1 and λ_2 are not real valued. In this scenario, it is assumed that the MOF pore radii values are larger than the interacting sphere radii, since the sphere can only enter the MOF pore if the sphere has a smaller radius. The true MOF pore is not excluded by introducing a condition for a minimum MOF pore radius, since the true MOF pore radius ($a =$ 5.757 Å) is greater than the hydrogen sphere's radius ($b_2 =$ 2.741 Å).

The total acceptance energy and maximum kinetic energy of the hydrated ferric ion is discussed in the next section.

3.4. DISCUSSION

It is important to understand the atomic scale interactions between the hydrated ferric ion and the MOF pore, and since it is problematic to directly observe what is happening at this scale by experiment, the use of physical laws can give this insight. This project uses the van der Waals

theory to describe the distance based interactions between non-bonded atoms and the Lennard-Jones potential to mathematically model the physical interactions.

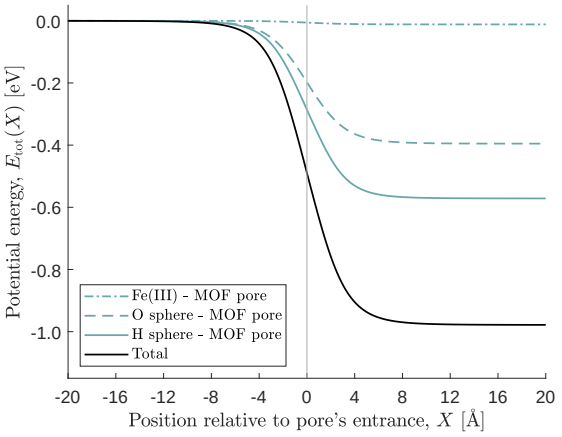
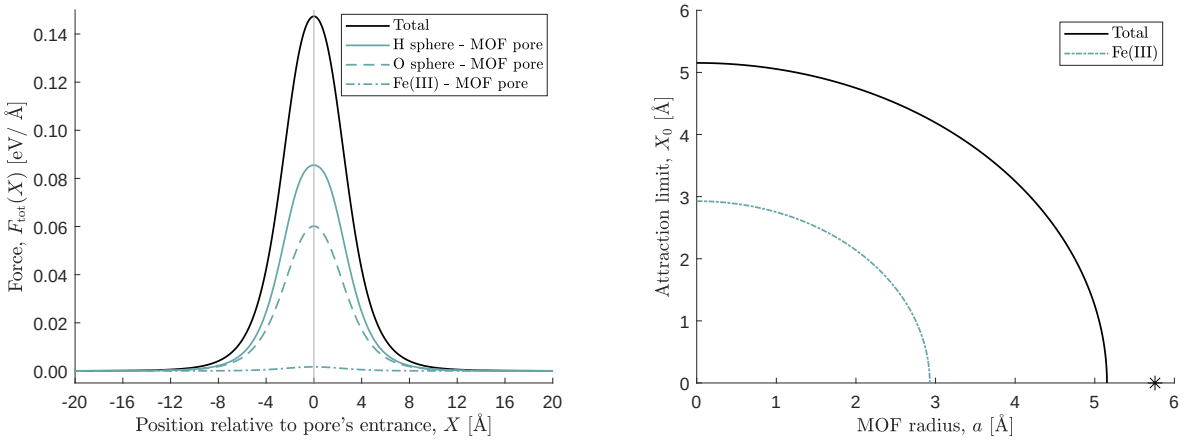


Figure 3.10: Interaction energy between hydrated ferric ion and semi-infinite cylindrical MOF pore, Equation (3.2). Vertical line marks location of pore opening.

Figure 3.10 shows the energy profiles of the hydrated ferric ion's interaction with the MOF pore. The ferric ion point contributes very little to the overall interaction energy, whereas the hydrogen sphere contributes the most. This is partly due to the fact that the hydrogen atoms are farthest from the axis of symmetry and closer to the cylindrical pore walls. It is energetically favourable for the hydrated ferric ion to enter and stay inside the MOF pore with a potential energy minimum of approximately $-0.978\,\text{eV}$.

The interaction force between the hydrated ferric ion and the MOF pore is shown in Figure 3.11(a). When the hydrated ferric ion is near the MOF pore's entrance, there is an attractive force due to the van der Waals force, i.e. a force directed to the right. The maximum interaction force is experienced when the hydrated ferric ion is at the entrance of the MOF pore and is approximately $0.147\,\text{eV}\,\text{Å}^{-1}$, nearly two orders of magnitude larger than the maximum interaction force between the ferric ion (alone) and the MOF pore. Once the hydrated ferric ion is sufficiently far into the MOF pore, it experiences zero net force.

Again, suppose there is a hypothetical MOF pore where the atom density remains the same as the true MOF pore and the MOF pore's radius a can be altered, such that the attraction limit for the interaction force is a function of a, shown in Figure 3.11(b). The attraction limit for the hydrated ferric ion was found numerically using MATLAB's inbuilt function `fzero`. Ideally, a MOF pore radius should be large enough so that the interaction force between a hydrated ferric ion and



(a) (b)

Figure 3.11: (a) Interaction force between hydrated ferric ion and semi-infinite cylindrical MOF pore, Equation (3.11). Vertical line marks the location of pore opening. (b) Attraction limit X_0 for ferric ion's and hydrated ferric ion's relative position with respect to radius of MOF pore. Asterisk indicates EuMOF pore's radius.

the MOF pore is always directed towards the MOF pore. In the case of the true MOF pore, the interaction force between the hydrated ferric ion and the MOF pore is always directed to the right, so that the hydrated ferric ion does not experience a change in the direction of the force. This is because the MOF's pore radius is beyond the total boundary curve, indicated by an asterisk in Figure 3.11(b). The addition of six water molecules increases the critical pore radius at which the hydrated ferric ion might be accepted (i.e. horizontal-intercept of the black solid line is greater than the horizontal-intercept of the turquoise dashed line), and the true MOF pore's radius remains outside of the bounded region of real roots. This means that both the ferric ion and the hydrated ferric ion will always be accepted into the MOF pore.

The acceptance energy for the ferric ion and the hydrated ferric ion can be calculated using the combination of MOF pore radius and the corresponding attraction limit, see Figure 3.12.

Again, solutions for the total acceptance energy and maximum kinetic energy for the hydrated ion in Figure 3.12 are for $a > b_2$ (where a is the radius of a hypothetical pore), so that the MOF pore radius is larger than the hydrogen sphere radius.

Between the ranges $4.949\,\text{Å} < a < 5.007\,\text{Å}$, the hydrated ferric ion would need an initial velocity towards the pore for it to enter the MOF pore, since the acceptance energy is negative in this region, while the maximum kinetic energy is positive. The additional six water molecules amplify the magnitude of the acceptance energy and maximum kinetic energy profiles, and shift the energy

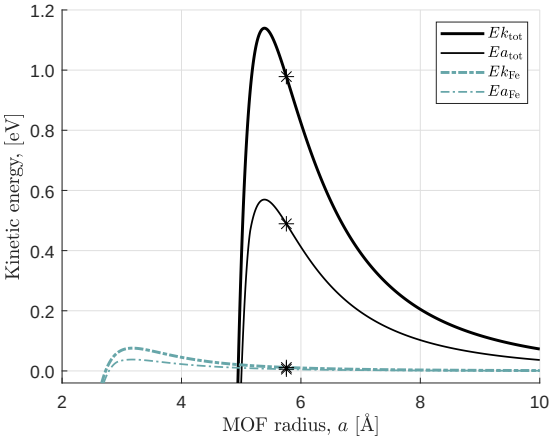


Figure 3.12: Total acceptance energy and maximum kinetic energy of ferric ion, Equations (3.25) and (3.26), and hydrated ferric ion, Equations (3.22) and (3.23). Asterisks indicate EuMOF pore's radius.

profiles to the right. That is, a pore of a larger radius is required to attract and trap the hydrated ferric ion. The maximum acceptance energy for the hydrated ferric ion, 0.565 eV, is fifteen times that of that for the ferric ion, 0.038 eV. The total acceptance energy gain as consequence of the interaction forces between the hydrated ferric ion and the true MOF pore is 0.489 eV.

The maximum kinetic energy gain as consequence of the interaction forces between the hydrated ferric ion and the true MOF pore results in an energy gain of 0.970 eV, the asterisk on the thick black line in Figure 3.12. In contrast, if the ferric ion alone is considered, this decreases to 0.012 eV. This makes intuitive sense, since there is a greater force acting on the hydrated ferric ion.

CHAPTER 4

INTERACTIONS BETWEEN A HYDRATED FERRIC ION AND A FINITE CYLINDRICAL MOF PORE

This chapter focuses on the interactions between a hydrated ferric ion and a MOF pore of finite depth, where the hydrated ferric ion is approximated by a point with two concentric spheres and the MOF pore is approximated by a finite cylinder, of depth d. This chapter primarily considers a pore with a depth of one unit cell, that is, $d = h$ (see Section 1.3.1). Section 4.4 considers longer finite pores. The results in this chapter are compared with those of the previous chapter for a semi-infinite cylinder.

4.1. INTERACTION ENERGIES

Maintaining the assumption that the MOF pore is cylindrical and the atoms are evenly spread over the surface, the total interaction energy between the hydrated ferric ion and the MOF pore has been defined by Equation (3.2). The subsections below calculate the individual contributions from the ferric ion, and the oxygen and hydrogen spheres.

4.1.1. Ferric ion point to MOF pore

The interaction energy between the ferric ion and the MOF pore is given by Equation (3.3). The atom-specific interaction energies in Equation (3.3) can be calculated by using Equation (2.3). The ferric ion is again treated as a point, reducing the double integral to a single integral over the surface of the MOF pore. The interaction energy between the point ferric ion and the finite MOF pore is given by

$$\begin{aligned} E_{\mathrm{Fe},k}(X) &= n_k \int_{S_1} U(\rho) \mathrm{d}S_1, \\ &= 2\pi\, a\, n_k \int_0^d \left[-\frac{A_{\mathrm{Fe},k}}{\rho^6} + \frac{B_{\mathrm{Fe},k}}{\rho^{12}} \right] \mathrm{d}x, \end{aligned} \tag{4.1}$$

where n_k is the mean surface density of atom type $k \in \{\mathrm{H}, \mathrm{O}, \mathrm{C}, \mathrm{Eu}\}$ and S_1 is the parameterisation of the surface of the MOF pore. After writing ρ in terms of x using Pythagoras, this integral may

be written as

$$E_{\mathrm{Fe},k}(X) = \frac{2\pi\, n_k}{a^4}\left[-A_{\mathrm{Fe},k}\, H_2(a,-X;d) + \frac{1}{a^6} B_{\mathrm{Fe},k}\, H_5(a,-X;d)\right], \tag{4.2}$$

where the H_n are definite integrals of powers of cosine functions as defined in Equation (D.3) (see Appendix D for details). The total interaction energy can then be calculated using Equation (3.3),

$$E_{\mathrm{Fe}}(X) = \frac{2\pi}{a^4}\sum_k n_k\left[-A_{\mathrm{Fe},k}\, H_2(a,-X;d) + \frac{1}{a^6} B_{\mathrm{Fe},k}\, H_5(a,-X;d)\right]. \tag{4.3}$$

Figure 4.1 shows the resulting interaction energies between the ferric ion and each element found in the finite MOF pore. A potential energy minimum exists at the mid-depth of the MOF pore at $-0.009\,\mathrm{eV}$; this point is the most energetically favourable position for the ferric ion inside of the MOF pore. Also note that the interaction energy profile is symmetric about the centre of the finite pore.

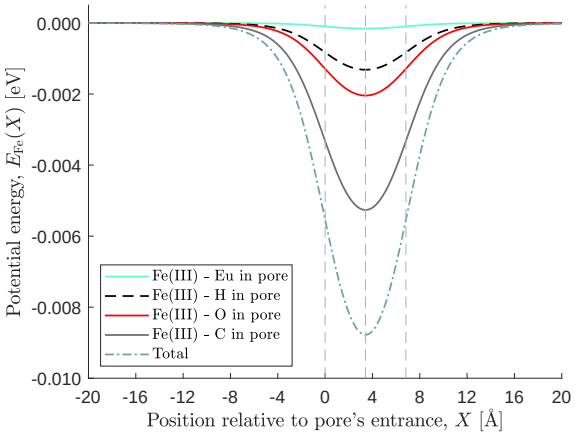


Figure 4.1: Interaction energy between ferric ion and finite cylindrical MOF pore with $d = h$, Equations (4.2) and (4.3). Vertical grey dashed lines mark location of pore's entrance, mid-depth and exit, from left to right.

4.1.2. Oxygen and hydrogen spheres to MOF pore

The total interaction energy between the oxygen sphere and the MOF pore is given by Equation (3.6). For atom type k in the MOF pore, the interaction energy between the surface of the oxygen sphere and the surface of the MOF pore can be approximated using Equation (2.3),

$$E_{\mathrm{OS},k}(X) = n_k\, n_{\mathrm{OS}} \int_{S_1}\int_{S_2} U(\rho)\,\mathrm{d}S_2\,\mathrm{d}S_1.$$

The inner integral was previously defined as $G(\rho)$ (Equation (3.7)) and is the integral of $U(\rho)$ over the surface of the sphere [1, 13]. The interaction energy between the oxygen sphere and a representative atom type in the MOF pore is found by integrating $G(\rho)$ over the surface of the MOF pore (details are shown in Appendix B),

$$\begin{aligned}
E_{\mathrm{OS},k}(X) &= n_k \int_{S_1} G(\rho)\mathrm{d}S_1, \\
&= 2\pi\, a\, n_k \int_0^d G(\rho)\mathrm{d}x, \\
&= 8\pi^2\, a\, b_1^2\, n_k\, n_{\mathrm{OS}}\, \lambda_1^{-5}\Big[-A_{\mathrm{O},k}\left(H_2(\lambda_1,-X;d) + 2\, b_1^2\, \lambda_1^{-2}\, H_3(\lambda_1,-X;d)\right) \\
&\quad + \frac{1}{5} B_{\mathrm{O},k}\, \lambda_1^{-6}\left(5\, H_5(\lambda_1,-X;d) + 80\, b_1^2\, \lambda_1^{-2} H_6(\lambda_1,-X;d) + 336\, b_1^4\, \lambda_1^{-4} H_7(\lambda_1,-X;d)\right. \\
&\quad \left. + 512\, b_1^6\, \lambda_1^{-6} H_8(\lambda_1,-X;d) + 256\, b_1^8\, \lambda_1^{-8} H_9(\lambda_1,-X;d)\right)\Big], \qquad (4.4)
\end{aligned}$$

where $\lambda_1^2 = a^2 - b_1^2$, a is the radius of the MOF pore, b_1 is the radius of the oxygen sphere, h is the height of the MOF pore and the $H_n(\lambda_1, -X; d)$ are definite integrals of powers of cosine functions defined in Appendix D.2.

The total interaction energy between the oxygen sphere and the finite MOF pore can be calculated by using Equation (3.6)

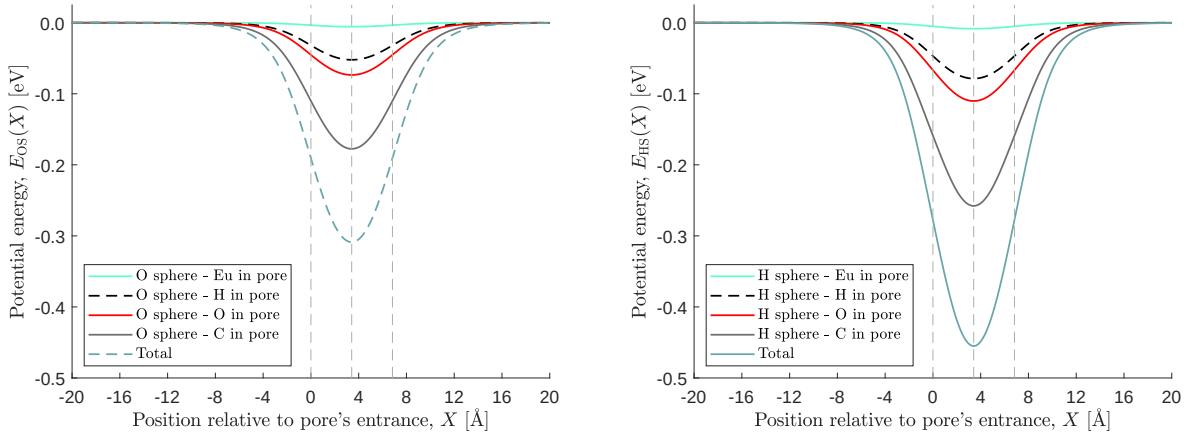
$$\begin{aligned}
E_{\mathrm{OS}}(X) &= 8\pi^2\, a\, b_1^2\, n_{\mathrm{OS}}\, \lambda_1^{-5} \sum_k n_k \Big[-A_{\mathrm{O},k}\left(H_2(\lambda_1,-X;d) + 2\, b_1^2\, \lambda_1^{-2}\, H_3(\lambda_1,-X;d)\right) \\
&\quad + \frac{1}{5} B_{\mathrm{O},k}\, \lambda_1^{-6}\left(5\, H_5(\lambda_1,-X;d) + 80\, b_1^2\, \lambda_1^{-2} H_6(\lambda_1,-X;d) + 336\, b_1^4\, \lambda_1^{-4} H_7(\lambda_1,-X;d)\right. \\
&\quad \left. + 512\, b_1^6\, \lambda_1^{-6} H_8(\lambda_1,-X;d) + 256\, b_1^8\, \lambda_1^{-8} H_9(\lambda_1,-X;d)\right)\Big]. \qquad (4.5)
\end{aligned}$$

Similarly, the total interaction energy between the hydrogen sphere and the MOF pore is

$$\begin{aligned}
E_{\mathrm{HS}}(X) &= 8\pi^2\, a\, b_2^2\, n_{\mathrm{HS}}\, \lambda_2^{-5} \sum_k n_k \Big[-A_{\mathrm{H},k}\left(H_2(\lambda_2,-X;d) + 2\, b_2^2\, \lambda_2^{-2}\, H_3(\lambda_2,-X;d)\right) \\
&\quad + \frac{1}{5} B_{\mathrm{H},k}\, \lambda_2^{-6}\left(5\, H_5(\lambda_2,-X;d) + 80\, b_2^2\, \lambda_2^{-2} H_6(\lambda_2,-X;d) + 336\, b_2^4\, \lambda_2^{-4} H_7(\lambda_2,-X;d)\right. \\
&\quad \left. + 512\, b_2^6\, \lambda_2^{-6} H_8(\lambda_2,-X;d) + 256\, b_2^8\, \lambda_2^{-8} H_9(\lambda_2,-X;d)\right)\Big]. \qquad (4.6)
\end{aligned}$$

where $\lambda_2^2 = a^2 - b_2^2$, a is the radius of the MOF pore and b_2 is the radius of the hydrogen sphere.

The energy profiles for the oxygen sphere and hydrogen sphere interacting with the MOF pore



(a) (b)

Figure 4.2: Interaction energy between (a) oxygen sphere (Equation (4.5)), (b) hydrogen sphere (Equation (4.6)) and finite cylindrical MOF pore with $d = h$. Vertical grey dashed lines mark location of pore's entrance, mid-depth and exit, from left to right.

are shown in Figure 4.2. The interaction of the water molecules with europium has the smallest magnitude, while the interaction of water molecules with carbon is the greatest. The potential energy is symmetric about the mid-depth of the MOF pore, and the minimum also occurs there. The potential energy minimum for the oxygen sphere is $-0.309\,\text{eV}$ and the hydrogen sphere is $-0.455\,\text{eV}$.

4.2. INTERACTION FORCES

The total interaction force between the hydrated ferric ion and the MOF pore is defined by Equation (3.11) and is calculated by using Equation (2.4). In subsections below, the interaction force between the ferric ion and the MOF pore is calculated. This information is used to investigate the attraction limit. That is, what might be possible if the radius of the MOF pore could be controlled is explored. Finally, the interaction force between the oxygen and hydrogen sphere and the MOF pore and their corresponding attraction limits are calculated.

4.2.1. Ferric ion point to MOF pore

Using Equation (2.4), the interaction force in the axial direction between a ferric ion and a representative atom type $k \in \{\text{Eu}, \text{H}, \text{O}, \text{C}\}$ in a MOF pore of finite depth is given by (see Appendix B.2

for details)

$$F_{\mathrm{Fe},k}(X) = 2\,\pi\,a\,n_k \left[\frac{A_{\mathrm{Fe},k}}{(a^2+X^2)^3} - \frac{B_{\mathrm{Fe},k}}{(a^2+X^2)^6} - \frac{A_{\mathrm{Fe},k}}{(a^2+(d-X)^2)^3} + \frac{B_{\mathrm{Fe},k}}{(a^2+(d-X)^2)^6} \right]. \quad (4.7)$$

The total interaction force between the ferric ion and the MOF pore is

$$F_{\mathrm{Fe}}(X) = 2\,\pi\,a \sum_k n_k \left[\frac{A_{\mathrm{Fe},k}}{(a^2+X^2)^3} - \frac{B_{\mathrm{Fe},k}}{(a^2+X^2)^6} - \frac{A_{\mathrm{Fe},k}}{(a^2+(d-X)^2)^3} + \frac{B_{\mathrm{Fe},k}}{(a^2+(d-X)^2)^6} \right]. \quad (4.8)$$

The interaction force between the ferric ion and the finite MOF pore is shown in Figure 4.3. Outside the entrance of the MOF pore, there is a force acting to the right, that is, the ferric ion is attracted towards the MOF pore. At the centre of the finite pore, the force changes direction. That is, a ferric ion located to the right of the centre experiences a force to the left, or back towards the centre of the pore. The force function is asymmetric about the centre of the pore and the maximum magnitude of the force ($0.002\,\mathrm{eV\,\AA^{-1}}$) occurs just outside the entrance (for the rightward force) and the exit (for the leftward force) of the MOF pore. Recall from Figure 4.1, that it is energetically favourable for the ferric ion to remain at the mid-depth of the MOF pore, which aligns with the location where the ferric ion experiences zero net force.

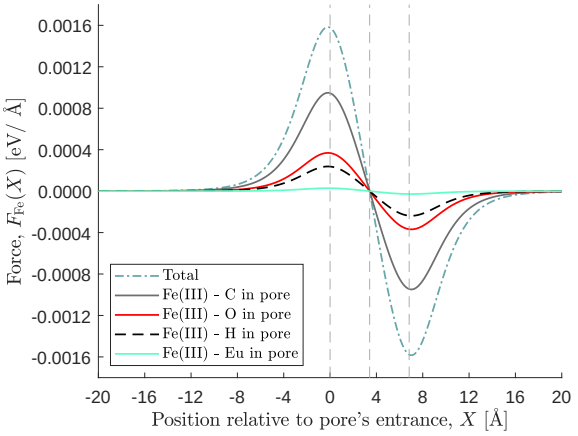


Figure 4.3: Interaction force between ferric ion and various atoms in finite cylindrical MOF pore (Equation (4.7)), together with total interaction force (Equation (4.8)). Vertical grey dashed lines mark the location of pore's entrance, mid-depth and exit, from left to right.

4.2.2. Ferric ion point's attraction limit

In a similar way to Subsection 3.2.2, suppose that a new MOF pore could be designed with any radius, while keeping the atom densities in the MOF pore the same as the true MOF structure.

That is, this subsection disregards the limits of MOF synthesises and the inherent chemistry.

Since the interaction force function is an odd function about $d/2$, this subsection calculates the equilibrium points ($X_0 \in [0, d/2)$) of the interaction force (4.8) to find the attraction limit for a finite cylindrical pore. Recall, that the attraction limit is the right-most distance into the MOF pore for the ferric ion to overcome all negative interaction force near (or at) the entrance of the MOF pore. In other words, the attraction limit is found when $F_{\text{Fe}}(X_0) = 0$. When there is no negative force near the entrance of the MOF pore, then the attraction limit is $X_0 = 0$.

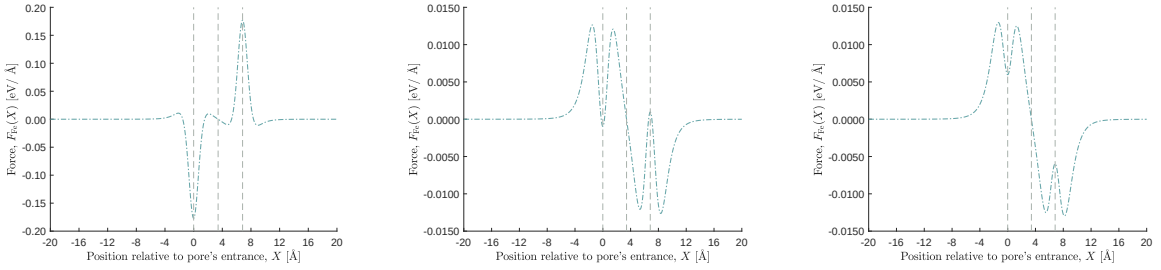
The requirement that $F_{\text{Fe}} = 0$ can be written in three different ways,

$$\sum_k n_k \, A_{\text{Fe},k} \left(\frac{1}{(X_0^2 + a^2)^3} - \frac{1}{((X_0 - d)^2 + a^2)^3} \right) = \sum_k n_k \, B_{\text{Fe},k} \left(\frac{1}{(X_0^2 + a^2)^6} - \frac{1}{((X_0 - d)^2 + a^2)^6} \right), \tag{4.9a}$$

$$\sigma_{\text{tot_Fe}}^6 \left(\frac{((X_0 - d)^2 + a^2)^6 - (X_0^2 + a^2)^6}{(X_0^2 + a^2)^3 \, ((X_0 - d)^2 + a^2)^3} \right) = ((X_0 - d)^2 + a^2)^3 - (X_0^2 + a^2)^3, \tag{4.9b}$$

$$\sigma_{\text{tot_Fe}}^6 \left[((X_0 - d)^2 + a^2)^3 + (X_0^2 + a^2)^3 \right] = (X_0^2 + a^2)^3 \, ((X_0 - d)^2 + a^2)^3. \tag{4.9c}$$

It is easily seen from Equation (4.9a) that the interaction force is zero when $X_0 = d/2$ for all values of h and a. Equation (4.9b) suggests that there are at most 11 roots. This implies that the ferric ion will experience a change in the force direction when near the entrance, inside and near the exit of the MOF pore at most 11 times. The `implicitplot` function in Maple suggests that there are five roots. Figure 4.4 shows interaction force profiles for varying values of the MOF pore radius, a. For MOF pore radii 2.500 Å and 2.920 Å, the ferric ion experiences directional change five times. On the other hand, when the MOF pore radius is 3.000 Å, the ferric ion experiences a force directional change only once at the MOF mid-depth.



(a) (b) (c)

Figure 4.4: Interaction forces between ferric ion and and finite cylindrical MOF pore (Equation (4.7)) with $d = h$, where MOF radius is (a) $a = 2.50$, (b) $a = 2.92$ and (c) $a = 3.00$. Vertical grey dashed lines mark location of pore's entrance, mid-depth and exit, from left to right.

Solving for the roots X_0 of Equation (4.9c) analytically is troublesome. In Figure 4.5(a), the roots are found numerically using MATLAB's inbuilt function, `fzero`. The figure shows the boundary where the ferric ion experiences a change in force direction as a function of the radius of the MOF pore. The graph below can be described in two pieces: a straight line and an ellipse. The grey dashed straight line at $X_0 = d/2$ coincides with the observation above, which is the MOF pore's mid-depth. That is, the force always changes direction at the centre of the pore, or $X_0 = d/2$ is always a solution to Equation (4.9). However, this point is excluded from the range of the attraction limit. For a pore radius greater than or equal to 2.929 Å (i.e. horizontal-intercept, which is greater than $\sigma_{\text{tot_Fe}}$), the only root is at $d/2$ and the attraction limit is $X_0 = 0$. This result is a consequence of the fact that the interaction force function for a finite pore is an odd function centred about the pore's mid-depth.

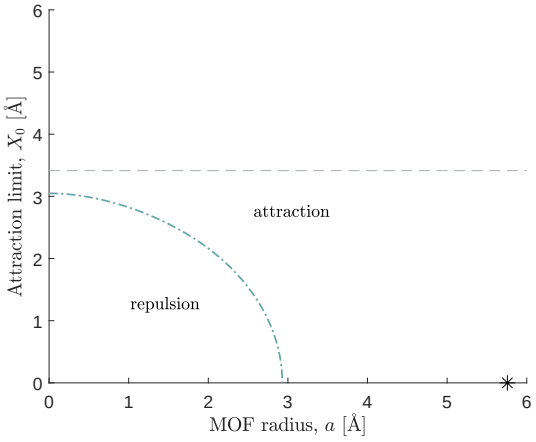


Figure 4.5: Attraction limit X_0 for ferric ion point as a function of radius of hypothetical finite cylinder with $d = h$. Asterisk indicates EuMOF pore's radius. Turquoise dot dashed line is ferric ion's attraction limit. Horizontal grey dashed line marks location of pore's mid-depth.

The curved line shows the right-most zero, such that $X_0 < d/2$, similar to what was observed in the case of a semi-infinite pore. The elliptic boundary establishes distances into the MOF pore where the ferric ion will experience a zero interaction force. Above the elliptic boundary, the ferric ion will always experience a force towards the MOF pore entrance and to the centre of the MOF pore. Below the elliptic boundary, the ferric ion will experience a force away from the MOF pore entrance.

The interaction force was calculated at the corresponding MOF pore radii a and attraction limits X_0, to confirm that the calculated interaction force is negligible (of the order 10^{-17}).

4.2.3. Oxygen and hydrogen spheres to MOF pore

In order to calculate the force in the axial direction between the oxygen sphere and the finite MOF pore, the derivative of the corresponding interaction energy, Equation (4.4), is calculated (see Appendix B.2 for detail). For atom type k, the interaction force between the oxygen sphere and the finite MOF pore is

$$\begin{aligned}
F_{\mathrm{OS},k}(X) = 8\pi^2\, a\, b_1^2\, n_k\, n_{\mathrm{OS}} \Bigg[& A_{\mathrm{O},k} \left(\frac{1}{(a^2 - b_1^2 + X^2)^3} + \frac{2\, b_1^2}{(a^2 - b_1^2 + X^2)^4} \right) - \frac{1}{5} B_{\mathrm{O},k} \left(\frac{5}{(a^2 - b_1^2 + X^2)^6} \right. \\
& \left. + \frac{80\, b_1^2}{(a^2 - b_1^2 + X^2)^7} + \frac{336\, b_1^4}{(a^2 - b_1^2 + X^2)^8} + \frac{512\, b_1^6}{(a^2 - b_1^2 + X^2)^9} + \frac{256\, b_1^8}{(a^2 - b_1^2 + X^2)^{10}} \right) \\
& - A_{\mathrm{O},k} \left(\frac{1}{(a^2 - b_1^2 + (d - X)^2)^3} + \frac{2\, b_1^2}{(a^2 - b_1^2 + (d - X)^2)^4} \right) \\
& + \frac{1}{5} B_{\mathrm{O},k} \left(\frac{5}{(a^2 - b_1^2 + (d - X)^2)^6} + \frac{80\, b_1^2}{(a^2 - b_1^2 + (d - X)^2)^7} + \frac{336\, b_1^4}{(a^2 - b_1^2 + (d - X)^2)^8} \right. \\
& \left. + \frac{512\, b_1^6}{(a^2 - b_1^2 + (d - X)^2)^9} + \frac{256\, b_1^8}{(a^2 - b_1^2 + (d - X)^2)^{10}} \right) \Bigg] .
\end{aligned}$$

The total interaction force between the oxygen sphere and the finite MOF pore is given by,

$$\begin{aligned}
F_{\mathrm{OS}}(X) = 8\pi^2\, a\, b_1^2\, n_{\mathrm{OS}} \sum_k n_k \Bigg[& A_{\mathrm{O},k} \left(\frac{1}{(a^2 - b_1^2 + X^2)^3} + \frac{2\, b_1^2}{(a^2 - b_1^2 + X^2)^4} \right) \\
& - \frac{1}{5} B_{\mathrm{O},k} \left(\frac{5}{(a^2 - b_1^2 + X^2)^6} + \frac{80\, b_1^2}{(a^2 - b_1^2 + X^2)^7} + \frac{336\, b_1^4}{(a^2 - b_1^2 + X^2)^8} + \frac{512\, b_1^6}{(a^2 - b_1^2 + X^2)^9} \right. \\
& \left. + \frac{256\, b_1^8}{(a^2 - b_1^2 + X^2)^{10}} \right) - A_{\mathrm{O},k} \left(\frac{1}{(a^2 - b_1^2 + (d - X)^2)^3} + \frac{2\, b_1^2}{(a^2 - b_1^2 + (d - X)^2)^4} \right) \\
& + \frac{1}{5} B_{\mathrm{O},k} \left(\frac{5}{(a^2 - b_1^2 + (d - X)^2)^6} + \frac{80\, b_1^2}{(a^2 - b_1^2 + (d - X)^2)^7} + \frac{336\, b_1^4}{(a^2 - b_1^2 + (d - X)^2)^8} \right. \\
& \left. + \frac{512\, b_1^6}{(a^2 - b_1^2 + (d - X)^2)^9} + \frac{256\, b_1^8}{(a^2 - b_1^2 + (d - X)^2)^{10}} \right) \Bigg] ,
\end{aligned} \tag{4.10}$$

where $k \in \{\mathrm{H}, \mathrm{O}, \mathrm{C}, \mathrm{Eu}\}$ denotes the atom type.

Similarly, the total interaction force between the hydrogen sphere and the finite MOF pore is

$$\begin{aligned}
F_{\mathrm{HS}}(X) = 8\pi^2\, a\, b_2^2\, n_{\mathrm{HS}} \sum_k n_k \Bigg[& A_{\mathrm{H},k} \left(\frac{1}{(a^2 - b_2^2 + X^2)^3} + \frac{2\, b_2^2}{(a^2 - b_2^2 + X^2)^4} \right) \\
& - \frac{1}{5} B_{\mathrm{H},k} \left(\frac{5}{(a^2 - b_2^2 + X^2)^6} + \frac{80\, b_2^2}{(a^2 - b_2^2 + X^2)^7} + \frac{336\, b_2^4}{(a^2 - b_2^2 + X^2)^8} + \frac{512\, b_2^6}{(a^2 - b_2^2 + X^2)^9} \right. \\
& \left. + \frac{256\, b_2^8}{(a^2 - b_2^2 + X^2)^{10}} \right) - A_{\mathrm{H},k} \left(\frac{1}{(a^2 - b_2^2 + (d - X)^2)^3} + \frac{2\, b_2^2}{(a^2 - b_2^2 + (d - X)^2)^4} \right)
\end{aligned}$$

$$+\frac{1}{5}B_{\mathrm{H},k}\left(\frac{5}{(a^2-b_2^2+(d-X)^2)^6}+\frac{80\,b_2^2}{(a^2-b_2^2+(d-X)^2)^7}+\frac{336\,b_2^4}{(a^2-b_2^2+(d-X)^2)^8}\right.$$
$$\left.+\frac{512\,b_2^6}{(a^2-b_2^2+(d-X)^2)^9}+\frac{256\,b_2^8}{(a^2-b_2^2+(d-X)^2)^{10}}\right)\Bigg]. \tag{4.11}$$

Figure 4.6 shows the interaction forces between the oxygen and hydrogen spheres, and the finite MOF pore. Regardless of where the water molecules are with respect to a pore entrance (or exit), the interaction forces are always directed towards the pore centre. Only at the mid-depth of the MOF pore do the water molecules experience zero net force. Similar to the interaction force with the ferric ion, the maximum magnitude of the interaction force for the water molecules occurs just outside the entrance and the exit of the MOF pore, and the force function is symmetric about the mid-depth of the pore. The maximum interaction force for the oxygen sphere and the hydrogen sphere is $0.057\,\mathrm{eV\,\AA^{-1}}$ and $0.082\,\mathrm{eV\,\AA^{-1}}$, respectively.

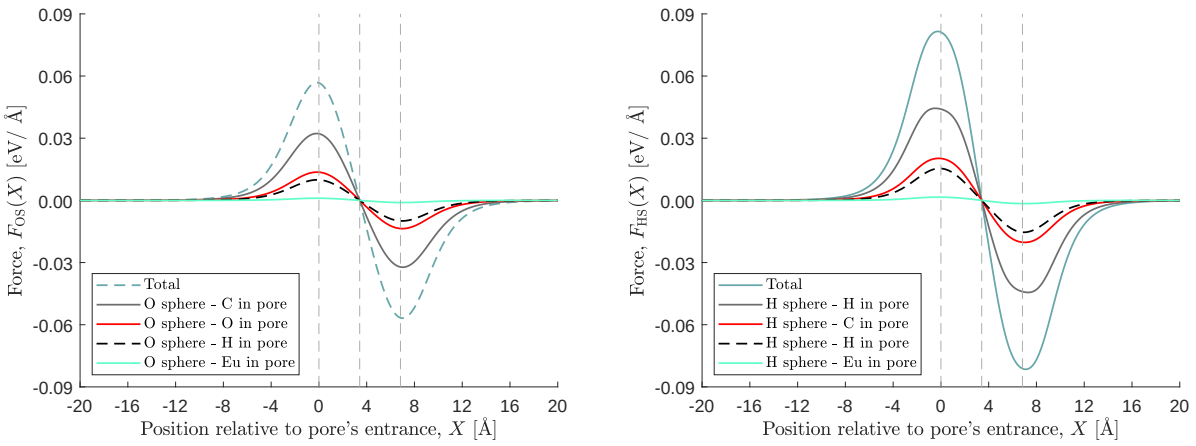


Figure 4.6: Interaction force between (a) oxygen sphere (Equation (4.10)), (b) hydrogen sphere (Equation (4.11)) and finite cylindrical MOF pore with $d = h$. Vertical grey dashed lines mark location of pore's entrance, mid-point and exit, from left to right.

4.2.4. Oxygen and hydrogen sphere's attraction limit

Again, consider a hypothetical MOF pore whereby a redesign of the MOF pore radius is possible while maintaining the same atom density of the true MOF pore. The right-most zero of the interaction force between the oxygen sphere and the hypothetical MOF pore is calculated by solving $F_{\mathrm{OS}}(X_0) = 0$. Caution is needed when considering numerical schemes to find the equilibrium points, since it must be remembered that the attraction limit is dependent on both the MOF pore radius a and the depth of the MOF pore d.

The left-most zero of the interaction force between the oxygen sphere and the hypothetical MOF pore can be found numerically using MATLAB's inbuilt function `fzero` (turquoise dashed line below the bottom grey dashed line in Figure 4.7). The right-most zeros are found numerically using a purpose-built Newton's method. Note that unlike in the semi-infinite case, the left-most and right-most zeros are not symmetric about the MOF pore entrance. This is because the horizontal-intercept is greater than the mid-depth, $d/2$.

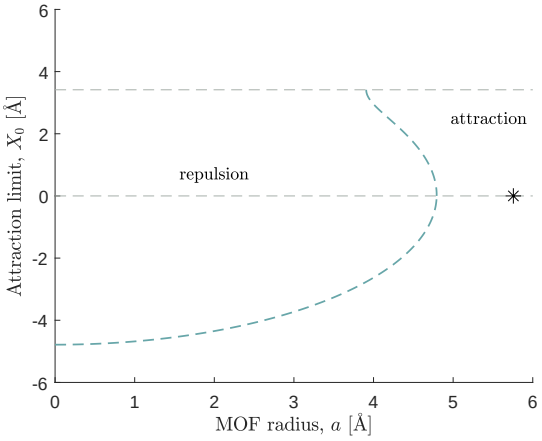


Figure 4.7: Attraction limit X_0 for oxygen sphere as a function of the radius of hypothetical finite cylinder with $d = h$. Asterisk indicates EuMOF pore's radius. Turquoise dashed line is oxygen sphere's attraction limit. Horizontal grey dashed lines mark location of pore's entrance and mid-depth, from bottom to top.

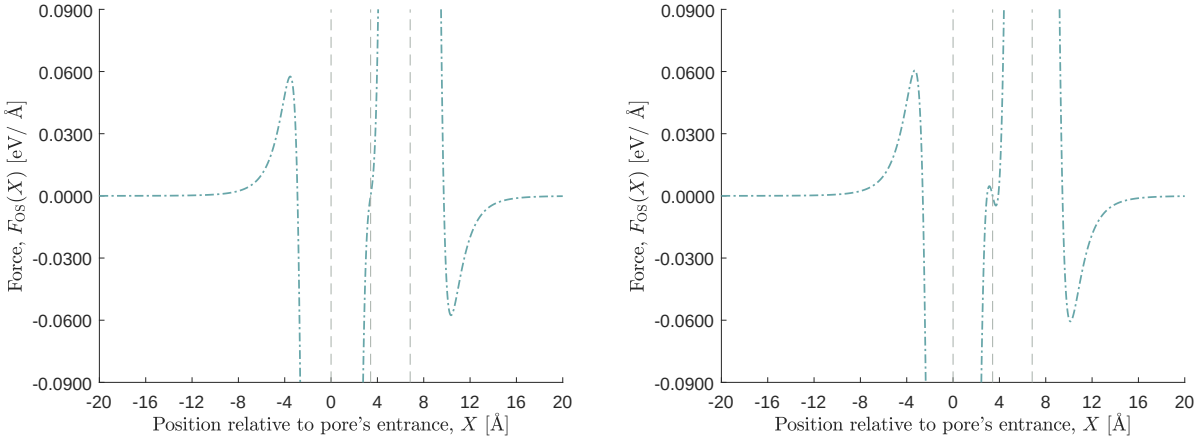
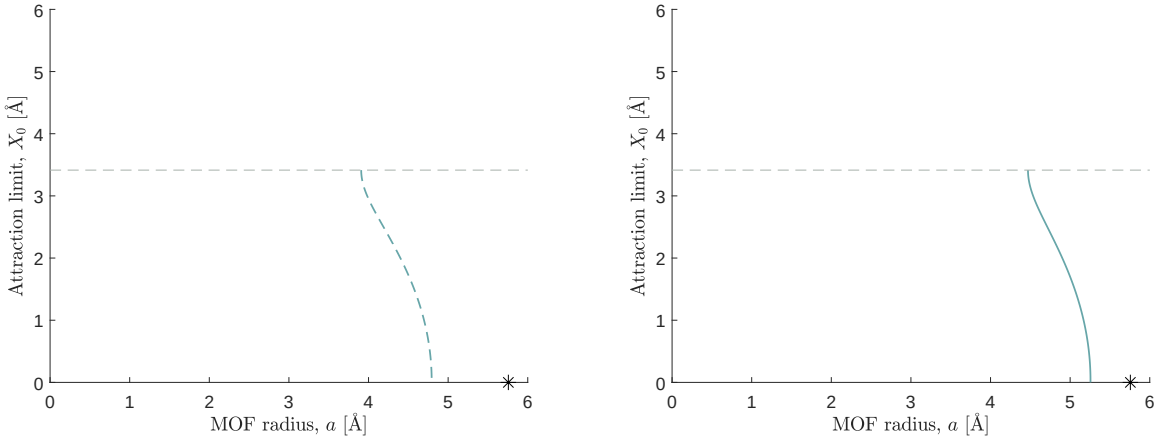


Figure 4.8: Interaction forces between oxygen sphere and hypothetical finite cylinder with $d = h$, where (a) $a = 3.80$ and (b) $a = 4.00$. Vertical grey dashed lines mark location of pore's entrance, mid-point and exit, from left to right.

Recall, that for the finite case, the MOF pore mid-depth $d/2$ is excluded from the definition of

an attraction limit, even though this is an equilibrium point for the interaction force. For a MOF pore radius between zero and the radius at which there is a local minimum (for the particular case shown in Figure 4.7, $a \in [0, 3.908)$), the oxygen sphere experiences only repulsion in the inside the MOF pore, for example Figure 4.8(a). That is, if the sphere is located to the left of the mid-depth, it experiences a force to the left, whereas if the sphere is located to the right of the mid-depth, it experiences a force to the right. For a MOF pore radius where $a \in [3.908, 4.793]$, the oxygen sphere experiences attraction towards the MOF pore mid-depth if it is located near the mid-depth. For example Figure 4.8(b), when the oxygen sphere is located very close to the mid-depth.

The attraction limit for the oxygen sphere is a function of both the MOF pore radius a and the MOF pore depth d. For the specific case where $d = h$, the oxygen sphere is unconditionally rejected from the MOF pore for pore radii $a \in [0, 3.908)$. The attraction limit for the oxygen sphere exists for a pore radius greater and equal to 3.908 Å. The oxygen sphere is conditionally accepted for MOF radii in the range $a \in [3.908, 4.793)$. That is, the oxygen sphere will experience a left-ward force near the pore entrance but a right-ward force at the pore mid-depth. The oxygen sphere is unconditionally accepted into the MOF pore for radii greater than 4.793 Å (horizontal-intercept in Figure 4.7).



(a) (b)

Figure 4.9: Attraction limits X_0 for (a) oxygen sphere and (b) hydrogen sphere as a function of radius of hypothetical finite cylinder with $d = h$. Asterisks indicate EuMOF pore's radius. Horizontal grey dashed lines mark location of pore's mid-depth. Panel (a) is reproduced portion of Figure 4.7.

Similarly, the attraction limit for the hydrogen sphere exists for a pore radius greater than or equal to 4.470 Å and the hydrogen sphere is conditionally accepted in the MOF pore for radii in the range $a \in [4.470, 5.256]$. As $d \to \infty$, the attraction limit for the finite case tends to the attraction limit

in the semi-infinite case (not shown here).

Figure 4.9 shows the attraction limits for the finite case for the oxygen sphere and the hydrogen sphere. In the case of the true MOF pore, both spheres are unconditionally attracted to the pore entrance, as shown by the asterisks lying to the right of the attraction limit boundary.

4.3. ACCEPTANCE AND KINETIC ENERGY

Recall that the acceptance energy, Equation (3.22), is the energy gained by the hydrated ferric ion as a consequence of the interaction force to displace it from the far (left) field to the attraction limit $X_0 \in [0, d/2)$ into the MOF pore. The acceptance energy was described in Chapter 2 and is calculated using Equation (2.5). The maximum kinetic energy gain of the hydrated ferric ion as a consequence of the interaction forces with a finite MOF pore is calculated using Equation (3.23) with Equation (2.7). Note that there is a slight difference when calculating the maximum kinetic energy in the finite case, where the upper bound of the integral is the pore mid-depth. This section maintains the idea of a hypothetical MOF pore where it is possible to vary the pore radius a.

4.3.1. Ferric ion point to MOF pore

Equation (3.24) is used to calculate the acceptance energy as a consequence of the interaction force between the ferric ion and atom type k in the MOF pore when the ferric ion is displaced from the far (left) field to the attraction limit. The acceptance energy for the ferric ion to be displaced from the left far field to pore depth $X_0 \in [0, d/2)$ by atom type k in the MOF pore gives (see Appendix B.3.1 for details),

$$Ea_{\mathrm{Fe},k} = \frac{2\pi\, n_k}{a^4}\left[A_{\mathrm{Fe},k}\, H_2(a, -X_0; d) - \frac{1}{a^6} B_{\mathrm{Fe},k}\, H_5(a, -X_0; d)\right].$$

The total acceptance energy for the ferric ion to enter the finite MOF pore is

$$Ea_{\mathrm{Fe}} = \frac{2\pi}{a^4}\sum_k n_k\left[A_{\mathrm{Fe},k}\, H_2(a, -X_0; d) - \frac{1}{a^6} B_{\mathrm{Fe},k}\, H_5(a, -X_0; d)\right]. \tag{4.12}$$

The maximum kinetic energy gain as consequence of the interaction force of atom type k to move

the ferric ion from the far (left) field to the pore mid-depth $d/2$ is (see Appendix B.3.2 for details),

$$Ek_{\mathrm{Fe},k} = \frac{4\pi\, n_k}{a^4}\left[A_{\mathrm{Fe},k}\, I_2(2a,d) - \frac{1}{a^6} B_{\mathrm{Fe},k}\, I_5(2a,d)\right].$$

The maximum energy gain as consequence of the interaction force moving the ferric ion from the far (left) field to the pore mid-depth $d/2$, is

$$Ek_{\mathrm{Fe}} = \frac{4\pi}{a^4}\sum_k n_k\left[A_{\mathrm{Fe},k}\, I_2(2a,d) - \frac{1}{a^6} B_{\mathrm{Fe},k}\, I_5(2a,d)\right]. \tag{4.13}$$

The total acceptance energy and the maximum kinetic energy gain of the ferric ion interacting with the true finite MOF pore is 0.006 eV and 0.009 eV, and indicated by asterisks in Figure 4.10.

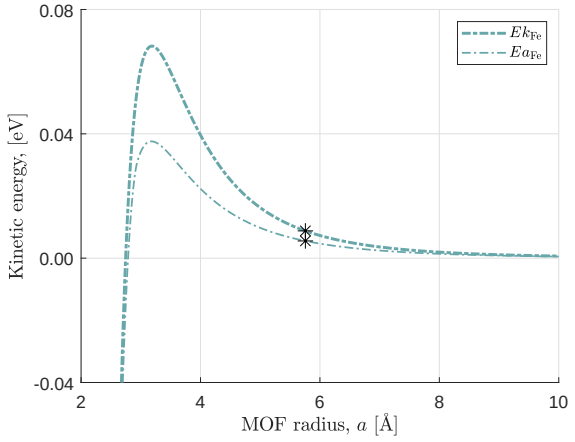


Figure 4.10: Total acceptance energy (Equation (4.13)) and the maximum kinetic energy (Equation (4.12)) as consequence of interaction force on ferric ion, $d = h$. Asterisks indicate EuMOF pore's radius.

Figure 4.10 shows energy profiles as functions of the MOF pore radius a for the acceptance energy and the maximum kinetic energy as a consequence of the interaction forces. For pore radii in the range $2.746\,\text{Å} < a < 2.787\,\text{Å}$, the ferric ion requires an initial velocity to negate the effects of the negative acceptance energy. For pore radii greater than 2.787 Å, the ferric ion will always be accepted into the MOF pore.

4.3.2. Oxygen and hydrogen spheres to MOF pore

The acceptance energy gained as a consequence of the interaction forces between the MOF pore and the oxygen and hydrogen spheres is calculated in order to account for the effects of the surrounding

water molecules. Equation (3.27) is used to calculate the energy gained as a consequence of the interaction force between the oxygen sphere and the MOF pore moving the oxygen sphere from the far (left) field to the attraction limit X_0. The contribution for atom type k using Equations (3.27) and (4.7) gives (see Appendix B.3.2 for details)

$$\begin{aligned} Ea_{\mathrm{OS},k} = 8\pi^2\, a\, b_1^2\, n_k\, n_{\mathrm{OS}}\, \lambda^{-5} \big[& A_{\mathrm{O},k} \left(H_2(\lambda_1, -X_0; d) + 2\, b_1^2\, \lambda_1^{-2}\, H_3(\lambda_1, -X_0; d) \right) \\ & -\frac{1}{5} \lambda_1^{-6}\, B_{\mathrm{O},k} \left(5\, H_5(\lambda_1, -X_0; d) + 80\, b_1^2\, \lambda_1^{-2} H_6(\lambda_1, -X_0; d) + 336\, b_1^4\, \lambda_1^{-4} H_7(\lambda_1, -X_0; d) \right. \\ & \left. +512\, b_1^6\, \lambda_1^{-6} H_8(\lambda_1, -X_0; d) + 256\, b_1^8\, \lambda_1^{-8} H_9(\lambda_1, -X_0; d) \right) \big] . \end{aligned}$$

The total acceptance energy for the oxygen sphere to enter the finite MOF pore is

$$\begin{aligned} Ea_{\mathrm{OS}} = 8\pi^2\, a\, b_1^2\, n_{\mathrm{OS}}\, \lambda^{-5} \sum_k n_k \big[& A_{\mathrm{O},k} \left(H_2(\lambda_1, -X_0; d) + 2\, b_1^2\, \lambda_1^{-2}\, H_3(\lambda_1, -X_0; d) \right) \\ & -\frac{1}{5} \lambda_1^{-6}\, B_{\mathrm{O},k} \left(5\, H_5(\lambda_1, -X_0; d) + 80\, b_1^2\, \lambda_1^{-2} H_6(\lambda_1, -X_0; d) + 336\, b_1^4\, \lambda_1^{-4} H_7(\lambda_1, -X_0; d) \right. \\ & \left. +512\, b_1^6\, \lambda_1^{-6} H_8(\lambda_1, -X_0; d) + 256\, b_1^8\, \lambda_1^{-8} H_9(\lambda_1, -X_0; d) \right) \big] . \end{aligned}$$

The maximum kinetic energy gain as consequence of the interaction force of atom type k to move the oxygen sphere from the far (left) field to the pore mid-depth $d/2$ is (see Appendix B.3.2 for details),

$$\begin{aligned} Ek_{\mathrm{OS},k} = 16\pi^2\, a\, b_1^2\, n_k\, n_{\mathrm{OS}}\, \lambda_1^{-5} \big[& A_{\mathrm{O},k} \left(I_2(2\lambda_1, d) + 2\, b_1^2\, \lambda_1^{-2}\, I_3(2\lambda_1, d) \right) \\ & -\frac{1}{5} \lambda_1^{-6}\, B_{\mathrm{O},k} \left(5\, I_5(2\lambda_1, d) + 80\, b_1^2\, \lambda_1^{-2} I_6(2\lambda_1, d) + 336\, b_1^4\, \lambda_1^{-4} I_7(2\lambda_1, d) \right. \\ & \left. +512\, b_1^6\, \lambda_1^{-6} I_8(2\lambda_1, d) + 256\, b_1^8\, \lambda_1^{-8} I_9(2\lambda_1, d) \right) \big] . \end{aligned}$$

The maximum kinetic energy gain of the oxygen sphere as a consequence of the interaction force is

$$\begin{aligned} Ek_{\mathrm{OS}} = 16\pi^2\, a\, b_1^2\, n_{\mathrm{OS}}\, \lambda_1^{-5} \sum_k n_k \big[& A_{\mathrm{O},k} \left(I_2(2\lambda_1, d) + 2\, b_1^2\, \lambda_1^{-2}\, I_3(2\lambda_1, d) \right) \\ & -\frac{1}{5} \lambda_1^{-6}\, B_{\mathrm{O},k} \left(5\, I_5(2\lambda_1, d) + 80\, b_1^2\, \lambda_1^{-2} I_6(2\lambda_1, d) + 336\, b_1^4\, \lambda_1^{-4} I_7(2\lambda_1, d) \right. \\ & \left. +512\, b_1^6\, \lambda_1^{-6} I_8(2\lambda_1, d) + 256\, b_1^8\, \lambda_1^{-8} I_9(2\lambda_1, d) \right) \big] . \end{aligned}$$

The total acceptance energy and the maximum kinetic energy gain of the oxygen sphere interacting

with the true MOF pore are 0.191 eV and 0.309 eV respectively, and indicated by asterisks in Figure 4.11(a).

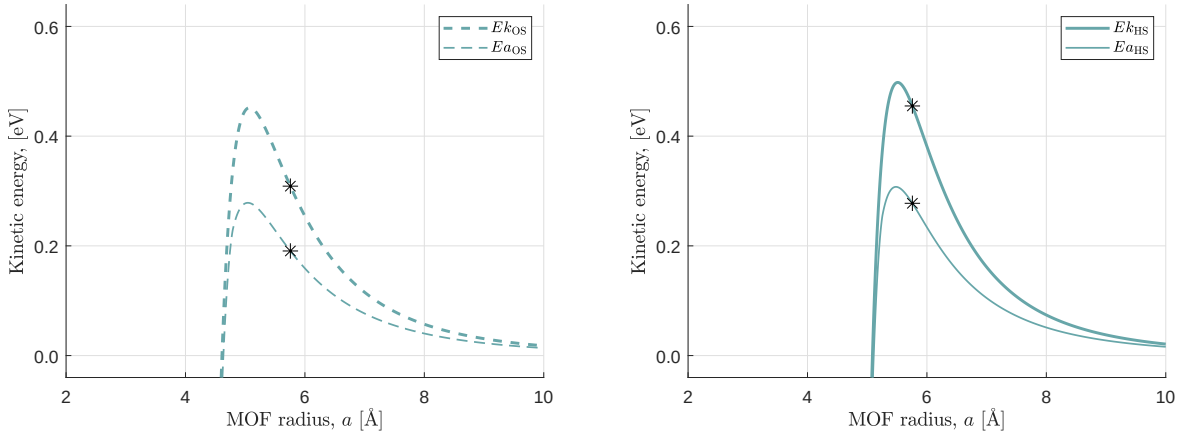
Similarly, the total acceptance energy for the hydrogen sphere to be accepted into the MOF pore and displaced to the attraction limit is

$$\begin{aligned} Ea_{\mathrm{HS}} = 8\pi^2\, a\, b_2^2\, n_{\mathrm{HS}}\, \lambda^{-5} \sum_k n_k \big[& A_{\mathrm{HS},k} \left(H_2(\lambda_2, -X_0; d) + 2\, b_2^2\, \lambda_2^{-2}\, H_3(\lambda_2, -X_0; d) \right) \\ & -\frac{1}{5} \lambda_2^{-6}\, B_{\mathrm{HS},k} \left(5\, H_5(\lambda_2, -X_0; d) + 80\, b_2^2\, \lambda_2^{-2} H_6(\lambda_2, -X_0; d) + 336\, b_2^4\, \lambda_2^{-4} H_7(\lambda_2, -X_0; d) \right. \\ & \left. +512\, b_2^6\, \lambda_2^{-6} H_8(\lambda_2, -X_0; d) + 256\, b_2^8\, \lambda_2^{-8} H_9(\lambda_2, -X_0; d) \right) \big] , \end{aligned}$$

and the maximum kinetic energy gain of the hydrogen sphere is

$$\begin{aligned} Ek_{\mathrm{HS}} = 16\pi^2\, a\, b_2^2\, n_{\mathrm{HS}}\, \lambda_2^{-5} \sum_k n_k \big[& A_{\mathrm{H},k} \left(I_2(2\lambda_2, d) + 2\, b_2^2\, \lambda_2^{-2}\, I_3(2\lambda_2, d) \right) \\ & -\frac{1}{5} \lambda_2^{-6}\, B_{\mathrm{H},k} \left(5\, I_5(2\lambda_2, d) + 80\, b_2^2\, \lambda_2^{-2} I_6(2\lambda_1, d) + 336\, b_2^4\, \lambda_2^{-4} I_7(\lambda_2, d) \right. \\ & \left. +512\, b_2^6\, \lambda_2^{-6} I_8(2\lambda_2, d) + 256\, b_2^8\, \lambda_2^{-8} I_9(2\lambda_2, d) \right) \big] . \end{aligned}$$

The total acceptance energy and the maximum kinetic energy gain of the hydrogen sphere interacting with the true MOF pore are 0.278 eV and 0.455 eV respectively, and indicated by asterisks in Figure 4.11(b).



(a) (b)

Figure 4.11: Total acceptance energy and maximum kinetic energy as consequence of interaction force of (a) oxygen and (b) hydrogen sphere, $d = h$. Asterisks indicate EuMOF pore's radius.

Figure 4.11 shows the acceptance energy for a MOF pore radii where the attraction limit exists

(Figure 4.11(a), $a > 3.908$ and Figure 4.11(b), $a > 4.470$). This is because for MOF pore radii below this threshold, the spheres only experience repulsion near and inside the MOF pore. In other words, for a MOF pore radius in the range $b_1 < a < 4.611\,\text{Å}$, the oxygen sphere is unconditionally rejected from the MOF pore.

The oxygen sphere requires a minimum MOF pore radius 4.634 Å to be accepted into the MOF pore. For a MOF pore radius in the range $4.611\,\text{Å} < a < 4.634\,\text{Å}$, the oxygen sphere would require an initial (rightward) velocity to negate the effects of the negative acceptance energy. In contrast, the hydrogen sphere requires an even larger MOF pore radius minimum, 5.109 Å. For a MOF pore radius in the range $5.088\,\text{Å} < a < 5.109\,\text{Å}$, the hydrogen sphere would require an initial (rightward) velocity to negate the effects of the negative acceptance energy.

4.4. DISCUSSION

In this chapter, the MOF pore was approximated by a finite cylinder with depth d and the van der Waals theory was applied to calculate the interactions between this finite MOF pore and a hydrated ferric ion. The results presented so far are primarily for $d = h$, that is, the magnitude of the MOF's b-axis vector.

The total interaction energy between the hydrated ferric ion and the finite MOF pore profiles are shown in Figure 4.12. The water molecules continue to contribute the majority of the interaction energy. The most energetically favourable position for the ferric ion is at the mid-point of the MOF pore, with a potential energy minimum of $-0.773\,\text{eV}$.

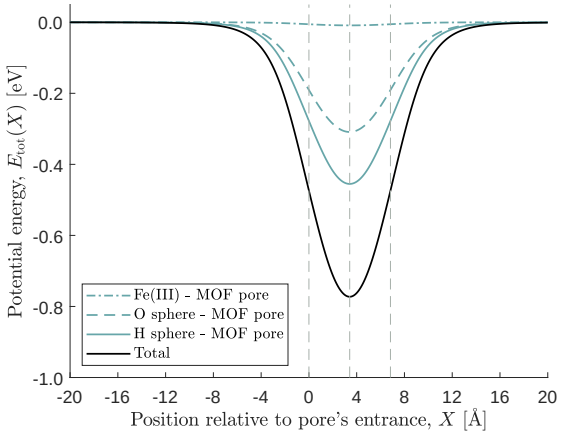


Figure 4.12: Interaction energy between hydrated ferric ion and finite cylindrical MOF pore with $d = h$, Equation (3.2). Vertical dashed lines mark location of pore's entrance, mid-depth and exit, from left to right.

Calculating the interaction forces between the hydrated ferric ion and the finite MOF pore gives further insight as to why the mid-point is the most favourable position. When the hydrated ferric ion is near the entrance of the pore, the interaction force is directed to the right, Figure 4.13. The hydrated ferric ion experiences no force at the MOF pore's mid-point and when near the exit there is a force directed to the left. The maximum interaction force for the hydrated ferric ion is $0.140\,\text{eV}\,\text{Å}^{-1}$.

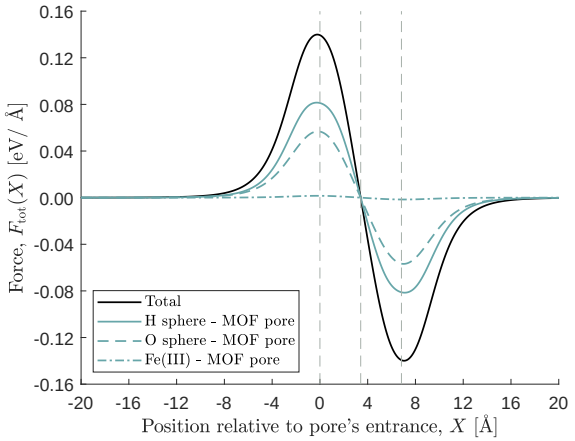
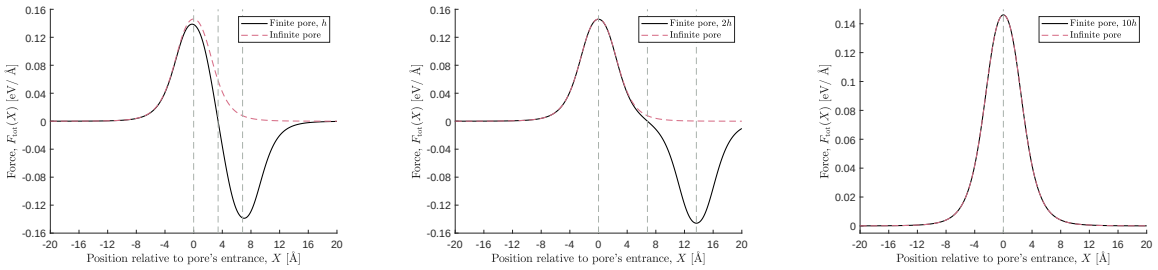


Figure 4.13: Interaction force between hydrated ferric ion and finite cylindrical MOF pore with $d = h$, Equation (3.11). Vertical grey dashed lines mark location of pore's entrance, mid-depth and exit, from left to right.

This indicates that if the hydrated ferric ion is inside the pore and is near the MOF pore's entrance or exit, the interaction forces will pull the hydrated ferric ion towards the pore centre point. Once the hydrated ferric ion is inside the MOF pore, it is likely to remain there.

Using the framework developed in this chapter and Chapter 2, it's possible to calculate the interaction force between a hydrated ferric ion and a finite MOF pore of any depth (noting that if the pore depth is not an integer multiple of the unit cell, and if the same atomic surface densities are maintained, the modelling may include a pore that has fractions of atoms). Figure 4.14 shows the interaction force profile between a hydrated ferric ion and a finite MOF pore of various depths, together with a profile for the semi-infinite pore for comparison. The point at which the interaction force is zero is always at the mid-depth of the finite pore. When the finite pore is sufficiently deep, the interaction force using the finite and semi-infinite cylindrical MOF pore approximations coincide near the pore entrance. The difference between the two approximations at the pore entrance, $X = 0$, when the finite MOF pore has depth $10h$ is less than 10^{-6} eV Å^{-1}.

Returning back to the hypothetical MOF pore where the pore radius can be chosen, looking at



(a) (b) (c)

Figure 4.14: Interaction force between hydrated ferric ion and finite cylindrical MOF pore, Equation (3.11), where MOF depth is (a) $d = h$, (b) $d = 2h$ and (c) $d = 10h$. Black solid line is the interaction force with finite MOF pore and blush dashed line is infinite MOF pore. Vertical grey dashed lines mark location of pore's entrance, mid-depth and exit, from left to right.

condition (4.9a), notice that the attraction limit is now based on two properties of the MOF pore: its radius a and its depth d. Condition (4.9) makes it obvious that the mid-depth of the MOF pore will always be the right-most zero ($X_0 \in (-\infty, h/2]$) regardless of the MOF pore radius a, however the pore mid-depth is excluded from the definition of the attraction limit in the finite case. The change in the MOF pore depth does not affect the qualitative behaviour of the interaction forces, see for example Figure 4.14.

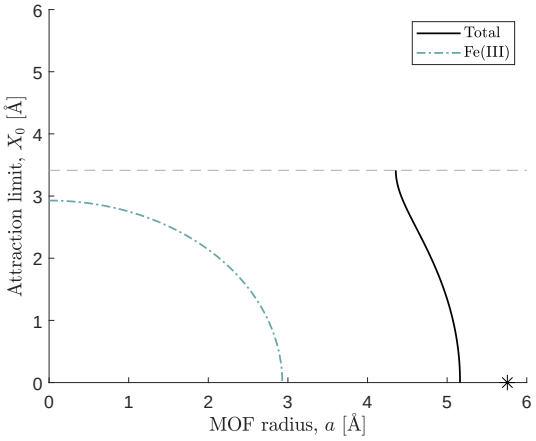


Figure 4.15: Attraction limit X_0 for ferric ion and hydrated ferric ion as a function of radius of hypothetical finite cylinder with $d = h$. Asterisk indicates EuMOF pore's radius.

Numerical calculations for the attraction limit show that the hydrated ferric ion will always be rejected from the MOF pore for pore radii less than 4.355 Å (see the solid black line in Figure 4.15). Unlike the semi-infinite case, for a finite MOF pore the attraction limit for the hydrated ferric ion is not an elliptic boundary. As the depth of the MOF pore increases, the attraction limit for the hydrated ferric ion tends to the semi-infinite case. Another noticeable difference between the finite

and semi-infinite MOF pore approximation, is that the hydrated ferric ion will always experience a change in the direction of the force (or have an equilibrium point) when interacting with the finite MOF pore; see the solid black line in Figure 4.15. In the case of the true MOF pore, the hydrated ferric ion will be accepted into the pore.

The total acceptance energy and the maximum kinetic energy gain of the hydrated ferric ion interacting with the true MOF pore are 0.474 eV and 0.773 eV respectively, and indicated by asterisks in Figure 4.16.

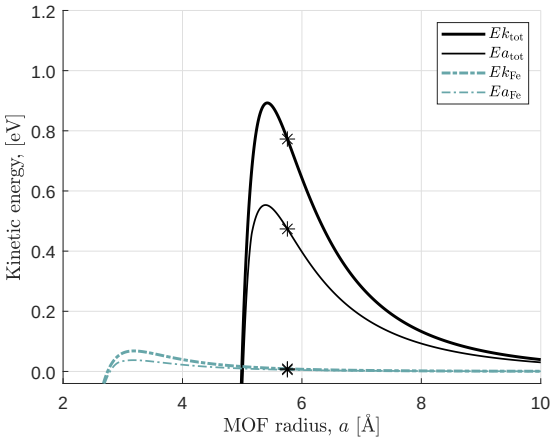


Figure 4.16: Total acceptance energy and maximum kinetic energy of ferric ion, Equations (4.12) and (4.13), and hydrated ferric ion, Equations (3.22) and (3.23), $d = h$. Asterisks indicate EuMOF pore's radius.

The hydrated ferric ion requires a minimum MOF pore radius 5.013 Å to be accepted into the MOF pore. The minimum radius for a hydrated ferric ion (x-intercept in Figure 4.16) is less than the minimum for a hydrogen sphere (x-intercept in Figure 4.11(b)). For a MOF pore radius 4.992 Å $< a <$ 5.013 Å, the hydrated ferric ion would require an initial velocity to be accepted into the MOF pore to negate the effects of the negative acceptance energy. Note that total acceptance energy and maximum kinetic energy solutions for the hydrated ferric ion are for a MOF pore radius greater than the interacting hydrogen sphere $a >$ 4.355 Å.

CHAPTER 5

CHANGES IN MODELLING ASSUMPTIONS

This chapter considers changes in the modelling assumptions to take into consideration more of the sensing environment and investigates the implications of the alternate assumptions on the results. The first section considers interactions between the MOF pore and other metal ions, since the sensor will be exposed to a solution containing many different metal ions. The next two sections approximate the MOF pore with a rectangular prism. This is a truer representation than the cylindrical approximation, since the top view of the MOF pore is a parallelogram. A comparison between the prism and the cylindrical approximation shows a small quantitative change, but qualitatively the results are the same. Section 5.4 studies how a ferric ion interacts with a blocked MOF pore. Section 5.5 considers the implication of a hydrated ferric ion interacting with multiple MOF pores. Lastly, the effect of temperature on the Lennard-Jones potential is investigated. This chapter concludes with a discussion.

All analysis and insight surrounding the study of the interactions between the ions and the EuBDC-OMe MOF are new, including the introduction of the analytical expressions for interaction energy and force between a point and prism.

5.1. INTERACTIONS BETWEEN OTHER METAL IONS AND A SEMI-INFINITE CYLINDRICAL MOF PORE

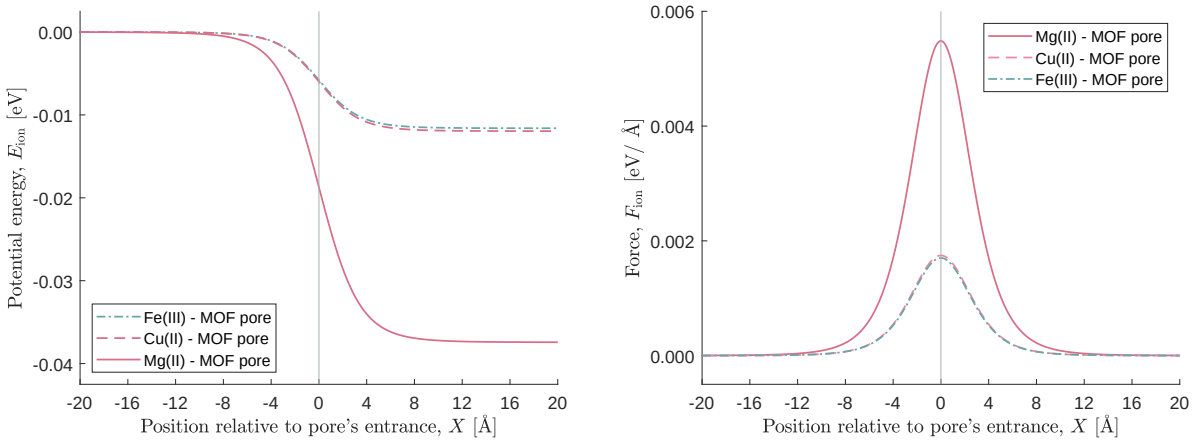
In practice, the sensor will be submerged in an analyte solution containing a mixture of ground rock, water and other chemicals. MOF pores can be clogged, hindering the ferric ions from occupying MOF pore entrances, and interfering with the sensing capabilities of the device. In addition, ferrous ions and other dications are likely to be attracted to the MOF pore along with the ferric ions. These dications do not cause the same changes in the intensity profile of the photoluminescence spectrum of the MOF as the ferric ions, however if they are attracted to the MOF pore in the same way, they have the potential to interfere with the sensor by blocking pores that may otherwise be occupied by ferric ions. Here, the interactions between two metal dications and the MOF pore are calculated, namely copper(II) and magnesium(II); the corresponding equilibrium distance and well-depth constants are given in Table 5.1. Since the equilibrium distance and well-depth constants for ferric ions are assumed to be the same as ferrous ions, the interaction force curves for ferrous ions will be the same as those presented in the previous chapters.

Atom type	van der Waals diameter, σ (Å)	Well-depth, ϵ (eV)
Copper(II), Cu	3.1137	0.0002
Magnesium(II), Mg	2.6914	0.0048

Table 5.1: Lennard-Jones parameters for copper(II) and magnesium(II) [37].

Note that only the unhydrated metal ions are considered here. In the case of each metal ion, the presence of water molecules only serves to magnify the overall contribution to interaction energy and force.

The metal dications are approximated by a point and the MOF pore is approximated by an semi-infinite cylinder. The geometry of the problem remains unchanged and is described in Figure 3.1 and the surrounding text. To calculate the total interaction energy and force between the metal ions and the semi-infinite MOF pore, Equations (3.3) and (3.12) are used, with the individual contributions given by Equations (3.5) and (3.13), respectively. The attractive and repulsive constants are adjusted according to the interacting dication.



(a) (b)

Figure 5.1: (a) Interaction energy between different metal ions and a semi-infinite cylindrical MOF pore. Blush dashed and solid line show interaction energy between a copper(II) ion and semi-infinite cylindrical MOF pore, and magnesium(II) ion and semi-infinite cylindrical MOF pore, respectively. Vertical line marks location of pore opening. Turquoise shows ferric ion. Turquoise dot dashed and blush dashed lines nearly lie on top of one another. (b) Interaction force between different ions and a semi-infinite cylindrical MOF pore.

Figure 5.1 shows the interactions of the copper(II) and magnesium(II) ions with the MOF pore. The ferric ion interaction curve (turquoise dot dashed line) is also shown for comparison. The interaction energy and the force profile for the copper(II) ions is very similar to the ferric ion. In contrast, the interaction energy and force between the magnesium(II) ion and the MOF pore is

significantly larger, indicating that magnesium(II) has a greater affinity to the MOF pore.

Consider again the hypothetical MOF pore, where the atom density of the MOF is maintained but the radius of the hypothetical MOF pore can change. Condition (3.15) still holds true and the attraction limits for the metal ions are shown in Figure 5.2. There is a very small range of pore radii for which the interaction force is repulsive for copper(II) and magnesium(II) ions, and attractive for ferric ions. For a MOF pore radius in the range 2.927 Å $< a <$ 2.975 Å, the MOF pore is selective for the ferric ions only. While this is an extremely narrow range and unlikely to occur in practice, it is an interesting observation.

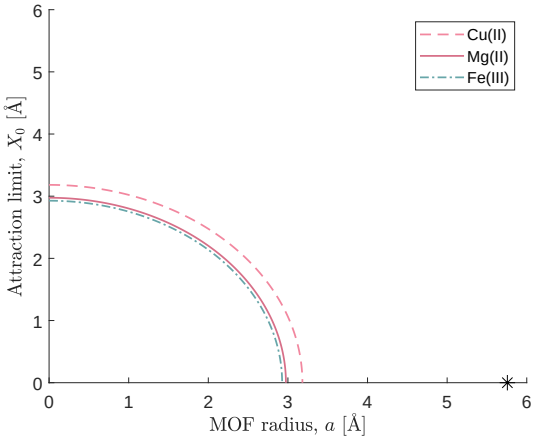


Figure 5.2: Attraction limit X_0 as a function of the radius of hypothetical semi-infinite cylinder. Turquoise dot dashed line shows equilibrium points between ferric ion and MOF pore. Blush dashed and solid line show equilibrium points between copper(II) and MOF pore, and magnesium(II) and MOF pore, respectively. Asterisk indicates EuMOF pore's radius.

Figure 5.1 shows that the interaction between the ferric ions and the MOF is very similar to the interaction between copper(II) ions and the MOF, while the interaction between magnesium(II) ions and the MOF is much greater in magnitude. In contrast, Figure 5.2 shows that in terms of the attraction limit, the ferric ions behave in a similar way to the magnesium(II) ions, while the attraction limit for copper(II) ions is greater. This can be explained as follows. The attractive constants for interactions of ferric ions and copper(II) ions with the MOF are almost the same magnitude (i.e. $A_{\mathrm{Fe},k} \approx A_{\mathrm{Cu},k}$), and the repulsive constants are the same order of magnitude but differ in value by approximately 50% (i.e. $B_{\mathrm{Fe},k} \approx 1.5 \times B_{\mathrm{Cu},k}$). As a consequence, the interaction energy and force are similar and copper(II) ions have a slightly greater interaction due to the slightly larger repulsive constants. On the other hand, the attraction limit depends on the ratio between the atom-density-weighted sum of the repulsive constants and the atom-density-weighted sum of

the attractive constants. This ratio is very similar for ferric and magnesium(II) ions, but due to the 50% greater variation of the repulsive constants for copper(II) ions ($B_{\mathrm{Cu},k}$), the attraction limit boundary for copper(II) ions is pushed farther to the right.

Although copper(II) and magnesium(II) are attracted to the MOF pores, in experimental testing the MOF is ferric ion selective, at least in terms of photoluminescence [41]. Copper and magnesium dications have very little effect on the emission ratio of the MOF bimodal luminescence peaks in either the absence or presence of ferric ions. Any available MOF pores may be occupied by copper(II) and magnesium(II) (instead of being occupied by ferric ions), but the sensor's fluorescence response is not affected by these dications.

5.2. INTERACTIONS BETWEEN A FERRIC ION AND A SEMI-INFINITE RECTANGULAR PRISM MOF PORE

A good first step to approximating the interactions between molecules and porous materials is to consider them as points, spheres and cylinders (that is, simple geometric shapes with rotational symmetry). However, not all molecular structures possess rotational symmetry and while the use of geometric shapes with rotational symmetry results in simplified expressions for the interaction energies, it is expected that the use of more representative shapes might result in more accurate calculations (although the calculations in this case will be more complicated). Baowan and Thamwattana [6] studied the absorption of water molecules into a silica gel by comparing three different approximate pore shapes: cylindrical, square prismatic, and conical. Baowan and Hill [4] found expressions for the interaction energy of a point with a line, a plane, a ring, a spherical surface, and a cylindrical surface. In these papers, the interactions are found in terms of series expansions and hypergeometric functions; expressions that are often considerably more complicated than those required in the case of symmetric approximations of molecular structures.

The MOF considered here possesses pores that in practice have an approximately parallelogram-shaped cross-section; in Chapters 2 to 4 these pores have been approximated by a cylinder. Figure 1.4(d) shows the MOF structure at the b-axis of symmetry and what is considered the "top" view of the pore. In this chapter, the parallelogram-shaped MOF pore is approximated by a rectangular prism, where the ligands are modelled as semi-infinite planes and the europium nodes with associated water molecules as semi-infinite lines. In Figure 1.5(b), the opposite faces of the unit cell are comprised of two ligands (where the benzene rings are facing each other) bridging four

europium metal ions (along the a-axis of symmetry), and the adjacent sides have a single diagonal ligand.

The prism formulation is based on that of Baowan and Thamwattana [6] to derive the interaction energy between a point and a rectangular prism, however all the relevant integrals are here evaluated analytically and expressed in terms of standard functions. This was not done in [6].

In the subsections that follow, first the parameters and geometry of the remodelled system are described, then the calculations and results of the van der Waals interaction energies and forces using the Lennard-Jones potential are presented.

5.2.1. Parameters and geometry of the remodelled system

Recall from Subsection 1.3.1, the molecular formula for the MOF crystal is $Eu_2(C_9H_6O_5)_3 \cdot 2\,H_2O$ and that these unit cells are repeated to create the MOF structures shown in Figures 1.4 and 1.5. A single pore is assumed to consist of two of these molecular unit cells together with four linking europium atoms and water molecules [41]. The europium nodes with associated water molecules are located along the edges of the prism, and so the europium ions and associated water molecules are approximated by four semi-infinite lines. The bridging ligands are approximated by four semi-infinite planes. The vertical planes are parallel to the a-axis of symmetry and have two bridging ligands. Table 1.2 provides a broad view of the location of corresponding atoms and Table 5.2 provides the number of each atom type at the node and ligand location.

Atomic type	Number per single pore/cell				
	Atoms at node	Nodes	Atoms in ligand	Ligands	Total atoms
Europium	2	4	0	0	8
Hydrogen	4	4	6	6	52
Oxygen	2	4	5	6	38
Carbon	0	0	9	6	54

Table 5.2: Number of atoms located at ligand and node, and split by atom type [41].

Figure 5.3 shows a ferric ion characterised by a point particle located on the centreline of a semi-infinite rectangular prism. The centreline of the prism is positioned along the x-axis and the entrance of the prism is located at the origin. The ferric ion initially has the coordinates $(X, 0, 0)$, where $X < 0$ and the prism is formed by the four planes given by $\{(x_p, y_p, z_p)|x_p \in [0, \infty), y_p = \pm\alpha, z_p \in [-\beta, \beta]\}$ and $\{(x_p, y_p, z_p)|x_p \in [0, \infty), y_p = [-\alpha, \alpha], z_p = \pm\beta\}$, where α and β are real constants.

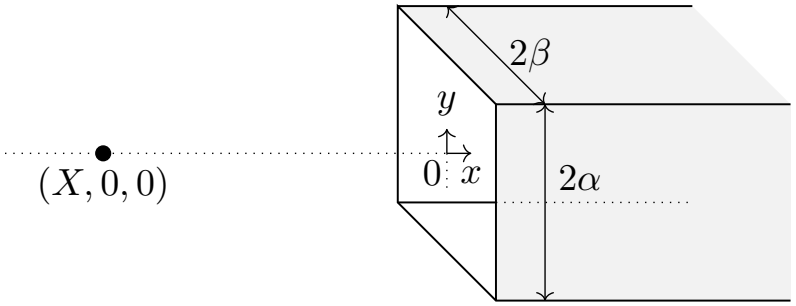


Figure 5.3: Schematic of ferric ion and MOF pore as approximated by semi-infinite rectangular prism.

The basis vectors can be used to map the entire MOF structure, where the b-axis basis vector is taken to be the depth of a unit cell. The a-axis and c-axis basis vectors are used to calculate the height and width of the pore in the prism approximation. Figure 5.4 shows the a-axis and c-axis basis vectors mapping on a pore opening, where the c-axis basis vector spans the width of two MOF pores.

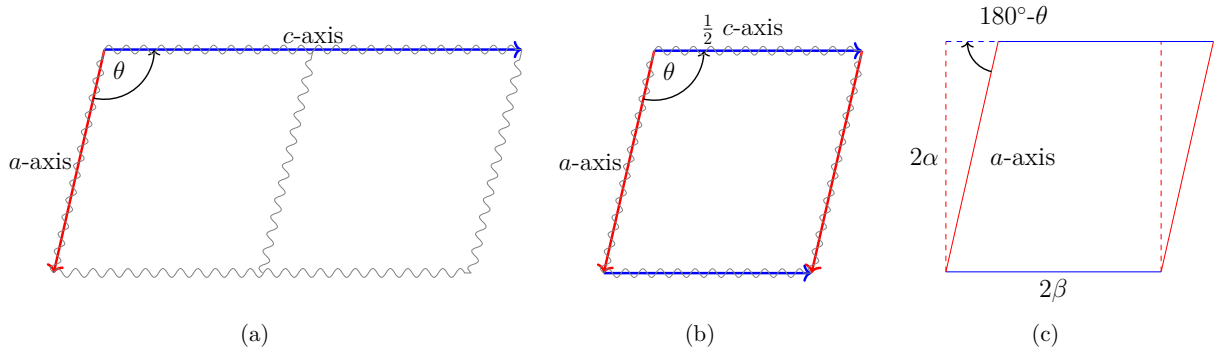


Figure 5.4: Visual justification of parameters used for prism approximation. Gray wavy lines represent MOF structure, red arrow line represents a-axis basis vector and blue arrow line represents c-axis basis vector. Red dashed line is the length of parallelogram and blue dashed line is extension of c-axis basis vector. (a) Mapping of MOF pores using a-axis and c-axis basis vectors. (b) Mapping a single MOF pore in terms of basis vectors. (c) Approximating parallelogram as rectangle.

The width of a single MOF pore is half the magnitude of the c-axis basis vector, Figure 5.4(b). Therefore, the width of the prism is taken to be half the magnitude of the c-axis basis vector (in Table 1.1), so that $2\beta = c\text{-axis}/2 = 10.488\,\text{Å}$, and the adjacent side of the parallelogram has the magnitude of the a-axis basis vector. Therefore, the height of the prism is $2\alpha = a\text{-axis} \times \sin(180 - \theta) = 11.2269\,\text{Å}$, seen as the red dashed line in Figure 5.4(c). This approximation ensures that the area of the rectangle is equal to the area of the parallelogram. Note that the vertical plane has two bridging ligands (parallel to the a-axis basis vector) and that the mean surface density for the vertical plane should be about twice that of the horizontal plane.

Ferric ions are typically associated with six water molecules when in solution [26]. However, only the interaction between the ferric ion (without associated water molecules) and the MOF pore is considered here. In order to compare the cylindrical and the prismatic approximations, the water molecules are ignored, since their inclusion only magnifies the total interaction energy and forces between the hydrated ferric ion and the MOF pore, and does not qualitatively change the behaviour.

5.2.2. Interaction energy

The cylindrical MOF approximation did not consider the specific location of each atom. In contrast, the rectangular prism MOF pore approximation allows for more precise consideration of atom-specific locations. Tables 1.2 and 5.2 highlight that europium atoms are only found at the nodes of the MOF pore and carbon atoms only in the ligands. On the other hand, hydrogen and oxygen atoms are found in both locations. Therefore, approximating the MOF pore with a rectangular prism provides the opportunity to specify a different atom density on each type of wall(plane)/edge(line) when the atoms are "smoothed" over the surface. This provides a more accurate approximation than the cylindrical construction where no specification of atom location can be taken into account. Consequently, the expression for the interaction energy contains two different types of calculations: one for the walls (planes), and one for the edges (lines). The atom density can be specified to be different on each structure, see Table 5.3.

Atomic type	Mean surface density, n_k		
	Line, Å^{-1}	Vertical plane, Å^{-2}	Horizontal plane, Å^{-2}
Europium	0.2929	0	0
Hydrogen	0.5857	0.1565	0.0838
Oxygen	0.2929	0.1304	0.0698
Carbon	0	0.2348	0.1257

Table 5.3: Mean density for each atom type for approximated prismatic MOF unit cell.

Maintaining the assumption that the MOF pore is prismatic and the atoms are evenly spread over each particular surface, the total interaction energy between the ferric ion and the MOF pore is defined by Equation (3.3).

The interaction energy between two surfaces is given by Equation (2.3) and from Section 3.1.1, the interaction energy between a point and a surface reduces the double integral to a single integral. Therefore, the interaction energy between a ferric ion point and a surface S_1 (the prism) with an

assumed uniformly distributed atomic surface density n_k is given by

$$E(\rho) = n_k \int_{S_1} U(\rho)\, dS_1$$

where n_k is the mean surface density of atom type k.

The interaction energy between a point and one semi-infinite line (representing any atoms that might be located along an edge of the prism) is given by

$$E_{\text{line}}(X) = n_k \int_0^\infty \left[-\frac{A}{((x-X)^2+\alpha^2+\beta^2)^3} + \frac{B}{((x-X)^2+\alpha^2+\beta^2)^6} \right] \mathrm{d}x, \tag{5.1}$$

where the semi-infinite line is one of the edges of the prism described at the beginning of this section, and $\rho^2 = (x-X)^2 + \alpha^2 + \beta^2$. Details for the evaluation of this integral are provided in Appendix C.1.1.

The interaction energy between a point and one vertical semi-infinite plane (that is, where $z_p = \pm\beta$) is given by

$$\begin{aligned} E_{\text{vert}}(X) &= n_k \int_0^\infty \int_{-\alpha}^{\alpha} \left[-\frac{A}{((x-X)^2+y^2+\beta^2)^3} + \frac{B}{((x-X)^2+y^2+\beta^2)^6} \right] \mathrm{d}y\, \mathrm{d}x, \\ &= 2\, n_k \int_0^\infty \int_0^{\alpha} \left[-\frac{A}{((x-X)^2+y^2+\beta^2)^3} + \frac{B}{((x-X)^2+y^2+\beta^2)^6} \right] \mathrm{d}y\, \mathrm{d}x, \end{aligned} \tag{5.2}$$

where the coordinates of the vertical semi-infinite plane are given by $(x, y, \pm\beta)$, $x \in [0, \infty)$, $y \in [-\alpha, \alpha]$, and $\rho^2 = (x-X)^2 + y^2 + \beta^2$. Details for the evaluation of this integral are provided in Appendix C.1.2. Similarly, the interaction energy between a point and one horizontal semi-infinite plane is given by

$$E_{\text{hori}}(X) = 2\, n_k \int_0^\infty \int_0^{\beta} \left[-\frac{A}{((x-X)^2+\alpha^2+z^2)^3} + \frac{B}{((x-X)^2+\alpha^2+z^2)^6} \right] \mathrm{d}z\, \mathrm{d}x, \tag{5.3}$$

where the coordinates on the horizontal semi-infinite plane are given by $(x, \pm\alpha, z)$, $x \in [0, \infty)$, $z \in [-\beta, \beta]$, and $\rho^2 = (x-X)^2 + \alpha^2 + z^2$.

The analytical evaluation of integral (5.1), (5.2) and (5.3) is not straightforward. Baowan and Thamwattana [6] calculated these integrals using series expansions, however they have been evaluated exactly here.

The MOF pore is characterised as four planes and four lines to represent the bridging ligands and

nodes of the MOF pore. The total interaction energy is given by the sum of the interaction energies between the point and the components of the prism (i.e. the four lines and four planes). As part of this calculation, the interaction energy between the point and the various atom types located on each surface are calculated as follows. Europium atoms in the MOF pore are only located at the nodes of the MOF pore, which are approximated by four semi-infinite lines. The interaction energy between the ferric ion point and the europium nodes is given by

$$E_{\mathrm{Fe,Eu}} = 4 \cdot E_{\mathrm{line}}(\rho; n_{\mathrm{Eu,line}}), \tag{5.4}$$

where $\rho^2 = (x - X)^2 + \alpha^2 + \beta^2$. Hydrogen atoms are located at the four nodes of the MOF pore (water molecules associated with the europium atoms) and in the bridging ligands. The interaction energy between the ferric ion point and the hydrogen atoms is given by

$$E_{\mathrm{Fe,H}} = 4 \cdot E_{\mathrm{line}}(\rho; n_{\mathrm{H,line}}) + 2 \cdot E_{\mathrm{vert}}(\rho_1; n_{\mathrm{H,vert}}) + 2 \cdot E_{\mathrm{hori}}(\rho_2; n_{\mathrm{H,hori}}), \tag{5.5}$$

where $\rho_1^2 = (x - X)^2 + y^2 + \beta^2$ and $\rho_2^2 = (x - X)^2 + \alpha^2 + z^2$. Note that the mean surface densities, n_k, for the vertical and horizontal planes and lines differ and are considered accordingly. Similarly, the interaction energy between the ferric ion point and the oxygen atoms in the MOF ligands and at the MOF nodes is given by

$$E_{\mathrm{Fe,O}} = 4 \cdot E_{\mathrm{line}}(\rho; n_{\mathrm{O,line}}) + 2 \cdot E_{\mathrm{vert}}(\rho_1; n_{\mathrm{O,vert}}) + 2 \cdot E_{\mathrm{hori}}(\rho_2; n_{\mathrm{O,hori}}). \tag{5.6}$$

Carbon atoms in the MOF pore are only located in the bridging ligands of the MOF pore, which are approximated by four semi-infinite planes (two vertical and two horizontal). The interaction energy between the ferric ion point and the carbon atoms in the MOF ligands is given by

$$E_{\mathrm{Fe,C}} = 2 \cdot E_{\mathrm{vert}}(\rho_1; n_{\mathrm{C,vert}}) + 2 \cdot E_{\mathrm{hori}}(\rho_2; n_{\mathrm{C,hori}}). \tag{5.7}$$

Therefore, the total interaction energy between the ferric ion point and the semi-infinite prism MOF pore is the sum all non-bonded interactions between the ferric ion point and each atom type found in the MOF pore, that is, Equation (3.5) with Equations (5.4)-(5.7).

Figure 5.5 shows the individual van der Waals interaction energies and forces between a ferric ion and each atom type found in the MOF pore approximated by a rectangular prism. The europium

nodes contribute the least to the interaction energy and force. This is attributed to europium having the fewest number of atoms in the pore and that europium atoms are only located at the corners of the prism, the furthermost point from the MOF pore centreline. In addition, europium has the smallest well-depth ϵ.

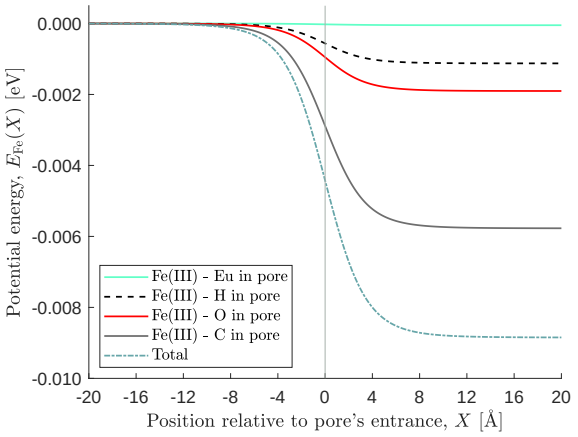


Figure 5.5: Interaction energy between ferric ion and semi-infinite prism MOF pore, Equations (5.4), (5.5), (5.6), (5.7) with (3.3). The vertical line marks the location of the pore opening.

In contrast, the interaction energy and force between the ferric ion and carbon atoms in the MOF pore contributes the most to the total energy and force. There are 54 carbon atoms in a single representative MOF pore and the average carbon-ferric ion distance ρ is shorter than the average europium-ferric ion distance, therefore carbon has a greater influence when interacting with the ferric ion. In addition, carbon has the largest well-depth.

The total interaction energy indicates that it is favourable for the ferric ion to reside in the MOF pore, as the ferric ion experiences a potential energy minimum ($-0.009\,\mathrm{eV}$) inside the MOF pore, Figure 5.5.

5.2.3. Interaction forces

The total interaction forces between the hydrated ferric ion and the MOF pore is defined by Equation (3.12) and is calculated by using Equation (2.4).

Due to the relationship between potential energy and force, sufficient qualitative physical information can be derived by studying either of the two. In [6] series solutions for only the potential energy here derived. However, the analytical solutions for the force functions are provided here.

The interaction force between a point and one semi-infinite line is given by (using Equation (5.1)

and see Appendix C.2.1 for details)

$$F_{\text{line}}(X) = n_k \left[\frac{A}{(X^2+\alpha^2+\beta^2)^3} - \frac{B}{(X^2+\alpha^2+\beta^2)^6} \right].$$

The interaction force between a point and one vertical semi-infinite plane is given by (using Equation (5.2) and see Appendix C.2.2 for details)

$$\begin{aligned} F_{\text{vert}}(X) = 2\,n_k \Bigg\{ & \frac{A}{8} \left[\frac{2\,\alpha}{(\alpha^2+\beta^2+X^2)^2\,(\beta^2+X^2)} + \frac{3\,\alpha}{(\alpha^2+\beta^2+X^2)\,(\beta^2+X^2)^2} \right. \\ & \left. +3\,(\beta^2+X^2)^{-5/2} \arctan\left(\frac{\alpha}{(\beta^2+X^2)^{1/2}} \right) \right] \\ & -\frac{B}{1280} \left[\frac{128\,\alpha}{(\alpha^2+\beta^2+X^2)^5\,(\beta^2+X^2)} + \frac{144\,\alpha}{(\alpha^2+\beta^2+X^2)^4\,(\beta^2+X^2)^2} \right. \\ & + \frac{168\,\alpha}{(\alpha^2+\beta^2+X^2)^3\,(\beta^2+X^2)^3} + \frac{210\,\alpha}{(\alpha^2+\beta^2+X^2)^2\,(\beta^2+X^2)^4} \\ & \left. + \frac{315\,\alpha}{(\alpha^2+\beta^2+X^2)\,(\beta^2+X^2)^5} + 315\,(\beta^2+X^2)^{-11/2} \arctan\left(\frac{\alpha}{(\beta^2+X^2)^{1/2}} \right) \right] \Bigg\}. \end{aligned}$$

The interaction force between a point and one horizontal semi-infinite plane is given by (using Equation (5.3))

$$\begin{aligned} F_{\text{hori}}(X) = 2\,n_k \Bigg\{ & \frac{A}{8} \left[\frac{2\,\beta}{(\alpha^2+\beta^2+X^2)^2\,(\alpha^2+X^2)} + \frac{3\,\beta}{(\alpha^2+\beta^2+X^2)\,(\alpha^2+X^2)^2} \right. \\ & \left. +3\,(\alpha^2+X^2)^{-5/2} \arctan\left(\frac{\beta}{(\alpha^2+X^2)^{1/2}} \right) \right] \\ & -\frac{B}{1280} \left[\frac{128\,\beta}{(\alpha^2+\beta^2+X^2)^5\,(\alpha^2+X^2)} + \frac{144\,\beta}{(\alpha^2+\beta^2+X^2)^4\,(\alpha^2+X^2)^2} \right. \\ & + \frac{168\,\beta}{(\alpha^2+\beta^2+X^2)^3\,(\alpha^2+X^2)^3} + \frac{210\,\beta}{(\alpha^2+\beta^2+X^2)^2\,(\alpha^2+X^2)^4} \\ & \left. + \frac{315\,\beta}{(\alpha^2+\beta^2+X^2)\,(\alpha^2+X^2)^5} + 315\,(\alpha^2+X^2)^{-11/2} \arctan\left(\frac{\beta}{(\alpha^2+X^2)^{1/2}} \right) \right] \Bigg\}. \end{aligned}$$

The total interaction force is given by the sum of the interaction forces between the point and the components of the prism, Equation (3.12).

The interaction force between the ferric ion point and the europium nodes (approximated by a line) is given by

$$F_{\text{Fe,Eu}} = 4 \cdot F_{\text{line}}(X; n_{\text{Eu,line}}). \tag{5.8}$$

The interaction force between the ferric ion point and the hydrogen atoms, in the MOF ligands

and at the MOF nodes, is given by

$$F_{\mathrm{Fe,H}} = 4 \cdot F_{\mathrm{line}}(X; n_{\mathrm{H,line}}) + 2 \cdot F_{\mathrm{vert}}(X; n_{\mathrm{H,vert}}) + 2 \cdot F_{\mathrm{hori}}(X; n_{\mathrm{H,hori}}). \tag{5.9}$$

The interaction force between the ferric ion point and the oxygen atoms in the MOF ligands and at the MOF nodes is given by

$$F_{\mathrm{Fe,O}} = 4 \cdot F_{\mathrm{line}}(X; n_{\mathrm{O,line}}) + 2 \cdot F_{\mathrm{vert}}(X; n_{\mathrm{O,vert}}) + 2 \cdot F_{\mathrm{hori}}(X; n_{\mathrm{O,hori}}). \tag{5.10}$$

The interaction force between the ferric ion point and the carbon atoms in the MOF ligands is given by

$$F_{\mathrm{Fe,C}} = 2 \cdot F_{\mathrm{vert}}(X; n_{\mathrm{C,vert}}) + 2 \cdot F_{\mathrm{hori}}(X; n_{\mathrm{C,hori}}). \tag{5.11}$$

Figure 5.6 shows the individual van der Waals interaction forces acting in the axial direction between a ferric ion and each atom type found in the MOF pore. The total interaction force is positive near the entrance of the prism MOF pore, indicating that there is an interaction force acting on the ferric ion directed to the right, so that the ferric ion experiences a force towards the MOF pore entrance. The maximum interaction force at the MOF pore entrance is approximately $0.001\,\mathrm{eV\,\AA^{-1}}$.

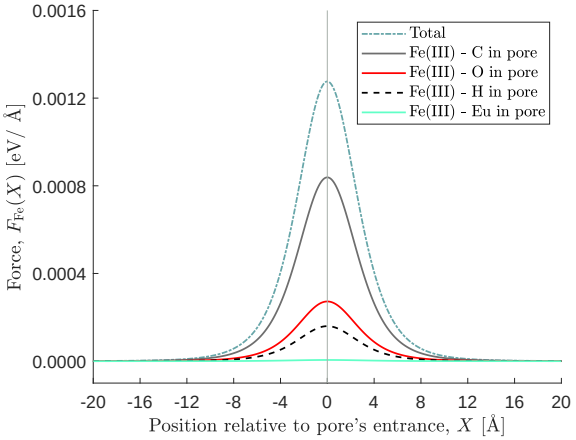


Figure 5.6: Interaction force between a ferric ion and a semi-infinite prism MOF pore, Equations (5.8), (5.9), (5.10), (5.7) and (3.14). The vertical line marks the location of the pore opening.

The next section compares the predictions of the cylindrical pore approximation to the prism approximation. The analytical expressions for the interaction energy and force between a point

and a semi-infinite prism are large and complex, and so the following section discusses whether a simpler fitted cylindrical approximation may be just as suitable.

5.3. PRISM VERSUS CYLINDER MOF PORE APPROXIMATION

This section compares the interactions between the ferric ion and the MOF pore as calculated using two different approximations for the MOF pore shape. The first approximation of the MOF pore is a cylinder, using the a-basis vector as the diameter of the cylinder. The prism MOF pore approximation is a rectangular prism and is a closer representation to that of the actual shape of the MOF pore.

The expressions describing the interactions in the case of the cylinder are much simpler than the case of a rectangular prism due to its rotational symmetry. In addition to comparing the cylindrical and prism approximations, cylinders with two different radii are also compared. The first mirrors the results shown in Chapter 3 where the diameter of the cylinder was taken to be the same as the length of the a-basis vector (denoted hereon as the *original cylindrical* approximation). In the second, the radius of the cylinder is chosen so that the area of the cylindrical pore opening is the same as the opening for the rectangular prism, $r = 2\sqrt{\alpha\beta/\pi} = 6.122$ Å (denoted hereon as the *fitted cylindrical* approximation). Figures 5.7(a) and (b) show the semi-infinite rectangular prism and semi-infinite cylindrical MOF pore approximations. Figure 5.7(c) shows the cross-section of each of the pores. Note that the fitted cylinder is larger than original cylinder and that a-axis $> 2\alpha$.

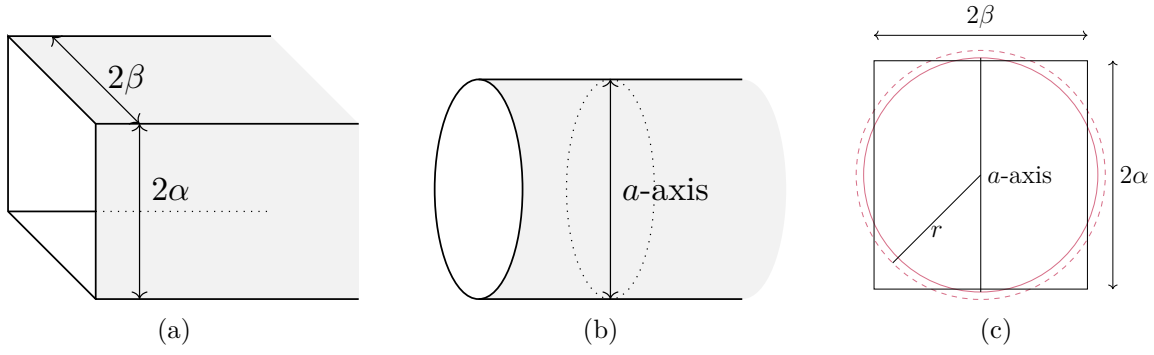


Figure 5.7: Approximation of EuBDC-OMe MOF pore (a) as semi-infinite rectangular prism and (b) as a semi-infinite cylinder. (c) Area difference between prism, original cylinder and fitted cylinder, depicted as solid black line, solid blush line and dashed blush line, respectively.

The continuum approach is maintained, and therefore for the cylindrical MOF pore calculations all atoms are assumed to be "smoothed" across the surface of the cylinder. Table 5.4 provides the mean densities that are required to calculate the interaction energy and force for both the original

and the fitted cylinders.

Atomic type	Mean surface density, n_k (Å^{-2}) Original cylinder, radius $\frac{1}{2}$ a-axis	Fitted cylinder, radius r
Europium	0.0324	0.0305
Carbon	0.2186	0.2056
Hydrogen	0.2105	0.1980
Oxygen	0.1538	0.1447

Table 5.4: Parameter values used incorporating physical attributes for cylindrical and fitted cylindrical MOF pore.

Figure 5.8 compares the interaction energy between a ferric ion and the MOF pore, showing the rectangular approximation, together with both the original and fitted cylinder approximations. The magnitude of the predicted potential energy minimum is much greater for the original cylindrical approximation than for both the rectangular prism and the fitted cylindrical approximations. The fitted cylinder and the rectangular prism, having the same cross-sectional area, provide very similar predictions for the interaction energy, demonstrating that in this scenario, it is sufficient to use the simpler cylindrical formulation, providing that the cross-sectional areas match. The following figures investigate in more detail the contributions of the planes and lines in the prism calculation, and the different atom types.

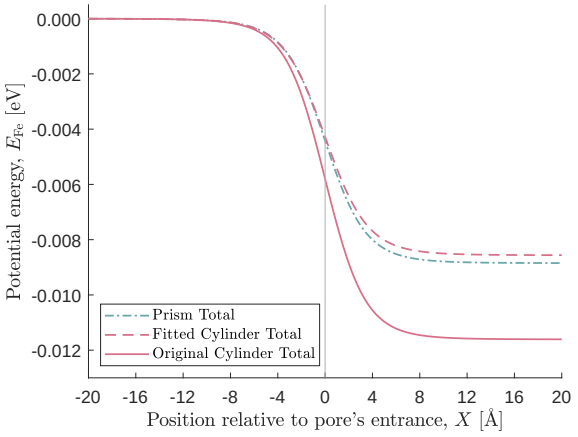
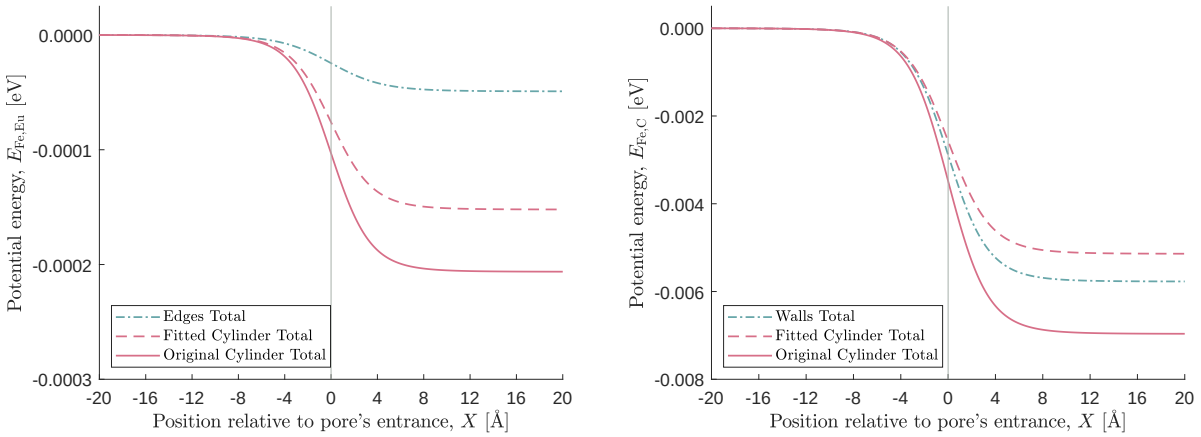


Figure 5.8: Interaction energy between ferric ion and various MOF pore approximations. Turquoise dot dashed line shows interaction energy between ferric ion and prism. Blush dashed and solid line show interaction energy between ferric ion and fitted cylindrical pore, ferric ion and original cylindrical pore, respectively. Vertical line marks location of pore opening.

The cylindrical approximations ignore the specific locations of the atoms and their respective distances from the x-axis. This is more problematic for the atoms located only along the edges of

the rectangular prism (the lines), such as the europium atoms and their associated water molecules in this particular MOF. The cylindrical approximation assumes that all atoms are smoothed over the surface of the cylinder, which, for the original cylinder, is closer to the x-axis on average than the edges of the rectangular prism. Consequently, the radial distance between the ferric ion and the pore surface is smaller so that the total interaction energy is much greater than if a truer representation of the pore shape was used.

Figure 5.9(a) shows the contribution of the ferric ion-europium interaction to the total potential energy. As expected, the europium contribution in both cylindrical approximations is greater in magnitude than the rectangular prism approximation, since both cylindrical radii are smaller than the radial distance from the pore centreline to the prism edges (7.682 Å) where the europium atoms are located.



(a) (b)

Figure 5.9: (a) Interaction energy between ferric ion and europium in pore. Turquoise dot dashed line shows interaction energy between ferric ion and prism. Blush dashed and solid line show interaction energy between ferric ion and fitted cylindrical pore, ferric ion and original cylindrical pore, respectively. Vertical line marks location of pore opening. (b) Interaction energy between ferric ion and carbon in pore.

In contrast, the situation for atoms located along the sides of the rectangular prism is more nuanced, Figure 5.9(b). As shown in Figure 5.7, sometimes the cylindrical approximation overestimates the distance between these atoms and the x-axis, while sometimes it underestimates the distance. In the case of the rectangular prism, the average distance of an atom on the vertical walls to the x-axis is given by

$$\frac{1}{2\alpha}\int_{-\alpha}^{\alpha}\sqrt{\beta^2+y^2}\,dy = \tfrac{1}{2}\sqrt{\alpha^2+\beta^2}+\frac{\beta^2}{4\alpha}\ln\left[\tfrac{1}{\beta^2}\left(2\alpha^2+\beta^2+2\alpha\sqrt{\alpha^2+\beta^2}\right)\right] = 6.120\ \text{Å}.$$

A corresponding expression can be derived for the average distance of an atom on the horizontal walls to the x-axis

$$\frac{1}{2\beta}\int_{-\beta}^{\beta}\sqrt{z^2+\alpha^2}\,dz = \tfrac{1}{2}\sqrt{\alpha^2+\beta^2}+\tfrac{\alpha^2}{4\beta}\ln\left[\tfrac{1}{\alpha^2}\left(\alpha^2+2\beta^2+2\beta\sqrt{\alpha^2+\beta^2}\right)\right] = 6.347\ \text{Å}.$$

Both these average distances are greater than original cylinder's radius (5.757 Å), confirming that the original cylinder approximation would overestimate the magnitude of the interaction energy. The fitted cylinder's radius (6.122 Å) is very close to the average distance of both the vertical and horizontal walls (less than 4% difference) and is strictly less than the average radial distance for the prism (6.229 Å),

$$\frac{1}{2\alpha+2\beta}\left(\int_{-\alpha}^{\alpha}\sqrt{\beta^2+y^2}\,dy+\int_{-\beta}^{\beta}\sqrt{z^2+\alpha^2}\,dz\right) = 6.229\ \text{Å}.$$

Even though there is a small difference between the fitted cylinder's radius and the average distance between the centreline and the vertical wall, there are twice as many atoms located on the vertical wall in the prism, so that the magnitude of the interaction energy is still underestimated when using the fitted cylinder approximation. The difference between the fitted cylinder radius and the average distance to the horizontal wall is not significant enough for the fitted cylinder approximation to overestimate the magnitude of the interaction energy. This further emphasises the sensitivity of the interaction energy calculation to variations in radial distance, and the importance of accounting for

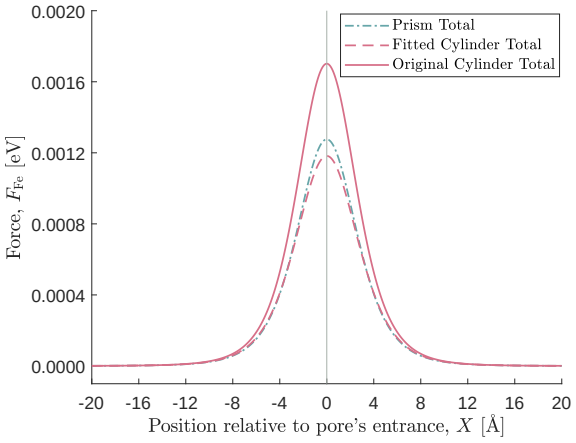


Figure 5.10: Interaction force between ferric ion and various MOF pore approximations. Turquoise dot dashed line shows interaction force between ferric ion and prism. Blush dashed and solid line show interaction force between ferric ion and fitted cylindrical pore, ferric ion and original cylindrical pore, respectively. Vertical line marks location of pore opening.

atom surface densities correctly. Although not shown here, there is a greater agreement between the fitted approximation and a perfect square.

Figure 5.10 shows the interaction force between a ferric ion and the three different approximations of the MOF pore, and reflects the findings discussed above for the interaction energy. The original cylindrical approximation overestimates the magnitude of the force in comparison to the rectangular prism approximation, however the fitted cylinder and rectangular prism approximations (with the same cross-sectional area) are much closer in magnitude.

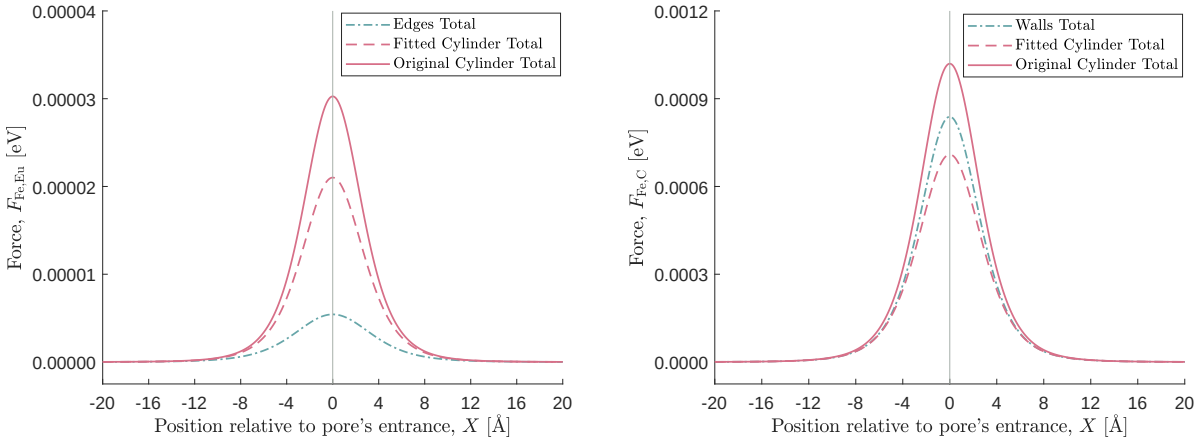


Figure 5.11: (a) Interaction force between ferric ion and europium in pore. Turquoise dot dashed line shows interaction force between ferric ion and prism. Blush dashed and solid line show interaction force between ferric ion and fitted cylindrical pore, ferric ion and original cylindrical pore, respectively. Vertical line marks location of pore opening. (b) Interaction force between ferric ion and carbon in pore.

In the same way as before, the contributions of the europium and carbon atoms for the three different approximations are compared. Figure 5.11 echoes the findings from Figure 5.9. Both cylindrical approximations overpredict the contribution of the europium ions because the radii of both cylinders is less than the distance from the prism edge to the x-axis. For the carbon atoms, the original cylinder approximation overpredicts their contribution. The fitted cylinder underpredicts the contribution of carbon atoms mainly due to a greater carbon atom density on the vertical planes which lies closer to the x-axis.

One important finding to note is that regardless of the shape used to approximate the MOF pore (rectangular prism or cylindrical), the qualitative behaviour is the same. That is, the force on the ferric ion is always directed to the right, indicating that the ferric ion will be attracted to the MOF pore entrance.

5.4. IMPLICATIONS OF A PORE BLOCKAGE

Thus far, all calculations have considered distances between atoms and the ion to be measured from centre-to-centre. That is, the atomic/ionic radii have not been included. This means that even though the MOF pore has been represented by a cylinder or a prism of a certain size, this is not a true representation of the available space within the pore. Neither has the size of the hydrated ferric ion been accurately represented.

The available space within the MOF pore has been theoretically predicted to be between 3-6 Å in diameter using a 3D molecular structure visualisation tool called Mercury [9] (compare this to the centre-to-centre distance used in the cylindrical model of approximately 12 Å). A more representative size of the hydrated ferric ion can also be calculated. The centre-to-centre distance between the ferric ion and the hydrogen sphere is $b_2 = 2.74$ Å, and the atomic radius of a hydrogen atom is 53 pm (=0.53 Å), so that a better representation for the diameter of a hydrated ferric ion is 6.54 Å. Consequently, the size of the hydrated ferric ion is greater than the available space in the MOF pore so that the hydrated ferric ion is geometrically too large to enter the free space inside the pore. As a consequence it will be attracted to the MOF pore, but will remain on the surface without entering [32]. Subsequent to these theoretical calculations, this finding was confirmed experimentally by Rozenberga *et al.* [41] by observing that the fluorescence sensing range of the MOF is affected by sonication time and particle size, indicating that hydrated ferric ions are associating to the surface of the MOF and not entering the pores. Since there are many pores on each crystal, there will eventually be a ferric (or other) ion located at the entrance of each. This section considers the interaction between a ferric ion and a MOF pore where the entrance is already occupied by another ferric ion.

This section maintains the geometry presented in Section 5.2, where the MOF pore is approximated by a semi-infinite prism, and is described in Figure 5.3 and the surrounding text. In addition, this section assumes that the MOF pore entrance is blocked by a ferric ion (not hydrated), where the Cartesian coordinates of the blocked ferric ion is $(0, 0, 0)$.

Note that considering an unhydrated ferric ion does not imply that the hydrated ferric ion underwent dehydration. A calculation involving an unhydrated ferric ion is sufficient to give an indication of the qualitative behaviour in the case of a blocked pore.

The van der Waals interactions are considered between all non-bonded atoms, that is, the ferric ion to the semi-infinite prism MOF pore, and the ferric ion to the ferric ion blocking the MOF pore

entrance. Therefore, the total interaction energy between the ferric ion and the blocked semi-infinite prism MOF pore is given by

$$E_{\text{Fe,blocked}}(X) = E_{\text{Fe,Eu}} + E_{\text{Fe,H}} + E_{\text{Fe,O}} + E_{\text{Fe,C}} + E_{\text{Fe,Fe}}.$$

In Section 5.2, the total interaction energy between the ferric ion point and the semi-infinite prism MOF pore was calculated using Equation (3.5) with Equations (5.4)-(5.7).

The interaction energy between a ferric ion point and the ferric ion located at the entrance of the MOF pore is (using (2.1))

$$E_{\text{Fe,Fe}}(X) = -\frac{A_{\text{Fe}}}{X^6} + \frac{B_{\text{Fe}}}{X^{12}}.$$

The total interaction force between the ferric ion and the blocked semi-infinite prism MOF pore is given by

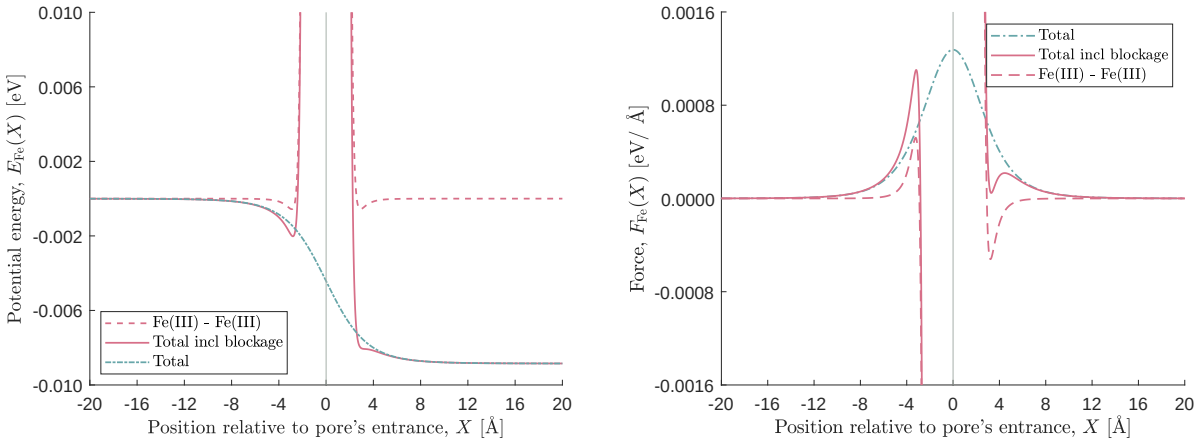
$$F_{\text{Fe,blocked}}(X) = F_{\text{Fe,Eu}} + F_{\text{Fe,H}} + F_{\text{Fe,O}} + F_{\text{Fe,C}} + F_{\text{Fe,Fe}}.$$

Similarly, the total interaction force between the ferric ion point and the semi-infinite prism MOF pore was calculated using Equation (3.12) with Equations (5.8)-(5.11).

The interaction force between a ferric ion point and the ferric ion located at the entrance of the MOF pore is (using (2.1))

$$F_{\text{Fe,Fe}}(X) = -6\frac{A_{\text{Fe}}}{X^7} + 12\frac{B_{\text{Fe}}}{X^{13}}.$$

Figure 5.12(a) shows that there is a local potential energy minimum at 2.81 Å to left of the pore entrance. A ferric ion farther away from the pore entrance experiences a force to the right (towards the MOF pore), while a ferric ion closer to the blocked entrance will experience a strong repulsive force (see Figure 5.12(b)). The potential energy minimum just outside the pore entrance is much smaller in magnitude than that of a vacant pore (compare with the minimum of the turquoise dot dashed line in Figure 5.12(a)), while the magnitude of the repulsive force close to the blocked pore is very large. As a consequence, in practice it is unlikely that a ferric ion will remain at this potential energy minimum, rather it will more likely move to occupy a vacant MOF pore. This means that more ferric ions will become associated to the MOF crystal, which in turn is likely to improve sensor performance.



(a) (b)

Figure 5.12: (a) Interaction energy between ferric ion and blocked semi-infinite prism MOF pore. Turquoise dot dashed line shows interaction energy between ferric ion and prism. Blush dashed and solid line show interaction energy between two ferric ions, and ferric ion and blocked MOF pore, respectively. Vertical line marks location of pore opening. (b) Interaction force between ferric ion and blocked semi-infinite prism MOF pore.

5.5. INTERACTIONS BETWEEN A HYDRATED FERRIC ION AND MULTIPLE MOF PORES

The previous chapters and sections only considered ferric ion interactions with a single MOF pore. However, in application, there are multiple MOF pores in a single crystal and multiple crystals in a polymer thin film. This section explores the influence of multiple pores acting on a ferric ion.

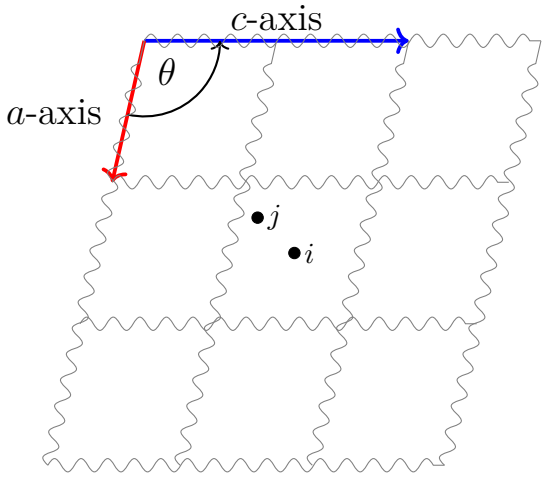


Figure 5.13: Simplified graphic of multiple MOF pores represented as gray wavy lines, red arrow represents a-axis basis vector and blue arrow represents c-axis basis vector. Angle θ as reported in Table 1.1. Black dots represent possible ferric ions locations.

Suppose a ferric ion is outside of the MOF pore on its centreline at location i as shown in Figure 5.13. The previous results predict that a ferric ion experiences a force directed towards the MOF pore entrance (i.e. into the page in Figure 5.13) and that ferric ion will then occupy that opening. Now consider a ferric ion near the MOF pore at location j, that is, outside the pore but not on the pore's centreline. If the nearest MOF pore opening is not occupied, a ferric ion originally located at j will likely occupy the centre MOF pore. This is due to the symmetry of the structure.

Suppose that the centre MOF pore is already occupied by a ferric ion and that a second ferric ion is located at j. As described in the previous section, the ferric ion located at j will experience a force directed away from the central MOF pore and it is likely that it will then occupy one of the surrounding MOF pores. More specifically, provided that the nearest MOF pore is unoccupied, the ferric ion will experience the greatest force in that direction and will consequently occupy that pore.

5.6. IMPLICATIONS OF CHANGE IN TEMPERATURE

Subsection 2.3 introduced the relationship between the Lennard-Jones potential and temperature. The quantitative effect of temperature change on the Lennard-Jones pair potential parameters (σ and ϵ) for the atom types studied in the microenvironment is not available. This section aims to use the available knowledge regarding the effect of temperature on the Lennard-Jones potential to determine the impact that temperature changes might have on the sensor, with particular interest in the thermodynamic effects on the van der Waals interactions between the hydrated ferric ion and the MOF pore. Since the sensor will be exposed to an environment with a temperature range from approximately 273 K to 373 K (i.e. from freezing to 100 °C).

Goldman [16] calculated estimates for the Lennard-Jones pair potential parameters (ϵ and σ/k) using Chandler-Weeks-Andersen perturbation theory as modified by Verlet and Wies [51, 52] for temperature ranges of various liquids. The temperature range for which the standard pair potential parameter values are valid was calculated using trial and error and a least squares fit to experimental data. Goldman reported a temperature range for constant pair potential for each liquid, with the narrowest range being 40 K (for example n-Pentane at 240-280K) and the widest range being 80 K (for example o-Xylene at 300-380K). The Lennard-Jones pair potentials were compared to other estimates (both experimental and theoretical) to verify their predictions.

Nasehzadeh *et al.* [33] extended Goldman's work and expressed the pair parameters as functions of

temperature. Nasehzadeh *et al.* followed a similar methodology to Goldman. However, instead of constant pair potentials, they used a simple linear regression analysis to express ϵ and σ/k (where k is the Boltzmann constant) as functions of temperature.

None of the studies described above investigate the atom types of relevance to this project. Benzene (a carbon-only molecule) is amongst the compounds studied in [16, 33], and is the closest comparable molecule to a carbon atom [37]. Therefore, the following arguments regarding the impact of temperature change on the pair parameters of relevance here is based on what occurs in the case of benzene.

In [33], the van der Waals diameter (Å) for benzene as function of temperature, T (K), is given by

$$\sigma(T) = 0.002531\,T + 4.11862,$$

while the well-depth is given by

$$\begin{aligned}\epsilon(T) &= k\,(-0.224\,T + 497.6146)\ \text{(J/mol)},\\ &= \frac{k}{q}\,(-2.315\times10^{-6}\,T + 0.005143)\ \text{(eV/particle)},\end{aligned}$$

where q is the charge of an electron.

The grey line in Figure 5.14 is the Lennard-Jones potential for carbon-carbon interactions [37], and the blush lines are potentials for benzene-benzene interactions at three different temperatures [33]. When temperature increases, benzene's well depth decreases and the van der Waals diameter increases. Benzene's well-depth at room temperature (dashed blush line, 293K) is about eight times greater than carbon in magnitude and benzene's van der Waals diameter σ is about 1.4 Å greater than carbon.

In the absence of literature regarding the atoms of relevance to this study, temperature variance is explored using a percentage change to the Lennard-Jones pair potentials. It is assumed that the pair potential values given in [37] are at room temperature. In the case of benzene, a temperature increase from 293 K to 373 K (i.e. 80 K greater than room temperature) corresponds to approximately 4% change in both the well-depth (ϵ decreases in magnitude) and the van der Waals diameter (σ increases). A temperature decrease from 293 K to 273 K (i.e. freezing) corresponds to approximately 1% increase in the well-depth and decrease in the van der Waals diameter.

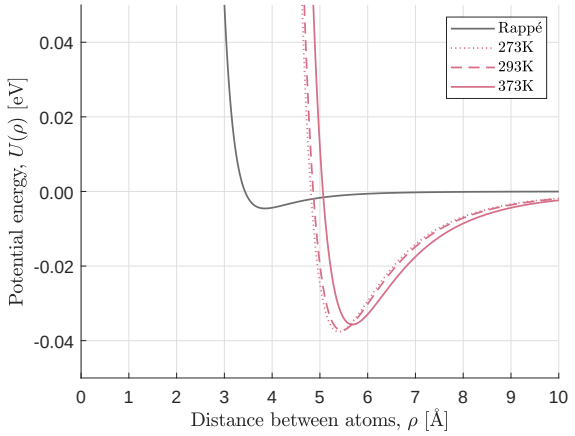


Figure 5.14: Lennard-Jones potential for interactions between carbon-carbon in grey and benzene-benzene in blush. Dotted, dashed and solid blush lines are Lennard-Jones potentials for benzene increasing temperature, $T = 273, 293, 373$ K.

The same percentage changes are applied to investigate the impact on carbon-carbon interactions. The outcome of this change in temperature on the carbon-carbon potential is shown in Figure 5.15. The result of the percentage change in the carbon pair potentials shows the same characteristic response to changes in temperature as for the benzene potential, where the van der Waals diameter increases with increasing temperature, and the well-depth decreases.

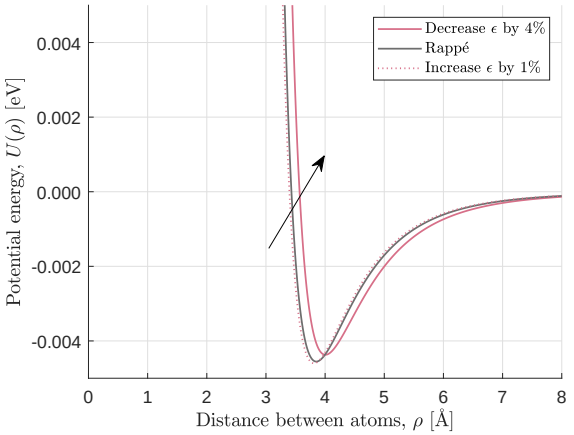


Figure 5.15: Lennard-Jones potential for interactions between carbon-carbon in grey using parameters in [37]. Dotted and solid blush lines show decreased and increased temperature respectively (both ϵ and σ are changed). Note that decrease (increase) in temperature corresponds to increase (decrease) in ϵ. Arrow shows direction of increasing temperature.

The percentage change is extended to the situation of interest here. The geometry presented in Section 5.2 is used, where the MOF pore is approximated by a semi-infinite prism and carbon atoms

are only located on the walls of the prism. Figure 5.16(a) shows the interaction energy between a ferric ion and the four semi-infinite carbon planes (no other MOF atom types are considered separately), and Figure 5.16(b) shows the total interaction energy between a ferric ion and a semi-infinite prismatic MOF pore (all relevant atom types are included). The qualitative characteristics of the interaction energy remain unchanged. However, an increase in temperature causes the inside of the MOF pore to become an increasingly favourable position for the ferric ion. This result seems contradictory with the intuition that an increase in temperature results in more kinetic energy so that the pore should be less attractive. While the decrease in well-depth with increasing temperature (shown in Figure 5.15) aligns with intuition, it is likely the horizontal translation of the potential energy curve in Figure 5.15 that results in the more favourable conditions inside the pore. At larger separation distances ($> 4\,\text{Å}$), the magnitude of the Lennard-Jones potential is greater for higher temperatures. The increase in the magnitude of the potential energy in Figure 5.16 is probably a consequence of this horizontal translation; at larger distances, an increase in temperature results in an increase in the magnitude of the potential energy.

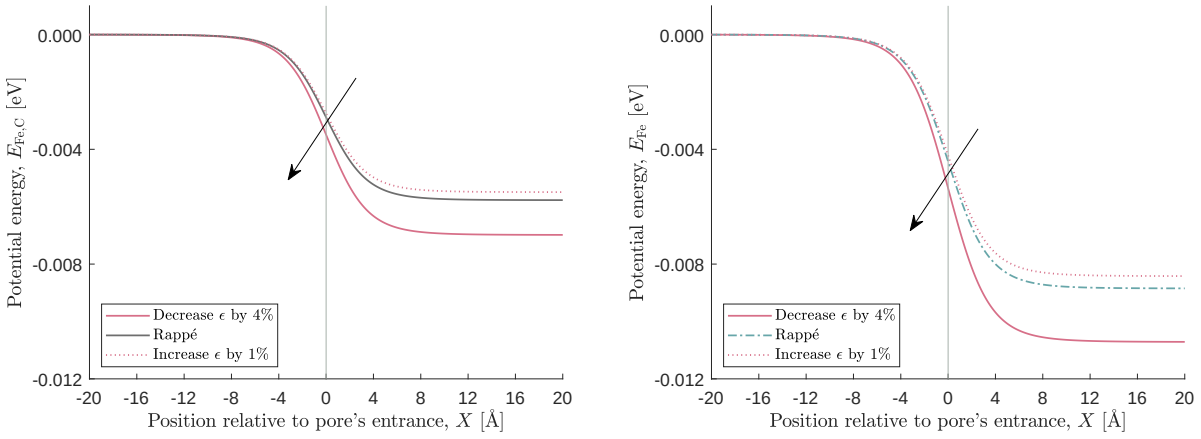
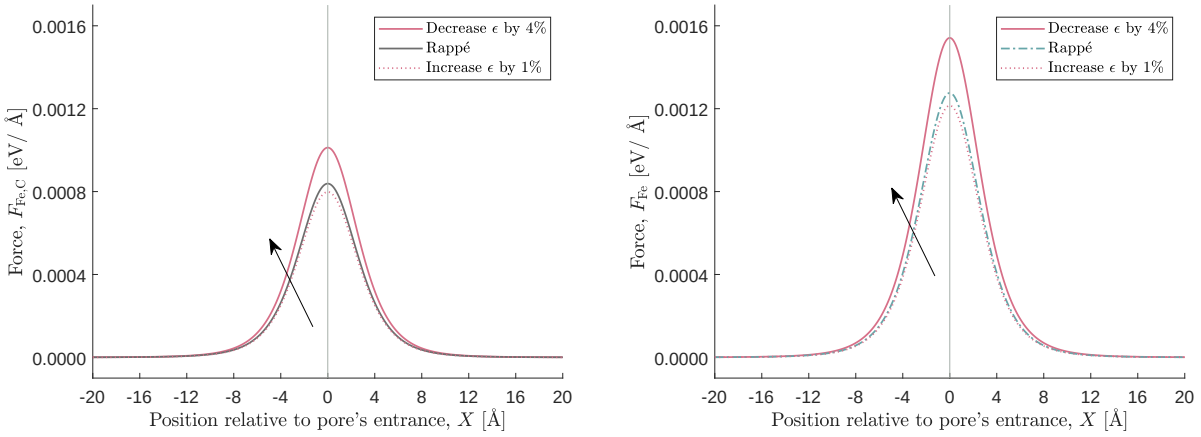


Figure 5.16: (a) Interaction energy between ferric ion and carbon in semi-infinite prismatic MOF pore. Dotted and solid blush lines show decreased and increased temperature respectively (both ϵ and σ are changed). Note that decrease (increase) in temperature corresponds to increase (decrease) in ϵ. Arrow shows direction of increasing temperature. Vertical line marks location of pore opening. (b) Interaction energy between ferric ion and semi-infinite prismatic MOF pore.

Similarly, Figure 5.17(a) shows the interaction force between a ferric ion and the four semi-infinite carbon planes, and Figure 5.16(b) shows the total interaction force between a ferric ion and a semi-infinite prismatic MOF pore. A increase in temperature results in an increased maximum interaction force at the MOF pore entrance, i.e. when temperature increases the ferric ion has a

greater affinity to the MOF pore.



(a) (b)

Figure 5.17: (a) Interaction force between ferric ion and carbon in semi-infinite prismatic MOF pore. Dotted and solid blush lines show decreased and increased temperature respectively (both ϵ and σ are changed). Note that decrease (increase) in temperature corresponds to increase (decrease) in ϵ. Arrow shows direction of increasing temperature. Vertical line marks location of pore opening. (b) Interaction force between ferric ion and semi-infinite prismatic MOF pore.

The changes in temperature do not distort the qualitative interaction between the ferric ion and the MOF pore, and the previously reported results remain true. It is energetically favourable for the ferric ion to reside inside the MOF pore. The interaction force is directed to the right, directing the ferric ion towards the MOF pore entrance and into the pore. An increase in temperature results in a lower potential energy minimum inside the MOF pore and a higher magnitude of the force as the ferric ion approaches the pore entrance. The opposite holds true for a decrease in temperature. The effect of temperature follows intuition, since an increase in temperature means that there is more kinetic energy in the system.

5.7. DISCUSSION

This chapter explored changes in the modelling assumptions to be more inclusive of the sensing environment and the sensor geometry.

In the leaching solution, there are other metal ions present, primarily copper(II) and magnesium(II), and Section 5.1 explored how they might interact with the sensor. The interaction energies, the interaction forces, and the attraction limits, X_0, between the metal ions and a semi-infinite cylindrical MOF pore were calculated, and compared to the interactions between a ferric ion and the

semi-infinite MOF pore. Interestingly, the attractive force between magnesium ions and the MOF pore is shown to be significantly larger than that for the ferric ions. Despite the attractive force being large for magnesium(II), the sensor will have many MOF crystals each with a large number of available pores, so that statistically a number of ferric ions should associate to the MOF pores, even if there are other metal ions present. Copper(II) and magnesium(II) do not affect the emission ratio change due to the ferric ion selectivity of the EuBDC-OMe MOF fluorescence. In addition, the concentration of ferric ions is not inferred from the magnitude of the emission peaks, rather the ratio of two of the ferric ions' emission peaks.

In Section 5.2, the MOF pore approximation was reconsidered to be more representative of the actual geometric shape of the prismatic MOF pore. A rectangular prism was chosen since it maintains some of the features of a parallelogram (four sides and edges, same base length and cross-sectional area), while still being mathematically tractable. The van der Waals interaction energy and force between a ferric ion point and the more complicated rectangular prism approximation was calculated. All the relevant integrals were evaluated analytically for the first time. Previously, analytical expressions had only been derived for the cylindrical approximation.

Numerical values for the prismatic MOF pore approximation indicate that the minimum potential energy of the ferric ion occurs inside the MOF pore; namely that the inside of the MOF pore is the most energetically favourable position for the ferric ion to reside. Further, numerical values for the interaction force indicate that the ferric ion experiences the force of greatest magnitude at the MOF pore entrance. The force is directed towards the MOF pore.

While the analytical expressions for the interaction energy between a point and a prism are much more complex than those between a point and a cylinder, the interaction energies and forces have the same qualitative behaviour regardless of the approximation (cylindrical or rectangular prism). The qualitative match is closest when the approximations have the same cross-sectional area.

Any differences between the cylindrical and the rectangular prism approximations can be understood by considering the distance between particular atoms in the pore structure and the centreline of the pore. For example, for the MOF pore considered here, the atoms located along the edges of the prism make a smaller contribution than the same atoms in the cylindrical approximation (where they are assumed to lie on the surface of the cylinder and as such are closer to the centreline). As a consequence, in the general case, it is important to consider whether any such atoms should be considered separately, particularly if their Lennard-Jones pair potential parameters (σ and ϵ) are

large compared to other atom types in the system.

This chapter also considered the interactions between a ferric ion and a blocked MOF pore. The results indicate that the second ferric ion experiences strong interaction forces directed away from the MOF pore at distances closer than 2.8 Å from the MOF pore entrance. Note that this distance is for ferric ion only interactions, without associated water molecules. When considering the interactions between a hydrated ferric ion and a MOF pore blocked by hydrated ferric ion, the first hydrated ferric ion would be located *outside* the pore entrance (rather than at the origin) and the centre-to-centre distances between the hydrated ferric ions will never be as close as 2.8 Å because of the surrounding water molecules. Consequently, it might be expected that the second (hydrated) ferric ion moves towards an alternative unoccupied pore, increasing the proportion of associated ferric ions and the sensitivity of the ferric ion sensor.

This leads to a short discussion considering the interaction between a ferric ion with many MOF pores. The most energetically favourable position for a second ferric ion is speculated to be the centreline of the closest vacant MOF pore entrance. In other words, if the entrance of the nearest pore is blocked, then the second ferric ion will likely occupy the next-nearest vacant MOF pore.

Finally, the effects of temperature on the interaction energies and forces between a ferric ion and a semi-infinite prismatic MOF pore were considered. An increase in temperature results in lower potential energy minimum inside the MOF pore and a higher magnitude of force as the ferric ion approaches the pore entrance. The opposite holds true for a decrease in temperature.

CHAPTER 6

CONCLUDING REMARKS FOR PART I

Part I aims to model the behaviour of a new ferric ion sensor at the atomic scale. In particular, it seeks to understand how ferric ions in solution interact with the MOF crystals embedded in the polymer composite. A continuum "smoothing" model in conjunction with the Lennard-Jones potential is used to investigate the van der Waals interactions between a hydrated ferric ion and a MOF pore which is approximated by a semi-infinite cylinder (and later a prism) with the relevant number of atoms smeared uniformly over the surface. The main findings are summarised and discussed below, followed by a section discussing experimental considerations.

6.1. SUMMARY

The van der Waals energy calculations predict that the most energetically favourable position for the ferric ion is inside the MOF pore, and away from the pore entrance, regardless of whether the ferric ion is hydrated or not. The hydration of the ferric ion significantly increases the magnitude of the interaction energy. The assumed radii of the oxygen and hydrogen spheres has an important effect on the magnitude of the interaction energy, both because of the proximity of the sphere to the MOF pore, and the larger surface area over which Equation (2.3) is integrated. The van der Waals force calculations show that the hydrated ferric ion has the greatest attraction force at the entrance of the MOF pore and would enter the MOF pore to remain inside at the location of the potential energy minimum. The van der Waals interaction force acting on a ferric ion to move it from the far (left) field to the far (right) field inside the MOF pore, would result in the ferric ion gaining a considerable amount of kinetic energy. The final kinetic energy of a hydrated ferric ion's is over 84 times greater than a ferric ion alone.

Initially, the MOF pore was modelled as a semi-infinite cylinder. The MOF pore was also modelled as a finite cylinder, and it was shown that the qualitative behaviour of the interactions between the MOF pore and hydrated ferric ion remained much the same. The physical behaviour at the entrance and the exit of the finite MOF pore were the same. In fact, MOF crystals with a depth greater than 68.29 Å (i.e., 10 h) can be approximated by a semi-infinite MOF pore and the results for a finite pore are indistinguishable from those for a semi-infinite pore. Since the EuBDC-OMe MOF crystals used in the sensor are typically nano-sized, using the semi-infinite pore is a valid approximation.

To understand the influence of the actual crystal pore geometry, the MOF pore was next approximated by a semi-infinite prism. The qualitative behaviour of the interactions between a ferric ion and a semi-infinite prismatic MOF pore remains as for the semi-infinite cylinder. The analytical expressions for the interactions between a ferric ion point and a semi-infinite prismatic MOF pore result in complicated expressions due to a loss of symmetry. Consequently, a method for determining the best approximating cylindrical pore was proposed. Specifically, the radius of the optimal approximating cylinder is such that the cross-sectional area matches with that of the prismatic approximation. This approach has not been tested for its applicability beyond the context of the current problem.

The Lennard-Jones calculations presented here use the atom centre-to-centre distances to model the MOF pore diameter and the diameter of the hydrogen sphere in a hydrated ferric ion. Consequently, both the true space in the MOF pore and the true size of the hydrogen sphere are underestimated. If the ionic radii of the hydrated ferric ion and the MOF pore are included in the modelling, the hydrated ferric ion is geometrically too large to enter the free space inside the pore. While a ferric ion with no coordinated water molecules can enter the MOF pore space, unhydrated ferric ions are unlikely to be present in a leaching solution. As a consequence, it is most likely that hydrated ferric ions will accumulate on the surface of the MOF crystal, and this conclusion is supported by synchrotron x-ray diffraction experiments [41]. The x-ray diffraction experiments reveal that the hydroxy groups remain on the ligands, thereby reducing available pore space. In [41], the authors hypothesise that there are only surface level interactions between the hydrated ferric ion and the MOF crystals. This finding is in contrast to the previously held assumption that ferric ions associate with hydroxy groups with MOF pores [59]. In practice, the fact that ferric ions associate to the surface of MOF crystals is a desirable property for "washing" and re-use of a sensor designed to detect and measure ferric ion concentrations in mineral processing situations. Re-use of the sensor ultimately results in a cost-saving.

The leaching solution into which the ferric ion sensor is submerged contains many other metal ions, and the interactions between two dications and a MOF pore were considered to investigate how competing ions may affect sensing or MOF pore occupancy. Magnesium(II) has a greater affinity to the MOF crystal than ferric ions. However, the association of magnesium(II) to the EuBDC-OMe MOF does not affect sensor readings as the MOF is a viable "turn-off" ferric ion sensor [41] (see also Subsection 1.2.1).

This raises the question of what happens when a ferric ion approaches a MOF pore that is already

occupied. Section 5.4 found that the approaching ferric ion will experience an interaction force away from the pore, so that the ferric ion can only occupy a vacant MOF pore, encouraging a more even distribution of ferric ions on the surface of the MOF crystal which is likely to improve sensor performance. An approaching ferric ion is most likely to occupy the closest vacant MOF pore.

Changes in temperature do not affect the qualitative results. However, temperature will influence the diffusion rate of ferric ions in an analyte solution.

6.2. EXPERIMENTAL CONSIDERATION

The power of mathematical modelling of the interactions between interacting non-bonded molecules resides in the fact that it can be applied to various interacting molecules with differing atomic compositions, since the models can be simply updated with the relevant physical parameters for the new modelling environment. The above section provided enough evidence to support the conclusion that, even though the MOF pore has a parallelogram shaped cross-section, using a simpler cylindrical pore as a first approximation provides reliable physical insights.

The work presented here considers only van der Waals interactions since the electrostatic Coulombic forces are assumed to be negligible. This is because the ionic strength of the solution is high and hence the Debye layer is small and overall double electric layer forces are screened (both in magnitude and in distance). In addition, the zeta potential (the electrical potential) of the MOF surface is of the order of milli-eV; if the zeta potential is positive, the crystal surface contribution to the interaction force will result in a small increase in attraction and if negative, the energy gain from the van der Waals forces would dominate the interaction.

Figure 1.2 shows a schematic of a possible sensing environment. The fact that hydrated ferric ions are attracted to the MOF pore but are geometrically too large to fit inside the pore means that the hydrated ferric ion may have an impact when it makes contact with the MOF surface. This is unlikely to lead to damage to the surface of the MOF crystals because hydrated ferric ions would require a kinetic energy of the order of 10-100 eV in order to damage the surface [44]. In addition, since ferric ions are unable to fit inside the MOF pore, the sensor will avoid double detection and subsequent overestimation of the ferric ion concentration. As a consequence, when the signals are processed, the ratio between the two florescence peaks will approach a constant as the number of available MOF pores decreases. If hydrated ferric ions did funnel into the pore, it might effect the detection time and accuracy of ferric ion concentration measurements.

The investigation of various other metal ions did not take into consideration their hydrated state when in the aqueous analyte solution. In aqueous solutions, metal ions are more likely to exist in their hydrated state with 4-6 associated water molecules (depending on the metal ion) [10]. Persson [35] provided a review article confirming that magnesium(II) and copper(II) typically have six associated water molecules in an aqueous solution. Any difference in the interactions as a consequence of the different ions will be completely overwhelmed by the interactions of the oxygen and hydrogen (water molecules) with the MOF pore, and therefore the effect of hydration was ignored in the present study. While investigating the interactions between three different metal ions and a MOF pore, it was shown that for a small specified range of a hypothetical MOF pore radius, the interaction force between a ferric ion and a MOF pore is strictly positive, while for magnesium(II) and copper(II) the interaction force in the same range is negative. In theory, experimentalists could effect any desired metal ion association with MOF crystals by altering the MOF pore sizes but it may be physically/chemically challenging and even impossible.

If the hydrated ions are to be investigated further, the radial distances between the metal ion and the oxygen atoms needs to be taken into consideration. The bond lengths between an oxygen atom and copper(II) ion is approximately[1] 2.13 Å, an oxygen atom and a ferric ion is 2.00 Å, and an oxygen atom and a magnesium(II) is 2.07 Å [35]. The coordination and configuration of hexa-aqua copper(II) ion may also need to be taken into account, since it has varying oxygen bond lengths.

This investigation facilitates the calculation of a critical pore depth of 68.29 Å. For pores deeper than this critical depth, the interaction force is always positive at the pore entrance with a maximum equal to the maximum force for a semi-infinite pore. As the pore depth decreases from this critical value, the maximum of the interaction force also decreases but remains directed to the right.

[1]The bond length between copper(II) and oxygen has three characteristic bond lengths: 1.96, 2.15, and 2.32 Å

Part II

Macroenvironment

Part II studies the environment at a colloidal scale to investigate how ferric ions diffuse through the analyte solution and the polymer composite to interact with the embedded MOF crystals. An important finding from Part I is that the hydrated ferric ions are too large to fit inside the MOF pores. Therefore, this part does not model ferric ion diffusion in the MOF pores.

Since ferric ions associate to the MOF crystals, they are treated here like a ferric ion sink. First, a single MOF crystal is considered at the solution-polymer boundary to observe how the MOF crystal affects ferric ion diffusion in mixed media and to determine what physical properties affect MOF occupancy. Second, MOF crystals distributed throughout the polymer are considered and the impact of MOF crystal density on ferric ion diffusion in the polymer is investigated to gain an understanding of how long the sensor should be exposed to an analyte solution to ensure an accurate reading is obtained.

The original contributions contained in Part II broadly fall into two categories: (i) insights, and (ii) mathematical contributions.

The insights regarding which ferric ion characteristics and MOF crystal characteristics primarily effect sensing time are new. For example, if the MOF crystal density in the polymer composite is high, then the sensor requires a longer exposure time for an accurate reading. Therefore, in solutions that are known to contain high ferric ion concentrations, sensor designers should experiment with a lower MOF crystal density.

In Chapter 7, the problem is formulated as a diffusion equation to be solved in two different regions together with a Robin boundary condition to represent the MOF crystal sink. This problem is solved numerically using purpose-written code in MATLAB. In Chapter 8, the behaviour of the system can be described by a partial differential equation (PDE) describing diffusion of ferric ions coupled with a pseudo ODE describing the MOF crystal sink. This coupled system of equations is transformed into a single equation and an approximate solution is found using analytical techniques.

CHAPTER 7

FERRIC ION DIFFUSION IN SOLUTION AND POLYMER: A MOF CRYSTAL AT THE SOLUTION-POLYMER BOUNDARY

Previously, the interactions between hydrated ferric ions and MOF pores were explored. The ferric ions are indeed attracted to the MOF pores and remain on the surface of the MOF crystals.

This chapter studies ferric ion diffusion through different media. Since the hydrated ferric ions are too large to diffuse into the MOF pores, the focus is solely on the diffusion of ferric ions through the analyte solution and the polymer composite. There is assumed to be one MOF crystal located on the surface of the polymer composite at the polymer-solution boundary; this MOF crystal acts as a sink for the ferric ions. First, a mathematical model is formulated to model the system. Second, nondimensional parameters for the one- and two-dimensional systems are found and their relative importance and impact on the system is discussed.

7.1. MATHEMATICAL MODELLING AND ASSUMPTIONS

Recall the proposed sensor design shown in the Introduction, Figure 1.9. Figure 7.1 depicts a cross section of the modelled ferric ion sensor, where MOF crystals are randomly distributed through the polymer composite. The sensor is submerged in an analyte solution during sensing.

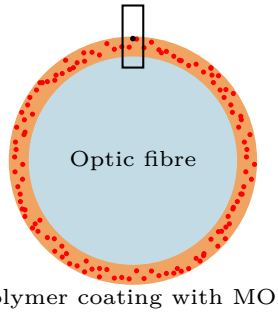


Figure 7.1: Two-dimensional cross section of optic fibre with MOF-polymer thin film. Red dots represent MOF crystals in orange polymer composite. Blue represents optic fibre core. Black rectangle encompasses small section to be studied.

A small section of the cross-section can be described approximately using a Cartesian co-ordinate frame, Figure 7.2. Consider the case where a MOF crystal is placed on the surface of the polymer composite, as indicated by the small black dot inside the rectangle in Figure 7.1. This results in

a sink at a mixed media boundary, the interface between the polymer composite and the analyte solution.

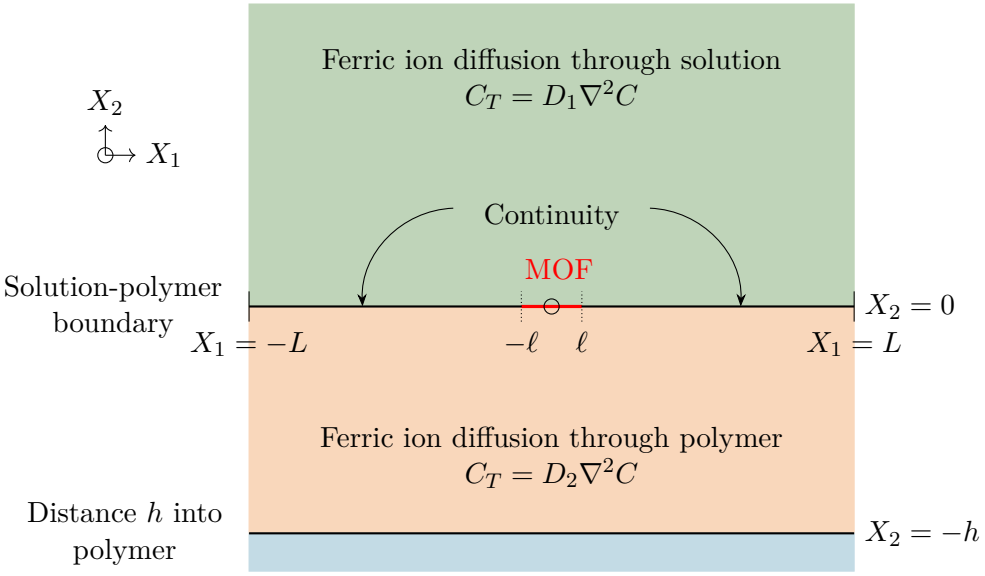


Figure 7.2: Two-dimensional system: X_1-axis is solution-polymer boundary, $X_2 > 0$ is distance into solution and $X_2 < 0$ is into polymer composite. Green represents solution being analysed. Red line represents single MOF crystal in orange polymer composite. Blue represents optic fibre core.

The MOF-polymer composite is exposed to a solution containing ferric ions, where the movement of ferric ions is governed by Brownian motion. The diffusivity of the ferric ions is assumed to be constant through the solution, denoted by D_1. Since in practice the polymer is kept hydrated and the ferric ions do not enter the MOF pores, the diffusivity of ferric ions in the polymer, D_2, is also assumed to be constant, such that $D_2 < D_1$ and the Vrentas-Duda theory is not applicable [15, 54, 55, 56]. As a consequence, the movement of ferric ions in both the solution and the polymer is assumed to be governed by the conventional diffusion equation with distinct diffusivities,

$$\begin{aligned} \frac{\partial}{\partial T}C(T,\mathbf{X}) &= D_1\nabla^2 C(T,\mathbf{X}) \qquad \text{for } X_2 \geq 0, \\ \frac{\partial}{\partial T}C(T,\mathbf{X}) &= D_2\nabla^2 C(T,\mathbf{X}) \qquad \text{for } X_2 < 0, \end{aligned}$$

where $C(T,\mathbf{X})$ is the concentration of ferric ions, and the origin is located at the centre of the MOF strip so that the X_1-axis coincides with the solution-polymer boundary. Here, ∇^2 is the usual Laplacian in two dimensions. The ferric ion concentration profile in the analyte solution is given by $C(T,\mathbf{X})$ for $X_2 \geq 0$, and the concentration in the polymer is given by $C(T,\mathbf{X})$ for $X_2 < 0$. The time since the sensor's exposure to the solution is given by T.

To ensure that continuity is maintained for boundaries shared by two media, two conditions are included at the solution-polymer boundary. The ferric ion concentration at the boundary is assumed to be the same when approaching from above or below the boundary, and the flux out of the solution is equivalent to the flux into the polymer [21],

$$C_+ = C_-, \qquad D_1 \frac{\partial C_+}{\partial X_2} = D_2 \frac{\partial C_-}{\partial X_2} \qquad \text{at } X_2 = 0,$$

where C_+ and C_- are ferric ion concentrations just above and below the boundary, respectively.

Far from the sensor in the direction of the analyte solution is the far field boundary condition, where the ferric ion concentration remains constant and equal to that of the bulk solution C_0. For numerical purposes, the location of this condition is set to be at $X_2 = L$, so that

$$C(T, X_1, L) = C_0 \qquad \text{at } X_2 = L,$$

where L is assumed to be a large distance away from the solution-polymer boundary. A no flux condition is assumed at a horizontal distance L away from the MOF centre (symmetry) and at the bottom boundary of the polymer composite,

$$\frac{\partial C}{\partial X_1} = 0 \qquad \text{at } X_1 = \pm L; \qquad \frac{\partial C}{\partial X_2} = 0 \qquad \text{at } X_2 = -h.$$

The flux condition at the solution-MOF interface is given by

$$D_1 \frac{\partial C_+}{\partial X_2} = a \left[k_{\text{on}} C \left(B_0 - B \right) - k_{\text{off}} B \right] \qquad \text{for } |X_1| \leq \ell, \qquad X_2 = 0,$$

where $B(T, X_1)$ is the occupancy of the MOF pores by the ferric ions, k_{on} is the association rate compared to the ferric ion concentration, k_{off} is the dissociation rate, B_0 is the total number of MOF pores (both occupied and available) for ferric ion occupation and a is a constant. Due to steric effects, the ferric ion only associates at the MOF pore's entrance and does not diffuse into the MOF pore. The first term captures the association of ferric ions to the MOF crystal and this term vanishes when the MOF crystal is completely occupied. The second term captures the dissociation of ferric ions from the MOF pore.

Ferric ions are assumed to only associate and dissociate from the MOF pores in the X_2-direction,

imposing a no-flux boundary condition to the sides of the MOF crystal,

$$\frac{\partial C}{\partial X_1} = 0 \qquad \text{for } |X_1| = \ell, \qquad X_2 = 0.$$

The occupancy of the MOF pores is governed by the pseudo ODE,

$$\frac{\partial B}{\partial T} = k_{\text{on}} C\,(B_0 - B) - k_{\text{off}} B \qquad \text{for } |X_1| \leq \ell, \qquad X_2 = 0.$$

In addition, since B_0 is the number of MOF pores available, $B(T, X_1) \in [0, B_0]$ and the total ferric ion occupancy in the MOF crystal is,

$$B_{tot}(T) = \int_{-\ell}^{\ell} B(T, X_1)\,\mathrm{d}X_1 \leq 2\,\ell\,B_0.$$

The assumed initial conditions are

$$C(0, \mathbf{X}) = C_0 \qquad \text{for } X_2 \geq 0; \qquad C(0, \mathbf{X}) = 0 \qquad \text{for } X_2 < 0;$$
$$B(0, X_1) = 0 \qquad \text{for } |X_1| \leq \ell, \qquad X_2 = 0.$$

7.1.1. Nondimensional two-dimensional model

Distance is nondimensionalised with the half-length of the MOF strip, ℓ, the ferric ion concentration with the bulk concentration, C_0, and the MOF binding site occupancy with the maximum occupancy, B_0. There are two options for the time scale: a diffusive time-scale where $\tau_D = \ell^2/D_1$, or an association time-scale where $\tau_A = 1/C_0 k_{\text{on}}$. At this stage, time is nondimensionalised with τ without specifying which time-scale, so that the system of equations can be written

$$\frac{\partial c}{\partial t} = s_1 \nabla^2 c \qquad \text{for } x_2 \geq 0; \qquad \frac{\partial c}{\partial t} = s_1 D \nabla^2 c \qquad \text{for } x_2 < 0; \tag{7.1}$$
$$\frac{\partial b}{\partial t} = s_2\,[c\,(1 - b) - s_3\,b] \qquad \text{for } |x_1| \leq 1, \qquad x_2 = 0, \tag{7.2}$$

where $D = D_2/D_1$, $s_1 = D_1\tau/\ell^2$, $s_2 = C_0 k_{\text{on}}\tau$ and $s_3 = k_{\text{off}}/C_0 k_{\text{on}}$ are nondimensional parameters. Again, neither of the two time-scales are favoured at this point because it is unknown which time-scale is the most appropriate choice, s_1 or s_2. If the problem is scaled with the diffusive time-scale, then $s_1 = 1$. If the problem is scaled with the association time-scale, then $s_2 = 1$.

The continuity conditions at the solution-polymer boundary become

$$c_+ = c_-, \qquad \frac{\partial c_+}{\partial x_2} = D\frac{\partial c_-}{\partial x_2} \qquad \text{at } x_2 = 0. \tag{7.3}$$

Far away from the solution-polymer boundary, the boundary condition becomes

$$c(t, x_1, L/\ell) = 1 \qquad \text{at } x_2 = L/\ell, \tag{7.4}$$

while the no flux boundary conditions at the sides and at the polymer-optic fibre boundary become

$$\frac{\partial c}{\partial x_1} = 0 \qquad \text{at } x_1 = \pm L/\ell; \qquad \frac{\partial c}{\partial x_2} = 0 \qquad \text{at } x_2 = -h/\ell. \tag{7.5}$$

At the solution-MOF boundary,

$$s_1\frac{\partial c_+}{\partial x_2} = s_4\, s_2\, [c\,(1-b) - s_3\, b] \qquad \text{for } |x_1| \le 1,\ x_2 = 0, \tag{7.6}$$

where $s_4 = a\, B_0/\ell\, C_0$ is a nondimensional parameter and the no-flux boundary conditions at the sides of the MOF crystal become

$$\frac{\partial c}{\partial x_1} = 0 \qquad \text{at } |x_1| = 1. \tag{7.7}$$

The initial conditions and the total MOF pore occupancy are

$$c(0, \mathbf{x}) = 1 \qquad \text{for } x_2 \ge 0; \qquad c(0, \mathbf{x}) = 0 \qquad \text{for } x_2 < 0; \tag{7.8}$$

$$b(0, x_1) = 0 \qquad \text{for } |x_1| \le 1, \qquad x_2 = 0; \tag{7.9}$$

$$b_{tot}(t) = \int_{-1}^{1} b(t, x_1)\, \mathrm{d}x_1 \le 2. \tag{7.10}$$

7.1.2. One-dimensional model

To obtain a preliminary indicator of the behaviour of the system and the importance of the various parameters, this model is further simplified. Figure 7.3 shows a simpler one-dimensional system, where the MOF crystal is represented by a red square, and diffusion in the polymer composite region is completely ignored.

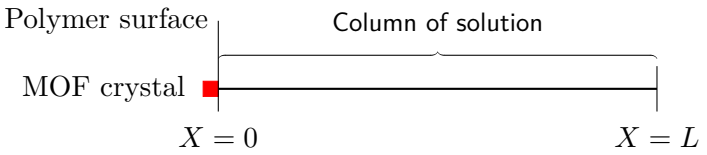


Figure 7.3: One-dimensional representation of ferric ions diffusing through column of solution with MOF crystal at left boundary.

The concentration of ferric ions is assumed to be only a function of two variables, $C(T, X)$, and the MOF pore occupancy is assumed to depend only on time, $B(T)$,

$$\begin{aligned} \frac{\partial C}{\partial T} &= D_1 \frac{\partial^2 C}{\partial X^2} && \text{for } X \geq 0, \\ \frac{\partial B}{\partial T} &= k_{\text{on}}\, C(B_0 - B) - k_{\text{off}}\, B && \text{at } X = 0. \end{aligned}$$

The corresponding flux condition at the boundary $X = 0$ is given by

$$D_1 \frac{\partial C}{\partial X} = a \left[k_{\text{on}}\, C(B_0 - B) - k_{\text{off}}\, B \right],$$

and the far field condition is $C(T, L) = C_0$, with initial conditions $C(0, X) = C_0$ and $B(0) = 0$.

7.1.3. Nondimensional one-dimensional model

Concentration, occupancy, length, and time are nondimensionalised in the same way as before, where ℓ is a characteristic length representative of the MOF crystal size, so that the system of equations becomes

$$\frac{\partial c}{\partial t} = s_1 \frac{\partial^2 c}{\partial x^2} \qquad \text{for } x \geq 0; \qquad \frac{\partial b}{\partial t} = s_2 \left[c\,(1 - b) - s_3\, b \right] \qquad \text{at } x = 0, \tag{7.11}$$

where the s_i are as previously defined. The nondimensional flux condition at the boundary $x = 0$ is

$$s_1 \frac{\partial c}{\partial x} = s_4\, s_2 \left[c\,(1 - b) - s_3\, b \right], \tag{7.12}$$

while the nondimensional far field condition at $x = L/\ell$ becomes

$$c(t, L/\ell) = 1, \tag{7.13}$$

and the initial conditions are given by

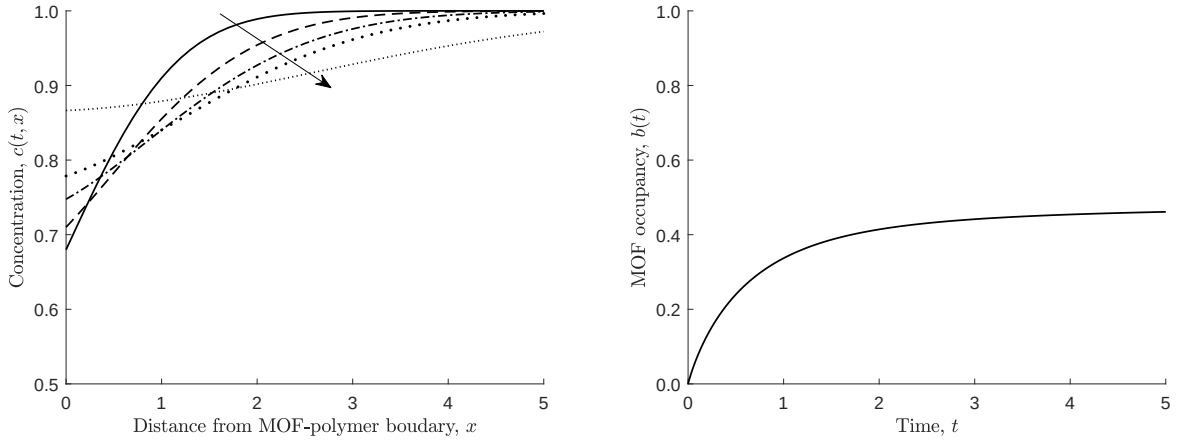
$$c(0, x) = 1, \ b(0) = 0. \tag{7.14}$$

7.2. VARIATION OF NONDIMENSIONAL PARAMETERS IN ONE-DIMENSIONAL MODEL

This section explores the effects of varying the nondimensional parameters, s_i and D, on the one-dimensional model. The impact on ferric ion concentration through a column of solution and MOF occupancy is discussed.

To our knowledge, no analytical solution exists for this system. Therefore the model is solved numerically with purpose-written code in MATLAB. The equation for $b(t)$ is solved using a explicit Runga-Kutta method, and the diffusion equation for $c(t, x)$ is solved with an implicit Crank-Nicolson scheme (see Appendix F for details).

When all nondimensional parameters are equal to unity, Figure 7.4(a) depicts the time evolution of the ferric ion concentration in solution and Figure 7.4(b) shows the MOF occupancy. Ferric ions in the solution initially associate rapidly to the MOF crystal, reducing the concentration in solution near the MOF crystal. Over time the ferric ion concentration returns to the steady state far field condition, Figure 7.4(a). Note that the MOF crystal's occupancy initially increases rapidly and then slowly increases, approaching steady state in the large time limit, 7.4(b).



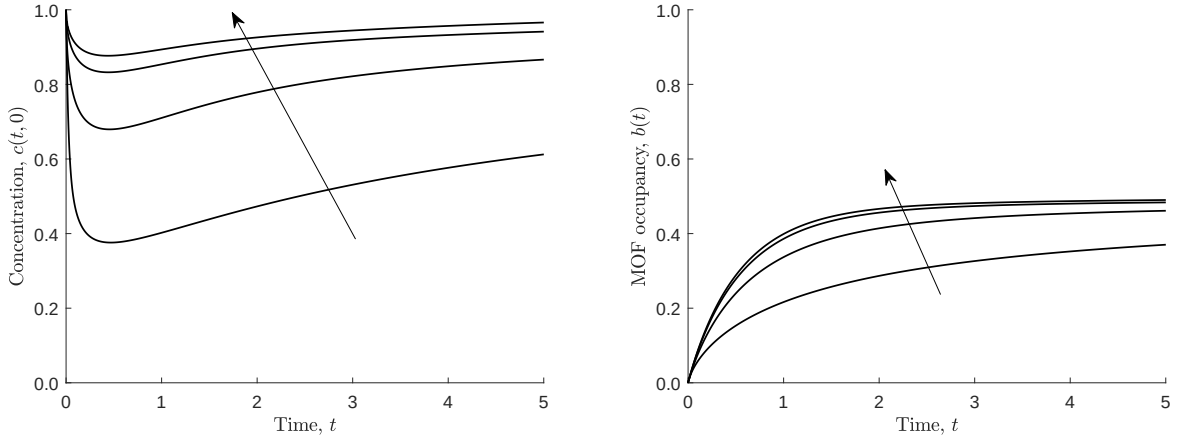
(a) (b)

Figure 7.4: (a) Nondimensional concentration of ferric ions in solution, $c(t, 0)$. Arrow indicates increasing time, $t = 0.5, 1, 1.5, 2, 5$. (b) Nondimensional MOF occupancy, $b(t)$. Here, $s_1 = s_2 = s_3 = s_4 = 1$.

The following subsections describe the impact of varying the parameters. In all cases for the one-dimensional numerical scheme $\Delta x = 0.1$, $\Delta t = 0.005$, and $L/\ell = 10$.

7.2.1. Varying the nondimensional diffusion coefficient, s_1

Figure 7.5 shows the effect of varying the nondimensional diffusion coefficient ($s_1 = D_1\tau/\ell^2$) on the ferric ion concentration in the solution at the MOF crystal and the MOF occupancy. A smaller nondimensional diffusion coefficient causes the concentration of ferric ions in solution to be more significantly reduced near the MOF boundary, and, following this initial reduction, it takes longer for the concentration in the solution to recover towards the steady state concentration. A larger nondimensional diffusion coefficient results in less reduction near the boundary because ferric ions can more readily diffuse from the column of solution. MOF occupancy reaches close to steady state sooner with a high nondimensional diffusion coefficient.



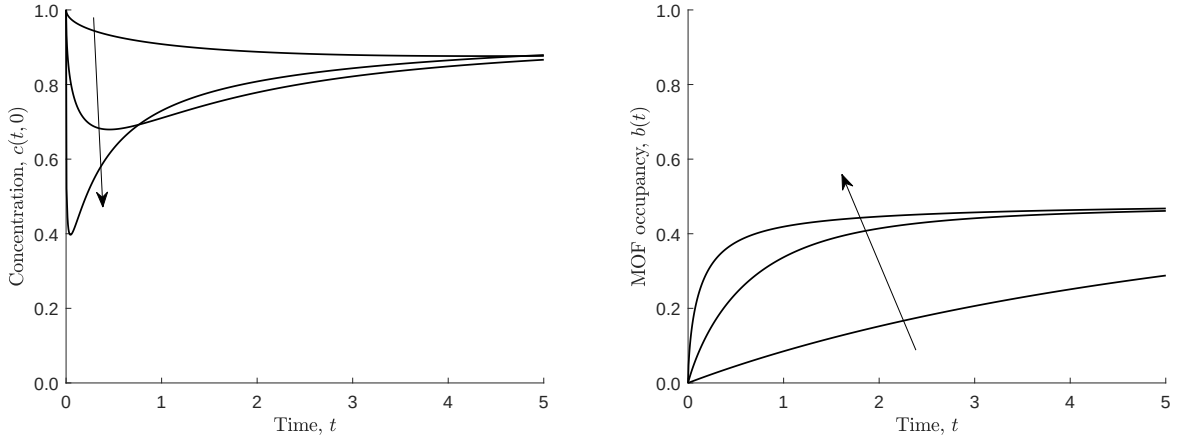
(a) (b)

Figure 7.5: Results for different values of nondimensional diffusion, $s_1 = 0.1, 1, 5, 10$ and $s_2 = s_3 = s_4 = 1$. Arrows indicate direction of increasing s_1. (a) Nondimensional concentration of ferric ions at MOF-polymer boundary, $c(t, 0)$. (b) Nondimensional MOF occupancy, $b(t)$.

7.2.2. Varying the effective association parameter, s_2

Increasing the effective association parameter ($s_2 = C_0 k_{\text{on}}\tau$) means that ferric ions associate to the MOF crystal faster than they diffuse through the solution. This results in the MOF occupancy reaching steady state sooner, Figure 7.6(b). When s_2 is large, the concentration near the solution-polymer boundary is reduced very quickly, followed by a slow increase as ferric ions diffuse from the rest of the region, Figure 7.6(a).

On exposure of the MOF to the solution, the concentration at the boundary varies significantly for different values of s_2. However, at large times, the ferric ion concentration and the MOF occupancy is largely independent of s_2.



(a) (b)

Figure 7.6: Results for different values of effective association, $s_2 = 0.1, 1, 10$ and $s_1 = s_3 = s_4 = 1$. Arrows indicate direction of increasing s_2. (a) Nondimensional concentration of ferric ions at MOF-polymer boundary, $c(t, 0)$. (b) Nondimensional MOF occupancy, $b(t)$.

7.2.3. Varying the effective dissociation parameter, s_3

The effective dissociation parameter ($s_3 = k_{\text{off}}/C_0 k_{\text{on}}$) captures the ferric ions that dissociate from the MOF crystal. Various values of s_3 are investigated, including $s_3 = 0$ which represents the situation when ferric ions can only associate, see Figure 7.7.

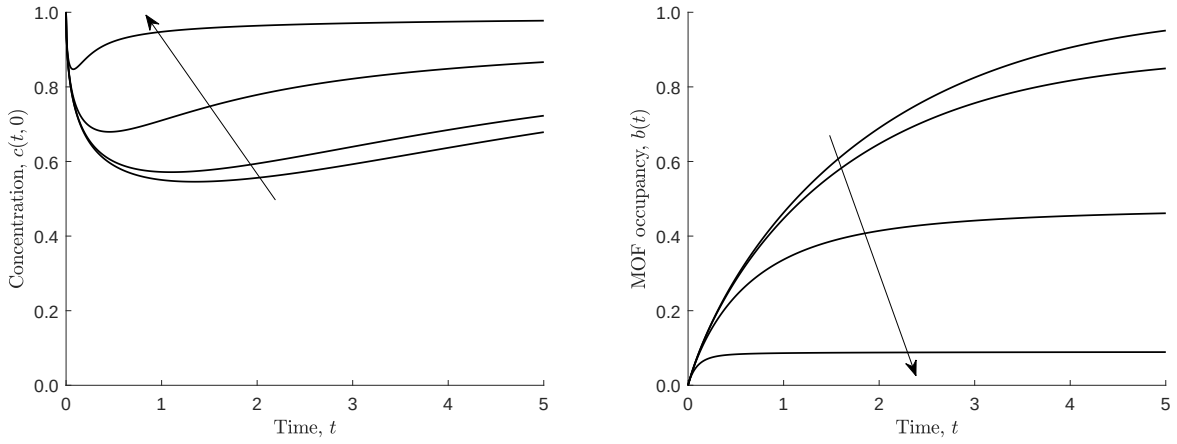
Increasing the effective dissociation parameter means that the ferric ions dissociate more readily and the nondimensional steady state MOF pore occupancy can be calculated from equation (7.11),

$$b_{\text{eq}} = b(t \to \infty) = \frac{1}{1 + s_3}, \tag{7.15}$$

a similar expression for the number of effective bound receptors at equilibrium is given in Squires et al. [45], with a different combination of parameters. (It is likely that the equilibrium constant K_D in Squires et al. [45] should be defined as $K_D = k_{\text{off}}/k_{\text{on}}$ rather than $K_D = k_{\text{on}}/k_{\text{off}}$ as stated. This also aligns with working in their Box 1.)

In the steady state, the occupancy of the pores is lower for larger values of the effective dissociation parameter, and the steady state is reached more quickly. In the case when the ferric ions cannot dissociate, that is $s_3 = 0$, the steady state MOF occupancy is equal to its maximum value ($b(t \to$

$\infty) = 1$), and the concentration of ferric ions at the MOF-solution boundary approaches the bulk concentration at large times.



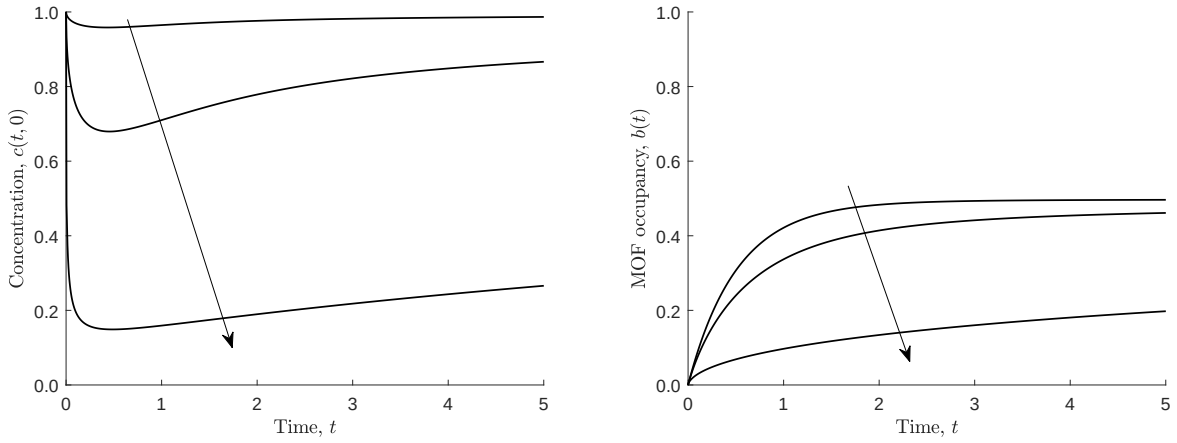
(a) (b)

Figure 7.7: Results for different values of effective dissociation, $s_3 = 0, 0.1, 1, 10$ and $s_1 = s_2 = s_4 = 1$. Arrows indicate direction of increasing s_3. (a) Nondimensional concentration of ferric ions at MOF-polymer boundary, $c(t, 0)$. (b) Nondimensional MOF occupancy, $b(t)$.

7.2.4. Varying the effective flux parameter, s_4

An important consequence of the flux condition is the time taken for the MOF crystal to approach steady state. Increasing the effective flux parameter ($s_4 = aB_0/\ell C_0$) increases the time taken to reach steady state (see Figure 7.8(b)). The increase affects ferric ion concentration at the MOF crystal boundary, as ferric ions quickly associate to the MOF crystal and the ferric ions do not diffuse fast enough for the MOF crystal to reach steady state in a timely manner, Figure 7.8(a).

The delay to reaching steady state is attributed to ferric ions associating to the MOF crystal faster and quickly depleting the ferric ions in the solution. A comparable mechanism is observed when increasing the effective association parameter, s_2. The effective association parameter is a MOF characteristic and an increase results in a shorter time for the MOF crystal to reach steady state, Figure 7.6(b). The ferric ion concentration at the MOF boundary is largely unchanged after $t = 4$, Figure 7.6(a). However, the effective flux parameter is a ferric ion characteristic and an increase in this parameter results in a longer time for the MOF crystal to reach steady state, Figure 7.8(b). The ferric ion concentration at the MOF boundary is very sensitive to the increase in the effective flux parameter, as seen by the long depletion time for a larger parameter value, Figure 7.8(a).



(a) (b)

Figure 7.8: Results for different values of effective flux, $s_4 = 0.1, 1, 10$ and $s_1 = s_2 = s_3 = 1$. Arrows indicate direction of increasing s_4. (a) Nondimensional concentration of ferric ions at MOF-polymer boundary, $c(t, 0)$. (b) Nondimensional MOF occupancy, $b(t)$.

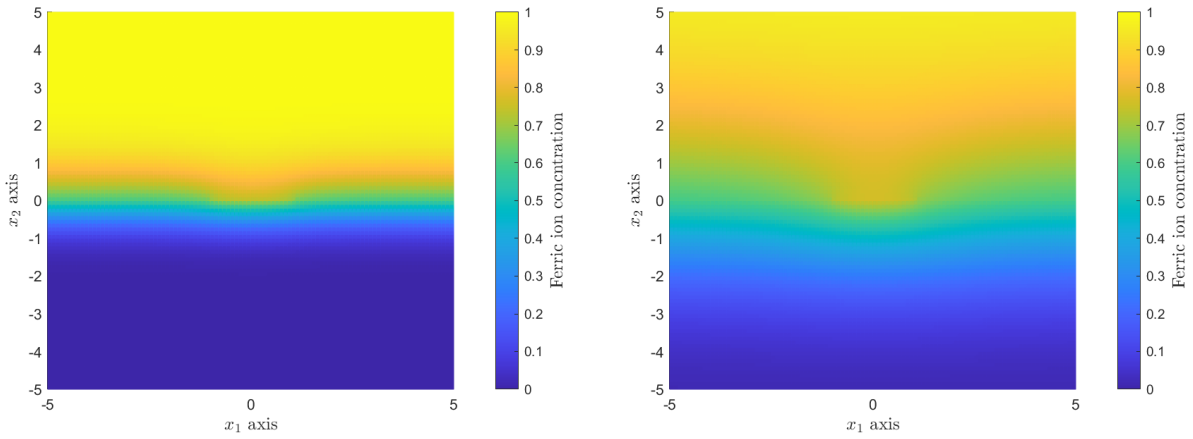
7.3. VARIATION OF NONDIMENSIONAL PARAMETERS IN TWO-DIMENSIONAL MODEL

This section returns to the nondimensional two-dimensional model and to the primary aim of this chapter which is to investigate ferric ion diffusion through a solution into a polymer composite with a MOF sink located at the boundary between the two media.

The MOF occupancy equation $b(t, x_1)$ is solved using an explicit Runga-Kutta method, and the diffusion equation for $c(t, \mathbf{x})$ is solved with a forward-time-centred-space finite difference scheme (see Appendix G for detail).

Figure 7.9 shows the ferric ion concentration for the domain $-5 \leq x_1 \leq 5$, $-5 \leq x_2 \leq 5$, where $x_2 < 0$ in the polymer and $x_2 \geq 0$ in the solution. The MOF crystal is located at $|x_1| \leq 1$ and $x_2 = 0$. Figures 7.9(a) and (b) show the ferric ion profiles at time $t = 0.5$ and 5, respectively. In all cases for the numerical two-dimensional scheme $\Delta x_1 = \Delta x_2 = 0.1$, $\Delta t = 0.0005$, $D = 0.5$ (unless otherwise stated) and $L/\ell = h/\ell = 10$.

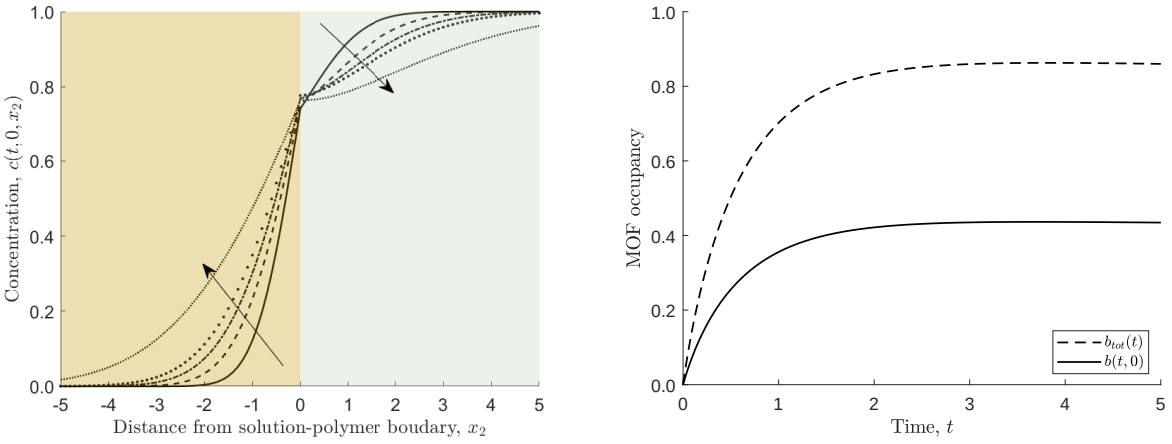
Figure 7.10(a) shows the ferric ion concentration along the line $x_1 = 0$, which shows the changes through the mixed media over time. In comparison to the one-dimensional model (Figure 7.4(a)), the two-dimensional model requires additional time to reach steady state. This is due to the size of the MOF crystal and the depth of the polymer composite. The MOF occupancy at the centre of the MOF ($b(t, 0)$) and the total MOF occupancy over the whole MOF crystal, (equation (7.10))



(a) (b)

Figure 7.9: Nondimensional concentration of ferric ions across two media $c(t, x_1, x_2)$. (a) At time $t = 0.5$. (b) At time $t = 5$.

is shown in Figure 7.10(b). Comparing Figure 7.10(b) with Figure 7.4(b) shows that the MOF occupancy as predicted by the two-dimensional model is very similar to that predicted by the one-dimensional model. However, the two-dimensional model includes the effect of the polymer on ferric ion diffusion and MOF occupancy.

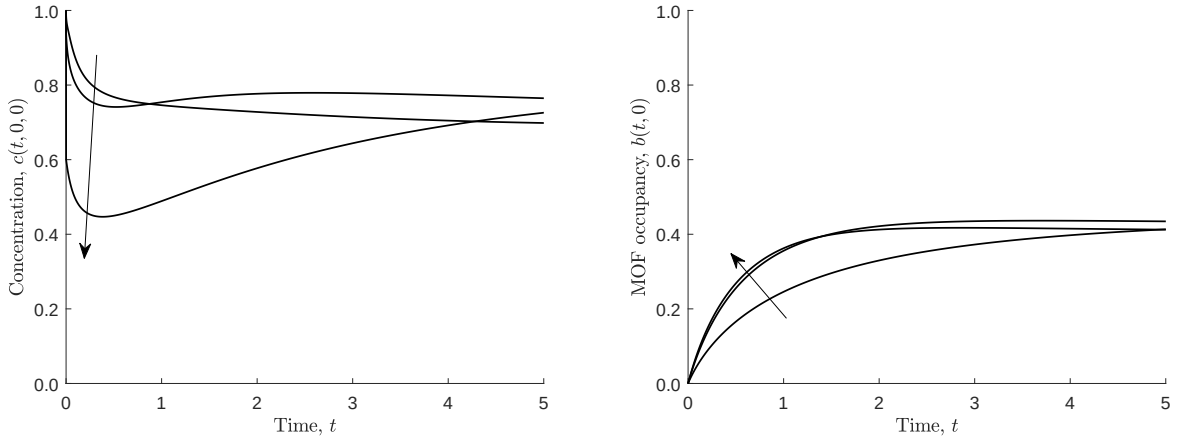


(a) (b)

Figure 7.10: (a) Nondimensional concentration of ferric ions through MOF-mid point across two media, $c(t, 0, x_2)$. Arrow indicates direction of increasing time, $t = 0.5, 1, 1.5, 2, 5$. (b) Nondimensional MOF occupancy, $b(t, 0)$ and $b_{tot}(t)$. Here, $s_1 = s_2 = s_3 = s_4 = 1$ and $D = 0.5$.

7.3.1. Varying the nondimensional diffusion coefficient, s_1

Figure 7.11 shows the effect of varying the nondimensional diffusion coefficient ($s_1 = 0.1, 1, 5$). For all values of s_1, the concentration in the solution near the MOF surface initially decreases before increasing towards the steady state value. For larger values of s_1, the decrease is more significant which is in contrast to the one-dimensional results, Figure 7.5.



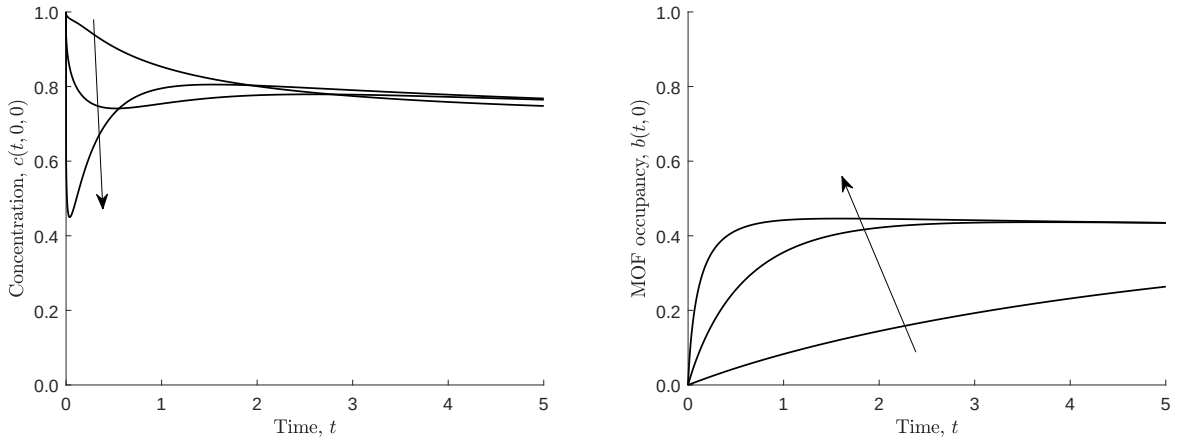
(a) (b)

Figure 7.11: Results for different values of nondimensional diffusion, $s_1 = 0.1, 1, 5$, $s_2 = s_3 = s_4 = 1$ and $D = 0.5$. Arrows indicate direction of increasing s_1. (a) Nondimensional concentration of ferric ions through MOF-mid point across two media, $c(t, 0, 0)$. (b) Nondimensional MOF occupancy, $b(t, 0)$.

Variation of the nondimensional constants has the same effect on the two-dimensional MOF occupancy $b(t, 0)$ profile when compared to the one-dimensional MOF occupancy $b(t)$. The two-dimensional ferric ion concentration at the centre of the MOF crystal behaves in a similar way to that of the one-dimensional ferric ion profile, Figure 7.4(a). However, more time is needed for the ferric ion concentration to reach steady state due to a larger MOF crystal surface area.

7.3.2. Varying the effective association parameter, s_2

The variation of the effective association parameter in the two-dimensional model remains mostly the same, Figure 7.12, in comparison to the one-dimensional model. However, note that the system independence of s_2 occurs in a shorter time period, Figure 7.12(a). The profiles of the MOF occupancy remain unchanged, Figure 7.12(b).

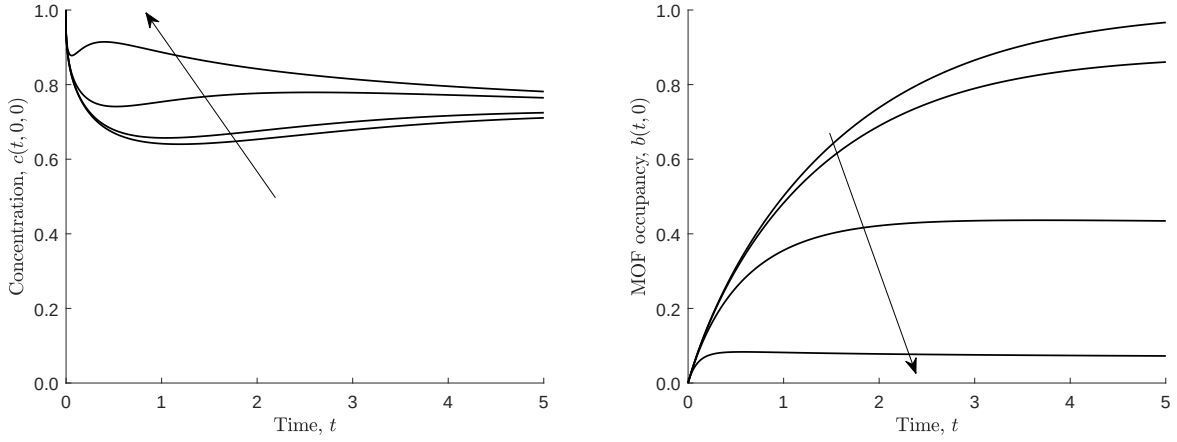


(a) (b)

Figure 7.12: Results for different values of effective association, $s_2 = 0.1, 1, 10$, $s_1 = s_3 = s_4 = 1$ and $D = 0.5$. Arrows indicate direction of increasing s_2. (a) Nondimensional concentration of ferric ions through MOF-mid point across two media, $c(t, 0, x_2)$. (b) Nondimensional MOF occupancy, $b(t, 0)$.

7.3.3. Varying the effective dissociation parameter, s_3

Although the changes in the two-dimensional model are similar to the one-dimensional model, there is less of a distinct effect on the ferric ion concentration when varying the effective dissociation parameter, shown in Figure 7.13(a). In addition, the MOF occupancy requires slightly more time to reach steady state, Figure 7.13(b).

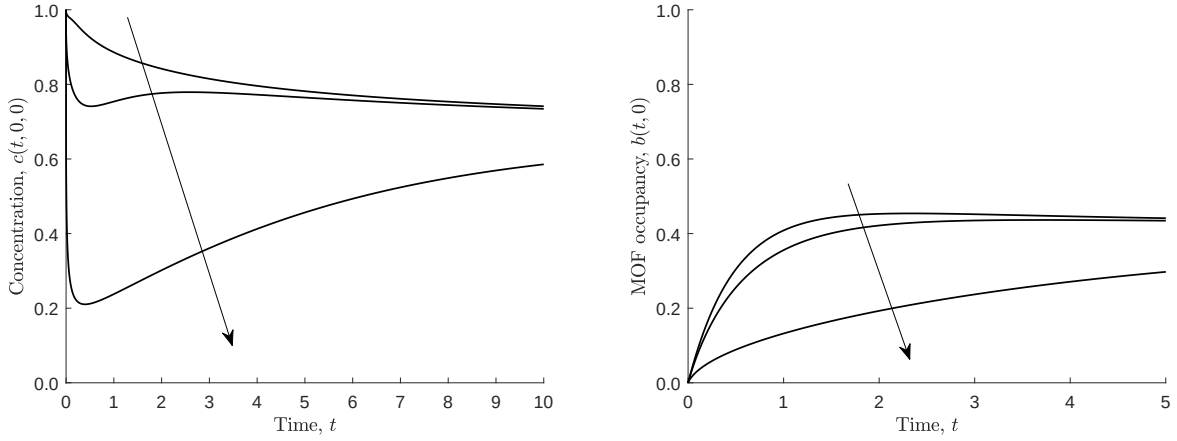


(a) (b)

Figure 7.13: Results for different values of effective dissociation, $s_3 = 0, 0.1, 1, 10$, $s_1 = s_2 = s_4 = 1$ and $D = 0.5$. Arrows indicate direction of increasing s_3. (a) Nondimensional concentration of ferric ions through MOF-mid point across two media, $c(t, 0, x_2)$. (b) Nondimensional MOF occupancy, $b(t, 0)$.

7.3.4. Varying the effective flux parameter, s_4

MOF occupancy at the centre of the crystal reaches steady state sooner in the two-dimensional model, Figure 7.14(b), when varying the effective flux parameter in comparison to the one-dimensional model. The profiles for the two-dimensional ferric ion concentration in early times are similar to the one-dimensional model. The difference between the two models lies at later times.



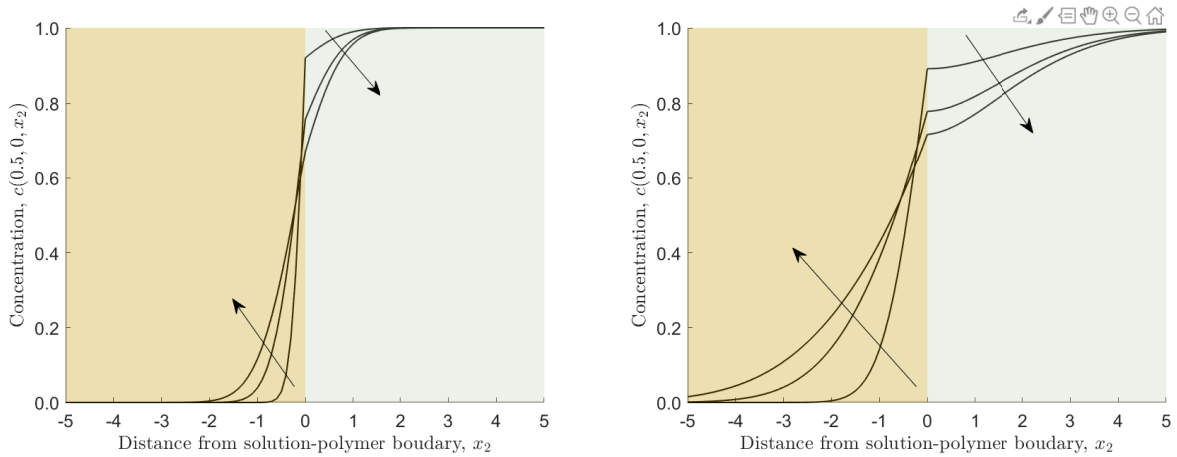
(a) (b)

Figure 7.14: Results for different values of effective flux, $s_4 = 0.1, 1, 10$, $s_1 = s_2 = s_3 = 1$ and $D = 0.5$. Arrows indicate direction of increasing s_4. (a) Nondimensional concentration of ferric ions through MOF-mid point across two media, $c(t, 0, 0)$. (b) Nondimensional MOF occupancy, $b(t, 0)$.

7.3.5. Varying the relative diffusion coefficient, D

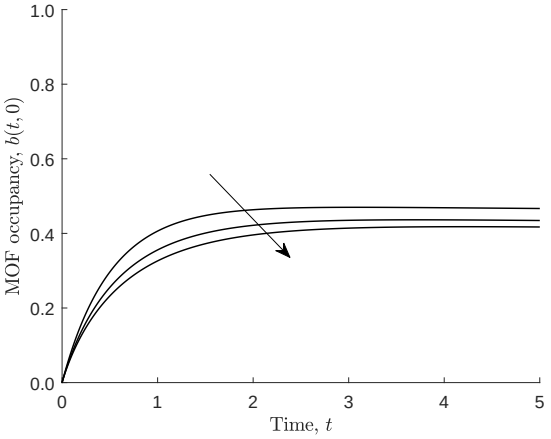
If ferric ion diffusivity in the solution and the polymer is the same, then the relative diffusion coefficient is unity, $D = D_2/D_1 = 1$. In practice, the diffusion coefficient of ferric ions in solution will exceed that in the polymer and the larger the difference the smaller the relative diffusion coefficient. Figure 7.15 shows the effects of varying the relative diffusion coefficient.

Decreasing the relative diffusion coefficient means that ferric ions take longer to diffuse into the polymer and away from the solution-polymer boundary. This affords the ferric ions more opportunity to associate to the MOF crystal. Figure 7.15(c) shows that the occupancy in the crystal is highest in the case of the smallest relative diffusion coefficient.



(a)

(b)



(c)

Figure 7.15: Results for different values of relative diffusion coefficient, $D = 0.1, 0.5, 1$ and $s_1 = s_2 = s_3 = s_4 = 1$. Arrows indicate direction of increasing D. (a)-(b) Nondimensional concentration of ferric ions through MOF-mid point across two media, $c(t, 0, x_2)$ at time $t = 0.5$ and 5, respectively. (c) Nondimensional MOF occupancy, $b(t, 0)$.

7.4. DISCUSSION

This chapter explores the physical mechanisms that influence the sensing capabilities of a proposed new ferric ion sensor. The sensing environment was modelled and the influence if various parameters on MOF occupancy and ferric ion concentration in the environment was observed. First, a two-dimensional model was examined to describe the diffusion of the ions through a solution and into a polymer layer, as well as their attachment to a MOF crystal located at the boundary of the two media. Second, a simplified model was examined that only considered diffusion through the solution, together with attachment to a MOF crystal at one end of the domain. The solutions to the corresponding nondimensional models are then analysed to investigate the importance of the

various nondimensional parameters.

The one-dimensional model indicates that at steady state, the occupancy of the MOF crystal is given by equation (7.15), and this occupancy depends only on the effective dissociation constant, $s_3 = k_{\text{off}}/C_0 k_{\text{on}}$. As a consequence, if the steady state occupancy, $B_{\text{eq}} = B(t \to \infty)$ can be measured with the new sensor in dimensional terms, and the association rate k_{on}, dissociation rate k_{off}, and maximum occupancy B_0 are known, then the concentration of ferric ions in solution can be calculated using

$$C_0 = \frac{k_{\text{off}} B_{\text{eq}}}{k_{\text{on}}(B_0 - B_{\text{eq}})}. \tag{7.16}$$

In practice, it is most likely to be useful to minimise the time taken to reach steady state so that sensing of multiple samples can be done quickly and efficiently. To achieve this, it would be helpful to have a large nondimensional diffusion coefficient s_1 and effective association constant s_2, and small effective flux constant s_4.

While the two-dimensional model is more representative of the proposed sensor and provides more information about the behaviour of the ferric ions in the solution and the polymer, many of the broad behaviours and impacts of changing the system parameters are captured by the simpler one-dimensional model. If the relative diffusion coefficient is small (i.e. $D < 1$), the polymer composite will hinder ferric ion diffusion in that region (in comparison to in the solution), so that ferric ions will have a greater opportunity to associate to the MOF crystals on the polymer surface.

CHAPTER 8

FERRIC ION DIFFUSION IN THE POLYMER: MOF CRYSTALS DISTRIBUTED THROUGHOUT THE POLYMER

The previous chapter is centred around ferric ion diffusion in two media and the characteristics of the MOF crystal occupancy. However, the density of the MOF crystals within the polymer composite were not considered.

This chapter studies ferric ion diffusion through the polymer composite, maintaining the assumption that ferric ions are too large to diffuse into the MOF pores. An important result from the previous chapter is that there are two time-scales: associative and diffusive. This chapter assumes that the MOF crystals reach steady state more quickly than the steady state for ferric ion concentration in the solution or polymer is reached.

The next section describes the mathematical modelling of the system using new definitions to include the MOF-polymer density ratio parameter with the updated modelling assumptions. The following section algebraically solves the modified ferric ion diffusion (modification caused by MOF sinks). Third, results for the nondimensional model are presented and discussed. The final section is a summary of this chapter's findings and their implications.

8.1. MATHEMATICAL MODELLING AND ASSUMPTIONS

Recall that the sensor design has MOF crystals distributed throughout the polymer composite. Figure 7.1 shows a schematic of a cross-section. Figure 8.1 shows the small section of the cross-section that is used to study the modified ferric ion diffusion in this chapter. In practice, MOF crystals are not only found at the surface of the polymer composite but are distributed throughout the thin film.

The previous chapter studied diffusion of ferric ions in both solution and the polymer composite and explained how ferric ion and MOF crystal characteristics affect ferric ion diffusion. The ferric ion association to MOF crystals and the diffusion of ferric ions in solution are both fast, but the diffusion of ferric ions in the polymer is slower. This chapter assumes that ferric ion diffusion in solution is fast enough that the solution part of the system can be ignored, since the main focus is the effect of MOF sinks on ferric ion diffusion through the polymer composite. Therefore, the polymer composite is the media of interest here. As such, the diffusive time-scale τ_D here is

the time-scale for diffusion in the polymer and not for diffusion in the solution as stated in the previous chapter. In addition, MOF crystals are assumed to be uniformly distributed throughout the MOF-polymer composite and not only on the surface of the polymer composite.

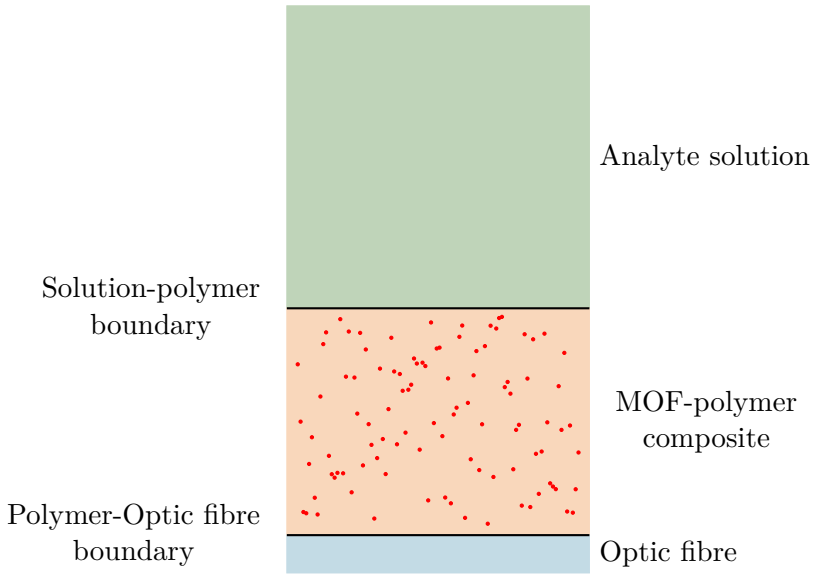


Figure 8.1: Small section of two-dimensional cross-section of optic fibre. Green represents solution being analysed. Red dots represent randomly distributed MOF crystals in orange polymer composite. Blue represents optic fibre core.

These assumptions simplify the mixed media, two-dimensional system into a single medium, one-dimensional system, Figure 8.2. The system now models ferric ions diffusing into the MOF-polymer composite with a ferric ion source at the solution-polymer boundary, $X = 0$, where $X \geq 0$ is the distance into the polymer composite measured from the solution-polymer boundary. The polymer-optic fibre boundary is assumed to be in the far (right) field.

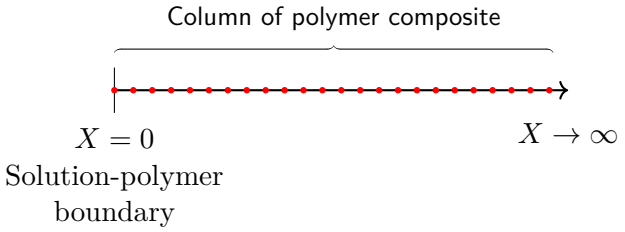


Figure 8.2: One-dimensional representation of ferric ions diffusing through column of polymer composite with uniformly distributed MOF crystals represented by red dots.

To model the impact of multiple MOF crystals distributed throughout the polymer composite, note that after taking into account the flux through the polymer/solution boundary, the total number of ferric ions must be conserved. The total ferric ion concentration is the sum of the ferric

ions in a dissolved state in the polymer composite, $C(T, X)$, and the ferric ions associated with MOF crystals in the polymer composite, $B(T, X)$. This chapter maintains the assumption that the movement of dissolved ferric ions through the polymer composite is governed by Brownian motion. The diffusivity of the dissolved ferric ions through the polymer is assumed to be constant, D.

The new time derivative of the total ferric ion concentration must be balanced by the divergence of flux of the dissolved ferric ion concentration in the polymer (mobile component),

$$\frac{\partial}{\partial T}\left[C(T, X) + B(T, X)\right] = D\frac{\partial^2 C}{\partial X^2} \qquad \text{for } X \geq 0,$$

where T is the time since the sensor's exposure to the solution. In this way, both phases of the ferric ion concentration are accounted for and an inclusion of a sink or source term is not necessary. Note that the linear diffusion equation no longer applies to the dissolved ferric ion concentration on its own, as seen in Chapter 7.

Ferric ion diffusion is assumed to be fast in the solution, such that there is a constant bath reservoir at the solution-polymer boundary,

$$C(T, 0) = C_0,$$

where C_0 is the bulk ferric ion concentration in the solution. Note that this boundary condition implies that there is a constant fresh flow of analyte solution across the polymer boundary. The ferric ion concentration in the polymer in the far (right) field is zero. The far (right) field boundary condition is given by

$$C(T, X) \to 0 \qquad \text{as } X \to \infty.$$

The density of ferric ions associated with the MOF crystals is governed by the pseudo ODE,

$$\frac{\partial B}{\partial T} = k_{\text{on}} C\left(B_0 - B\right) - k_{\text{off}} B \qquad \text{for } X \geq 0,$$

where k_{on} is the association rate compared to the ferric ion concentration, k_{off} is the ferric ion dissociation rate, $B_0 = m_s\,\rho$ is the total maximum ferric ion association with the MOF crystals in the polymer. Here, m_s is the maximum mass of ferric ions that can associate with a single MOF crystal and ρ is the linear MOF density in the polymer composite where the MOF crystals are evenly distributed.

Note that there is a subtle change in the definition of $B(T, X)$ which changes its units of measure.

Here, $B(T, X)$ is measured in terms of the associated ferric ion density and not the length/area of the MOF crystal, that is, $B(T, X)$ has units moles per metre (and not metre cubed since this is a one-dimensional system).

The assumed initial conditions are

$$\begin{aligned} C(0, X) &= 0 \qquad \text{for } X \geq 0, \\ B(0, X) &= 0 \qquad \text{for } X \geq 0. \end{aligned}$$

8.1.1. Nondimensional model

Distance is nondimensionalised with the reciprocal of the MOF density, $1/\rho$, the ferric ion concentration with the total maximum ferric ion association with the MOF crystals B_0, and time with the diffusive time-scale $\tau_D = 1/\rho^2 D$. The system of equations can be written as

$$\frac{\partial}{\partial t}\left[c + b\right] = \frac{\partial^2 c}{\partial x^2} \qquad \text{for } x \geq 0, \tag{8.1}$$

$$\frac{\partial b}{\partial t} = s_2[c\,(1 - b) - s_3 b] \qquad \text{for } x \geq 0, \tag{8.2}$$

where $s_2 = B_0 k_{\text{on}}/D\rho^2\,(= m_s k_{\text{on}}/D\rho)$ and $s_3 = k_{\text{off}}/k_{\text{on}}B_0\,(= k_{\text{off}}/k_{\text{on}} m_s \rho)$ are nondimensional constants.

The bath reservoir condition at the solution-polymer boundary becomes

$$c(t, 0) = \frac{C_0}{B_0}, \tag{8.3}$$

while the far (right) boundary condition becomes

$$c(t, x) \to 0 \qquad \text{as } x \to \infty. \tag{8.4}$$

The initial conditions become

$$\begin{aligned} c(0, x) &= 0 \qquad \text{for } x \geq 0, \\ b(0, x) &= 0 \qquad \text{for } x \geq 0. \end{aligned} \tag{8.5}$$

8.2. SOLUTION FOR FERRIC ION CONCENTRATION

There are two ways to incorporate sinks into the diffusion equation, either at the boundary condition or to include the sink in the governing equation. In the previous chapter, the system was modelled as the former. The assumption here that $\tau_D \gg \tau_A$ allows for latter. In doing so, the ferric ion concentration $c(t, x)$ can be solved for.

The assumption that $\tau_D \gg \tau_A$ implies that the MOF crystals reach steady state much sooner than steady state for dissolved ferric ions. Therefore, Equation (8.2) reaches steady state quickly

$$\frac{\partial b}{\partial t} = s_2 \left[c(1 - b) - s_3 b \right] = 0,$$

so that

$$b_{\text{eq}} = \frac{c}{c + s_3} = 1 - \frac{s_3}{c + s_3}, \tag{8.6}$$

where $b_{\text{eq}}(t, x)$ is the equilibrium density of ferric ions associated to a MOF crystal at large times. Note the similarity between Equations (7.15) and (8.6).

Therefore, at large times $b_{\text{eq}}(t, x)$ can be expressed as a function of $c(t, x)$ and can be substituted into Equation (8.1) that maintains the conservation of total ferric ion density in the polymer composite, such that

$$\frac{\partial}{\partial t} \left[c + 1 - \frac{s_3}{c + s_3} \right] = \frac{\partial}{\partial t} \left[c - \frac{s_3}{c + s_3} \right] = \frac{\partial}{\partial x} \left[\frac{\partial c}{\partial x} \right], \tag{8.7}$$

where the sum of $c(t, x)$ and $b_{\text{eq}}(t, x)$ is the total ferric ion density in the system (both dissolved and associated). As a consequence, the governing equation for the total ferric ion diffusion in the polymer is expressed so that it incorporates the effect of the MOF crystals acting as ferric ion sinks.

To solve for the modified total ferric ion density using Equation (8.7) algebraically, let $u = c - \frac{s_3}{c+s_3}$. The concentration, $c(t, x)$, can be expressed in terms of $u(t, x)$,

$$c = \frac{1}{2} \left\{ (u - s_3) + \left[(u + s_3)^2 + 4 s_3 \right]^{1/2} \right\}, \tag{8.8}$$

where the positive root is taken because ferric ion concentration in the polymer is always non-

negative. Then

$$\frac{\partial c}{\partial x} = \frac{1}{2}\left\{1 + \left[1 - \frac{4s_3}{4s_3 + (u+s_3)^2}\right]^{1/2}\right\}\frac{\partial u}{\partial x}, \tag{8.9}$$

The nonlinear modified diffusion coefficient $D(u)$ is defined as

$$D(u) = \frac{1}{2}\left\{1 + \left[1 - \frac{4s_3}{4s_3 + (u+s_3)^2}\right]^{1/2}\right\}. \tag{8.10}$$

Due to the non-linearity of the modified diffusion coefficient, it is important to understand its nature, particularly its boundedness. The upper bound is

$$D(u) \to 1 \text{ as } u \to \infty,$$

and the lower bound is

$$\begin{aligned} D(u) &\to \frac{1}{2}\left\{1 + \frac{s_3}{(4s_3 + s_3^2)^{1/2}}\right\} \text{ as } u \to 0, \\ &\to \frac{1}{2}\left\{1 + \frac{1}{(4/s_3 + 1)^{1/2}}\right\} \text{ as } u \to 0, \end{aligned}$$

which lies between $\frac{1}{2}$ and 1. Therefore $D(u)$ is bounded and $D(u) \in (\frac{1}{2}, 1)$.

Alternatively, to prove the boundedness of $D(u)$, Equation (8.9) and the Taylor series expansion can be used as follows. If $(u+s_3)^2/4s_3$ is small compared to 1, then using the Taylor series expansion,

$$\begin{aligned} \frac{\partial c}{\partial x} &= \frac{1}{2}\left\{1 + \left[1 - \frac{1}{1 + (u+s_3)^2/4s_3}\right]^{1/2}\right\}\frac{\partial u}{\partial x}, \\ &\approx \frac{1}{2}\left\{1 + \left[1 - 1 + \frac{(u+s_3)^2}{4s_3}\right]^{1/2}\right\}\frac{\partial u}{\partial x}, \\ &= \frac{1}{2}\left\{1 + \frac{(u+s_3)}{2\sqrt{s_3}}\right\}\frac{\partial u}{\partial x}, \\ &\approx \frac{1}{2}\frac{\partial u}{\partial x}. \end{aligned}$$

On the other hand, if $4s_3/(u+s_3)^2$ is small compared to 1, then using the Taylor series expansion,

$$\begin{aligned}
\frac{\partial c}{\partial x} &= \frac{1}{2}\left\{1+\left[1-\frac{4s_3}{(u+s_3)^2}\cdot\frac{1}{1+4s_3/(u+s_3)^2}\right]^{1/2}\right\}\frac{\partial u}{\partial x},\\
&\approx \frac{1}{2}\left\{1+\left[1-\frac{4s_3}{(u+s_3)^2}+\frac{(4s_3)^2}{(u+s_3)^4}\right]^{1/2}\right\}\frac{\partial u}{\partial x},\\
&\approx \frac{1}{2}\left\{1+\left[\left(1-\frac{4s_3}{(u+s_3)^2}\right)^2\right]^{1/2}\right\}\frac{\partial u}{\partial x},\\
&= \frac{1}{2}\left\{2-\frac{4s_3}{(u+s_3)^2}\right\}\frac{\partial u}{\partial x},\\
&\approx \frac{\partial u}{\partial x}.
\end{aligned}$$

Again, $D(u)$ is bounded, and $D(u) \in (\frac{1}{2}, 1)$.

As a consequence, the problem can be approximated with a linear diffusion equation for $u(t,x)$,

$$\frac{\partial u}{\partial t} = \mathcal{D}\frac{\partial^2 u}{\partial x^2},$$

where $\mathcal{D}$ is assumed to be constant and $\mathcal{D} \in (\frac{1}{2}, 1)$

The bath reservoir at the solution-polymer boundary is

$$u(t,0) = \frac{C_0}{B_0} - \frac{s_3}{\frac{C_0}{B_0}+s_3}.$$

The far (right) boundary is

$$u(t,x) \to -1 \qquad \text{as } x \to \infty,$$

while the initial condition is

$$u(0,x) = -1, \qquad x \geq 0.$$

A solution to the linear diffusion equation can be written in terms of the error function, and using the initial and boundary conditions given above leads to the solution

$$u(t,x) = -(1+\alpha)\,\mathrm{erf}\left[\frac{x}{2\sqrt{\mathcal{D}\,t}}\right] + \alpha,$$

where

$$\alpha = \frac{C_0}{B_0} - \frac{s_3}{\frac{C_0}{B_0} + s_3}.$$

Consequently, the concentration is given by

$$c = \frac{1}{2}\left\{(u - s_3) + \left[(u + s_3)^2 + 4s_3\right]^{1/2}\right\}, \tag{8.11}$$

where the initial and boundary conditions for $c(t, x)$ are satisfied.

8.3. VARIATION OF NONDIMENSIONAL PARAMETERS

This section explores the effects of varying the nondimensional parameters ($\mathcal{D}$, s_3, C_0/B_0) on ferric ion diffusion through the polymer composite.

Note that the effective diffusion parameter, s_3, explicitly appears in the final algebraic expression for the ferric ion concentration, however the other nondimensional parameters from Chapter 7 (s_1, s_2, s_4) do not. Since the (polymer) diffusive time-scale is chosen, s_1 is unity, and it has been assumed that MOF crystals reach steady state quickly, the effective association parameter s_2 and the effective flux parameter s_4 no longer effect the ferric ion concentration. Consequently, they do not appear in the solution (8.11).

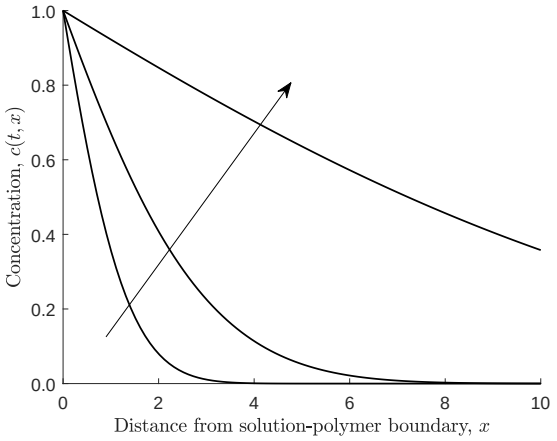


Figure 8.3: Nondimensional concentration of ferric ions in solution, $c(t, x)$, Equation (8.11). Arrow indicates increasing time, $t = 1, 5, 100$. Here $\mathcal{D} = 0.75, s_3 = 1$ and $C_0/B_0 = 1$.

Figure 8.3 shows the ferric ion concentration profile in the polymer composite at various times, where the effective dissociation parameter and the effective bath reservoir are unity ($s_3 = C_0/B_0 = 1$) and the modified diffusion coefficient is the mean of its bounded domain ($\mathcal{D} = 0.75$). The ferric

ion concentration profiles are comparable to the expected solutions to the normal linear diffusion equation, with the concentration decreasing with distance from the solution-polymer boundary and increasing everywhere with time. Near the end of Subsection 8.3.2, there is a discussion regarding how this solution differs to a solution to the linear diffusion equation.

8.3.1. Varying the modified diffusion coefficient, $\mathcal{D}$

The modified diffusion coefficient ($\mathcal{D} \in (\frac{1}{2}, 1)$) captures the effect the MOF sinks have on the dissolved ferric ion concentration in the polymer composite. Figure 8.4(a) shows that increasing the modified diffusion coefficient results in an increase in ferric ion concentration at a given timestamp and Figure 8.4(b) shows the regions for predicted ferric ion concentration given the domain of $\mathcal{D}$ at various times.

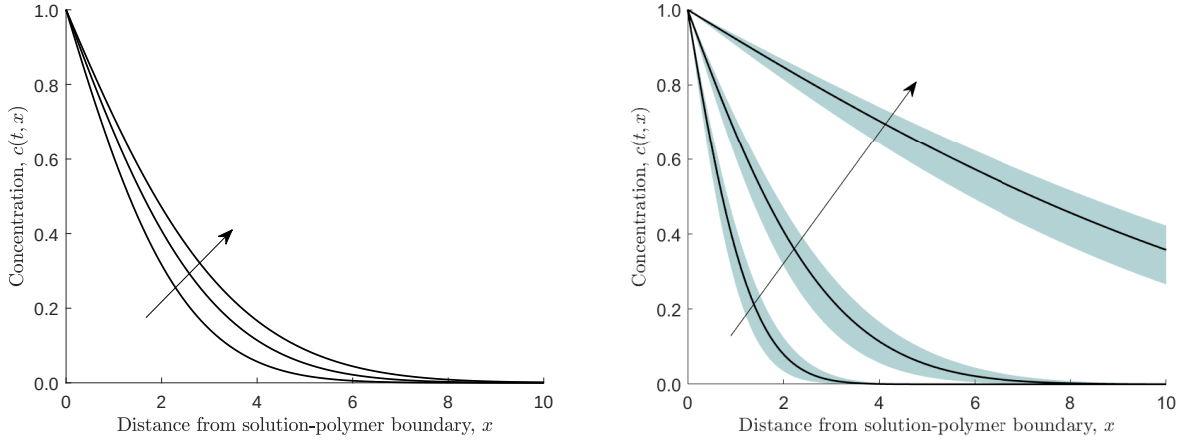


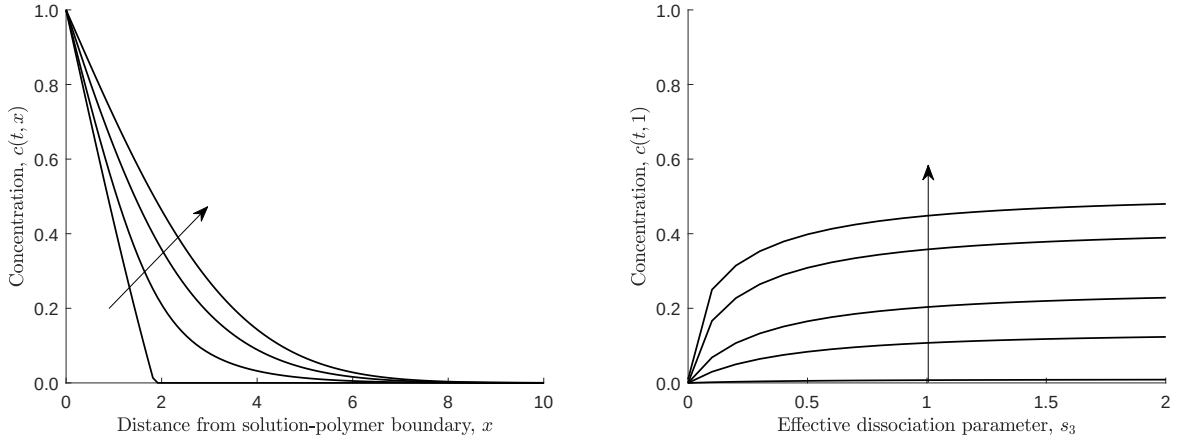
Figure 8.4: Nondimensional concentration of ferric ions in solution, $c(t, x)$, Equation (8.11). (a) Arrow indicates increasing $\mathcal{D}$, $\mathcal{D} = 0.5, 0.75, 1$. Here $t = 5, s_3 = 1$ and $C_0/B_0 = 1$. (b) Arrow indicates increasing t, $t = 1, 5, 100$. Turquoise regions for bounded values of modified diffusion coefficient, $\mathcal{D}$.

In this case where $\mathcal{D} = 1$, the sensor would require less time for it to be completely saturated for an accurate reading. If $\mathcal{D}$ is less than unity, this means that the MOF crystals slow the dissolved ferric ion diffusion through the polymer composite, so that the sensor would need to be exposed to a solution for a longer period of time.

8.3.2. Varying the effective dissociation parameter, s_3

Recall, that the effective dissociation parameter ($s_3 = k_{\text{off}}/k_{\text{on}}B_0$) describes the effect of ferric ion dissociation from MOF crystals. Increasing the dissociation parameter means that ferric ions

are more likely to dissociate from the MOF crystals. Figure 8.5(a) clearly shows this relationship between the ferric ions and the dissociation parameter, and confirms the alignment between the mathematics and intuitive reasoning. Increasing the value of the dissociative parameter leads to an increase in ferric ion concentration, since more ions are diffusing through the polymer from the bath reservoir and the already associated ferric ions are released back into the polymer.



(a) (b)

Figure 8.5: Nondimensional concentration of ferric ions in solution, $c(t,x)$, Equation (8.11). (a) Arrow indicates increasing s_3, $s_3 = 0, 0.1, 0.5, 10$. Here $t = 5, \mathcal{D} = 0.75$ and $C_0/B_0 = 1$. (b) Effective dissociation parameter s_3 along x-axis. Arrow indicates increasing time t, $t = 0.1, 0.3, 0.5, 1, 1.5$. Here $x = 1, \mathcal{D} = 0.75$ and $C_0/B_0 = 1$.

A less apparent property of the effective dissociative parameter that was not evident from the Chapter 7 investigation, is that further increases in s_3 beyond approximately $s_3 = 2$ have a diminishing accumulative effect on ferric ion concentration. Figure 8.5(b) shows that the ferric ion concentration has the greatest sensitivity when $s_3 \leq 1$. This means that for large values of the effective dissociation parameter there is likely to be a diminishing sensitivity for ferric ion concentration.

If $s_3 \to \infty$, then

$$u(t,x) \to -\frac{C_0}{B_0}\,\mathrm{erf}\left[\frac{x}{2\sqrt{\mathcal{D}\,t}}\right] + \frac{C_0}{B_0} - 1,$$

and from the definition of u, $c(t,x) \to u(t,x) + 1$ as $s_3 \to \infty$. If $\mathcal{D} = 1$, then the solution for $c(t,x)$ as $s_3 \to \infty$ is a solution to the linear diffusion equation for $c(t,x)$ (Equations (8.1) and (8.3)-(8.5)). This general solution describes the ferric ion concentration as if it were unaffected by the MOF crystal sinks; this will be referred to as the undisrupted ferric ion concentration.

The turquoise regions in Figure 8.6 indicates how sensitive the ferric ion concentration is to the effective dissociative parameter. The shaded regions are larger than the regions covered by the modified

diffusion coefficient in Figure 8.4, indicating the ferric ion concentration has a greater sensitivity to the effective dissociative parameter than the modified diffusion coefficient. The light turquoise regions showing the range where $s_3 \in [0, 1]$ are larger than the dark regions where $s_3 \in [1, \infty)$, reinforcing the notion that small values of s_3 have the greatest impact on ferric ion concentration profiles. Although not shown here, as $\mathcal{D} \to 1$, the difference between the dark turquoise region and the undisrupted ferric ion concentration diminishes.

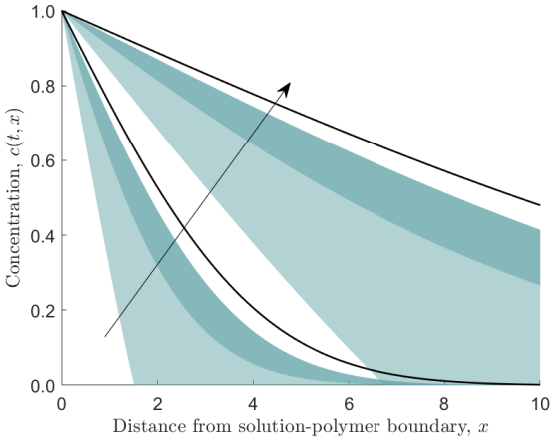


Figure 8.6: Nondimensional concentration of ferric ions in solution, $c(t, x)$, Equation (8.11). Arrow indicates increasing t, $t = 5, 100$. Here $C_0/B_0 = 1$. Light turquoise regions for bounded values of effective dissociation parameter, $s_3 \in [0, 1]$ and $\mathcal{D} = 0.75$. Dark turquoise regions where $s_3 \in [1, \infty)$ and $\mathcal{D} = 0.75$. Black lines where $s_3 \to \infty$ and $\mathcal{D} = 1$.

8.3.3. Varying the effective bath reservoir, C_0/B_0

The effective bath reservoir (C_0/B_0 where $B_0 = m_s\rho$) is the ratio of bulk ferric ion concentration to the total maximum number of ferric ions that can associate to the MOF crystals in the polymer composite. Increasing the effective bath reservoir means that either the bulk concentration of ferric ions is increasing or the MOF density in the polymer composite is decreasing. Figure 8.7 shows that an increase in the effective bath reservoir results in an increase in ferric ion concentration in the polymer composite. The ferric ion concentration profile approximately scales linearly with the effective bath reservoir.

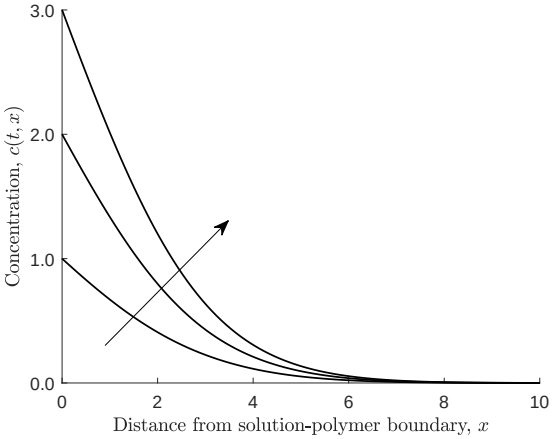


Figure 8.7: Nondimensional concentration of ferric ions in solution, $c(t, x)$, Equation (8.11). Arrow indicates increasing C_0/B_0, $C_0/B_0 = 1, 2, 3$. Here $t = 5, \mathcal{D} = 0.75$ and $s_3 = 1$.

8.3.4. Varying MOF density, ρ

Since the effective bath reservoir (C_0/B_0) and the effective dissociation parameter ($s_3 = k_{\text{off}}/k_{\text{on}}B_0$) both implicitly contain the MOF density ($B_0 = m_s\rho$), studying the effects of these parameters separately does not give the complete insight as to how MOF density impacts the ferric ion diffusion in the polymer composite.

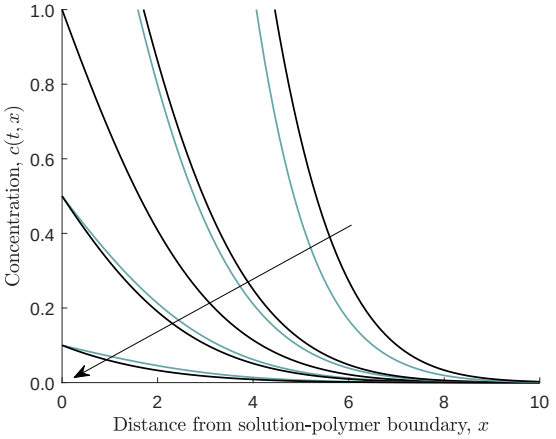


Figure 8.8: Nondimensional concentration of ferric ions in solution, $c(t, x)$, Equation (8.11). Arrow indicates increasing ρ. Here $t = 5$ and $\mathcal{D} = 0.75$. Black lines represent dual effect on effective dissociation parameter and bath reservoir, s.t. $s_3 = C_0/B_0 = 0.1, 0.5, 1, 2, 10$. Turquoise lines represent change in only effective bath reservoir, s.t. $s_3 = 1$ and $C_0/B_0 = 0.1, 0.5, 1, 2, 10$.

The black lines in Figure 8.8 shows that increasing MOF density in the polymer composite (i.e. decreasing both s_3 and C_0/B_0) results in a decrease in ferric ion concentration (as indicated by the arrow). When $s_3, C_0/B_0$ are large, the polymer composite has a low MOF crystal density allowing

for ferric ions to diffuse faster through the polymer composite. That is, there are fewer sinks to dampen diffusion. Increasing C_0/B_0 only and keeping s_3 constant ($s_3 = 1$) underestimates the ferric ion concentration as indicated by the turquoise lines. This is because increasing C_0/B_0 only, ignores the impact of accounting for the increase in dissociation of ferric ions s_3 due to the increase of MOF crystal density.

8.4. DISCUSSION

This chapter re-examines ferric ion diffusion and the impact of uniformly distributed MOF crystal sinks throughout the polymer composite. The previous chapter highlighted that there are two time-scales. An important assumption made in this chapter is that the MOF crystals becomes saturated with ferric ions very quickly. In other words, the association time-scale is much shorter than the diffusive time-scale $\tau_D \gg \tau_A$, or the steady state for association occurs more rapidly than the polymer composite becomes fully saturated with ferric ions. Even though this assumption does not allow us to find an analytical solution for the concentration of ferric ions associated with the MOF crystal ($B(T, X)$), it provides the necessary logic to find an analytical solution for the ferric ion concentration in the polymer composite modified by uniformly distributed MOF sinks in the polymer composite.

Solving for the ferric ion concentration gave rise to a new nondimensional parameter, the modified diffusion coefficient within the MOF-polymer composite, where $\mathcal{D} \in (\frac{1}{2}, 1)$. The greater the disruption the MOF sinks cause to ferric ion concentration, the smaller the modified diffusion coefficient is. A larger modified diffusion coefficient will cause the ferric ion steady state to be reached sooner.

Since the modelling in this chapter takes into consideration the MOF density ρ, the nondimensionalised system incorporates MOF density in the nondimensional parameters. This dimensional parameter modifies two nondimensional parameters: the effective dissociation parameter $s_3 = k_{\text{off}}/k_{\text{on}}B_0$ (first described in Chapter 7) and the effective bath reservoir C_0/B_0, where $B_0 = m_s\,\rho$.

Increasing MOF crystal density (i.e. increasing both s_3 and C_0/B_0) leads to an increase in ferric ion concentration within the polymer. Simultaneously increasing (or decreasing) these parameters by the same factor gives insight into how MOF density ρ affects ferric ion concentration. When s_3 and C_0/B_0 are large, it means that there is a low MOF density in the polymer composite, and the ferric ion concentration profile reaches steady state sooner. When s_3 and C_0/B_0 are small, there

is a high MOF density. This would require the sensor to be exposed to an analyte solution for a longer period of time for an accurate reading. Alternatively, varying the MOF crystal surface area that ferric ions can associate with, m_s, gives a similar result.

CHAPTER 9

CONCLUDING REMARKS FOR PART II

Part II aims to understand diffusion through the different components of a ferric ion sensor. In particular, the modelling contained in Part II develops an understanding of ferric ion diffusion through solution and into the polymer composite, and an understanding of how ferric ion association with MOF crystals affects ferric ion diffusion. Two cases are studied: a single MOF crystal at the solution-polymer boundary (Chapter 7) and uniformly distributed MOF crystals throughout the polymer composite (Chapter 8). The first case uses numerical methods to gain an understanding of what physical properties affect ferric ion concentration and MOF occupancy in both one- and two-dimensional scenarios. The second case uses a coupled system of equations to incorporate the effect of MOF crystal sinks to gain an understanding of how physical properties can hinder ferric ion diffusion, in particular the implicit effect of MOF density in the polymer composite. The main findings are summarised and discussed below, followed by a section discussing experimental considerations.

9.1. SUMMARY

Part I establishes that ferric ions are too large to diffuse into the MOF pore, therefore they only associate to the surface of the MOF crystal. Chapter 7 models a single MOF crystal at the solution-polymer boundary and shows that there are two nondimensional quantities relating to the MOF crystals that primarily determine system behaviour: the effective association parameter, s_2, and the effective dissociation parameter, s_3. The greater the affinity ferric ions have to associate with a MOF crystal, the sooner the MOF crystal reaches equilibrium steady state. This means a larger effective association parameter, s_2, is most desirable. In physical terms, this corresponds to a larger association rate, k_{on}. Alternatively, a greater effective dissociation parameter, s_3, also corresponds to a decrease in the time for a MOF crystal to reach steady state. In physical terms, this corresponds to a larger dissociation rate, k_{off}, or a smaller association rate, k_{on}. These MOF characteristics also impact how much time is needed for the ferric ion concentration in the polymer composite to reach steady state, that is the MOF characteristics affect ferric ion concentration in the polymer as well as MOF occupancy. Larger effective association and dissociation parameters result in the ferric ion concentration reaching steady state sooner, and therefore the sensor requires less exposure time.

Interestingly, if the association rate, the dissociation rate, the number of available MOF pores and

the equilibrium number of occupied MOF pores (post sensor exposure) are known, then Equation (7.16) can be used as a proxy to predict the ferric ion concentration in solution.

There are also two nondimensional quantities related to the ferric ions and the mixed media (solution and polymer composite): the nondimensional diffusion coefficient, s_1, and the effective flux parameter, s_4. For larger values of s_1 (i.e. larger diffusivity in solution), the ferric ion concentration reaches equilibrium in solution sooner, allowing for the ferric ion steady state in the polymer to be reached sooner. In physical terms, this means that ferric ions should have a large diffusivity in solution. If the effective flux parameter is small, then ferric ion concentration reaches steady state sooner. In physical terms, this corresponds to a smaller number of available MOF pores for ferric ions to associate with.

When considering ferric ion diffusion in mixed media (with a relative diffusion coefficient, $D = D_2/D_1$), the most favourable scenario in the case where MOF crystals are located only on the surface of the polymer is for there to be a large difference between ferric ion diffusion in the solution versus the polymer (that is, diffusivity in the polymer composite should be comparatively smaller than in solution). This allows for more time for the MOF crystals on the polymer surface to reach their steady state. However, this is not practical as MOF crystals are actually distributed throughout the polymer composite and not only on the surface. If ferric ion diffusion in the polymer is high, the time taken to reach steady state in the polymer is reduced.

Since MOF crystals act as ferric ion sinks, increasing MOF density in the polymer composite or increasing MOF surface area increases the time for the dissolved ferric ion concentration to reach steady state.

While some physical parameters of the system cannot be practically changed, the aim of the sensor is to have enough MOF crystals to have an accurate reading so that any other parameters that can be physically changed can be manipulated in such a way as to improve sensor performance. As it is often the case, a delicate balance is required.

9.2. EXPERIMENTAL CONSIDERATION

Knowledge of how the different physical properties affect ferric ion concentration and MOF occupancy can be used to predict optimal time frames for a ferric ion sensor to be exposed to an analyte solution. The aim is not necessarily to shorten the time taken to reach steady state, but to understand the optimal length of exposure so that the sensor achieves an accurate reading. On the

other hand, if the aim of an experimentalist is to reduce time to steady state, then the information provided here gives an indication of which parameters might be manipulated to best achieve this goal.

The relative ferric ion diffusion coefficient between the solution and the polymer can be manipulated to some degree by altering the synthesis process. The above investigation suggests that a larger relative diffusion coefficient, $D = D_2/D_1$, is beneficial for crystals on the surface of the polymer composite. In order for the relative diffusion coefficient to be large, the polymer composite must be denser to inhibit diffusion and/or the polymer composite should be hydrophilic. In the proposed sensor design, the MOF crystals are actually distributed throughout the polymer composite not only on the polymer surface, so that hindering diffusion to those crystals not located on the surface will hamper florescence sensing. In order for ferric ions to associate to MOF crystals inside the polymer composite, the polymer should be designed so that the relative diffusion coefficient is close to unity. This would ensure that the ferric ions associate with MOF crystals close to the optic fibre, so that when light is pulsed through the fibre, the florescence reading is a truer reflection of the ferric ion concentration in the analyte solution.

It may be counter-intuitive that an increase in MOF density in the polymer composite requires that the sensor is exposed a longer time to give an accurate reading. For solutions that have a high concentration of ferric ions, it is likely to be favourable that the sensor has a lower MOF-polymer composite density. Alternatively, for solutions that have a low concentration of ferric ions, a higher MOF-polymer composite density ratio is likely to be useful.

Part III

Mathematical Exploration

Part III is a mathematical investigation of the governing equations established in Part II to describe the interactions between ferric ion diffusion and MOF occupancy. This part is solely mathematically focussed and explores various methods to establish solution(s) for a PDE and a system of PDEs.

First, an alternative method can be applied to solve the newly established conservation of ferric ion density PDE (Equation (8.7)), which makes use of perturbation methods, and the Laplace and Fourier transforms. The newly established PDE is a result of the manipulation in Chapter 8 to explicitly capture the effects of the MOF sinks on ferric ion concentration instead of MOF sinks at the boundary.

Second, Lie point symmetries are used to establish exact solutions for a system of equations with one PDE and one pseudo ODE.

The original work contained in Part III is the mathematical contributions. The solution using the perturbation method highlights the distinctive effect of ferric ion dissociation from MOF crystals on ferric ion diffusion. The solutions are written in terms of the integral

$$\int \frac{\exp\left(a\,(x-b)^2\right)}{\operatorname{erf}(c\,x)}\,\mathrm{d}x$$

where a, b and c are constants, and which could not be evaluated analytically.

The Lie point symmetries for the PDE (Chapter 8) and the system of PDEs (from Chapter 7) are also found and some reduced equations are provided.

CHAPTER 10

PERTURBATION METHODS FOR SOLVING A MODIFIED DIFFUSION EQUATION

In Chapter 8 the assumption that MOF occupancy reaches steady state much sooner than ferric ion concentration through the polymer composite ($\tau_D \gg \tau_A$), allowed for a system of PDEs to be expressed as a single PDE (Equation (8.7)). This chapter provides an alternative method to solve the PDE as given by the nondimensional model in Subsection 8.1.1, for the governing equation (8.7) with boundary conditions (8.3) and (8.4), and initial condition (8.5).

Assume the relative dissociation parameter is small, such that $\epsilon = s_3$. Then Equation (8.7) becomes

$$\frac{\partial}{\partial t}\left[c - \frac{\epsilon}{c+\epsilon}\right] = \frac{\partial^2 c}{\partial x^2}.$$

Evaluating the derivative with respect to nondimensional time t and multiplying by $(c+\epsilon)^2$ gives

$$\left[c^2 + 2\epsilon c + \epsilon^2 + \epsilon\right]\frac{\partial c}{\partial t} = \left[c^2 + 2\epsilon c + \epsilon^2\right]\frac{\partial^2 c}{\partial x^2}. \tag{10.1}$$

After applying a perturbation expansion to Equation (10.1) by letting $c(t,x) = c_0(t,x) + \epsilon c_1(t,x) + O(\epsilon^2)$, the left-hand side of Equation (10.1) becomes

$$\begin{aligned}\left[c^2 + 2\epsilon c + \epsilon^2 + \epsilon\right]\frac{\partial c}{\partial t} &= \left[c_0^2 + 2\epsilon c_0 c_1 + 2\epsilon c_0 + \epsilon\right]\frac{\partial}{\partial t}(c_0 + \epsilon c_1) + O(\epsilon^2),\\ &= \left[c_0^2 + 2\epsilon c_0 c_1 + 2\epsilon c_0 + \epsilon\right]\frac{\partial}{\partial t}c_0 + \epsilon c_0^2\frac{\partial}{\partial t}c_1 + O(\epsilon^2),\end{aligned}$$

and the right-hand side becomes

$$\begin{aligned}\left[c^2 + 2\epsilon c + \epsilon^2\right]\frac{\partial^2 c}{\partial x^2} &= \left[c_0^2 + 2\epsilon c_0 c_1 + 2\epsilon c_0\right]\frac{\partial^2}{\partial x^2}(c_0 + \epsilon c_1) + O(\epsilon^2),\\ &= \left[c_0^2 + 2\epsilon c_0 c_1 + 2\epsilon c_0\right]\frac{\partial^2 c_0}{\partial x^2} + \epsilon c_0^2\frac{\partial^2 c_1}{\partial x^2} + O(\epsilon^2).\end{aligned}$$

Grouping terms of the order of 1 ($O(1)$) gives

$$\frac{\partial c_0}{\partial t} = \frac{\partial^2 c_0}{\partial x^2}.$$

Grouping terms of the order of ϵ ($O(\epsilon)$) gives

$$\begin{aligned}
[2c_0c_1 + 2c_0 + 1]\frac{\partial c_0}{\partial t} + c_0^2\frac{\partial c_1}{\partial t} &= [2c_0c_1 + 2c_0]\frac{\partial^2 c_0}{\partial x^2} + c_0^2\frac{\partial^2 c_1}{\partial x^2}, \\
\frac{\partial c_0}{\partial t} + c_0^2\frac{\partial c_1}{\partial t} &= c_0^2\frac{\partial^2 c_1}{\partial x^2}, \\
\frac{1}{c_0^2}\frac{\partial c_0}{\partial t} + \frac{\partial c_1}{\partial t} &= \frac{\partial^2 c_1}{\partial x^2}, \\
\frac{\partial c_1}{\partial t} &= \frac{\partial^2 c_1}{\partial x^2} + \frac{\partial}{\partial t}\frac{1}{c_0}.
\end{aligned}$$

The following sections solve for the unperturbed ferric ion concentration $c_0(t, x)$ and the perturbed ferric ion concentration $c_1(t, x)$.

10.1. UNPERTURBED FERRIC ION CONCENTRATION

The governing equation for the diffusion of the unperturbed ferric ion concentration is,

$$\frac{\partial c_0}{\partial t} = \frac{\partial^2 c_0}{\partial x^2}, \qquad x \geq 0. \tag{10.2}$$

The bath reservoir at the solution-polymer boundary gives the condition

$$c_0(t, 0) = \frac{C_0}{B_0},$$

while conditions far away from the solution-polymer boundary and into the polymer composite motivates the far (right) condition,

$$c_0(t, x) \to 0, \qquad \text{as } x \to \infty.$$

The initial condition is

$$c_0(0, x) = 0, \qquad x \geq 0.$$

A solution to the unperturbed ferric ion concentration in the polymer composite can be expressed as the error function, and solving for the diffusion equation given the above initial and boundary

conditions gives

$$c_0(t,x) = -\frac{C_0}{B_0}\,\mathrm{erf}\left(\frac{x}{2\sqrt{t}}\right) + \frac{C_0}{B_0}. \tag{10.3}$$

10.2. PERTURBED FERRIC ION CONCENTRATION

The governing equation for the diffusion of the perturbed ferric ion concentration is,

$$\frac{\partial c_1}{\partial t} = \frac{\partial^2 c_1}{\partial x^2} + \frac{\partial}{\partial t}\frac{1}{c_0}, \qquad x \geq 0. \tag{10.4}$$

The bath reservoir at the solution-polymer boundary is

$$c_1(t,0) = 0.$$

The far (right) boundary condition is

$$c_1(t,x) \to 0, \qquad \text{as } x \to \infty.$$

The initial condition becomes

$$c_1(0,x) = 0, \qquad x \geq 0.$$

Since the final term of Equation (10.4) is a first order derivative with respect to nondimensional time, Laplace and Fourier transformations can be used to solve the PDE. First, apply the Laplace transform with respect to t to the terms in Equation (10.4),

$$\mathcal{L}_t\left\{\frac{\partial}{\partial t}c_1(t,x)\right\} = s\,\bar{c_1}(s,x) - c_1(0,x) = s\,\bar{c_1}(s,x),$$
$$\mathcal{L}_t\left\{\frac{\partial^2}{\partial x^2}c_1(t,x)\right\} = \frac{\partial^2}{\partial x^2}\bar{c_1}(s,x),$$

where the bar notation denotes that the Laplace transform is applied to a function.

Then Equation (10.4) becomes

$$s\,\bar{c_1} - \frac{\partial^2 \bar{c_1}}{\partial x^2} = \mathcal{L}_t\left\{\frac{\partial}{\partial t}\frac{1}{c_0(t,x)}\right\}. \tag{10.5}$$

Equation (10.5) can be solved as a pseudo ODE, such that the homogeneous component of the

solution is

$$\bar{c_1}(s,x) = \beta_1(s)\exp(\sqrt{s}x) + \beta_2(s)\exp(-\sqrt{s}x).$$

Using Maple, the general solution is

$$\begin{aligned}\bar{c_1}(s,x) = \beta_1(s)\exp(\sqrt{s}x) + \beta_2(s)\exp(-\sqrt{s}x) - \frac{1}{2\sqrt{s}}\exp(\sqrt{s}x)\int \exp(-\sqrt{s}x)\,\mathcal{L}_t\left\{\frac{\partial}{\partial t}\frac{1}{c_0}\right\}\mathrm{d}x \\ + \frac{1}{2\sqrt{s}}\exp(-\sqrt{s}x)\int \exp(\sqrt{s}x)\,\mathcal{L}_t\left\{\frac{\partial}{\partial t}\frac{1}{c_0}\right\}\mathrm{d}x, \qquad (10.6)\end{aligned}$$

where the $\beta_i(s)$ are functions of s that can be found using the initial and boundary conditions.

Evaluating the integrals in Equation (10.6) is especially difficult because it requires the Laplace transform of the reciprocal of the error function. If this does exist, then the solution to Equation (10.4) can be found by evaluating the integrals alone and taking the inverse Laplace transform with respect to s.

In an attempt to further evaluate Equation (10.5), the Fourier transform with respect to x is applied to the terms in Equation (10.5),

$$\begin{aligned}\mathcal{F}_x\{s\bar{c_1}(s,x)\} &= s\,\tilde{\bar{c_1}}(s,k), \\ \mathcal{F}_x\left\{\frac{\partial^2}{\partial x^2}\bar{c_1}(s,x)\right\} &= (i\,k)^2\tilde{\bar{c_1}}(s,k) = -k^2\tilde{\bar{c_1}}(s,k),\end{aligned}$$

where the tilde notation denotes that the Fourier transform is applied to a function.

Equation (10.5) becomes

$$s\,\tilde{\bar{c_1}} + k^2\tilde{\bar{c_1}} = \mathcal{F}_x\mathcal{L}_t\left\{\frac{\partial}{\partial t}\frac{1}{c_0}\right\},$$

where the resulting expression can be rearranged to solve for $\tilde{\bar{c_1}}(s,k)$,

$$\tilde{\bar{c_1}} = \frac{1}{s+k^2}\,\mathcal{F}_x\mathcal{L}_t\left\{\frac{\partial}{\partial t}\frac{1}{c_0}\right\}. \qquad (10.7)$$

Now, apply the the inverse Fourier and Laplace transforms to the left hand side of Equation (10.7),

$$\mathcal{L}_t^{-1}\mathcal{F}_x^{-1}\{\tilde{\bar{c_1}}(s,k)\} = c_1(t,x).$$

The right hand side of Equation (10.7) needs to be considered more carefully as it cannot be expanded further using partial fractions. To apply the inverse transformations, the convolution integral is used as follows.

In general, suppose the Laplace transforms for functions $f(t)$ and $g(t)$ are denoted by $F(s)$ and $G(s)$ respectively, such that

$$\mathcal{L}\{f * g\} = F(s)\,G(s) \quad \Longleftrightarrow \quad \mathcal{L}_t^{-1}\{F(s)\,G(s)\} = (f * g)(t),$$

where the convolution integral is defined as

$$\begin{aligned}(f * g)(t) &= \int_0^t f(t-\tau)\,g(\tau)\mathrm{d}\tau,\\ &= \int_0^t f(\tau)\,g(t-\tau)\mathrm{d}\tau,\\ &= (g * f)(t),\end{aligned}$$

and $f(t)$ and $g(t)$ are piecewise continuous functions on $[0,\infty)$.

Separating the factors of the right hand side of Equation (10.7), and applying the inverse Laplace transform to the individual factors gives

$$\begin{aligned}\mathcal{L}_t^{-1}\left\{\frac{1}{s+k^2}\right\} &= \exp(-k^2 t),\\ \mathcal{L}_t^{-1}\mathcal{F}_x\mathcal{L}_t\left\{\frac{\partial}{\partial t}\frac{1}{c_0(t,x)}\right\} &= \mathcal{L}_t^{-1}\mathcal{L}_t\mathcal{F}_x\left\{\frac{\partial}{\partial t}\frac{1}{c_0(t,x)}\right\} = \mathcal{F}_x\left\{\frac{\partial}{\partial t}\frac{1}{c_0(t,x)}\right\}.\end{aligned}$$

Therefore, applying the inverse Laplace transform to the right hand side of Equation (10.7) while using the convolution integral becomes

$$\mathcal{L}_t^{-1}\left\{\frac{1}{s+k^2}\,\mathcal{L}_t\mathcal{F}_x\left\{\frac{\partial}{\partial t}\frac{1}{c_0}\right\}\right\} = \int_0^t \exp(-k^2(t-\tau))\,\mathcal{F}_x\left\{\frac{\partial}{\partial \tau}\frac{1}{c_0(\tau,x)}\right\}\mathrm{d}\tau.$$

Note that this integral is difficult to evaluate because it requires the Fourier transform of the reciprocal of the error function (unknown).

Applying the inverse Fourier and Laplace transforms to Equation (10.7) gives,

$$\begin{aligned} c_1(t,x) &= \mathcal{F}_x^{-1}\left\{\int_0^t \exp(-k^2(t-\tau))\,\mathcal{F}_x\left\{\frac{\partial}{\partial\tau}\frac{1}{c_0(\tau,x)}\right\}\mathrm{d}\tau\right\}, \\ &= \int_0^t \mathcal{F}_x^{-1}\left\{\exp(-k^2(t-\tau))\,\mathcal{F}_x\left\{\frac{\partial}{\partial\tau}\frac{1}{c_0(\tau,x)}\right\}\right\}\mathrm{d}\tau, \end{aligned} \tag{10.8}$$

Similarly, in order to apply the inverse Fourier transform on last term of Equation (10.8) using the convolution integral, the inverse Fourier transform applied to the individual factors is evaluated, giving

$$\begin{aligned} \mathcal{F}_x^{-1}\left\{\exp(-k^2(t-\tau))\right\} &= \mathcal{F}_x^{-1}\left\{\exp(-k^2(t-\tau))\right\}, \\ &= \frac{2}{\sqrt{4\pi(t-\tau)}}\exp\left(-\frac{x^2}{4(t-\tau)}\right), \\ \mathcal{F}_x^{-1}\mathcal{F}_x\left\{\frac{\partial}{\partial\tau}\frac{1}{c_0(\tau,x)}\right\} &= \frac{\partial}{\partial\tau}\frac{1}{c_0(\tau,x)}, \end{aligned}$$

Finally, the perturbed ferric ion concentration in the polymer composite can be expressed as

$$c_1(t,x) = \int_0^t\int_{-\infty}^{\infty}\frac{1}{\sqrt{\pi}(t-\tau)^{1/2}}\exp\left(-\frac{(x-\xi)^2}{4(t-\tau)}\right)\left[\frac{\partial}{\partial\tau}\frac{1}{c_0(\tau,\xi)}\right]\mathrm{d}\xi\,\mathrm{d}\tau, \tag{10.9}$$

where $c_0(t,x)$ is given by Equation (10.3). It is difficult to evaluate Equation (10.9) analytically because the exponential function in the integrand is not the derivative form of the error function found in $c_0(\tau,\xi)$.

10.3. DISCUSSION

This chapter used an alternative method to solve the PDE (8.7) by using perturbation methods, where the dissolved ferric ion concentration is $c = c_0 + s_3\,c_1$. The unperturbed ferric ion concentration $c_0(t,x)$ is given by a solution to the linear diffusion equation (10.3). In contrast, the method to solve for the perturbed ferric ion concentration $c_1(t,x)$ is much more complicated, where perturbation is caused by the MOF crystals acting as ferric ion sinks. The perturbed ferric ion concentration could be calculated by numerically integrating Equation (10.9), however this is not done here.

CHAPTER 11

LIE GROUP METHODS FOR SOLVING MODEL EQUATIONS

This chapter uses Lie point symmetries to find exact solutions to the differential equations presented in Part II. The Lie symmetry method searches for transformations that leave the differential equations invariant, thereby giving information about new variables that can be used to either reduce the number of independent variables (in the case of PDEs) or reduce the order of the equations (in the case of ODEs). These reductions sometimes lead to simpler solvable differential equations, allowing a solution to the original differential equation to be found. This chapter follows the notation presented in Olver [34].

Consider a PDE with two independent variables, $u(t,x)$, that is

$$F(t,x,u,u_t,u_x,u_{tt},u_{xt},u_{xx})=0, \tag{11.1}$$

where the subscripts of u denote the partial derivatives of $u(t,x)$ with respect to the independent variables.

Classical Lie point symmetries find transformations that leave the governing equation (11.1) invariant under the transformation, so that

$$F(t,x,u,u_t,u_x,u_{tt},u_{xt},u_{xx})=F(\bar{t},\bar{x},\bar{u},\bar{u}_{\bar{t}},\bar{u}_{\bar{x}},\bar{u}_{\bar{t}\bar{t}},\bar{u}_{\bar{t}\bar{x}},\bar{u}_{\bar{x}\bar{x}})=0, \tag{11.2}$$

where

$$\bar{t}=t+\epsilon\xi^1(t,x,u)+O(\epsilon^2),\quad \bar{x}=x+\epsilon\xi^2(t,x,u)+O(\epsilon^2),\quad \bar{u}=u+\epsilon\eta(t,x,u)+O(\epsilon^2).$$

The requirement that the differential equation be invariant (11.2) leads to an overdetermined linear system of equations (the so-called determining equations) to solve for the infinitesimals, $\xi^1(t,x,u),\xi^2(t,x,u)$ and $\eta(t,x,u)$. If these equations can be solved, the symmetry can be characterised by the generator

$$\Gamma=\xi^1(t,x,u)\frac{\partial}{\partial t}+\xi^2(t,x,u)\frac{\partial}{\partial x}+\eta(t,x,u)\frac{\partial}{\partial u},$$

where the generator Γ leaves the PDE invariant. Since the governing equation is a second order PDE, it is required that

$$\Gamma^{(2)} F|_{F=0} = 0, \tag{11.3}$$

where $\Gamma^{(2)}$ is the second prolongation (extension) of the symmetry generator and is given by

$$\Gamma^2 = \xi^1 \frac{\partial}{\partial t} + \xi^2 \frac{\partial}{\partial x} + \eta \frac{\partial}{\partial u} + \zeta_t \frac{\partial}{\partial u_t} + \zeta_x \frac{\partial}{\partial u_x} + \zeta_{tt} \frac{\partial}{\partial u_{tt}} + \zeta_{xt} \frac{\partial}{\partial u_{xt}} + \zeta_{xx} \frac{\partial}{\partial u_{xx}}.$$

The ζ can be calculated by

$$\begin{aligned}
\zeta_t(t,x,u) &= \mathrm{D}_t \eta - u_t \, \mathrm{D}_t \xi^1 - u_x \, \mathrm{D}_t \xi^2, \\
\zeta_x(t,x,u) &= \mathrm{D}_x \eta - u_t \, \mathrm{D}_x \xi^1 - u_x \, \mathrm{D}_x \xi^2, \\
\zeta_{tt}(t,x,u) &= \mathrm{D}_t \zeta_t - u_{tt} \, \mathrm{D}_t \xi^1 - u_{tx} \, \mathrm{D}_t \xi^2, \\
\zeta_{xt}(t,x,u) &= \mathrm{D}_t \zeta_x - u_{xt} \, \mathrm{D}_t \xi^1 - u_{xx} \, \mathrm{D}_t \xi^2, \\
\zeta_{xx}(t,x,u) &= \mathrm{D}_x \zeta_x - u_{xt} \, \mathrm{D}_x \xi^1 - u_{xx} \, \mathrm{D}_x \xi^2,
\end{aligned}$$

where D_i is the total derivative with respect to the independent variables

$$\begin{aligned}
\mathrm{D}_t &= \frac{\partial}{\partial t} + u_t \frac{\partial}{\partial u} + u_{tt} \frac{\partial}{\partial u_t} + u_{xt} \frac{\partial}{\partial u_x} + \dots, \\
\mathrm{D}_x &= \frac{\partial}{\partial x} + u_x \frac{\partial}{\partial u} + u_{xx} \frac{\partial}{\partial u_x} + u_{xt} \frac{\partial}{\partial u_t} + \dots .
\end{aligned}$$

Further details can be found in the many excellent texts on the topic including those by Olver [34], Ibragimov [25] and Hill [22].

11.1. EXACT SOLUTION TO MODIFIED DIFFUSION EQUATION

In Chapter 8, a PDE modelling the conservation of mass of ferric ions was introduced. The nondimensional PDE is given by Equation (8.7) (as shown below again)

$$\frac{\partial}{\partial t}\left[c - \frac{s_3}{c + s_3}\right] = \frac{\partial}{\partial x}\left[\frac{\partial c}{\partial x}\right]. \tag{11.4}$$

Dimsym [43] is a package written for Reduce [20] for the determinations of symmetries. That

is, given a differential equation (or a system of differential equations) it solves the determining equations to find $\xi^1(t,x,u), \xi^2(t,x,u)$ and $\eta(t,x,u)$. The symmetries admitted by Equation (8.7) can be characterised by

$$\begin{aligned}\Gamma_1 &= \frac{\partial}{\partial t},\\ \Gamma_2 &= \frac{\partial}{\partial x},\\ \Gamma_3 &= 2t\frac{\partial}{\partial t} + x\frac{\partial}{\partial x}.\end{aligned}$$

Symmetries Γ_1 and Γ_2 represent translations in time and space respectively. A more interesting exact solution can be found by using Γ_3.

The characteristic equation corresponding to Γ_3 is

$$\frac{\mathrm{d}t}{2t} = \frac{\mathrm{d}x}{x} = \frac{\mathrm{d}c}{0}.$$

The constants of integration each represent an invariant quality that can be used as one of the new variables. The invariants can be found by integrating pairs of the characteristic equation and solving for the constant of integration. By pairing the x and t terms, the new independent variable is found to be $\phi = x/\sqrt{t}$. The zero in the denominator of the third term implies that the new dependent variable is given by $u(\phi) = c(t,x)$. Using these new variables, Equation (8.7) can be reduced to a nonlinear second order ODE,

$$u'' + \frac{\phi}{2}\left[1 + \frac{s_3}{(u+s_3)^2}\right]u' = 0. \tag{11.5}$$

Following similar techniques to those used in Chapter 10, perturbation methods can be applied to Equation (11.5) to find a solution. Assuming that s_3 is small such that $\epsilon = s_3$ and applying the perturbation expansion $u(\phi) = u_0(\phi) + \epsilon u(\phi) + O(\epsilon^2)$ gives the zeroth and first order equations

$$u_0'' + \frac{\phi}{2}u_0' = 0, \tag{11.6}$$

$$u_1'' + \frac{\phi}{2}u_1' = -\frac{\phi}{2}\frac{u_0'}{u_0^2}. \tag{11.7}$$

Solving Equation (11.6) gives,

$$u_0(\phi) = a_1 \operatorname{erf}\left(\frac{\phi}{2}\right) + a_2,$$

where a_i are constants of integration. Thus,

$$c_0(t,x) = a_1 \operatorname{erf}\left(\frac{x}{2\sqrt{t}}\right) + a_2.$$

Consider Equation (11.7). Multiplying (11.7) by the integrating factor $\exp(\phi^2/4)$ and integrating with respect to ϕ gives,

$$u_1'(\phi) = -\frac{1}{2}u_0'(\phi)\int \frac{\phi}{u_0^2}\mathrm{d}\phi + a_3 \exp\left(-\frac{\phi^2}{4}\right), \tag{11.8}$$

where a_3 is a constant of integration.

Integrating Equation (11.8) using integration by parts, gives

$$\begin{aligned} u_1(\phi) &= -\frac{1}{2}u_0(\phi)\int \frac{\phi}{u_0^2}\mathrm{d}\phi + \frac{1}{2}\int \frac{\phi}{u_0}\mathrm{d}\phi + a_3 \int \exp\left(-\frac{\phi^2}{4}\right)\mathrm{d}\phi, \\ &= \frac{1}{2}\int^{\phi} \frac{\gamma\left(u_0(\gamma) - u_0(\phi)\right)}{u_0(\gamma)^2}\mathrm{d}\gamma + a_3\sqrt{\pi}\operatorname{erf}\left(\frac{\phi}{2}\right) + a_4. \end{aligned}$$

where a_4 is a constant of integration. Again, the difficulty here lies with integrating the reciprocal of the error function.

In terms of the original dependent and independent variables, $c(t,x) = u(\phi)$, where $u(\phi) = u_0(\phi) + s_3 u_1(\phi)$ and $\phi = x/\sqrt{t}$.

11.2. EXACT SOLUTIONS TO A SYSTEM OF PARTIAL DIFFERENTIAL EQUATIONS

Section 7.1.3 introduces a nondimensional system of PDEs to describe ferric ion diffusion and MOF occupancy at the solution-polymer boundary (Equations (7.11)), as shown below

$$\frac{\partial c}{\partial t} = s_1 \frac{\partial^2 c}{\partial x^2} \qquad \text{for } x \geq 0; \qquad \frac{\partial b}{\partial t} = s_2\left[c\,(1-b) - s_3\, b\right] \qquad \text{at } x = 0,$$

where s_1, s_2, s_3 are nondimensional parameters given in Section 7.1.1.

This section looks for a solution of this system of equations.

11.2.1. Ferric ion diffusion and MOF occupancy where s_3 is non-zero

Dimsym reports that a special case may occur when s_1, s_2 or s_3 are zero. The cases when $s_1 = 0$ or $s_2 = 0$ are trivial and as such they will not be explored. However, when $s_3 = 0$ (that is, there is no dissociation), there are two new symmetries admitted. This is explored later in this section.

The symmetries admitted by system (7.11) (with $s_3 \neq 0$) are

$$\begin{aligned}
\Gamma_1 &= \frac{\partial}{\partial t}, \\
\Gamma_2 &= \frac{\partial}{\partial x}, \\
\Gamma_3 &= 2t\frac{\partial}{\partial t} + x\frac{\partial}{\partial x} - 2(c+s_3)\frac{\partial}{\partial c} + 2(b-1)\frac{\partial}{\partial b}.
\end{aligned}$$

The characteristic equation corresponding to Γ_3 is

$$\frac{\mathrm{d}t}{2t} = \frac{\mathrm{d}x}{x} = -\frac{\mathrm{d}c}{2(c+s_3)} = \frac{\mathrm{d}b}{2(b-1)}.$$

Taking successive pairs of the characteristic equation gives the new variables,

$$\phi = \frac{x}{\sqrt{t}}, \quad u(\phi) = t\,(c(t,x) + s_3), \quad v(\phi) = \frac{1}{t}\,(b-1)\,u(\phi).$$

The ferric ion diffusion equation can be transformed to a second order ODE

$$u'' + \frac{1}{2s_1}\,\phi\,u' + \frac{1}{s_1}\,u = 0. \tag{11.9}$$

Using Maple, Equation (11.9) has the solution

$$u(\phi) = -\phi\,\exp\left(-\frac{\phi^2}{4s_1}\right)\,\left[a_1\pi\,\mathrm{erf}\left(\sqrt{-\frac{1}{4s_1}}\phi\right) - a_2\right] + 2a_1\sqrt{-s_1\,\pi}.$$

where a_i are constants of integration. Therefore,

$$c(t,x) = -\frac{x}{t^{3/2}}\,\exp\left(-\frac{x^2}{4s_1\,t}\right)\,\left[a_1\pi\,\mathrm{erf}\left(\sqrt{-\frac{x^2}{4s_1\,t}}\right) - a_2\right] + \frac{2a_1\,\sqrt{-s_1\,\pi}}{t} - s_3.$$

The equation describing the MOF occupancy can be transformed to a first order ODE,

$$v' - \frac{1}{\phi}(2s_2u^2 + 2u + \phi u')\, v = \frac{2s_2s_3}{\phi}u^2. \tag{11.10}$$

Finding the integrating factor of Equation (11.10) and integrating with respect to ϕ, gives

$$v(\phi) = 2s_2s_3 \exp\left(u(\phi) + 2\int \frac{(u(\phi)^2 + u(\phi))}{\phi}\mathrm{d}\phi\right)\int \frac{u(\phi)^2}{\phi}\exp\left(-u(\phi) - 2\int \frac{(u(\phi)^2 + u(\phi))}{\phi}\mathrm{d}\phi\right)\mathrm{d}\phi.$$

where

$$\int \frac{u(\phi)}{\phi}\mathrm{d}\phi = 2a_1\sqrt{-s_1\,\pi}\ln(\phi) + a_2\sqrt{s_1\,\pi}\ \mathrm{erf}\left(\frac{\phi}{2\sqrt{s_1}}\right) - a_1\pi\int \exp\left(-\frac{\phi^2}{4\,s_1}\right)\ \mathrm{erf}\left(\sqrt{-\frac{1}{4s_1}}\phi\right)\mathrm{d}\phi,$$

and

$$\begin{aligned}\int \frac{u(\phi)^2}{\phi}\mathrm{d}\phi = {} & -4a_1^2\,s_1\,\pi\ln(\phi) - a_2^2 s_1 \exp\left(-\frac{\phi^2}{2\,s_1}\right) + 4a_1\,a_2\,\pi\sqrt{-s_1^2}\,\mathrm{erf}\left(\frac{\phi}{2\sqrt{s_1}}\right) \\ & + 2a_1\,a_2\,s_1\ \exp\left(-\frac{\phi^2}{2\,s_1}\right)\ \mathrm{erf}\left(\sqrt{-\frac{1}{4s_1}}\phi\right) + 2a_1\,a_2\sqrt{-s_1^2}\ \mathrm{erf}\left(\sqrt{\frac{1}{4s_1}}\phi\right) \\ & + a_1^2\pi^2\int \phi\exp\left(-\frac{\phi^2}{2\,s_1}\right)\ \mathrm{erf}\left(\sqrt{-\frac{1}{4s_1}}\phi\right)^2\mathrm{d}\phi \\ & - 4a_1^2\pi^{3/2}\sqrt{-s_1}\int \exp\left(-\frac{\phi^2}{4\,s_1}\right)\ \mathrm{erf}\left(\sqrt{-\frac{1}{4s_1}}\phi\right)\mathrm{d}\phi.\end{aligned}$$

While some of the integrals in the above expressions can be evaluated as shown, some could not be evaluated analytically. The MOF occupancy can then be found using $b(t,x) = 1 + tv(\phi)/u(\phi)$.

For the system described in Chapter 7, the nondimensional diffusion coefficient, s_1, is strictly positive. Therefore, the exact solutions for $c(t,x)$ and $b(t,x)$ above are complex. Although, these are mathematically correct solutions given the system of PDEs, the complex solutions do not make sense in terms of ferric ion concentration profiles or MOF occupancy.

11.2.2. Ferric ion diffusion and MOF occupancy when $s_3 = 0$

Next, consider the case where ferric ions associate with the MOF crystal but cannot dissociate ($s_3 = 0$), i.e. when the binding energy is stronger than the kinetic energy. The symmetries

admitted by Equation (7.11) with $s_3 = 0$, are

$$\begin{aligned}
\Gamma_1 &= \frac{\partial}{\partial t}, \\
\Gamma_2 &= \frac{\partial}{\partial x}, \\
\Gamma_3 &= 2t\frac{\partial}{\partial t} + x\frac{\partial}{\partial x} + 2(b-1)\ln(b-1)\frac{\partial}{\partial b}, \\
\Gamma_4 &= (b-1)\ln(b-1)\frac{\partial}{\partial b} + c\frac{\partial}{\partial c}, \\
\Gamma_\infty &= -(b-1)\,H(t,x)\frac{\partial}{\partial b} - \frac{1}{s_2}\,H_t(t,x)\frac{\partial}{\partial c} \text{ where } H_{xxt} = H_{tt},
\end{aligned}$$

where Γ_∞ is known as the infinite-parameter Lie group of point transformations.

Below, Γ_3 is used to find a set of invariants that will reduce the system of PDEs to a system of ODEs. The reduction resulting from the use of Γ_4, does not produce any useful results and therefore not presented here.

The characteristic equation corresponding to Γ_3 is

$$\frac{\mathrm{d}t}{2t} = \frac{\mathrm{d}x}{x} = \frac{\mathrm{d}c}{0} = \frac{\mathrm{d}b}{2(b-1)\ln(b-1)}.$$

Taking successive pairs of the characteristic equation gives the new variables,

$$\phi = \frac{x}{\sqrt{t}}, \quad u(\phi) = c(t,x), \quad v(\phi) = \frac{\ln(b(t,x)-1)}{t}.$$

The ferric ion diffusion equation (the first equation from (7.11)) can be transformed to a second order ODE

$$u'' + \frac{1}{2s_1}\phi u' = 0,$$

which has the solution

$$u(\phi) = \frac{a_1\sqrt{\pi}}{2}\,\mathrm{erf}\left(\frac{1}{2\sqrt{s_1}}\phi\right) + a_2,$$

where a_i are constants of integration. Thus the concentration can be written

$$c(t,x) = \frac{a_1\sqrt{\pi}}{2}\,\mathrm{erf}\left(\frac{x}{2\sqrt{s_1\,t}}\right) + a_2.$$

This solution is one of the general solutions to the linear diffusion equation and it can be made to

satisfy inital and boundary conditions. For example,

$$c(t,x) = -\operatorname{erf}\left(\frac{x}{2\sqrt{s_1\,t}}\right) + 1,$$

satisfies the conditions

$$c(t,0) = 1 \quad \text{and} \quad c(0,x) = 0.$$

Therefore, $c(t,x)$ is a realistic solution describing the ferric ion concentration.

The equation describing the MOF occupancy (the second equation from (7.11)) can be transformed to a first order ODE,

$$v' - 2\frac{1}{\phi}v = 2s_2\frac{1}{\phi}u.$$

This equation can be integrated using the integrating factor technique to find

$$\begin{aligned} v(\phi) &= 2s_2\phi^2 \int \frac{1}{\phi^3}u(\phi)\mathrm{d}\phi, \\ &= 2a_2\,a_3\,s_2\,\phi^2 - a_2\,s_2 - \frac{a_1\,\sqrt{\pi}}{2}\left[1 + \frac{\phi^2}{2s_2}\right]\operatorname{erf}\left(\frac{1}{2\sqrt{s_1}}\phi\right) \\ &\quad - \frac{a_1\,s_2}{2\sqrt{s_1}}\,\phi\exp\left(-\frac{\phi^2}{4s_1}\right), \end{aligned}$$

where $b(t,x) = \exp(t\,v(\phi)) + 1$. It is difficult for the exact solution for $b(t,x)$ to satisfy any sensible initial condition.

11.3. DISCUSSION

This chapter used Lie point symmetries to find exact solutions to the model equations presented in earlier chapters. It was shown that the exact solutions for the MOF occupancy and the ferric ion concentration can be expressed in terms of the exponential function and the error function, that is, similar functions to those used in Chapters 8 and 10.

While the solutions presented here solve the relevant PDEs, they cannot be made to satisfy all the necessary initial and boundary conditions.

CHAPTER 12

FINAL REMARKS AND FUTURE WORK

The quality of mined copper ore is gradually decreasing, while the demand for copper increases due to the electrification of many industries. The constraints of supply and demand of copper has created the need for research projects dedicated to optimising the entire value chain of mines. In addition to using the obvious sciences (engineering and chemistry) to address these problems, mathematics can be used to help solve mining and physical chemistry problems more broadly. Mathematics may give unexpected insights and a deeper understanding to the problems at hand.

The research in this research project is motivated by a newly developed ferric ion sensor that will aid the optimisation of the minerals leaching operations in a mine. In particular, the results of this research provide theoretical insight into how ferric ions interact with the MOF crystals embedded in the sensor, and how the ferric ion and the sensor characteristics influence sensing time.

Part I of this thesis focusses on the van der Waals interactions between ferric ions and MOF crystals. While the hydrated ferric ions are attracted to the MOF crystals, they are too large to fit inside the MOF pores. The finding means that it is easier to "wash" and re-use the sensor, leading to cost savings and reduced material wastage.

Since ferric ions in solution typically occur in their hydrated state, the interaction of both oxygen and hydrogen spherical shells with the cylindrical MOF pore are investigated. Interestingly, the water molecules contribute the majority of the interaction energy and force between the hydrated ferric ion and the MOF pore.

In general, there are four possible factors that may affect the attraction of a molecule to a pore: (i) the Lennard-Jones pair potential parameters of the various interacting atom types, (ii) the overall geometric structure of the ion and pore, and whether or not the interacting molecule is a hydrated ion, and if so (iii) the number of associated water molecules the ion has and (iv) the bond length(s) between the ion and the water molecules (in particular, the oxygen atoms).

This thesis investigated three MOF pore approximations: (i) semi-infinite cylinder, (ii) finite cylinder and (iii) semi-infinite rectangular prism. The qualitative behaviour of the interactions between a (hydrated) ferric ion and a MOF pore remain the same for all pore shapes. There are similarities between the interaction energy calculations between a point/sphere and a semi-infinite cylindrical pore, and between a point/sphere and a finite cylindrical pore, and it is simple to switch between

the two. The semi-infinite pore calculations use the function $J_n(x, y) = I_n(0, 1)I_n(x, y)$, while the finite pore approximation uses $H_n(x, y) = I_n(x, y + c)I_n(x, y)$.

The MOF pore from the "top" view is similar to a parallelogram. Therefore, a natural extension of investigating a more accurate MOF approximation is to derive analytical expressions for the interactions between a point/sphere and a slanted plane and to determine how well the rectangular prism approximates a parallelogram prism. The MOF pore approximated by a parallelogram prism is shown in Figure 12.1 below.

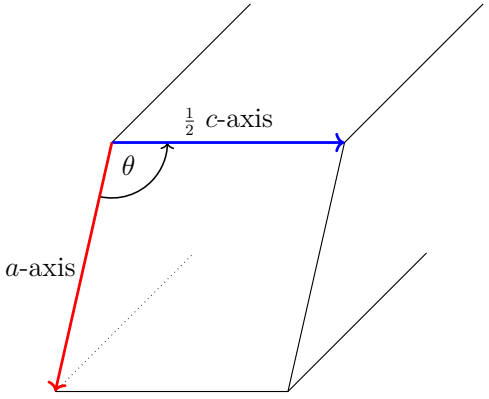


Figure 12.1: Schematic of MOF pore as approximated by semi-infinite parallelogram prism.

The interaction energy calculation between a point and a semi-infinite rectangular prism (four planes and four lines) is far more complex in comparison to calculations between a point and a cylinder. As a result of this complexity, a new rule-of-thumb is introduced to model a semi-infinite rectangular prism as a semi-infinite cylindrical pore, by matching their cross-sectional areas. However, some discretion needs to be applied when modelling a MOF pore, as special considerations need to be taken for the atom location and density. For example, if some atom types are solely located at the prism's edges, then they should be approximated by a semi-infinite line located at an appropriate distance from the centreline, rather than smoothing over the cylinder surface. However, additional work is needed to determine the robustness of the rule-of-thumb in Section 5.3 for matching the cross-sectional area of the "real" pore to a fitted cylindrical pore to simplify calculations of the van der Waals interactions.

In Chapter 5, further changes in the modelling are incorporated in order to include more of the sensing environment. The key findings in the final chapters of Part I are that: (i) other metal ions in the analyte solution are attracted to the MOF crystals but they do not affect the florescence sensing, (ii) changes in temperature do not affect the qualitative behaviours of the van der Waals

interactions, (iii) a ferric ion will experience repulsion near the MOF pore entrance if the entrance is blocked by another ferric ion, and (iv) a hydrated ferric ion will likely occupy the closest available MOF pore.

The surfaces of the MOF crystals are not perfect and typically have defects such as floating ligands and collapsed entrances. There are many alternative ways of modelling this environment, for example: (i) the surface of the MOF crystal can be modelled as a flat or sinusoidal plane, (ii) floating ligands could be modelled as lines of atoms attached to the pore entrance, (iii) a pore with a collapsed entrance could be modelled as a cylinder with a truncated cone attached to the entrance. Ultimately, the most appropriate approximation of the MOF pore is dependent upon what information is required.

Another consideration of the sensing environment would be to determine the minimum distance, δ, between two hydrated ferric ions (Figure 12.2), such that the repulsive force between them is negligible. This will give an approximation to the maximum mass of ferric ions that can associate with a single MOF crystal, m_s. If the centreline of neighbouring pores on the MOF crystal surface are much closer than this minimum distance, it may not be possible for two neighbouring pores to be occupied at the same time.

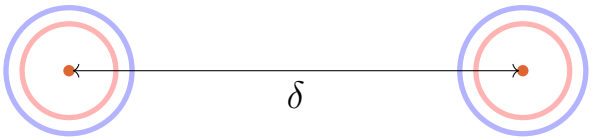


Figure 12.2: Two hydrated ferric ions approximated by points and two concentric spheres, distance δ apart.

Part II of this thesis focusses on ferric ion diffusion in a solution and a MOF-polymer thin film, both in one-dimension and two-dimensions. The results from the numerical investigation found that there are two times scales: diffusive and associative. It takes a longer time for the concentration of dissolved ferric ions in the polymer composite to reach steady state, than it takes for the number of ferric ions associated with MOF crystals to reach steady state. It also follows that a thicker polymer composite coating would require comparatively more time for ferric ions to diffuse to the bottom.

The inherent properties of ferric ions, MOF crystals and the polymer composite will dictate the order of magnitude of the nondimensional parameters and the studies herein will indicate whether longer exposure times are necessary. If ferric ions have a large diffusivity in solution and a great

affinity to associate to MOF crystals, then the sensor requires shorter exposure times to provide an accurate florescence reading. If the polymer composite has a higher MOF density, then the sensor requires longer exposure times. Polymers with low MOF densities are better suited for analyte solutions that are typically known to have high ferric ion concentrations.

Whilst investigating the effects of MOF density on dissolved ferric ion concentration in the polymer composite, a partial differential equation describing the modified total ferric ion density is established (as seen by the equation below),

$$\frac{\partial u}{\partial t} = \frac{\partial}{\partial x}\left[D(u)\frac{\partial u}{\partial x}\right],$$

where $D(u)$ is the modified diffusion coefficient in Equation (8.10) and is bounded. A continuation of this investigation is to search for an analytical solution to the nonlinear diffusion equation.

An alternative way to investigate this problem is to reformulate the model in Part II as a reaction-diffusion problem with a spatially dependent (periodic) sink term to represent association at the MOF crystals.

Part III of this thesis explores the partial differential equations arising in Part II and attempts to solve them analytically. All methods used here to search for analytical solutions to describe the dissolved ferric ion density and the associated ferric ion density with MOF crystals result in solutions containing the exponential and error functions.

Some of the analytic solutions in Part III required that the reciprocal of the error function be evaluated, as shown by the general forms below

$$\int \frac{\exp\left(a\,(x-b)^2\right)}{\operatorname{erf}(c\,x)}\,\mathrm{d}x \quad \text{and} \quad \int \frac{x}{\operatorname{erf}(c\,x)}\,\mathrm{d}x,$$

where a, b and c are constants. If analytical solutions to these integrals can be evaluated, then the solutions in Part III can be evaluated analytically, instead of using numerical integration.

REFERENCES

[1] O. O. Adisa, B.J. Cox, and J.M. Hill. Encapsulation of methane molecules into carbon nanotubes. *Physica B: Condensed Matter*, 406(1):88–93, 2011.

[2] M. H. Alshehri. Continuum modelling for encapsulation of anticancer drugs inside nanotubes. *Mathematics*, 9(19):2469, 2021.

[3] S. Bahrani, R. Aslani, S. A. Hashemi, S. M. Mousavi, and M. Ghaedil. *Adsorption: Fundamental processes and applications*, volume 33 of *Interface Science and Technology*. Elsevier, 2021.

[4] D. Baowan and J. M. Hill. Mathematical modeling of interaction energies between nanoscale objects: A review of nanotechnology applications. *Advances in Mechanical Engineering*, 8(11):1–16, 2016.

[5] D. Baowan, J. M. Hill, and W. Bacsa. Continuous approximation for interaction energy of adamantane encapsulated inside carbon nanotubes. *Chemical Physics Letters*, 693:34–39, 2018.

[6] D. Baowan and N. Thamwattana. Modelling adsorption of a water molecule into various pore structures of silica gel. *Journal of Mathematical Chemistry*, 49:2291–2307, 2011.

[7] BHP. Copper, 2020. [Online; accessed 10 February 2020].

[8] W. M. Bloch. Personal Communication, July 2020.

[9] W. M. Bloch. Personal Communication, March 2021.

[10] W. M. Bloch. Personal Communication, February 2023.

[11] E. J. Carr and T. W. Turner. A semi-analytical solution for multilayer diffusion in a composite medium consisting of a large number of layers. *Applied Mathematical Modelling*, 40(15-16):7034–7050, 2016.

[12] S. Chaturvedi and P. N. Dave. Removal of iron for safe drinking water. *Desalination*, 303:1–11, 2012.

[13] B. J. Cox, N. Thamwattana, and J. M. Hill. Mechanics of atoms and fullerenes in single-walled carbon nanotubes. I. Acceptance and suction energies. *Proceedings of the Royal Society A: Mathematical, Physical and Engineering Sciences*, 463(2078):461–477, 2007.

[14] T. M. C. Faro, G. P. Thim, and M. S. Skaf. A Lennard-Jones plus Coulomb potential for Al^{3+} ions in aqueous solutions. *The Journal of Chemical Physics*, 132(11):114509, 2010.

[15] H. Fujita. Notes on free volume theories. *Polymer Journal*, 23(12):1499–1506, 1991.

[16] S. Goldman. Estimation of Lennard-Jones 6-12 pair potential parameters from vapor pressures and thermodynamic perturbation theory. *The Journal of Physical Chemistry*, 80(15):1697–1700, 1976.

[17] I. S. Gradshteyn and I. M. Ryzhik. *Table of Integrals, Series, and Products: Indefinite integrals of elementary functions*. Academic Press, 1980.

[18] D. W. Hahn and M. N. Özisik. *Heat conduction*. John Wiley & Sons, 2012.

[19] B. Hardy, C. Corgnale, R. Chahine, M. A. Richard, S. Garrison, D. Tamburello, D. Cossement, and D. Anton. Modeling of adsorbent based hydrogen storage systems. *International Journal of Hydrogen Energy*, 37(7):5691—5705, 2012.

[20] A. C. Hearn and J. P. Fitch (Eds). *Reduce User's Manual*. Konrad-Zuse-Zentrum, Berlin, 1996.

[21] R. I. Hickson, S. I. Barry, G. N. Mercer, and H. S. Sidhu. Finite difference schemes for multilayer diffusion. *Mathematical and Computer Modelling*, 54(1-2):210–220, 2011.

[22] J. M. Hill. *Differential Equations and Group Methods for Scientists and Engineers*. CRC Press, 1992.

[23] K. L. Hogsden and J. S. Harding. Consequences of acid mine drainage for the structure and function of benthic stream communities: a review. *Freshwater Science*, 31(1):108–120, 2012.

[24] A. J. Howarth, A. W. Peters, N. A. Vermeulen, T. C. Wang, J. T. Hupp, and O. K. Farha. Best practices for the synthesis, activation, and characterization of metal-organic frameworks. *Chemistry of Materials*, 29(1):26–39, 2017.

[25] N. H. Ibragimov and N. K. Ibragimov. *Elementary Lie Group Analysis and Ordinary Differential Equations*. Wiley New York, 1999.

[26] A. A. Jarzecki, A. D. Anbar, and T. G. Spiro. DFT analysis of $Fe(H_2O)_6^{3+}$ and $Fe(H_2O)_6^{2+}$ structure and vibrations; implications for isotope fractionation. *The Journal of Physical Chemistry A*, 108(14):2726–2732, 2004.

[27] M. Krasowska. Personal Communication, September 2022.

[28] P. Kratochvil, R. F. T. Septo, and U. W. Suter. Glossary of basic terms in polymer science (IUPAC Recommendations 1996). *Pure and Applied Chemistry*, 68(12):2287–2311, 1996.

[29] J. E. Lennard-Jones and A. F. Devonshire. Critical phenomena in gases-I. *Proceedings of the Royal Society of London. Series A-Mathematical and Physical Sciences*, 163(912):53–70, 1937.

[30] J. E. Lennard-Jones and A. F. Devonshire. Critical phenomena in gases. II. Vapour pressures and boiling points. *Proceedings of the Royal Society of London. Series A, Mathematical and Physical Sciences*, 165(920):1–11, 1938.

[31] P. Li, L. F. Song, and K. M. Merz Jr. Parameterization of highly charged metal ions using the 12-6-4 LJ-type nonbonded model in explicit water. *The Journal of Physical Chemistry B*, 119(3):883–895, 2015.

[32] K. I. Louw, B. H. Bradshaw-Hajek, and J. M. Hill. Interaction of ferric ions with europium metal organic framework and application to mineral processing sensing. *Philosophical Magazine*, 102(13):1231–1246, 2022.

[33] A. Nasehzadeh, M. Mohseni, and K. Azizi. The effect of temperature on the Lennard–Jones (6–12) pair potential function. *Journal of Molecular Structure: THEOCHEM*, 589-590:329–335, 2002.

[34] P. J. Olver. *Applications of Lie Groups to Differential Equations*. Springer- Verlag New York, 1986.

[35] I. Persson. Structures of hydrated metal ions in solid state and aqueous solution. *Liquids*, 2(3):210–242, 2022.

[36] E. Peters. Hydrometallurgical process innovation. *Hydrometallurgy*, 29(1-3):431–459, 1992. Hydrometallurgy, Theory and Practice Proceedings of the Ernest Peters International Symposium. Part A.

[37] A. K. Rappé, C. J. Casewit, K. S. Colwell, W. A. Goddard III, and W. M. Skiff. UFF, a full periodic table force field for molecular mechanics and molecular dynamics simulations. *Journal of the American Chemical Society*, 114(25):10024–10035, 1992.

[38] P. J. Rivero, J. Goicoechea, and F. J. Arregui. Optical fiber sensors based on polymeric sensitive coatings. *Polymers*, 10(3):280, 2018.

[39] L. Rozenberga. *Metal organic framework based optical fibre sensor for Fe^{3+} concentration measurements*. PhD thesis, Future Industries Institute, UniSA STEM, 2023.

[40] L. Rozenberga, W. Skinner, D. G. Lancaster, W. M. Bloch, A. Blencowe, T. Gillam, M. Krasowska, and D. A. Beattie. Europium metal organic framework incorporation in polyHEMA for luminescence tuning and Fe^{3+} sensor optimisation. submitted, 2022.

[41] L. Rozenberga, W. Skinner, D. G. Lancaster, W. M. Bloch, A. Blencowe, M. Krasowska, and D. A. Beattie. A europium metal-organic framework for dual Fe^{3+} ion and pH sensing. *Scientific Reports*, 12(1):11982, 2022.

[42] S. K. Sahoo, D. Sharma, R. K. Bera, G. Crisponi, and J. F. Callan. Iron(III) selective molecular and supramolecular fluorescent probes. *Chemical Society Reviews*, 41:7195–7227, 2012.

[43] J. Sheering, A. K. Head, and G. E. Prince. Dimsym and LIE: symmetry determination packages. *Mathematical and Computer Modelling*, 25(8-9):153–164, 1997.

[44] W. Skinner. Personal Communication, May 2023.

[45] T. M. Squires, R. J. Messinger, and S. R. Manalis. Making it stick: convection, reaction and diffusion in surface-based biosensors. *Nature biotechnology*, 26(4):417–426, 2008.

[46] S. Stephan, K Langenbach, and H. Hasse. Interfacial properties of binary Lennard-Jones mixtures by molecular simulation and density gradient theory. *The Journal of Chemical Physics*, 150(17):174704, 2019.

[47] K. Stevens, N. Thamwattana, and T. Tran-Duc. Continuum modeling with functional Lennard-Jones parameters for methane storage inside various carbon nanostructures. *ACS Omega*, 7(34):29773–29786, 2022.

[48] N. Thamwattana, P. Sarapat, and Y. Chan. Mechanics and dynamics of lysozyme immobilisation inside nanotubes. *Journal of Physics: Condensed Matter*, 31(26):265901, 2019.

[49] J. E. Thomas, S. St. C. Smart, and W. M. Skinner. Kinetic factors for oxidative and non-oxidative dissolution of iron sulfides. *Minerals Engineering*, 13(10-11):1149–1159, 2000.

[50] M. F. Vajargah. A review on the effects of heavy metals on aquatic animals. *Journal of Biomedical Research and Environmental Sciences*, 2:865–869, 2021.

[51] L. Verlet and J. Weis. Equilibrium theory of simple liquids. *Physical Review A*, 5(2):939, 1972.

[52] L. Verlet and J. Weis. Perturbation theory for the thermodynamic properties of simple liquids. *Molecular Physics*, 24(5):1013–1024, 1972.

[53] R. D. Vocke. Atomic weights of the elements 1997. *Pure and Applied Chemistry*, 71(8):1593––1607, 1999.

[54] J. S. Vrentas and J. L. Duda. Diffusion in polymer-solvent systems. I. Reexamination of the free-volume theory. *Journal of Polymer Science: Polymer Physics Edition*, 15(3):403–416, 1977.

[55] J. S. Vrentas and J. L. Duda. Diffusion in polymer-solvent systems. II. A predictive theory for the dependence of diffusion coefficients on temperature, concentration, and molecular weight. *Journal of Polymer Science: Polymer Physics Edition*, 15(3):417–439, 1977.

[56] J. S. Vrentas and J. L. Duda. Molecular diffusion in polymer solutions. *AIChE Journal*, 25(1):1–24, 1979.

[57] K. Vuori. Direct and indirect effects of iron on river ecosystems. *Annales Zoologici Fennici*, 32:317–329, 1995.

[58] C. Wang and J. L. Babitt. Liver iron sensing and body iron homeostasis. *Blood, The Journal of the American Society of Hematology*, 133:18–29, 2019.

[59] H. Xu, Y. Dong, Y. Wu, W. Ren, T. Zhao, S. Wang, and J. Gao. An-OH group functionalized MOF for ratiometric Fe^{3+} sensing. *Journal of Solid State Chemistry*, 258:441–446, 2018.

[60] E. Yariv. Small Péclet-number mass transport to a finite strip: An advection–diffusion-reaction model of surface-based biosensors. *Journal of Applied Mathematics*, 31:763–781, 2020.

[61] L. Zarkova and U. Hohm. Effective (n-6) lennard-jones potentials with temperature-dependent parameters introduced for accurate calculation of equilibrium and transport properties of ethene, propene, butene, and cyclopropane. *Journal of Chemical & Engineering Data*, 54(6):1648–1655, 2009.

APPENDIX A

CALCULATION OF THE INTERACTION ENERGY AND FORCE BETWEEN EITHER A POINT OR A SPHERE AND A SEMI-INFINITE CYLINDER

The geometry of the problem is described in Figure 3.1 and the surrounding text.

A.1. STEP-BY-STEP CALCULATIONS FOR INTERACTION ENERGY

The continuum Lennard-Jones approximation of the interaction energy of non-bonded atoms is described by Equation (2.3), where S_1 describes the surface of the semi-infinite cylinder with a mean surface density of n_1 and S_2 describes the surface of the interacting object with a mean surface density of n_2.

A.1.1. Point to semi-infinite cylinder

When considering the interacting energies between a point and a semi-infinite cylinder, the Lennard-Jones potential is integrated only along the surface of the semi-infinite cylinder,

$$\begin{aligned} E &= n_1 \int_{S_1} U(\rho) \mathrm{d}S_1, \\ &= 2\pi\, a\, n_1 \int_0^\infty \left[-\frac{A}{\rho^6} + \frac{B}{\rho^{12}} \right] \mathrm{d}x, \\ &= 2\pi\, a\, n_1 \int_0^\infty \left[-\frac{A}{(a^2 + (x-X)^2)^3} + \frac{B}{(a^2 + (x-X)^2)^6} \right] \mathrm{d}x, \end{aligned} \tag{A.1}$$

where $\rho^2 = a^2 + (x - X)^2$. Let $x_* = x - X$, then at the upper bound of integration $x = 0$, $x_* = -X$, and at the lower bound of integration as $x \to \infty$, $x_* \to \infty$, so that

$$E = 2\pi\, a\, n_1 \int_{-X}^\infty \left[-\frac{A}{(a^2 + x_*^2)^3} + \frac{B}{(a^2 + x_*^2)^6} \right] \mathrm{d}x_*.$$

Let $x_* = a \tan\psi$, then $a^2 + x_*^2 = a^2 + a^2 \tan^2\psi = a^2 \sec^2\psi$ and $\mathrm{d}x_* = a \sec^2\psi \, \mathrm{d}\psi$. The bounds of integration are transformed as follows: as $x_* \to \infty$, $\psi = \pi/2$ and $x_* = -X$, then $\psi = \psi_0 =$

$-\arctan[X/a]$. Therefore

$$\begin{aligned} E &= 2\pi\, a\, n_1 \int_{\psi_0}^{\frac{\pi}{2}} \left[-\frac{A}{(a^2 \sec^2\psi)^3} + \frac{B}{(a^2 \sec^2\psi)^6} \right] a\, \sec^2\psi \mathrm{d}\psi, \\ &= \frac{2\pi\, n_1}{a^4} \int_{\psi_0}^{\frac{\pi}{2}} \left[-A \cos^4\psi + \frac{1}{a^6} B \cos^{10}\psi \right] \mathrm{d}\psi. \end{aligned} \tag{A.2}$$

Equation (A.2) can be expressed in terms of integrals of powers of cosine functions, $J_n(a, -X)$ define in Appendix D. The potential energy of a point interacting with a semi-infinite cylinder is

$$E = \frac{2\pi\, n_1}{a^4} \left[-A\, J_2(a, -X) + \frac{1}{a^6} B\, J_5(a, -X) \right]. \tag{A.3}$$

A.1.2. Sphere to semi-infinite cylinder

Assuming the continuum approach to calculate the interaction energies between a sphere and a semi-infinite cylinder, as a result the surface of both objects are integrated over,

$$E = n_1\, n_2 \int_{S_1} \int_{S_2} U(\rho)\, \mathrm{d}S_2\, \mathrm{d}S_1,$$

where S_1 is the surface of the semi-infinite cylinder with a corresponding mean surface density of atoms n_1, and S_2 is the surface of the sphere with a mean surface density of atoms, n_2.

Denoting the integral over the surface of the sphere as $G(\rho)$ [1, 13],

$$\begin{aligned} G(\rho) &= n_2 \int_{S_2} U(\rho)\, \mathrm{d}S_2, \\ &= \frac{\pi\, b\, n_2}{\rho} \left[\frac{A}{2} \left(\frac{1}{(\rho+b)^4} - \frac{1}{(\rho-b)^4} \right) - \frac{B}{5} \left(\frac{1}{(\rho+b)^{10}} - \frac{1}{(\rho-b)^{10}} \right) \right], \\ &= 4\pi\, b^2\, n_2 \left[-A \left(\frac{1}{(\rho^2-b^2)^3} + \frac{2\, b^2}{(\rho^2-b^2)^4} \right) + \frac{1}{5} B \left(\frac{5}{(\rho^2-b^2)^6} + \frac{80\, b^2}{(\rho^2-b^2)^7} \right. \right. \\ &\quad \left. \left. + \frac{336\, b^4}{(\rho^2-b^2)^8} + \frac{512\, b^6}{(\rho^2-b^2)^9} + \frac{256\, b^8}{(\rho^2-b^2)^{10}} \right) \right]. \end{aligned}$$

The total interaction energy between the two objects is calculated by integrating over the surface

of the cylinder,

$$
\begin{aligned}
E &= n_1 \int_{S_1} G(\rho)\mathrm{d}S_1 \\
&= 2\pi\, a\, n_1 \int_0^\infty G(\rho)\mathrm{d}x, \\
&= 8\pi^2\, a\, b^2\, n_1\, n_2 \int_0^\infty \left[-A\left(\frac{1}{(\rho^2-b^2)^3} + \frac{2\,b^2}{(\rho^2-b^2)^4} \right) + \frac{1}{5}B\left(\frac{5}{(\rho^2-b^2)^6} + \frac{80\,b^2}{(\rho^2-b^2)^7} \right.\right. \\
&\quad \left.\left. + \frac{336\,b^4}{(\rho^2-b^2)^8} + \frac{512\,b^6}{(\rho^2-b^2)^9} + \frac{256\,b^8}{(\rho^2-b^2)^{10}} \right) \right] \mathrm{d}x, \\
&= 8\pi^2\, a\, b^2\, n_1\, n_2 \int_0^\infty \left[-A\left(\frac{1}{(a^2-b^2+(x-X)^2)^3} + \frac{2\,b^2}{(a^2-b^2+(x-X)^2)^4} \right) \right. \\
&\quad + \frac{1}{5}B\left(\frac{5}{(a^2-b^2+(x-X)^2)^6} + \frac{80\,b^2}{(a^2-b^2+(x-X)^2)^7} + \frac{336\,b^4}{(a^2-b^2+(x-X)^2)^8} \right. \\
&\quad \left.\left. + \frac{512\,b^6}{(a^2-b^2+(x-X)^2)^9} + \frac{256\,b^8}{(a^2-b^2+(x-X)^2)^{10}} \right) \right] \mathrm{d}x,
\end{aligned} \tag{A.4}
$$

where $\rho^2 = a^2 + (x-X)^2$. Let $\lambda^2 = a^2 - b^2$ and $x_* = x - X$, $\mathrm{d}x_* = \mathrm{d}x$. Then

$$
\begin{aligned}
E &= 8\pi^2\, a\, b^2\, n_1\, n_2 \int_{-X}^\infty \left[-A\left(\frac{1}{(\lambda^2+x_*^2)^3} + \frac{2\,b^2}{(\lambda^2+x_*^2)^4} \right) + \frac{1}{5}B\left(\frac{5}{(\lambda^2+x_*^2)^6} + \frac{80\,b^2}{(\lambda^2+x_*^2)^7} \right.\right. \\
&\quad \left.\left. + \frac{336\,b^4}{(\lambda^2+x_*^2)^8} + \frac{512\,b^6}{(\lambda^2+x_*^2)^9} + \frac{256\,b^8}{(\lambda^2+x_*^2)^{10}} \right) \right] \mathrm{d}x_*, \\
&= 8\pi^2\, a\, b^2\, n_1\, n_2\, \lambda \int_\psi^{\frac{\pi}{2}} \left[-A\,\lambda^{-6}\, \left(\cos^4\psi' + 2\,b^2\,\lambda^{-2}\,\cos^6\psi' \right) + \frac{1}{5}B\,\lambda^{-12}\left(5\,\cos^{10}\psi' \right.\right. \\
&\quad \left.\left. + 80\,b^2\,\lambda^{-2}\cos^{12}\psi' + 336\,b^4\,\lambda^{-4}\cos^{14}\psi' + 512\,b^6\,\lambda^{-6}\cos^{16}\psi' + 256\,b^8\,\lambda^{-8}\cos^{18}\psi' \right) \right]\, \mathrm{d}\psi',
\end{aligned} \tag{A.5}
$$

after performing a trig substitute $x_* = \lambda\tan\psi'$. This expression can be rewritten in terms of $J_n(\lambda, -X)$, defined in Appendix D, so that the interaction energy between a sphere and a semi-infinite cylinder is

$$
\begin{aligned}
E &= 8\pi^2\, a\, b^2\, n_1\, n_2\, \lambda^{-5} \left[-A\left(J_2(\lambda,-X) + 2\,b^2\,\lambda^{-2}\,J_3(\lambda,-X) \right) \right. \\
&\quad + \frac{1}{5}B\,\lambda^{-6}\left(5\,J_5(\lambda,-X) + 80\,b^2\,\lambda^{-2}J_6(\lambda,-X) + 336\,b^4\,\lambda^{-4}J_7(\lambda,-X) \right. \\
&\quad \left.\left. + 512\,b^6\,\lambda^{-6}J_8(\lambda,-X) + 256\,b^8\,\lambda^{-8}J_9(\lambda,-X) \right) \right].
\end{aligned} \tag{A.6}
$$

A.2. STEP-BY-STEP CALCULATIONS FOR INTERACTION FORCES

The interaction forces in the axial (x) direction between a point or a sphere and a semi-infinite cylinder can be calculated using Equations (2.3) and (2.4).

A.2.1. Point atom to semi-infinite cylinder

Using the interaction energy between a point and semi-infinite cylinder, Equation (A.1), and the relationship between the energy and the force, then the van der Waals force in the axial direction, Equation (2.4), due to the interaction with the entire surface of the finite cylinder is given by

$$\begin{aligned} F(X) &= \frac{\mathrm{d}\,E}{\mathrm{d}\rho}\,\frac{(x-X)}{\rho}, \\ &= 2\,\pi\,a\,n_1 \int_0^{\infty} \left[6\frac{A}{\rho^7} - 12\frac{B}{\rho^{13}}\right]\,\frac{(x-X)}{\rho}\,\mathrm{d}x. \end{aligned}$$

Using $\rho^2 = (x-X)^2 + a^2$, the integral and the bounds of integration are transformed. The interaction forces between a point and a semi-infinite cylinder is

$$\begin{aligned} F(X) &= 2\,\pi\,a\,n_1 \int_{\sqrt{X^2+a^2}}^{\infty} \left[6\frac{A}{\rho^7} - 12\frac{B}{\rho^{13}}\right]\,\mathrm{d}\rho, \\ &= 2\,\pi\,a\,n_1 \left[-\frac{A}{\rho^6} + \frac{B}{\rho^{12}}\right]\Bigg|_{\sqrt{X^2+a^2}}^{\infty}, \\ &= 2\,\pi\,a\,n_1 \left[\frac{A}{(X^2+a^2)^3} - \frac{B}{(X^2+a^2)^6}\right]. \end{aligned} \tag{A.7}$$

A.2.2. Sphere to semi-infinite cylinder

Using the interaction energy between a sphere and semi-infinite cylinder, Equation (A.4), and the relationship between the energy and the force, then the van der Waals force in the axial direction, Equation (2.4), due to the interaction with the entire surface of the finite cylinder is given by

$$\begin{aligned} F(X) = 8\pi^2\,a\,b^2\,n_1\,n_2 \int_0^{\infty} \Bigg[2\rho\,A\left(\frac{3}{(\rho^2-b^2)^4} + \frac{8\,b^2}{(\rho^2-b^2)^5}\right) - \frac{2}{5}\rho\,B\left(\frac{30}{(\rho^2-b^2)^7} + \frac{560\,b^2}{(\rho^2-b^2)^8}\right. \\ \left. + \frac{2688\,b^4}{(\rho^2-b^2)^9} + \frac{4608\,b^6}{(\rho^2-b^2)^{10}} + \frac{2560\,b^8}{(\rho^2-b^2)^{11}}\right)\Bigg]\,\frac{(x-X)}{\rho}\,\mathrm{d}x, \end{aligned}$$

After writing the integral in terms of ρ only (where $\rho^2 = (x-X)^2 + a^2$), integrating and substituting

the bounds of integration, the interaction force between a sphere and a semi-infinite cylinder is

$$F(X) = 8\pi^2\, a\, b^2\, n_1\, n_2 \left[A \left(\frac{1}{(a^2 - b^2 + X^2)^3} + \frac{2\, b^2}{(a^2 - b^2 + X^2)^4} \right) - \frac{1}{5} B \left(\frac{5}{(a^2 - b^2 + X^2)^6} + \frac{80\, b^2}{(a^2 - b^2 + X^2)^7} + \frac{336\, b^4}{(a^2 - b^2 + X^2)^8} + \frac{512\, b^6}{(a^2 - b^2 + X^2)^9} + \frac{256\, b^8}{(a^2 - b^2 + X^2)^{10}} \right) \right]. \quad \text{(A.8)}$$

A.3. STEP-BY-STEP CALCULATIONS FOR KINETIC ENERGY

Assuming that the attraction limit is given by $\mathsf{X_0}$ and that the point (or sphere) is far (left) from the entrance of the semi-infinite cylinder, the acceptance energy is calculated by using Equation (2.5) and the maximum kinetic energy of a point (and sphere) is given by Equation (2.6)

A.3.1. Point atom to semi-infinite cylinder

The acceptance energy for a point to enter into the semi-infinite cylinder is calculated by

$$\begin{aligned} Ea &= 2\pi\, a\, n_1 \int_{-\infty}^{X_0} \left[\frac{A}{(X^2 + a^2)^3} - \frac{B}{(X^2 + a^2)^6} \right] \mathrm{d}X, \\ &= \frac{2\pi\, n_1}{a^4} \int_{-\frac{\pi}{2}}^{\psi} \left[A \cos^4 \psi' - \frac{1}{a^6} B \cos^{10} \psi' \right] \mathrm{d}\psi', \end{aligned}$$

by using a trig substitution, $X = a \tan \psi'$. Acceptance energy can be rewritten in terms of the functions defined in Appendix D, $J_n(a, -X_0)$,

$$Ea = \frac{2\pi\, n_1}{a^4} \left[A\, J_2(a, -X_0) - \frac{1}{a^6} B\, J_5(a, -X_0) \right]. \quad \text{(A.9)}$$

Considering maximum kinetic energy for a point to move from far (left) field to far (right) into the cylinder,

$$\begin{aligned} Ek &= 2\pi\, a\, n_1 \int_{-\infty}^{\infty} \left[\frac{A}{(X^2 + a^2)^3} - \frac{B}{(X^2 + a^2)^6} \right] \mathrm{d}X, \\ &= \frac{2\pi\, n_1}{a^4} \left[A \left(\frac{3\pi}{8} \right) - \frac{1}{a^6} B \left(\frac{63\pi}{256} \right) \right], \\ &= \frac{3\pi^2\, n_1}{128\, a^4} \left[32\, A - \frac{21}{a^6} B \right]. \end{aligned} \quad \text{(A.10)}$$

A.3.2. Sphere to semi-infinite cylinder

The acceptance energy for a sphere to enter into the semi-infinite cylinder is calculated by

$$\begin{aligned}
Ea &= 8\pi^2\, a\, b^2\, n_1\, n_2 \int_{-\infty}^{X_0} \left[A \left(\frac{1}{(a^2-b^2+X^2)^3} + \frac{2\,b^2}{(a^2-b^2+X^2)^4} \right) \right. \\
&\quad -\frac{1}{5} B \left(\frac{5}{(a^2-b^2+X^2)^6} + \frac{80\,b^2}{(a^2-b^2+X^2)^7} + \frac{336\,b^4}{(a^2-b^2+X^2)^8} + \frac{512\,b^6}{(a^2-b^2+X^2)^9} \right. \\
&\quad \left. \left. + \frac{256\,b^8}{(a^2-b^2+X^2)^{10}} \right) \right] \mathrm{d}X, \\
&= 8\pi^2\, a\, b^2\, n_1\, n_2\, \lambda \int_{-\frac{\pi}{2}}^{\psi} \left[A\,\lambda^{-6} \left(\cos^4\psi' + 2\,b^2\,\lambda^{-2}\,\cos^6\psi' \right) \right. \\
&\quad -\frac{1}{5} B\,\lambda^{-12} \left(5\,\cos^{10}\psi' + 80\,b^2\,\lambda^{-2}\cos^{12}\psi' + 336\,b^4\,\lambda^{-4}\cos^{14}\psi' + 512\,b^6\,\lambda^{-6}\cos^{16}\psi' \right. \\
&\quad \left. \left. +256\,b^8\,\lambda^{-8}\cos^{18}\psi' \right) \right] \mathrm{d}\psi',
\end{aligned}$$

where $\lambda^2 = a^2 - b^2$ and using a trig substitution, $X = \lambda \tan\psi'$. Acceptance energy can be rewritten in terms of the functions defined in Appendix D, $J_n(\lambda, -X_0)$,

$$\begin{aligned}
Ea &= 8\pi^2\, a\, b^2\, n_1\, n_2\, \lambda^{-5} \left[A \left(J_2(\lambda,-X_0) + 2\,b^2\,\lambda^{-2}\,J_3(\lambda,-X_0) \right) \right. \\
&\quad -\frac{1}{5}\lambda^{-6}\,B \left(5\,J_5(\lambda,-X_0) + 80\,b^2\,\lambda^{-2} J_6(\lambda,-X_0) + 336\,b^4\,\lambda^{-4} J_7(\lambda,-X_0) \right. \\
&\quad \left. \left. +512\,b^6\,\lambda^{-6} J_8(\lambda,-X_0) + 256\,b^8\,\lambda^{-8} J_9(\lambda,-X_0) \right) \right]. \qquad \text{(A.11)}
\end{aligned}$$

Considering maximum kinetic energy for a sphere to move from far (left) field to far (right) into the cylinder,

$$\begin{aligned}
Ek &= 8\pi^2\, a\, b^2\, n_1\, n_2 \int_{-\infty}^{\infty} \left[A \left(\frac{1}{(\lambda^2+X^2)^3} + \frac{2\,b^2}{(\lambda^2+X^2)^4} \right) \right. \\
&\quad -\frac{1}{5} B \left(\frac{5}{(\lambda^2+X^2)^6} + \frac{80\,b^2}{(\lambda^2+X^2)^7} + \frac{336\,b^4}{(\lambda^2+X^2)^8} + \frac{512\,b^6}{(\lambda^2+X^2)^9} \right. \\
&\quad \left. \left. + \frac{256\,b^8}{(\lambda^2+X^2)^{10}} \right) \right] \mathrm{d}X, \\
&= 8\pi^2\, a\, b^2\, n_1\, n_2 \lambda^{-5} \left[A \left(\frac{3\pi}{8} + 2\,b^2\,\lambda^{-2} \left(\frac{5\pi}{16} \right) \right) \right. \\
&\quad -\frac{1}{5}\lambda^{-6}\,B \left(5 \left(\frac{63\pi}{256} \right) + 80\,b^2\,\lambda^{-2} \left(\frac{231\pi}{1024} \right) + 336\,b^4\,\lambda^{-4} \left(\frac{429\pi}{2048} \right) \right. \\
&\quad \left. \left. +512\,b^6\,\lambda^{-6} \left(\frac{6435\pi}{32768} \right) + 256\,b^8\,\lambda^{-8} \left(\frac{12155\pi}{65536} \right) \right) \right],
\end{aligned}$$

$$= \pi^3\, a\, b^2\, n_1\, n_2 \lambda^{-5} \left[A\left(3 + 5\, b^2\, \lambda^{-2}\right) - \frac{1}{80} \lambda^{-6}\, B\, \left(315 + 2310\, b^2\, \lambda^{-2} \right.\right.$$
$$\left.\left. + 9009\, b^4\, \lambda^{-4} + 12870\, b^6\, \lambda^{-6} + 12155\, b^8\, \lambda^{-8}\right)\right] . \qquad \text{(A.12)}$$

APPENDIX B

CALCULATION OF THE INTERACTION ENERGY AND FORCE BETWEEN EITHER A POINT OR A SPHERE AND A FINITE CYLINDER

The geometry of the problem is described in Figure 3.1 and the surrounding text, however the cylinder has a finite depth d.

B.1. STEP-BY-STEP CALCULATIONS FOR INTERACTION ENERGY

The continuum Lennard-Jones approximation of the interaction energy of non-bonded atoms is described by Equation (2.3), where S_1 describes the surface of the finite cylinder with a mean surface density of n_1 and S_2 describes the surface of the interacting object with a mean surface density of n_2.

B.1.1. Point to finite cylinder

When considering the interacting energies between a point and a finite cylinder, the Lennard-Jones potential is integrated only along the surface of the finite cylinder,

$$\begin{aligned} E(X) &= n_1 \int_{S_1} U(\rho) \mathrm{d}S_1, \\ &= 2\pi\, a\, n_1 \int_0^d \left[-\frac{A}{\rho^6} + \frac{B}{\rho^{12}} \right] \mathrm{d}x, \\ &= 2\pi\, a\, n_1 \int_0^d \left[-\frac{A}{(a^2 + (x-X)^2)^3} + \frac{B}{(a^2 + (x-X)^2)^6} \right] \mathrm{d}x, \end{aligned} \tag{B.1}$$

where $\rho^2 = a^2 + (x-X)^2$. Let $x_* = x - X$, then at the upper bound of integration $x = 0$, $x_* = -X$, and at the lower bound of integration as $x = d$, $x_* = d - X$, so that

$$E(X) = 2\pi\, a\, n_1 \int_{-X}^{d-X} \left[-\frac{A}{(a^2 + x_*^2)^3} + \frac{B}{(a^2 + x_*^2)^6} \right] \mathrm{d}x_*.$$

Let $x_* = a \tan\psi$, then $\mathrm{d}x_* = a \sec^2\psi\, \mathrm{d}\psi$. The bounds of integration are transformed as follows: at $x_* = -X$, then $\psi = \psi_1 = -\arctan[X/a]$ and at $x_* = -X$, then $\psi = \psi_2 = \arctan[d - X/a]$.

Therefore

$$E(X) = 2\pi\, a\, n_1 \int_{\psi_1}^{\psi_2} \left[-\frac{A}{(a^2 \sec^2\psi)^3} + \frac{B}{(a^2 \sec^2\psi)^6} \right] a\, \sec^2\psi \mathrm{d}\psi,$$
$$= \frac{2\pi\, n_1}{a^4} \int_{\psi_1}^{\psi_2} \left[-A \cos^4\psi + \frac{1}{a^6} B \cos^{10}\psi \right] \mathrm{d}\psi. \tag{B.2}$$

Equation (B.2) can be expressed in terms of integrals of the powers of cosine functions, $H_n(a, -X; d)$ define in Appendix D. The potential energy of a point interacting with a finite cylinder is

$$E(X) = \frac{2\pi\, n_1}{a^4} \left[-A\, H_2(a, -X; d) + \frac{1}{a^6} B\, H_5(a, -X; d) \right]. \tag{B.3}$$

B.1.2. Sphere to finite cylinder

Assuming the continuum approach to calculate the interaction energies between a sphere and a finite cylinder, as a result the surface of both objects are integrated over,

$$E(X) = n_1\, n_2 \int_{S_1} \int_{S_2} U(\rho)\, \mathrm{d}S_2\, \mathrm{d}S_1,$$

where S_1 is the surface of the finite cylinder with a corresponding mean surface density of atoms n_1, and S_2 is the surface of the sphere with a mean surface density of atoms, n_2.

Denoting the integral over the surface of the sphere as $G(\rho)$ [1, 13],

$$G(\rho) = n_2 \int_{S_2} U(\rho)\, \mathrm{d}S_2,$$
$$= \frac{\pi\, b\, n_2}{\rho} \left[\frac{A}{2} \left(\frac{1}{(\rho+b)^4} - \frac{1}{(\rho-b)^4} \right) - \frac{B}{5} \left(\frac{1}{(\rho+b)^{10}} - \frac{1}{(\rho-b)^{10}} \right) \right],$$
$$= 4\pi\, b^2\, n_2 \left[-A \left(\frac{1}{(\rho^2-b^2)^3} + \frac{2\, b^2}{(\rho^2-b^2)^4} \right) + \frac{1}{5} B \left(\frac{5}{(\rho^2-b^2)^6} + \frac{80\, b^2}{(\rho^2-b^2)^7} \right.$$
$$\left. + \frac{336\, b^4}{(\rho^2-b^2)^8} + \frac{512\, b^6}{(\rho^2-b^2)^9} + \frac{256\, b^8}{(\rho^2-b^2)^{10}} \right) \right].$$

The total interacting energy between the sphere and finite cylinder is calculated by integrating over

the surface of the finite cylinder,

$$
\begin{aligned}
E(X) &= n_1 \int_{S_1} G(\rho)\mathrm{d}S_1, \\
&= 2\pi\, a\, n_1 \int_0^d G(\rho)\mathrm{d}x, \\
&= 8\pi^2\, a\, b^2\, n_1\, n_2 \int_0^d \left[-A\left(\frac{1}{(\rho^2-b^2)^3} + \frac{2\,b^2}{(\rho^2-b^2)^4} \right) + \frac{1}{5} B \left(\frac{5}{(\rho^2-b^2)^6} + \frac{80\,b^2}{(\rho^2-b^2)^7} \right.\right. \\
&\quad \left.\left. + \frac{336\,b^4}{(\rho^2-b^2)^8} + \frac{512\,b^6}{(\rho^2-b^2)^9} + \frac{256\,b^8}{(\rho^2-b^2)^{10}} \right) \right] \mathrm{d}x, \\
&= 8\pi^2\, a\, b^2\, n_1\, n_2 \int_0^d \left[-A\left(\frac{1}{(a^2-b^2+(x-X)^2)^3} + \frac{2\,b^2}{(a^2-b^2+(x-X)^2)^4} \right) \right. \\
&\quad + \frac{1}{5} B \left(\frac{5}{(a^2-b^2+(x-X)^2)^6} + \frac{80\,b^2}{(a^2-b^2+(x-X)^2)^7} + \frac{336\,b^4}{(a^2-b^2+(x-X)^2)^8} \right. \\
&\quad \left.\left. + \frac{512\,b^6}{(a^2-b^2+(x-X)^2)^9} + \frac{256\,b^8}{(a^2-b^2+(x-X)^2)^{10}} \right) \right] \mathrm{d}x,
\end{aligned}
\tag{B.4}
$$

where $\rho^2 = a^2 + (x-X)^2$. Let $\lambda^2 = a^2 - b^2$ and $x_* = x - X$, $\mathrm{d}x_* = \mathrm{d}x$. Then

$$
\begin{aligned}
E(X) &= 8\pi^2\, a\, b^2\, n_1\, n_2 \int_{-X}^{d-X} \left[-A\left(\frac{1}{(\lambda^2+x_*^2)^3} + \frac{2\,b^2}{(\lambda^2+x_*^2)^4} \right) + \frac{1}{5} B \left(\frac{5}{(\lambda^2+x_*^2)^6} + \frac{80\,b^2}{(\lambda^2+x_*^2)^7} \right.\right. \\
&\quad \left.\left. + \frac{336\,b^4}{(\lambda^2+x_*^2)^8} + \frac{512\,b^6}{(\lambda^2+x_*^2)^9} + \frac{256\,b^8}{(\lambda^2+x_*^2)^{10}} \right) \right] \mathrm{d}x_*, \\
&= 8\pi^2\, a\, b^2\, n_1\, n_2\, \lambda \int_{\psi_1}^{\psi_2} \left[-A\,\lambda^{-6} \left(\cos^4\psi' + 2\,b^2\,\lambda^{-2}\,\cos^6\psi' \right) + \frac{1}{5} B\,\lambda^{-12} \left(5\,\cos^{10}\psi' \right.\right. \\
&\quad \left.\left. + 80\,b^2\,\lambda^{-2}\cos^{12}\psi' + 336\,b^4\,\lambda^{-4}\cos^{14}\psi' + 512\,b^6\,\lambda^{-6}\cos^{16}\psi' + 256\,b^8\,\lambda^{-8}\cos^{18}\psi' \right) \right] \mathrm{d}\psi',
\end{aligned}
\tag{B.5}
$$

after performing a trig substitution $x_* = \lambda \tan\psi'$. This expression can rewritten in terms of $H_n(\lambda, -X; d)$, defined in Appendix D, so that the interaction energy between a sphere and a finite cylinder is

$$
\begin{aligned}
E(X) &= 8\pi^2\, a\, b^2\, n_1\, n_2\, \lambda^{-5} \left[-A \left(H_2(\lambda,-X;d) + 2\,b^2\,\lambda^{-2}\,H_3(\lambda,-X;d) \right) \right. \\
&\quad + \frac{1}{5} B\,\lambda^{-6} \left(5\,H_5(\lambda,-X;d) + 80\,b^2\,\lambda^{-2} H_6(\lambda,-X;d) + 336\,b^4\,\lambda^{-4} H_7(\lambda,-X;d) \right. \\
&\quad \left.\left. + 512\,b^6\,\lambda^{-6} H_8(\lambda,-X;d) + 256\,b^8\,\lambda^{-8} H_9(\lambda,-X;d) \right) \right].
\end{aligned}
\tag{B.6}
$$

B.2. STEP-BY-STEP CALCULATIONS FOR INTERACTION FORCE

The interaction forces in the axial (x) direction between a point or a sphere and a finite cylinder can be calculated using Equations (2.3) and (2.4).

B.2.1. Point to finite cylinder

Using the interaction energy between a point and finite cylinder, Equation (B.1), and the relationship between the energy and the force, then the van der Waals force in the axial direction, Equation (2.4), due to the interaction with the entire surface of the finite cylinder is given by

$$\begin{aligned} F(X) &= \frac{\mathrm{d}\,E}{\mathrm{d}\rho}\frac{(x-X)}{\rho}, \\ &= 2\,\pi\,a\,n_1 \int_0^d \left[6\frac{A}{\rho^7} - 12\frac{B}{\rho^{13}}\right]\,\frac{(x-X)}{\rho}\,\mathrm{d}x. \end{aligned}$$

Using $\rho^2 = (x-X)^2 + a^2$, the integral and the bounds of integration are transformed. The interaction forces between a point and a finite cylinder is

$$\begin{aligned} F(X) &= 2\,\pi\,a\,n_1 \int_{\rho_1}^{\rho_2} \left[6\frac{A}{\rho^7} - 12\frac{B}{\rho^{13}}\right]\,\mathrm{d}\rho, \\ &= 2\,\pi\,a\,n_1 \left[-\frac{A}{\rho^6} + \frac{B}{\rho^{12}}\right]\Bigg|_{\rho_1}^{\rho_2}, \\ &= 2\,\pi\,a\,n_1 \left[\frac{A}{(a^2+X^2)^3} - \frac{B}{(a^2+X^2)^6} - \frac{A}{(a^2+(d-X)^2)^3} + \frac{B}{(a^2+(d-X)^2)^6}\right]. \end{aligned} \tag{B.7}$$

B.2.2. Sphere to finite cylinder

Using the interaction energy between a sphere and finite cylinder, Equation (B.4), and the relationship between the energy and the force, then the van der Waals force in the axial direction, Equation (2.4), due to the interaction with the entire surface of the finite cylinder is given by

$$\begin{aligned} F(X) = 8\pi^2\,a\,b^2\,n_1\,n_2 \int_0^d \Bigg[2\rho\,A\left(\frac{3}{(\rho^2-b^2)^4} + \frac{8\,b^2}{(\rho^2-b^2)^5}\right) - \frac{2}{5}\rho\,B\left(\frac{30}{(\rho^2-b^2)^7} + \frac{560\,b^2}{(\rho^2-b^2)^8}\right. \\ \left. + \frac{2688\,b^4}{(\rho^2-b^2)^9} + \frac{4608\,b^6}{(\rho^2-b^2)^{10}} + \frac{2560\,b^8}{(\rho^2-b^2)^{11}}\right)\Bigg]\,\frac{(x-X)}{\rho}\,\mathrm{d}x. \end{aligned}$$

After writing the integral in terms of ρ only (where $\rho^2 = (x-X)^2 + a^2$), integrating and substituting

the bounds of integration, the interaction force between a sphere and a finite cylinder is

$$
\begin{aligned}
F(X) = 8\pi^2\, a\, b^2\, n_1\, n_2 \Bigg[& A\left(\frac{1}{(a^2-b^2+X^2)^3}+\frac{2\,b^2}{(a^2-b^2+X^2)^4}\right)-\frac{1}{5}B\left(\frac{5}{(a^2-b^2+X^2)^6}\right.\\
& \left.+\frac{80\,b^2}{(a^2-b^2+X^2)^7}+\frac{336\,b^4}{(a^2-b^2+X^2)^8}+\frac{512\,b^6}{(a^2-b^2+X^2)^9}+\frac{256\,b^8}{(a^2-b^2+X^2)^{10}}\right)\\
& -A\left(\frac{1}{(a^2-b^2+(d-X)^2)^3}+\frac{2\,b^2}{(a^2-b^2+(d-X)^2)^4}\right)\\
& +\frac{1}{5}B\left(\frac{5}{(a^2-b^2+(d-X)^2)^6}+\frac{80\,b^2}{(a^2-b^2+(d-X)^2)^7}+\frac{336\,b^4}{(a^2-b^2+(d-X)^2)^8}\right.\\
& \left.+\frac{512\,b^6}{(a^2-b^2+(d-X)^2)^9}+\frac{256\,b^8}{(a^2-b^2+(d-X)^2)^{10}}\right)\Bigg]. \qquad \text{(B.8)}
\end{aligned}
$$

B.3. STEP-BY-STEP CALCULATIONS FOR KINETIC ENERGY

Assuming that the attraction limit is given by $\mathsf{X_0}$ and that the point (or sphere) is far from the entrance of the finite cylinder, the acceptance energy (and maximum kinetic energy) is calculated by using Equation (2.7)

B.3.1. Point to finite cylinder

The acceptance energy for the point to be accepted into the finite cylinder is calculated by

$$
\begin{aligned}
Ea &= 2\pi\, a\, n_1 \int_{-\infty}^{X_0}\left[\frac{A}{(a^2+X^2)^3}-\frac{B}{(a^2+X^2)^6}-\frac{A}{(a^2+(d-X)^2)^3}+\frac{B}{(a^2+(d-X)^2)^6}\right]\mathrm{d}X,\\
&= \frac{2\pi\, n_1}{a^4}\int_{\frac{\pi}{2}}^{\psi_0}\left[A\cos^4\psi-\frac{1}{a^6}B\cos^{10}\psi\right]\mathrm{d}\psi-\frac{2\pi\, n_1}{a^4}\int_{\frac{\pi}{2}}^{\tau_0}\left[A\cos^4\tau-\frac{1}{a^6}B\cos^{10}\tau\right]\mathrm{d}\tau,
\end{aligned}
$$

by using a trig substitution $X=-a\tan\psi$ and $X=d-a\tan\tau$. Acceptance energy can be rewritten in terms of functions defined in Appendix D, $J_n(a,-X_0)$ and $H_n(a,-X_0;d)$,

$$
\begin{aligned}
Ea &= \frac{2\pi\, n_1}{a^4}\left[A\, J_2(a,-X_0)-\frac{1}{a^6}B\, J_5(a,-X_0)-A\, J_2(a,d-X_0)+\frac{1}{a^6}B\, J_5(a,d-X_0)\right],\\
&= \frac{2\pi\, n_1}{a^4}\left[A\, H_2(a,-X_0;d)-\frac{1}{a^6}B\, H_5(a,-X_0;d)\right]. \qquad \text{(B.9)}
\end{aligned}
$$

Considering the maximum kinetic energy gain by a point to move from the far (left) field to distance

$d/2$ into the cylinder (i.e, to the middle of the cylinder's depth),

$$
\begin{aligned}
Ek &= 2\pi\, a\, n_1 \int_{-\infty}^{d/2} \left[\frac{A}{(X^2+a^2)^3} - \frac{B}{(X^2+a^2)^6}\right] \mathrm{d}X \\
&\quad - 2\,\pi\, a\, n_1 \int_{-\infty}^{d/2} \left[\frac{A}{(a^2+(d-X)^2)^3} - \frac{B}{(a^2+(d-X)^2)^6}\right] \mathrm{d}X, \\
&= \frac{2\pi\, n_1}{a^4}\left[A\left(J_2\left(a,\frac{d}{2}\right) - J_2\left(a,-\frac{d}{2}\right)\right) - \frac{1}{a^6}B\left(J_5\left(a,\frac{d}{2}\right) - J_5\left(a,-\frac{d}{2}\right)\right)\right], \\
&= \frac{2\pi\, n_1}{a^4}\left[A\, H_2\left(a,-\frac{d}{2};d\right) - \frac{1}{a^6}B\, H_5\left(a,-\frac{d}{2};d\right)\right], \\
&= \frac{2\pi\, n_1}{a^4}\left[A\left(I_2\left(a,\frac{d}{2}\right) - I_2\left(a,-\frac{d}{2}\right)\right) - \frac{1}{a^6}B\left(I_5\left(a,\frac{d}{2}\right) - I_5\left(a,-\frac{d}{2}\right)\right)\right], \\
&= \frac{4\pi\, n_1}{a^4}\left[A\, I_2\left(a,\frac{d}{2}\right) - \frac{1}{a^6}B\, I_5\left(a,\frac{d}{2}\right)\right], \\
&= \frac{4\pi\, n_1}{a^4}\left[A\, I_2\left(2a,d\right) - \frac{1}{a^6}B\, I_5\left(2a,d\right)\right].
\end{aligned} \tag{B.10}
$$

B.3.2. Sphere to finite cylinder

The acceptance energy for the sphere to be accepted into the finite cylinder is calculated by

$$
\begin{aligned}
Ea &= 8\pi^2\, a\, b^2\, n_1\, n_2 \int_{-\infty}^{X_0} \left[A\left(\frac{1}{(a^2-b^2+X^2)^3} + \frac{2\,b^2}{(a^2-b^2+X^2)^4}\right)\right. \\
&\quad -\frac{1}{5}B\left(\frac{5}{(a^2-b^2+X^2)^6} + \frac{80\,b^2}{(a^2-b^2+X^2)^7} + \frac{336\,b^4}{(a^2-b^2+X^2)^8} + \frac{512\,b^6}{(a^2-b^2+X^2)^9}\right. \\
&\quad \left.\left. +\frac{256\,b^8}{(a^2-b^2+X^2)^{10}}\right)\right] \mathrm{d}X \\
&\quad - 8\pi^2\, a\, b^2\, n_1\, n_2 \int_{-\infty}^{X_0} \left[A\left(\frac{1}{(a^2-b^2+(h-X)^2)^3} + \frac{2\,b^2}{(a^2-b^2+(h-X)^2)^4}\right)\right. \\
&\quad -\frac{1}{5}B\left(\frac{5}{(a^2-b^2+(d-X)^2)^6} + \frac{80\,b^2}{(a^2-b^2+(d-X)^2)^7} + \frac{336\,b^4}{(a^2-b^2+(d-X)^2)^8}\right. \\
&\quad \left.\left. +\frac{512\,b^6}{(a^2-b^2+(d-X)^2)^9} + \frac{256\,b^8}{(a^2-b^2+(d-X)^2)^{10}}\right)\right] \mathrm{d}X, \\
&= 8\pi^2\, a\, b^2\, n_1\, n_2\, \lambda \int_{\frac{\pi}{2}}^{\psi_0} \left[A\,\lambda^{-6}\,\left(\cos^4\psi + 2\,b^2\,\lambda^{-2}\,\cos^6\psi\right)\right. \\
&\quad -\frac{1}{5}B\,\lambda^{-12}\left(5\,\cos^{10}\psi + 80\,b^2\,\lambda^{-2}\cos^{12}\psi + 336\,b^4\,\lambda^{-4}\cos^{14}\psi + 512\,b^6\,\lambda^{-6}\cos^{16}\psi\right. \\
&\quad \left.\left. +256\,b^8\,\lambda^{-8}\cos^{18}\psi\right)\right] \mathrm{d}\psi \\
&\quad - 8\pi^2\, a\, b^2\, n_1\, n_2\, \lambda \int_{\frac{\pi}{2}}^{\tau_0} \left[A\,\lambda^{-6}\,\left(\cos^4\tau + 2\,b^2\,\lambda^{-2}\,\cos^6\tau\right)\right. \\
&\quad -\frac{1}{5}B\,\lambda^{-12}\left(5\,\cos^{10}\tau + 80\,b^2\,\lambda^{-2}\cos^{12}\tau + 336\,b^4\,\lambda^{-4}\cos^{14}\tau + 512\,b^6\,\lambda^{-6}\cos^{16}\tau\right.
\end{aligned}
$$

$$+256\,b^8\,\lambda^{-8}\cos^{18}\tau\big)\big]\;\mathrm{d}\tau,$$

where $\lambda^2 = a^2 - b^2$ and by using the trig substitutions $X_0 = -\lambda\tan\psi$ and $X_0 = d - \lambda\tan\tau$. Acceptance energy can be rewritten in terms of the functions define in Appendix D, $H_n(\lambda, -X_0; d)$,

$$\begin{aligned}
Ea = 8\pi^2\,a\,b^2\,n_1\,n_2\,\lambda^{-5}\,\big[&A\left(H_2(\lambda,-X_0;d) + 2\,b^2\,\lambda^{-2}\,H_3(\lambda,-X_0;d)\right)\\
&-\frac{1}{5}\lambda^{-6}\,B\,\left(5\,H_5(\lambda,-X_0;d) + 80\,b^2\,\lambda^{-2}H_6(\lambda,-X_0;d) + 336\,b^4\,\lambda^{-4}H_7(\lambda,-X_0;d)\right.\\
&\left.+512\,b^6\,\lambda^{-6}H_8(\lambda,-X_0;d) + 256\,b^8\,\lambda^{-8}H_9(\lambda,-X_0;d)\right)\big]\,. \qquad \text{(B.11)}
\end{aligned}$$

Considering the maximum kinetic energy gain by a sphere to move from the far (left) field to distance $d/2$ into the cylinder,

$$\begin{aligned}
Ek = 8\pi^2\,a\,b^2\,n_1\,n_2\int_{-\infty}^{d/2}\,&\left[A\left(\frac{1}{(\lambda^2+X^2)^3} + \frac{2\,b^2}{(\lambda^2+X^2)^4}\right)\right.\\
&-\frac{1}{5}B\left(\frac{5}{(\lambda^2+X^2)^6} + \frac{80\,b^2}{(\lambda^2+X^2)^7} + \frac{336\,b^4}{(\lambda^2+X^2)^8} + \frac{512\,b^6}{(\lambda^2+X^2)^9}\right.\\
&\left.\left.+\frac{256\,b^8}{(\lambda^2+X^2)^{10}}\right)\right]\mathrm{d}X\\
&-8\pi^2\,a\,b^2\,n_1\,n_2\int_{-\infty}^{d/2}\,\left[A\left(\frac{1}{(\lambda^2+(d-X)^2)^3} + \frac{2\,b^2}{(\lambda^2+(d-X)^2)^4}\right)\right.\\
&-\frac{1}{5}B\left(\frac{5}{(\lambda^2+(d-X)^2)^6} + \frac{80\,b^2}{(\lambda^2+(d-X)^2)^7} + \frac{336\,b^4}{(\lambda^2+(d-X)^2)^8}\right.\\
&\left.\left.+\frac{512\,b^6}{(\lambda^2+(d-X)^2)^9} + \frac{256\,b^8}{(\lambda^2+(d-X)^2)^{10}}\right)\right]\mathrm{d}X,\\
=8\pi^2\,a\,b^2\,n_1\,n_2\,\lambda^{-5}\,&\left[A\left(H_2\left(a,-\frac{d}{2};d\right) + 2\,b^2\,\lambda^{-2}\,H_3\left(a,-\frac{d}{2};d\right)\right)\right.\\
&-\frac{1}{5}\lambda^{-6}\,B\,\left(5\,H_5\left(a,-\frac{d}{2};d\right) + 80\,b^2\,\lambda^{-2}H_6\left(a,-\frac{d}{2};d\right) + 336\,b^4\,\lambda^{-4}H_7\left(a,-\frac{d}{2};d\right)\right.\\
&\left.\left.+512\,b^6\,\lambda^{-6}H_8\left(a,-\frac{d}{2};d\right) + 256\,b^8\,\lambda^{-8}H_9\left(a,-\frac{d}{2};d\right)\right)\right]\,,\\
=16\pi^2\,a\,b^2\,n_1\,n_2\,\lambda^{-5}\,&\left[A\left(I_2(2\lambda,d) + 2\,b^2\,\lambda^{-2}\,I_3(2\lambda,d)\right)\right.\\
&-\frac{1}{5}\lambda^{-6}\,B\,\left(5\,I_5(2\lambda,d) + 80\,b^2\,\lambda^{-2}I_6(2\lambda,d) + 336\,b^4\,\lambda^{-4}I_7(2\lambda,d)\right.\\
&\left.\left.+512\,b^6\,\lambda^{-6}I_8(2\lambda,d) + 256\,b^8\,\lambda^{-8}I_9(2\lambda,d)\right)\right]\,. \qquad \text{(B.12)}
\end{aligned}$$

APPENDIX C

CALCULATION OF THE INTERACTION ENERGY AND FORCE BETWEEN A POINT AND A SEMI-INFINITE RECTANGULAR PRISM

The geometry of the problem is described in Figure 5.3 and the surrounding text.

C.1. STEP-BY-STEP CALCULATIONS FOR INTERACTION ENERGY

The continuum Lennard-Jones approximation of the interaction energy of non-bonded atoms is described by Equation (2.3), where S_1 describes the surface elements of the semi-infinite rectangular prism with a mean surface density of n_1 and S_2 describes the surface of the interacting object with a mean surface density of n_2.

C.1.1. Point to semi-infinite line

When considering the interacting energies in a three-dimensional Cartesian coordinate frame, between a point (x_p, y_p, z_p) and a semi-infinite line (x_q, y_q, z_q), the Lennard-Jones potential is integrated only along the semi-infinite line,

$$\begin{aligned} E &= n_1 \int_{S_1} U(\rho) \mathrm{d}S_1, \\ &= n_1 \int_0^\infty \left[-\frac{A}{\rho^6} + \frac{B}{\rho^{12}} \right] \mathrm{d}x, \\ &= n_1 \int_0^\infty \left[-\frac{A}{((x-X)^2+\alpha^2+\beta^2)^3} + \frac{B}{((x-X)^2+\alpha^2+\beta^2)^6} \right] \mathrm{d}x, \end{aligned} \tag{C.1}$$

where $(x_p, y_p, z_p) = (X, 0, 0)$ and $(x_q, y_q, z_q) = (x, \alpha, \beta)$, $x \in \mathbb{R}^+ \cup \{0\}$, α and β are real constants, $\rho^2 = (x-X)^2 + \alpha^2 + \beta^2$. Let $x_* = x - X$, then at the upper bound of integration $x = 0$, $x_* = -X$, and at the lower bound of integration as $x \to \infty$, $x_* \to \infty$, so that

$$E = n_1 \int_{-X}^\infty \left[-\frac{A}{(x_*^2+\alpha^2+\beta^2)^3} + \frac{B}{(x_*^2+\alpha^2+\beta^2)^6} \right] \mathrm{d}x_*.$$

Let $\lambda^2 = \alpha^2 + \beta^2$ and $x_* = \lambda \tan\psi$, then $\lambda^2 + x_*^2 = \lambda^2 + \lambda^2 \tan^2\psi = \lambda^2 \sec^2\psi$ and $\mathrm{d}x_* = \lambda \sec^2\psi \, \mathrm{d}\psi$. The bounds of integration are transformed as follows: as $x_* \to \infty$, $\psi = \pi/2$ and $x_* = -X$, then

$\psi = \psi_0 = \arctan[-X/\lambda]$. We then obtain

$$\begin{aligned} E &= n_1 \int_{\psi_0}^{\frac{\pi}{2}} \left[-\frac{A}{(\lambda^2 \sec^2\psi)^3} + \frac{B}{(\lambda^2 \sec^2\psi)^6} \right] \lambda \sec^2\psi \mathrm{d}\psi, \\ &= n_1 \lambda^{-5} \int_{\psi_0}^{\frac{\pi}{2}} \left[-A\cos^4\psi + \lambda^{-6} B \cos^{10}\psi \right] \mathrm{d}\psi. \end{aligned} \tag{C.2}$$

Equation (C.2) can be expressed in terms of integrals of powers of cosine functions, $J_n(\lambda, -X)$ define in Appendix D. The potential energy of a point interacting with a semi-infinite cylinder is therefore

$$E = n_1 \lambda^{-5} \left[-A\, J_2(\lambda, -X) + \lambda^{-6} B\, J_5(\lambda, -X) \right]. \tag{C.3}$$

C.1.2. Point to perpendicular semi-infinite plane

When considering the interacting energies in a three-dimensional Cartesian coordinate frame, between a point (x_p, y_p, z_p) and a semi-infinite plane (x_q, y_q, z_q), the Lennard-Jones potential is integrated only along the surface of the semi-infinite plane,

$$\begin{aligned} E &= n_1 \int_{S_1} U(\rho) \mathrm{d}S_1, \\ &= n_1 \int_0^\infty \int_{\alpha_1}^{\alpha_2} \left[-\frac{A}{\rho^6} + \frac{B}{\rho^{12}} \right] \mathrm{d}y\, \mathrm{d}x, \\ &= n_1 \int_0^\infty \int_{\alpha_1}^{\alpha_2} \left[-\frac{A}{((x-X)^2 + y^2 + \beta^2)^3} + \frac{B}{((x-X)^2 + y^2 + \beta^2)^6} \right] \mathrm{d}y\, \mathrm{d}x, \end{aligned} \tag{C.4}$$

where $(x_p, y_p, z_p) = (X, 0, 0)$ and $(x_q, y_q, z_q) = (x, y, \beta)$, $x \in \mathbb{R}^+ \cup \{0\}$, $y \in \{\alpha_1, \alpha_2\}$, α_i and β are real constants, and $\rho^2 = (x-X)^2 + y^2 + \beta^2$.

Redefine λ to be $\lambda^2 = (x-X)^2 + \beta^2$ and $y = \lambda \tan\psi$, then $\lambda^2 + y^2 = \lambda^2 + \lambda^2 \tan^2\psi = \lambda^2 \sec^2\psi$ and $\mathrm{d}y = \lambda \sec^2\psi\, \mathrm{d}\psi$. Then the upper bound of integration $y = \alpha_2$, $\psi_2 = \arctan[\alpha_2/\lambda]$, and at the lower bound of integration at $y = \alpha_1$, $\psi_1 = \arctan[\alpha_1/\lambda]$, so that

$$\begin{aligned} E &= n_1 \int_0^\infty \int_{\psi_1}^{\psi_2} \left[-\frac{A}{(\lambda^2 \sec^2\psi)^3} + \frac{B}{(\lambda^2 \sec^2\psi)^6} \right] \lambda \sec^2\psi\, \mathrm{d}\psi\, \mathrm{d}x, \\ &= n_1 \int_0^\infty \lambda^{-5} \int_{\psi_1}^{\psi_2} \left[-A\cos^4\psi + \lambda^{-6} B \cos^{10}\psi \right] \mathrm{d}\psi\, \mathrm{d}x. \end{aligned} \tag{C.5}$$

Equation (C.5) can be expressed in terms of integrals of powers of cosine functions, $I_n(\lambda, \alpha_i)$ define

in Appendix D. Therefore the potential energy functions can be written as

$$\begin{aligned} E &= n_1 \int_0^\infty \lambda^{-5} \left[-A \left(I_2(\lambda, \alpha_2) - I_2(\lambda, \alpha_1) \right) + \lambda^{-6} B \left(I_5(\lambda, \alpha_2) - I_5(\lambda, \alpha_1) \right) \right] \mathrm{d}x, \\ &= 2\, n_1 \int_0^\infty \lambda^{-5} \left[-A\, I_2(\lambda, \alpha_2) + \lambda^{-6} B\, I_5(\lambda, \alpha_2) \right] \mathrm{d}x. \end{aligned} \tag{C.6}$$

If α_2 and α_1 are equidistant from the y-axis, i.e. $\alpha_2 = |\alpha_1|$, the result can be simplified to Equation (C.6). From this point on, the α's subscript will be dropped for readability purposes and the second integral will be evaluated separately for the attractive and repulsive terms.

Solution for attractive part

Here, the analytical solution is valuated for the attractive term.

$$\begin{aligned} \int_0^\infty \lambda^{-5}\, I_2(\lambda, \alpha)\, \mathrm{d}x &= \int_0^\infty \lambda^{-5} \left[\frac{1}{4} \frac{\alpha\, \lambda^3}{(\lambda^2 + \alpha^2)^2} + \frac{3}{8} \frac{\alpha\, \lambda}{(\lambda^2 + \alpha^2)} + \frac{3}{8} \arctan\left(\frac{\alpha}{\lambda}\right) \right] \mathrm{d}x, \\ &= \int_{\lambda_0}^\infty \left[\frac{1}{4} \frac{\alpha}{\lambda^2 (\lambda^2 + \alpha^2)^2} + \frac{3}{8} \frac{\alpha}{\lambda^4 (\lambda^2 + \alpha^2)} \right] \frac{\lambda}{(\lambda^2 - \beta^2)^{1/2}} \mathrm{d}\lambda \\ &\quad + \int_0^\infty \frac{3}{8}\, \lambda^{-5} \arctan\left(\frac{\alpha}{\lambda}\right) \mathrm{d}x, \\ &= \int_{\lambda_0}^\infty \left[-\frac{1}{8\,\alpha^3} \frac{1}{\lambda} + \frac{3}{8\,\alpha} \frac{1}{\lambda^3} \right] \frac{1}{(\lambda^2 - \beta^2)^{1/2}} \mathrm{d}\lambda \qquad \text{(C.7)} \\ &\quad + \int_{\lambda_0}^\infty \left[\frac{1}{8\,\alpha^3} \frac{\lambda}{(\lambda^2 + \alpha^2)} - \frac{1}{4\,\alpha} \frac{\lambda}{(\lambda^2 + \alpha^2)^2} \right] \frac{1}{(\lambda^2 - \beta^2)^{1/2}} \mathrm{d}\lambda \qquad \text{(C.8)} \\ &\quad + \int_0^\infty \frac{3}{8}\, \lambda^{-5} \arctan\left(\frac{\alpha}{\lambda}\right) \mathrm{d}x, \qquad \text{(C.9)} \end{aligned}$$

where $\lambda^2 = (x - X)^2 + \beta^2$ and $\lambda_0 = (X^2 + \beta^2)^{1/2}$. The result will be solved in three separate parts, as the parts require slightly different techniques to be solved. Now consider Equation (C.7),

$$\begin{aligned} &\int_{\lambda_0}^\infty \left[-\frac{1}{8\,\alpha^3} \frac{1}{\lambda} + \frac{3}{8\,\alpha} \frac{1}{\lambda^3} \right] \frac{1}{(\lambda^2 - \beta^2)^{1/2}} \mathrm{d}\lambda \\ &\quad = \int_{\theta_0}^{\pi/2} \left[-\frac{1}{8\,\alpha^3} \cdot \frac{1}{\beta} + \frac{3}{8\,\alpha} \cdot \frac{1}{\beta^3} \cos^2\theta \right] \mathrm{d}\theta, \\ &\quad = -\frac{1}{8\,\alpha^3\,\beta} J_0(\beta, -X) + \frac{3}{8\,\alpha\,\beta^3} J_1(\beta, -X), \end{aligned}$$

where $\cos\theta = \beta/\lambda$ and $\theta_0 = \arctan[-X/\beta]$. The final result can be written in terms of the definite integrals for the cosine functions, $J_n(\beta, -X)$.

Consider Equation (C.8),

$$\int_{\lambda_0}^{\infty} \left[\frac{1}{8\,\alpha^3} \frac{\lambda}{(\lambda^2+\alpha^2)} - \frac{1}{4\,\alpha} \frac{\lambda}{(\lambda^2+\alpha^2)^2} \right] \frac{1}{(\lambda^2-\beta^2)^{1/2}}\,\mathrm{d}\lambda$$
$$= \int_{w_0}^{\infty} \left[\frac{1}{8\,\alpha^3} \cdot \frac{1}{w} - \frac{1}{4\,\alpha} \cdot \frac{1}{w^3} \right] \frac{1}{(w^2-(\alpha^2+\beta^2))^{1/2}} \mathrm{d}w,$$

where $w^2 = \lambda^2 + \alpha^2$ and $w_0 = (\alpha^2+\beta^2+X^2)^{1/2}$. The resulting integral in terms of w can be further transformed into an integrand of cosine functions, such that

$$\int_{w_0}^{\infty} \left[\frac{1}{8\,\alpha^3} \cdot \frac{1}{w} - \frac{1}{4\,\alpha} \cdot \frac{1}{w^3} \right] \frac{1}{(w^2-(\alpha^2+\beta^2))^{1/2}} \mathrm{d}w$$
$$= \int_{\theta_0}^{\pi/2} \left[\frac{1}{8\,\alpha^3} \cdot \frac{1}{(\alpha^2+\beta^2)^{1/2}} - \frac{1}{4\,\alpha} \cdot \frac{1}{(\alpha^2+\beta^2)^{3/2}} \cos^2\theta \right] \mathrm{d}\theta,$$
$$= \frac{1}{8\,\alpha^3\,(\alpha^2+\beta^2)^{1/2}} J_0(\sqrt{\alpha^2+\beta^2}, -X) - \frac{1}{4\,\alpha\,(\alpha^2+\beta^2)^{3/2}} J_1(\sqrt{\alpha^2+\beta^2}, -X),$$

where $\cos\theta = \sqrt{\alpha^2+\beta^2}/w$ and $\theta_0 = \arctan[-X/\sqrt{\alpha^2+\beta^2}]$. The final result can be written in terms of the definite integrals for the cosine functions, $J_n(\sqrt{\alpha^2+\beta^2}, -X)$.

Consider Equation (C.9),

$$\int_0^{\infty} \frac{3}{8} \left((x-X)^2+\beta^2\right)^{-5/2} \arctan\left(\frac{\alpha}{((x-X)^2+\beta^2)^{1/2}} \right) \mathrm{d}x = \frac{3}{8\,\alpha^3} \int_0^{w_0} \frac{w^3 \arctan w}{(\alpha^2-\beta^2\,w^2)^{1/2}} \mathrm{d}w,$$

where $w = \alpha/\sqrt{(x-X)^2+\beta^2}$ and $w_0 = \alpha/\sqrt{\beta^2+X^2}$.

$$\frac{3}{8\,\alpha^3} \int_0^{w_0} \frac{w^3 \arctan w}{(\alpha^2-\beta^2\,w^2)^{1/2}} \mathrm{d}w$$
$$= -\frac{3}{8\,\alpha^3\,\beta^2} \int_0^{w_0} w\,(\alpha^2-\beta^2\,w^2)^{1/2} \arctan w\,\mathrm{d}w$$
$$+ \frac{3}{8\,\alpha\,\beta^2} \int_0^{w_0} w\,(\alpha^2-\beta^2\,w^2)^{-1/2} \arctan w\,\mathrm{d}w,$$
$$= -\frac{3}{8\,\alpha^3\,\beta^2} \left[-\frac{(\alpha^2-\beta^2\,w^2)^{3/2}}{3\,\beta^2} \arctan w \Big|_0^{w_0} + \frac{1}{3\,\beta^2} \int_0^{w_0} \frac{(\alpha^2-\beta^2\,w^2)^{3/2}}{1+w^2}\,\mathrm{d}w \right]$$
$$+ \frac{3}{8\,\alpha\,\beta^2} \left[-\frac{(\alpha^2-\beta^2\,w^2)^{1/2}}{\beta^2} \arctan w \Big|_0^{w_0} + \frac{1}{\beta^2} \int_0^{w_0} \frac{(\alpha^2-\beta^2\,w^2)^{1/2}}{1+w^2}\,\mathrm{d}w \right],$$
$$= -\frac{(\alpha^2-\beta^2\,w_0^2)^{1/2}}{8\,\alpha^3\,\beta^4} (2\,\alpha^2+\beta^2\,w_0^2) \arctan w_0$$
$$+ \frac{1}{8\,\alpha^3\,\beta^4} \int_0^{w_0} \frac{(\alpha^2-\beta^2\,w^2)^{1/2}\,(2\,\alpha^2+\beta^2\,w^2)}{1+w^2}\,\mathrm{d}w,$$

$$= -\frac{(\alpha^2 - \beta^2\, w_0^2)^{1/2}}{8\,\alpha^3\,\beta^4}\,(2\,\alpha^2 + \beta^2\, w_0^2)\,\arctan w_0 + \frac{1}{8\,\alpha^3\,\beta^2}\int_0^{w_0}(\alpha^2 - \beta^2\, w^2)^{1/2}\,\mathrm{d}w$$
$$+ \frac{(2\,\alpha^2 - \beta^2)}{8\,\alpha^3\,\beta^4}\int_0^{w_0}\frac{(\alpha^2 - \beta^2\, w^2)^{1/2}}{1 + w^2}\,\mathrm{d}w,$$

To solve the remaining integrals, let $\beta\, w = \alpha \sin\theta$ and $\theta_0 = \arccos[-X/(\beta^2 + X^2)^{1/2}]$, then

$$\int_0^\infty \frac{3}{8}\,((x - X)^2 + \beta^2)^{-5/2}\,\arctan\left(\frac{\alpha}{((x - X)^2 + \beta^2)^{1/2}}\right)\mathrm{d}x$$
$$= -\frac{(\alpha^2 - \beta^2\, w_0^2)^{1/2}}{8\,\alpha^3\,\beta^4}\,(2\,\alpha^2 + \beta^2\, w_0^2)\,\arctan w_0 + \frac{1}{8\,\alpha\,\beta^3}\int_0^{\theta_0}\cos^2\theta\,\mathrm{d}\theta$$
$$+ \frac{(2\,\alpha^2 - \beta^2)}{8\,\alpha\,\beta^5}\int_0^{\theta_0}\frac{1}{1 + k^2\,\tan^2\theta}\,\mathrm{d}\theta,$$
$$= \frac{1}{8\,\beta^4}\frac{X\left(3\,\beta^2 + 2X^2\right)}{(\beta^2 + X^2)^{3/2}}\arctan\left(\frac{\alpha}{(\beta^2 + X^2)^{1/2}}\right) + \frac{1}{8\,\alpha\,\beta^3}\,G_0(-X, \beta)$$
$$+ \frac{2\alpha^2 - \beta^2}{8\,\alpha^3\,\beta^4}\left[(\beta^2 + \alpha^2)^{1/2}\arctan\left(\frac{(\beta^2 + \alpha^2)^{1/2}}{-X}\right) - \beta\,\arctan\left(\frac{\beta}{-X}\right)\right],$$

where $k^2 = 1 + (\alpha/\beta)^2$ and $G_0(-X, \beta)$ is defined as a trigonometric integral in Appendix E.

Solution for repulsive part

Here, the analytical solution is valuated for the repulsive term.

$$\int_0^\infty \lambda^{-11}\, I_5(\lambda, \alpha)\mathrm{d}x$$
$$= \int_0^\infty \lambda^{-11}\left[\frac{1}{10}\,\frac{\alpha\,\lambda^9}{(\lambda^2 + \alpha^2)^5} + \frac{9}{80}\,\frac{\alpha\,\lambda^7}{(\lambda^2 + \alpha^2)^4} + \frac{21}{160}\,\frac{\alpha\,\lambda^5}{(\lambda^2 + \alpha^2)^3} + \frac{21}{128}\,\frac{\alpha\,\lambda^3}{(\lambda^2 + \alpha^2)^2}\right.$$
$$\left. + \frac{63}{256}\frac{\alpha\,\lambda}{(\lambda^2 + \alpha^2)} + \frac{63}{256}\arctan\left(\frac{\alpha}{\lambda}\right)\right]\mathrm{d}x,$$
$$= \int_{\lambda_0}^\infty \left[\frac{1}{10}\,\frac{\alpha}{\lambda^2\,(\lambda^2 + \alpha^2)^5} + \frac{9}{80}\,\frac{\alpha}{\lambda^4\,(\lambda^2 + \alpha^2)^4} + \frac{21}{160}\,\frac{\alpha}{\lambda^6\,(\lambda^2 + \alpha^2)^3} + \frac{21}{128}\,\frac{\alpha}{\lambda^8\,(\lambda^2 + \alpha^2)^2}\right.$$
$$\left. + \frac{63}{256}\frac{\alpha}{\lambda^{10}\,(\lambda^2 + \alpha^2)}\right]\frac{\lambda}{(\lambda^2 - \beta^2)^{1/2}}\,\mathrm{d}\lambda$$
$$+ \int_0^\infty \frac{63}{256}\lambda^{-11}\arctan\left(\frac{\alpha}{\lambda}\right)\mathrm{d}x,$$
$$= \int_{\lambda_0}^\infty \left[\frac{7}{256\,\alpha^9}\frac{1}{\lambda} - \frac{9}{256\,\alpha^7}\frac{1}{\lambda^3} + \frac{63}{1280\,\alpha^5}\frac{1}{\lambda^5} - \frac{21}{256\,\alpha^3}\frac{1}{\lambda^7} + \frac{63}{256\,\alpha}\frac{1}{\lambda^9}\right]\frac{1}{(\lambda^2 - \beta^2)^{1/2}}\,\mathrm{d}\lambda \quad \text{(C.10)}$$
$$+ \int_{\lambda_0}^\infty \left[-\frac{7}{256\,\alpha^9}\frac{\lambda}{(\lambda^2 + \alpha^2)} + \frac{1}{128\,\alpha^7}\frac{\lambda}{(\lambda^2 + \alpha^2)^2} - \frac{1}{160\,\alpha^5}\frac{\lambda}{(\lambda^2 + \alpha^2)^3} + \frac{1}{80\,\alpha^3}\frac{\lambda}{(\lambda^2 + \alpha^2)^4}\right.$$
$$\left. - \frac{1}{10\,\alpha}\frac{\lambda}{(\lambda^2 + \alpha^2)^5}\right]\frac{1}{(\lambda^2 - \beta^2)^{1/2}}\,\mathrm{d}\lambda \quad \text{(C.11)}$$

$$+\int_0^\infty \frac{63}{256}\lambda^{-11}\arctan\left(\frac{\alpha}{\lambda}\right)\mathrm{d}x. \tag{C.12}$$

where $\lambda^2=(x-X)^2+\beta^2$ and $\lambda_0=(X^2+\beta^2)^{1/2}$. The result will be solved in three separate parts and employ the same methods as done for the attractive part. Now consider Equation (C.10),

$$\begin{aligned}
&\int_{\lambda_0}^\infty\left[\frac{7}{256\,\alpha^9}\frac{1}{\lambda}-\frac{9}{256\,\alpha^7}\frac{1}{\lambda^3}+\frac{63}{1280\,\alpha^5}\frac{1}{\lambda^5}-\frac{21}{256\,\alpha^3}\frac{1}{\lambda^7}+\frac{63}{256\,\alpha}\frac{1}{\lambda^9}\right]\frac{1}{(\lambda^2-\beta^2)^{1/2}}\,\mathrm{d}\lambda\\
&\quad=\int_{\theta_0}^{\pi/2}\left[\frac{7}{256\,\alpha^9}\cdot\frac{1}{\beta}-\frac{9}{256\,\alpha^7}\cdot\frac{1}{\beta^3}\cos^2\theta+\frac{63}{1280\,\alpha^5}\cdot\frac{1}{\beta^5}\cos^4\theta-\frac{21}{256\,\alpha^3}\cdot\frac{1}{\beta^7}\cos^6\theta\right.\\
&\qquad\left.+\frac{63}{256\,\alpha}\cdot\frac{1}{\beta^9}\cos^8\theta\right]\mathrm{d}\theta,\\
&\quad=\frac{7}{256\,\alpha^9\,\beta}J_0(\beta,-X)-\frac{9}{256\,\alpha^7\,\beta^3}J_1(\beta,-X)+\frac{63}{1280\,\alpha^5\,\beta^5}J_2(\beta,-X)-\frac{21}{256\,\alpha^3\,\beta^7}J_3(\beta,-X)\\
&\qquad+\frac{63}{256\,\alpha\,\beta^9}J_4(\beta,-X),
\end{aligned}$$

where $\cos\theta=\beta/\lambda$ and $\theta_0=\arctan[-X/\beta]$. The final result can be written in terms of the definite integrals for the cosine functions, $J_n(\beta,-X)$.

Consider Equation (C.11),

$$\begin{aligned}
&\int_{\lambda_0}^\infty\left[-\frac{7}{256\,\alpha^9}\frac{\lambda}{(\lambda^2+\alpha^2)}+\frac{1}{128\,\alpha^7}\frac{\lambda}{(\lambda^2+\alpha^2)^2}-\frac{1}{160\,\alpha^5}\frac{\lambda}{(\lambda^2+\alpha^2)^3}+\frac{1}{80\,\alpha^3}\frac{\lambda}{(\lambda^2+\alpha^2)^4}\right.\\
&\quad\left.-\frac{1}{10\,\alpha}\frac{\lambda}{(\lambda^2+\alpha^2)^5}\right]\frac{1}{(\lambda^2-\beta^2)^{1/2}}\,\mathrm{d}\lambda\\
&\quad=\int_{w_0}^\infty\left[-\frac{7}{256\,\alpha^9}\frac{1}{w}+\frac{1}{128\,\alpha^7}\frac{1}{w^3}-\frac{1}{160\,\alpha^5}\frac{1}{w^5}+\frac{1}{80\,\alpha^3}\frac{1}{w^7}-\frac{1}{10\,\alpha}\frac{1}{w^9}\right]\frac{1}{(w^2-(\alpha^2+\beta^2))^{1/2}}\,\mathrm{d}w,
\end{aligned}$$

where $w^2=\lambda^2+\alpha^2$ and $w_0=(\alpha^2+\beta^2+X^2)^{1/2}$. The resulting integral in terms of w can be

further transformed into an integrand of cosine functions, such that

$$
\begin{aligned}
&\int_{w_0}^{\infty}\left[-\frac{7}{256\,\alpha^9}\frac{1}{w}+\frac{1}{128\,\alpha^7}\frac{1}{w^3}-\frac{1}{160\,\alpha^5}\frac{1}{w^5}+\frac{1}{80\,\alpha^3}\frac{1}{w^7}-\frac{1}{10\,\alpha}\frac{1}{w^9}\right]\frac{1}{(w^2-(\alpha^2+\beta^2))^{1/2}}\,\mathrm{d}w\\
&\quad=\int_{\theta_0}^{\pi/2}\left[-\frac{7}{256\,\alpha^9}\cdot\frac{1}{(\alpha^2+\beta^2)^{1/2}}+\frac{1}{128\,\alpha^7}\cdot\frac{1}{(\alpha^2+\beta^2)^{3/2}}\cos^2\theta-\frac{1}{160\,\alpha^5}\frac{1}{(\alpha^2+\beta^2)^{5/2}}\cos^4\theta\right.\\
&\qquad\left.+\frac{1}{80\,\alpha^3}\frac{1}{(\alpha^2+\beta^2)^{7/2}}\cos^6\theta-\frac{1}{10\,\alpha}\frac{1}{(\alpha^2+\beta^2)^{9/2}}\cos^8\theta\right]\mathrm{d}\theta,\\
&\quad=-\frac{7}{256\,\alpha^9\,(\alpha^2+\beta^2)^{1/2}}J_0(\sqrt{\alpha^2+\beta^2},-X)+\frac{1}{128\,\alpha^7\,(\alpha^2+\beta^2)^{3/2}}J_1(\sqrt{\alpha^2+\beta^2},-X)\\
&\qquad-\frac{1}{160\,\alpha^5\,(\alpha^2+\beta^2)^{5/2}}J_2(\sqrt{\alpha^2+\beta^2},-X)+\frac{1}{80\,\alpha^3\,(\alpha^2+\beta^2)^{7/2}}J_3(\sqrt{\alpha^2+\beta^2},-X)\\
&\qquad-\frac{1}{10\,\alpha\,(\alpha^2+\beta^2)^{9/2}}J_4(\sqrt{\alpha^2+\beta^2},-X),
\end{aligned}
$$

where $\cos\theta=\sqrt{\alpha^2+\beta^2}/w$ and $\theta_0=\arctan[-X/\sqrt{\alpha^2+\beta^2}]$. The final result can be written in terms of the definite integrals for the cosine functions, $J_n(\sqrt{\alpha^2+\beta^2},-X)$.

Now consider Equation (C.12),

$$
\int_0^{\infty}\frac{63}{256}\left((x-X)^2+\beta^2\right)^{-11/2}\arctan\left(\frac{\alpha}{((x-X)^2+\beta^2)^{1/2}}\right)\mathrm{d}x=\frac{63}{256\,\alpha^9}\int_0^{w_0}\frac{w^9\,\arctan w}{(\alpha^2-\beta^2\,w^2)^{1/2}}\mathrm{d}w,
$$

where $w=\alpha/\sqrt{(x-X)^2+\beta^2}$ and $w_0=\alpha/\sqrt{\beta^2+X^2}$.

$$
\begin{aligned}
&\frac{63}{256\,\alpha^9}\int_0^{w_0}\frac{w^9\,\arctan w}{(\alpha^2-\beta^2\,w^2)^{1/2}}\mathrm{d}w\\
&\quad=-\frac{63}{256\,\alpha^9\,\beta^2}\int_0^{w_0}w^7\,(\alpha^2-\beta^2\,w^2)^{1/2}\,\arctan w\,\mathrm{d}w\\
&\qquad+\frac{63}{256\,\alpha^7\,\beta^2}\int_0^{w_0}w^7\,(\alpha^2-\beta^2\,w^2)^{-1/2}\,\arctan w\,\mathrm{d}w,\\
&\quad=-\frac{63}{256\,\alpha^9\,\beta^2}\left[-\frac{(\alpha^2-\beta^2\,w^2)^{3/2}(35\,\beta^6\,w^6+30\,\alpha^2\beta^4\,w^4+24\,\alpha^4\,\beta^2\,w^2+16\,\alpha^6)}{315\,\beta^8}\arctan w\right|_0^{w_0}\\
&\qquad\left.-\frac{1}{315\,\beta^8}\int_0^{w_0}\frac{(\alpha^2-\beta^2\,w^2)^{3/2}(35\,\beta^6\,w^6+30\,\alpha^2\beta^4\,w^4+24\,\alpha^4\,\beta^2\,w^2+16\,\alpha^6)}{1+w^2}\,\mathrm{d}w\right]\\
&\qquad+\frac{63}{256\,\alpha^7\,\beta^2}\left[-\frac{(\alpha^2-\beta^2\,w^2)^{1/2}(5\,\beta^6\,w^6+6\,\alpha^2\beta^4\,w^4+8\,\alpha^4\,\beta^2\,w^2+16\,\alpha^6)}{35\,\beta^8}\arctan w\right|_0^{w_0}\\
&\qquad\left.-\frac{1}{35\,\beta^8}\int_0^{w_0}\frac{(\alpha^2-\beta^2\,w^2)^{1/2}(5\,\beta^6\,w^6+6\,\alpha^2\beta^4\,w^4+8\,\alpha^4\,\beta^2\,w^2+16\,\alpha^6)}{1+w^2}\,\mathrm{d}w\right],\\
&\quad=-\frac{1}{1280\,\alpha^9\,\beta^{10}}\left(\alpha^2-\beta^2\,w_0^2\right)^{1/2}\left(35\,\beta^8w_0^8+40\,\alpha^2\,\beta^6\,w_0^6+48\,\alpha^4\,\beta^4\,w_0^4+64\,\alpha^6\,\beta^2\,w_0^2\right.
\end{aligned}
$$

$$
\begin{aligned}
&\quad +128\,\alpha^8\big)\,\arctan w_0\\
&+\frac{1}{1280\,\alpha^9\,\beta^{10}}\int_0^{w_0}\frac{\left(\alpha^2-\beta^2\,w^2\right)^{1/2}}{1+w^2}\left(35\,\beta^8w^8+40\,\alpha^2\,\beta^6\,w^6+48\,\alpha^4\,\beta^4\,w^4+64\,\alpha^6\,\beta^2\,w^2\right.\\
&\quad \left.+128\,\alpha^8\right)\mathrm{d}w,\\
&=-\frac{1}{1280\,\alpha^9\,\beta^{10}}\left(\alpha^2-\beta^2\,w_0^2\right)^{1/2}\left(35\,\beta^8w_0^8+40\,\alpha^2\,\beta^6\,w_0^6+48\,\alpha^4\,\beta^4\,w_0^4+64\,\alpha^6\,\beta^2\,w_0^2\right.\\
&\quad \left.+128\,\alpha^8\right)\,\arctan w_0\\
&+\frac{35}{1280\,\alpha^9\,\beta^2}\int_0^{w_0}w^6\,\left(\alpha^2-\beta^2\,w^2\right)^{1/2}\mathrm{d}w\\
&+\frac{\left(40\,\alpha^2-35\,\beta^2\right)}{1280\,\alpha^9\,\beta^4}\int_0^{w_0}w^4\,\left(\alpha^2-\beta^2\,w^2\right)^{1/2}\mathrm{d}w\\
&+\frac{\left(48\,\alpha^4-40\,\alpha^2\,\beta^2+35\,\beta^4\right)}{1280\,\alpha^9\,\beta^6}\int_0^{w_0}w^2\,\left(\alpha^2-\beta^2\,w^2\right)^{1/2}\mathrm{d}w\\
&+\frac{\left(64\,\alpha^6-48\,\alpha^4\,\beta^2+40\,\alpha^2\,\beta^4-35\,\beta^6\right)}{1280\,\alpha^9\,\beta^8}\int_0^{w_0}\left(\alpha^2-\beta^2\,w^2\right)^{1/2}\mathrm{d}w\\
&+\frac{\left(128\,\alpha^8-64\,\alpha^6\,\beta^2+48\,\alpha^4\,\beta^4-40\,\alpha^2\,\beta^6+35\,\beta^8\right)}{1280\,\alpha^9\,\beta^{10}}\int_0^{w_0}\frac{\left(\alpha^2-\beta^2\,w^2\right)^{1/2}}{1+w^2}\mathrm{d}w
\end{aligned}
$$

To solve the remaining integrals, let $\beta\,w=\alpha\sin\theta$ and $\theta_0=\arccos[-X/(\beta^2+X^2)^{1/2}]$, then

$$
\begin{aligned}
&\int_0^{\infty}\frac{63}{256}\left((x-X)^2+\beta^2\right)^{-11/2}\arctan\left(\frac{\alpha}{((x-X)^2+\beta^2)^{1/2}}\right)\mathrm{d}x\\
&=-\frac{1}{1280\,\alpha^9\,\beta^{10}}\left(\alpha^2-\beta^2\,w_0^2\right)^{1/2}\left(35\,\beta^8w_0^8+40\,\alpha^2\,\beta^6\,w_0^6+48\,\alpha^4\,\beta^4\,w_0^4+64\,\alpha^6\,\beta^2\,w_0^2\right.\\
&\quad \left.+128\,\alpha^8\right)\,\arctan w_0\\
&+\frac{35}{1280\,\alpha\,\beta^9}\int_0^{\theta_0}\sin^6\theta\,\cos^2\theta\mathrm{d}\theta\\
&+\frac{\left(40\,\alpha^2-35\,\beta^2\right)}{1280\,\alpha^3\,\beta^9}\int_0^{\theta_0}\sin^4\theta\,\cos^2\theta\mathrm{d}\theta\\
&+\frac{\left(48\,\alpha^4-40\,\alpha^2\,\beta^2+35\,\beta^4\right)}{1280\,\alpha^5\,\beta^9}\int_0^{\theta_0}\sin^2\theta\,\cos^2\theta\mathrm{d}\theta\\
&+\frac{\left(64\,\alpha^6-48\,\alpha^4\,\beta^2+40\,\alpha^2\,\beta^4-35\,\beta^6\right)}{1280\,\alpha^7\,\beta^9}\int_0^{\theta_0}\cos^2\theta\mathrm{d}\theta\\
&+\frac{\left(128\,\alpha^8-64\,\alpha^6\,\beta^2+48\,\alpha^4\,\beta^4-40\,\alpha^2\,\beta^6+35\,\beta^8\right)}{1280\,\alpha^7\,\beta^{11}}\int_0^{\theta_0}\frac{1}{1+k^2\tan^2\theta}\mathrm{d}\theta\\
&=\frac{1}{1280\,\beta^{10}}\cdot\frac{X}{(\beta^2+X^2)^{1/2}}\left(\frac{35\,\beta^8}{(\beta^2+X^2)^4}+\frac{40\,\beta^6}{(\beta^2+X^2)^3}+\frac{48\,\beta^4}{(\beta^2+X^2)^2}\right.\\
&\quad \left.+\frac{64\,\beta^2}{(\beta^2+X^2)}+128\right)\,\arctan\left(\frac{\alpha}{(\beta^2+X^2)^{1/2}}\right)
\end{aligned}
$$

$$
\begin{aligned}
&+ \frac{35}{1280\,\alpha\,\beta^9}\,G_3(-X,\beta) \\
&+ \frac{\left(40\,\alpha^2 - 35\,\beta^2\right)}{1280\,\alpha^3\,\beta^9}\,G_2(-X,\beta) \\
&+ \frac{\left(48\,\alpha^4 - 40\,\alpha^2\,\beta^2 + 35\,\beta^4\right)}{1280\,\alpha^5\,\beta^9}\,G_1(-X,\beta) \\
&+ \frac{\left(64\,\alpha^6 - 48\,\alpha^4\,\beta^2 + 40\,\alpha^2\,\beta^4 - 35\,\beta^6\right)}{1280\,\alpha^7\,\beta^9}\,G_0(-X,\beta) \\
&+ \frac{\left(128\,\alpha^8 - 64\,\alpha^6\,\beta^2 + 48\,\alpha^4\,\beta^4 - 40\,\alpha^2\,\beta^6 + 35\,\beta^8\right)}{1280\,\alpha^9\,\beta^{10}}\left[(\beta^2+\alpha^2)^{1/2}\arctan\left(\frac{(\beta^2+\alpha^2)^{1/2}}{-X}\right)\right. \\
&\quad \left.-\beta\,\arctan\left(\frac{\beta}{-X}\right)\right]
\end{aligned}
$$

where $k^2 = 1 + (\alpha/\beta)^2$ and $G_i(-X,\beta)$ is defined as a trigonometric integral in Appendix E.

Complete analytical result

$$
\begin{aligned}
E &= 2\,n_1 \int_0^\infty \lambda^{-5}\left[-A\,I_2(\lambda,\alpha)+\lambda^{-6}B\,I_5(\lambda,\alpha)\right]\mathrm{d}x \\
&= -2\,n_1\,A\cdot\frac{1}{8\,\alpha^3\,\beta^4}\left\{-\beta^3\,J_0(\beta,-X)+3\,\alpha^2\,\beta\,J_1(\beta,-X)\right. \\
&\quad+\frac{\beta^4}{(\alpha^2+\beta^2)^{1/2}}J_0(\sqrt{\alpha^2+\beta^2},-X)-\frac{2\,\alpha^2\,\beta^4}{(\alpha^2+\beta^2)^{3/2}}J_1(\sqrt{\alpha^2+\beta^2},-X) \\
&\quad+\frac{\alpha^3\,X}{(\beta^2+X^2)^{3/2}}\left(3\,\beta^2+2\,X^2\right)\arctan\left(\frac{\alpha}{(\beta^2+X^2)^{1/2}}\right) \\
&\quad+\alpha^2\,\beta\,G_0(-X,\beta) \\
&\quad+(2\,\alpha^2-\beta^2)\left[(\beta^2+\alpha^2)^{1/2}\arccos\left(\frac{-X}{(\beta^2+\alpha^2+X^2)^{1/2}}\right)\right. \\
&\qquad\left.\left.-\beta\,\arccos\left(\frac{-X}{(\beta^2+X^2)^{1/2}}\right)\right]\right\} \\
&\quad+2\,n_1\,B\cdot\frac{1}{1280\,\alpha^9\,\beta^{10}}\left\{35\,\beta^9\,J_0(\beta,-X)-45\,\alpha^2\,\beta^7\,J_1(\beta,-X)+63\,\alpha^4\,\beta^5\,J_2(\beta,-X)\right. \\
&\quad-105\,\alpha^6\,\beta^3\,J_3(\beta,-X)+315\,\alpha^8\,\beta\,J_4(\beta,-X) \\
&\quad-\frac{35\,\beta^{10}}{(\alpha^2+\beta^2)^{1/2}}J_0(\sqrt{\alpha^2+\beta^2},-X)+\frac{10\,\alpha^2\,\beta^{10}}{(\alpha^2+\beta^2)^{3/2}}J_1(\sqrt{\alpha^2+\beta^2},-X) \\
&\quad-\frac{8\,\alpha^4\,\beta^{10}}{(\alpha^2+\beta^2)^{5/2}}J_2(\sqrt{\alpha^2+\beta^2},-X)+\frac{16\,\alpha^6\,\beta^{10}}{(\alpha^2+\beta^2)^{7/2}}J_3(\sqrt{\alpha^2+\beta^2},-X) \\
&\quad-\frac{128\,\alpha^8\,\beta^{10}}{(\alpha^2+\beta^2)^{9/2}}J_4(\sqrt{\alpha^2+\beta^2},-X) \\
&\quad+\frac{\alpha^9\,X}{(\beta^2+X^2)^{9/2}}\left(315\,\beta^8+840\,\beta^6\,X^2+1008\,\beta^4\,X^4+576\,\beta^2\,X^6\right. \\
&\qquad\left.+128\,X^8\right)\arctan\left(\frac{\alpha}{(\beta^2+X^2)^{1/2}}\right) \\
&\quad+35\,\alpha^8\,\beta\,G_3(-X,\beta)+\left(40\,\alpha^8\,\beta-35\,\alpha^6\,\beta^3\right)G_2(-X,\beta) \\
&\quad+\left(48\,\alpha^8\,\beta-40\,\alpha^6\,\beta^3+35\,\alpha^4\,\beta^5\right)G_1(-X,\beta) \\
&\quad+\left(64\,\alpha^8\,\beta-48\,\alpha^6\,\beta^3+40\,\alpha^4\,\beta^5-35\,\alpha^2\,\beta^7\right)G_0(-X,\beta) \\
&\quad+\left(128\,\alpha^8-64\,\alpha^6\,\beta^2+48\,\alpha^4\,\beta^4-40\,\alpha^2\,\beta^6+35\,\beta^8\right)\left[(\beta^2+\alpha^2)^{1/2}\arccos\left(\frac{-X}{(\beta^2+\alpha^2+X^2)^{1/2}}\right)\right. \\
&\qquad\left.\left.\left.-\beta\,\arccos\left(\frac{-X}{(\beta^2+X^2)^{1/2}}\right)\right]\right\}.
\end{aligned}
$$

C.2. STEP-BY-STEP CALCULATIONS FOR INTERACTION FORCES

The interaction forces in the axial (x) direction between a point and a semi-infinite rectangular prism can be calculated using Equations (2.3) and (2.4).

C.2.1. Point to semi-infinite straight line

Using the interaction energy between a point and semi-infinite straight line, Equation (C.1), and the relationship between the energy and the force, then the van der Waals force in the axial direction, Equation (2.4), due to the interaction with the entire surface of the infinite line is given by

$$\begin{aligned} F(X) &= \frac{\mathrm{d}\,E}{\mathrm{d}\rho}\,\frac{(x-X)}{\rho}, \\ &= n_1 \int_0^\infty \frac{\mathrm{d}}{\mathrm{d}\rho}\left[-\frac{A}{\rho^6}+\frac{B}{\rho^{12}}\right]\,\frac{(x-X)}{\rho}\,\mathrm{d}x. \end{aligned}$$

Using $\rho^2 = (x-X)^2+\alpha^2+\beta^2$, we can transform the integral and the bounds of integration to obtain

$$\begin{aligned} F(X) &= n_1 \int_{\rho_0}^\infty \frac{\mathrm{d}}{\mathrm{d}\rho}\left[-\frac{A}{\rho^6}+\frac{B}{\rho^{12}}\right]\,\mathrm{d}\rho, \\ &= n_1 \left[-\frac{A}{\rho^6}+\frac{B}{\rho^{12}}\right]\Bigg|_{\rho_0}^\infty, \\ &= n_1 \left[\frac{A}{(X^2+\alpha^2+\beta^2)^3}-\frac{B}{(X^2+\alpha^2+\beta^2)^6}\right], \end{aligned} \tag{C.13}$$

where $\rho_0 = (X^2+\alpha^2+\beta^2)^{1/2}$.

C.2.2. Point to perpendicular semi-infinite plane

Using the interaction energy between a point and semi-infinite straight plane, Equation C.6, and the relationship between the energy and the force, then the van der Waals force in the axial direction, Equation (2.4), due to the interaction with the entire surface of the infinite plane is given by

$$F(X) = 2\,n_1 \int_{\rho_0}^\infty \frac{\mathrm{d}}{\mathrm{d}\rho}\lambda^{-5}\left[-A\,I_2(\lambda,\alpha)+\lambda^{-6}B\,I_5(\lambda,\alpha)\right]\,\frac{(x-X)}{\rho}\,\mathrm{d}x,$$

where $\lambda^2 = (x-X)^2+\beta^2$.

We can transform the integral and the bounds of integration in terms of ρ,

$$\begin{aligned}
F(X) &= 2\,n_1 \int_{\rho_0}^{\infty} \frac{\mathrm{d}}{\mathrm{d}\rho} \Big[-A\,(\rho^2-\alpha^2)^{-5/2}\,I_2\left((\rho^2-\alpha^2)^{1/2},\alpha\right) \\
&\qquad +B\,(\rho^2-\alpha^2)^{-11/2}\,I_5((\rho^2-\alpha^2)^{1/2},\alpha)\Big]\,\mathrm{d}\rho, \\
&= 2\,n_1 \Big[-A\,(\rho^2-\alpha^2)^{-5/2}\,I_2\left((\rho^2-\alpha^2)^{1/2},\alpha\right) \\
&\qquad +B\,(\rho^2-\alpha^2)^{-11/2}\,I_5\left((\rho^2-\alpha^2)^{1/2},\alpha\right)\Big]\Big|_{\rho_0}^{\infty},
\end{aligned}$$

where $\rho^2 = (x-X)^2+\alpha^2+\beta^2$ at $y=\alpha$ and $\rho_0^2 = X^2+\alpha^2+\beta^2$ at $y=\alpha$.

Simplification for attractive part

$$\begin{aligned}
&(\rho^2-\alpha^2)^{-5/2}\,I_2\left((\rho^2-\alpha^2)^{1/2},\alpha\right)\Big|_{\rho_0}^{\infty} \\
&\quad = \frac{1}{4}\,\frac{\alpha}{\rho^4\,(\rho^2-\alpha^2)} + \frac{3}{8}\frac{\alpha}{\rho^2\,(\rho^2-\alpha^2)^2} + \frac{3}{8}(\rho^2-\alpha^2)^{-5/2}\arctan\left(\frac{\alpha}{(\rho^2-\alpha^2)^{1/2}}\right)\Big|_{\rho_0}^{\infty}, \\
&\quad = -\frac{1}{4}\,\frac{\alpha}{(\alpha^2+\beta^2+X^2)^2\,(\beta^2+X^2)} - \frac{3}{8}\frac{\alpha}{(\alpha^2+\beta^2+X^2)\,(\beta^2+X^2)^2} \\
&\qquad - \frac{3}{8}(\beta^2+X^2)^{-5/2}\arctan\left(\frac{\alpha}{(\beta^2+X^2)^{1/2}}\right).
\end{aligned}$$

Simplification for repulsive part

$$\begin{aligned}
&(\rho^2-\alpha^2)^{-11/2}\,I_5\left((\rho^2-\alpha^2)^{1/2},\alpha\right)\Big|_{\rho_0}^{\infty} \\
&\quad = \frac{1}{10}\,\frac{\alpha}{\rho^{10}\,(\rho^2-\alpha^2)} + \frac{9}{80}\,\frac{\alpha}{\rho^8\,(\rho^2-\alpha^2)^2} + \frac{21}{160}\,\frac{\alpha}{\rho^6\,(\rho^2-\alpha^2)^3} + \frac{21}{128}\,\frac{\alpha}{\rho^4\,(\rho^2-\alpha^2)^4} \\
&\qquad + \frac{63}{256}\frac{\alpha}{\rho^2\,(\rho^2-\alpha^2)^5} + \frac{63}{256}(\rho^2-\alpha^2)^{-11/2}\arctan\left(\frac{\alpha}{(\rho^2-\alpha^2)^{1/2}}\right)\Big|_{\rho_0}^{\infty}, \\
&\quad = -\frac{1}{10}\,\frac{\alpha}{(\alpha^2+\beta^2+X^2)^5\,(\beta^2+X^2)} - \frac{9}{80}\,\frac{\alpha}{(\alpha^2+\beta^2+X^2)^4\,(\beta^2+X^2)^2} \\
&\qquad - \frac{21}{160}\,\frac{\alpha}{(\alpha^2+\beta^2+X^2)^3\,(\beta^2+X^2)^3} - \frac{21}{128}\,\frac{\alpha}{(\alpha^2+\beta^2+X^2)^2\,(\beta^2+X^2)^4} \\
&\qquad - \frac{63}{256}\frac{\alpha}{(\alpha^2+\beta^2+X^2)\,(\beta^2+X^2)^5} - \frac{63}{256}(\beta^2+X^2)^{-11/2}\arctan\left(\frac{\alpha}{(\beta^2+X^2)^{1/2}}\right).
\end{aligned}$$

Complete analytical result

$$
\begin{aligned}
F(X) = 2\,n_1 \Bigg\{ & A \cdot \frac{1}{8} \left[\frac{2\,\alpha}{(\alpha^2+\beta^2+X^2)^2\,(\beta^2+X^2)} + \frac{3\,\alpha}{(\alpha^2+\beta^2+X^2)\,(\beta^2+X^2)^2} \right. \\
& \left. +3\,(\beta^2+X^2)^{-5/2} \arctan\left(\frac{\alpha}{(\beta^2+X^2)^{1/2}} \right) \right] \\
& -B \cdot \frac{1}{1280} \left[\frac{128\,\alpha}{(\alpha^2+\beta^2+X^2)^5\,(\beta^2+X^2)} + \frac{144\,\alpha}{(\alpha^2+\beta^2+X^2)^4\,(\beta^2+X^2)^2} \right. \\
& + \frac{168\,\alpha}{(\alpha^2+\beta^2+X^2)^3\,(\beta^2+X^2)^3} + \frac{210\,\alpha}{(\alpha^2+\beta^2+X^2)^2\,(\beta^2+X^2)^4} \\
& \left. \left. + \frac{315\,\alpha}{(\alpha^2+\beta^2+X^2)\,(\beta^2+X^2)^5} + 315\,(\beta^2+X^2)^{-11/2} \arctan\left(\frac{\alpha}{(\beta^2+X^2)^{1/2}} \right) \right] \right\}. \quad \text{(C.14)}
\end{aligned}
$$

APPENDIX D

EXPANSION OF AND DEFINITION FOR THE INDEFINITE INTEGRAL $\cos^{2n}\theta$, I_n

From a book by Gradshteyn and Ryzhik [17] Section 2.512(2), the indefinite integral for the trigonometry function $\cos^{2n}\theta$ can be defined as follows,

$$\begin{aligned} I_n(x,y) &= \int \cos^{2n}\theta \,\mathrm{d}\theta \\ &= \frac{\sin\theta}{2n}\left[\cos^{2n-1}\theta + \sum_{k=1}^{n-1}\frac{(2n-1)(2n-3)...(2n-2k+1)}{2^k(n-1)(n-2)...(n-k)}\cos^{2n-2k-1}\theta\right] \\ &\quad + \frac{(2n-1)!!}{2^n(n)!}\,\theta \\ &= \frac{y}{2n}\left[\frac{x^{2n-1}}{(x^2+y^2)^n} + \sum_{k=1}^{n-1}\frac{(2n-1)(2n-3)...(2n-2k+1)}{2^k(n-1)(n-2)...(n-k)}\,\frac{x^{2n-2k-1}}{(x^2+y^2)^{n-k}}\right] \\ &\quad + \frac{(2n-1)!!}{2^n(n)!}\,\arctan\left(\frac{y}{x}\right), \end{aligned} \tag{D.1}$$

where $(n)!!$ is the double factorial notation. The function $I_n(x,y)$ can be expressed in the three forms, where $\tan\theta = y/x$, gives $\sin\theta = y/(x^2+y^2)^{1/2}$ and $\cos\theta = x/(x^2+y^2)^{1/2}$. The constant of integration is ignored because these integrals are valuated at points of integration in the main chapters.

Forms of Equation (D.1) used in the main chapters are,

$$I_0(x,y) = \int \mathrm{d}\theta = \theta = \arctan\left(\frac{y}{x}\right)$$

$$\begin{aligned} I_1(x,y) &= \int \cos^2\theta \,\mathrm{d}\theta \\ &= \frac{1}{2}\,\sin\theta\,\cos\theta + \frac{1}{2}\,\theta \\ &= \frac{1}{2}\,\frac{y\,x}{(x^2+y^2)} + \frac{1}{2}\arctan\left(\frac{y}{x}\right) \end{aligned}$$

$$
\begin{aligned}
I_2(x,y) &= \int \cos^4\theta \,\mathrm{d}\theta \\
&= \frac{1}{4}\,\sin\theta\,\cos^3\theta + \frac{3}{8}\sin\theta\,\cos\theta + \frac{3}{8}\,\theta \\
&= \frac{1}{4}\,\frac{y\,x^3}{(x^2+y^2)^2} + \frac{3}{8}\frac{y\,x}{(x^2+y^2)} + \frac{3}{8}\arctan\left(\frac{y}{x}\right)
\end{aligned}
$$

$$
\begin{aligned}
I_3(x,y) &= \int \cos^6\theta \,\mathrm{d}\theta \\
&= \frac{1}{6}\,\sin\theta\,\cos^5\theta + \frac{5}{24}\,\sin\theta\,\cos^3\theta + \frac{5}{16}\sin\theta\,\cos\theta + \frac{5}{16}\,\theta \\
&= \frac{1}{6}\,\frac{y\,x^5}{(x^2+y^2)^3} + \frac{5}{24}\,\frac{y\,x^3}{(x^2+y^2)^2} + \frac{5}{16}\frac{y\,x}{(x^2+y^2)} + \frac{5}{16}\arctan\left(\frac{y}{x}\right)
\end{aligned}
$$

$$
\begin{aligned}
I_4(x,y) &= \int \cos^8\theta \,\mathrm{d}\theta \\
&= \frac{1}{8}\,\sin\theta\,\cos^7\theta + \frac{7}{48}\,\sin\theta\,\cos^5\theta + \frac{35}{192}\,\sin\theta\,\cos^3\theta + \frac{35}{128}\sin\theta\,\cos\theta \\
&\quad + \frac{35}{128}\,\theta \\
&= \frac{1}{8}\,\frac{y\,x^7}{(x^2+y^2)^4} + \frac{7}{48}\,\frac{y\,x^5}{(x^2+y^2)^3} + \frac{35}{192}\,\frac{y\,x^3}{(x^2+y^2)^2} + \frac{35}{128}\frac{y\,x}{(x^2+y^2)} \\
&\quad + \frac{35}{128}\arctan\left(\frac{y}{x}\right)
\end{aligned}
$$

$$
\begin{aligned}
I_5(x,y) &= \int \cos^{10}\theta \,\mathrm{d}\theta \\
&= \frac{1}{10}\,\sin\theta\,\cos^9\theta + \frac{9}{80}\,\sin\theta\,\cos^7\theta + \frac{21}{160}\,\sin\theta\,\cos^5\theta + \frac{21}{128}\,\sin\theta\,\cos^3\theta \\
&\quad + \frac{63}{256}\sin\theta\,\cos\theta + \frac{63}{256}\,\theta \\
&= \frac{1}{10}\,\frac{y\,x^9}{(x^2+y^2)^5} + \frac{9}{80}\,\frac{y\,x^7}{(x^2+y^2)^4} + \frac{21}{160}\,\frac{y\,x^5}{(x^2+y^2)^3} + \frac{21}{128}\,\frac{y\,x^3}{(x^2+y^2)^2} \\
&\quad + \frac{63}{256}\frac{y\,x}{(x^2+y^2)} + \frac{63}{256}\arctan\left(\frac{y}{x}\right)
\end{aligned}
$$

$$
\begin{aligned}
I_6(x,y) &= \int \cos^{12}\theta \,\mathrm{d}\theta \\
&= \frac{1}{12}\,\sin\theta\,\cos^{11}\theta + \frac{11}{120}\,\sin\theta\,\cos^{9}\theta + \frac{33}{320}\,\sin\theta\,\cos^{7}\theta + \frac{77}{640}\,\sin\theta\,\cos^{5}\theta \\
&\quad + \frac{77}{512}\,\sin\theta\,\cos^{3}\theta + \frac{231}{1024}\sin\theta\,\cos\theta + \frac{231}{1024}\,\theta \\
&= \frac{1}{12}\,\frac{y\,x^{11}}{(x^2+y^2)^6} + \frac{11}{120}\,\frac{y\,x^{9}}{(x^2+y^2)^5} + \frac{33}{320}\,\frac{y\,x^{7}}{(x^2+y^2)^4} + \frac{77}{640}\,\frac{y\,x^{5}}{(x^2+y^2)^3} \\
&\quad + \frac{77}{512}\,\frac{y\,x^{3}}{(x^2+y^2)^2} + \frac{231}{1024}\frac{y\,x}{(x^2+y^2)} + \frac{231}{1024}\arctan\left(\frac{y}{x}\right)
\end{aligned}
$$

$$
\begin{aligned}
I_7(x,y) &= \int \cos^{14}\theta \,\mathrm{d}\theta \\
&= \frac{1}{14}\,\sin\theta\,\cos^{13}\theta + \frac{13}{168}\,\sin\theta\,\cos^{11}\theta + \frac{143}{1680}\,\sin\theta\,\cos^{9}\theta + \frac{429}{4480}\,\sin\theta\,\cos^{7}\theta \\
&\quad + \frac{143}{1280}\,\sin\theta\,\cos^{5}\theta + \frac{143}{1024}\,\sin\theta\,\cos^{3}\theta + \frac{429}{2048}\sin\theta\,\cos\theta + \frac{429}{2048}\,\theta \\
&= \frac{1}{14}\,\frac{y\,x^{13}}{(x^2+y^2)^7} + \frac{13}{168}\,\frac{y\,x^{11}}{(x^2+y^2)^6} + \frac{143}{1680}\,\frac{y\,x^{9}}{(x^2+y^2)^5} + \frac{429}{4480}\,\frac{y\,x^{7}}{(x^2+y^2)^4} \\
&\quad + \frac{143}{1280}\,\frac{y\,x^{5}}{(x^2+y^2)^3} + \frac{143}{1024}\,\frac{y\,x^{3}}{(x^2+y^2)^2} + \frac{429}{2048}\frac{y\,x}{(x^2+y^2)} + \frac{429}{2048}\arctan\left(\frac{y}{x}\right)
\end{aligned}
$$

$$
\begin{aligned}
I_8(x,y) &= \int \cos^{16}\theta \,\mathrm{d}\theta \\
&= \frac{1}{16}\,\sin\theta\,\cos^{15}\theta + \frac{15}{224}\,\sin\theta\,\cos^{13}\theta + \frac{65}{896}\,\sin\theta\,\cos^{11}\theta + \frac{143}{1792}\,\sin\theta\,\cos^{9}\theta \\
&\quad + \frac{1287}{14336}\,\sin\theta\,\cos^{7}\theta + \frac{429}{4096}\,\sin\theta\,\cos^{5}\theta + \frac{2145}{16384}\,\sin\theta\,\cos^{3}\theta + \frac{6435}{32768}\sin\theta\,\cos\theta \\
&\quad + \frac{6435}{32768}\,\theta \\
&= \frac{1}{16}\,\frac{y\,x^{15}}{(x^2+y^2)^8} + \frac{15}{224}\,\frac{y\,x^{13}}{(x^2+y^2)^7} + \frac{65}{896}\,\frac{y\,x^{11}}{(x^2+y^2)^6} + \frac{143}{1792}\,\frac{y\,x^{9}}{(x^2+y^2)^5} \\
&\quad + \frac{1287}{14336}\,\frac{y\,x^{7}}{(x^2+y^2)^4} + \frac{429}{4096}\,\frac{y\,x^{5}}{(x^2+y^2)^3} + \frac{2145}{16384}\,\frac{y\,x^{3}}{(x^2+y^2)^2} + \frac{6435}{32768}\frac{y\,x}{(x^2+y^2)} \\
&\quad + \frac{6435}{32768}\arctan\left(\frac{y}{x}\right)
\end{aligned}
$$

$$
\begin{aligned}
I_9(x,y) &= \int \cos^{18}\theta \,\mathrm{d}\theta \\
&= \frac{1}{18}\,\sin\theta\,\cos^{17}\theta + \frac{17}{288}\,\sin\theta\,\cos^{15}\theta + \frac{85}{1344}\,\sin\theta\,\cos^{13}\theta + \frac{1105}{16128}\,\sin\theta\,\cos^{11}\theta \\
&\quad + \frac{2431}{32256}\,\sin\theta\,\cos^{9}\theta + \frac{2431}{28672}\,\sin\theta\,\cos^{7}\theta + \frac{2431}{24576}\,\sin\theta\,\cos^{5}\theta + \frac{12155}{98304}\,\sin\theta\,\cos^{3}\theta \\
&\quad + \frac{12155}{65536}\sin\theta\,\cos\theta + \frac{12155}{65536}\,\theta \\
&= \frac{1}{18}\,\frac{y\,x^{17}}{(x^2+y^2)^9} + \frac{17}{288}\,\frac{y\,x^{15}}{(x^2+y^2)^8} + \frac{85}{1344}\,\frac{y\,x^{13}}{(x^2+y^2)^7} + \frac{1105}{16128}\,\frac{y\,x^{11}}{(x^2+y^2)^6} \\
&\quad + \frac{2431}{32256}\,\frac{y\,x^{9}}{(x^2+y^2)^5} + \frac{2431}{28672}\,\frac{y\,x^{7}}{(x^2+y^2)^4} + \frac{2431}{24576}\,\frac{y\,x^{5}}{(x^2+y^2)^3} + \frac{12155}{98304}\,\frac{y\,x^{3}}{(x^2+y^2)^2} \\
&\quad + \frac{12155}{65536}\frac{y\,x}{(x^2+y^2)} + \frac{12155}{65536}\arctan\left(\frac{y}{x}\right)
\end{aligned}
$$

D.1. DEFINITE INTEGRAL EVALUATED AT $\frac{\pi}{2}$ AND ψ, J_N

Define the function $J_n(x,y)$ in terms of $I_n(x,y)$,

$$
\begin{aligned}
J_n(x,y) &= \int_{\psi}^{\pi/2} \cos^{2n}\psi' \,\mathrm{d}\psi', \\
&= I_n(0,1) - I_n(x,y),
\end{aligned}
\tag{D.2}
$$

where $\tan\psi = y/x$, gives $\sin\psi = y/(x^2+y^2)^{1/2}$ and $\cos\psi = x/(x^2+y^2)^{1/2}$, or $x = \cos\psi$ and $y = \sin\psi$.

Forms of Equation (D.2) used in this thesis are,

$$
\begin{aligned}
J_0(x,y) &= \int_{\psi}^{\pi/2} \mathrm{d}\psi', \\
&= \int_{-\pi/2}^{-\psi} \mathrm{d}\psi', \\
&= \frac{\pi}{2} - \left[\arctan\left(\frac{y}{x}\right)\right].
\end{aligned}
$$

$$
\begin{aligned}
J_1(x,y) &= \int_{\psi}^{\pi/2} \cos^2\psi' \,\mathrm{d}\psi', \\
&= \int_{-\pi/2}^{-\psi} \cos^2\psi' \,\mathrm{d}\psi', \\
&= \frac{1}{2}\cdot\frac{\pi}{2} - \left[\frac{1}{2}\arctan\left(\frac{y}{x}\right)\right].
\end{aligned}
$$

$$
\begin{aligned}
J_2(x,y) &= \int_{\psi}^{\pi/2} \cos^4\psi' \,\mathrm{d}\psi', \\
&= \int_{-\pi/2}^{-\psi} \cos^4\psi' \,\mathrm{d}\psi', \\
&= \frac{3}{8}\cdot\frac{\pi}{2} - \left[\frac{1}{4}\,\frac{y\,x^3}{(x^2+y^2)^2} + \frac{3}{8}\frac{y\,x}{(x^2+y^2)} + \frac{3}{8}\arctan\left(\frac{y}{x}\right)\right].
\end{aligned}
$$

$$
\begin{aligned}
J_3(x,y) &= \int_{\psi}^{\pi/2} \cos^6\psi' \,\mathrm{d}\psi', \\
&= \int_{-\pi/2}^{-\psi} \cos^6\psi' \,\mathrm{d}\psi', \\
&= \frac{5}{16}\cdot\frac{\pi}{2} - \left[\frac{1}{6}\,\frac{y\,x^5}{(x^2+y^2)^3} + \frac{5}{24}\,\frac{y\,x^3}{(x^2+y^2)^2} + \frac{5}{16}\frac{y\,x}{(x^2+y^2)} + \frac{5}{16}\arctan\left(\frac{y}{x}\right)\right].
\end{aligned}
$$

$$
\begin{aligned}
J_4(x,y) &= \int_{\psi}^{\pi/2} \cos^8\psi' \,\mathrm{d}\psi', \\
&= \int_{-\pi/2}^{-\psi} \cos^8\psi' \,\mathrm{d}\psi', \\
&= \frac{35}{128}\cdot\frac{\pi}{2} - \left[\frac{1}{8}\,\frac{y\,x^7}{(x^2+y^2)^4} + \frac{7}{48}\,\frac{y\,x^5}{(x^2+y^2)^3} + \frac{35}{192}\,\frac{y\,x^3}{(x^2+y^2)^2} + \frac{35}{128}\frac{y\,x}{(x^2+y^2)}\right. \\
&\quad \left. + \frac{35}{128}\arctan\left(\frac{y}{x}\right)\right].
\end{aligned}
$$

$$
\begin{aligned}
J_5(x,y) &= \int_{\psi}^{\pi/2} \cos^{10}\psi' \,\mathrm{d}\psi', \\
&= \int_{-\pi/2}^{-\psi} \cos^{10}\psi' \,\mathrm{d}\psi', \\
&= \frac{63}{256}\cdot\frac{\pi}{2} - \left[\frac{1}{10}\,\frac{y\,x^9}{(x^2+y^2)^5} + \frac{9}{80}\,\frac{y\,x^7}{(x^2+y^2)^4} + \frac{21}{160}\,\frac{y\,x^5}{(x^2+y^2)^3} + \frac{21}{128}\,\frac{y\,x^3}{(x^2+y^2)^2}\right. \\
&\quad \left. + \frac{63}{256}\frac{y\,x}{(x^2+y^2)} + \frac{63}{256}\arctan\left(\frac{y}{x}\right)\right].
\end{aligned}
$$

$$
\begin{aligned}
J_6(x,y) &= \int_{\psi}^{\pi/2} \cos^{12}\psi' \,\mathrm{d}\psi', \\
&= \int_{-\pi/2}^{-\psi} \cos^{12}\psi' \,\mathrm{d}\psi', \\
&= \frac{231}{1024}\cdot\frac{\pi}{2} - \left[\frac{1}{12}\,\frac{y\,x^{11}}{(x^2+y^2)^6} + \frac{11}{120}\,\frac{y\,x^9}{(x^2+y^2)^5} + \frac{33}{320}\,\frac{y\,x^7}{(x^2+y^2)^4} + \frac{77}{640}\,\frac{y\,x^5}{(x^2+y^2)^3}\right. \\
&\quad \left. + \frac{77}{512}\,\frac{y\,x^3}{(x^2+y^2)^2} + \frac{231}{1024}\frac{y\,x}{(x^2+y^2)} + \frac{231}{1024}\arctan\left(\frac{y}{x}\right)\right].
\end{aligned}
$$

$$
\begin{aligned}
J_7(x,y) &= \int_{\psi}^{\pi/2} \cos^{14}\psi' \,\mathrm{d}\psi', \\
&= \int_{-\pi/2}^{-\psi} \cos^{14}\psi' \,\mathrm{d}\psi', \\
&= \frac{429}{2048}\cdot\frac{\pi}{2} - \left[\frac{1}{14}\,\frac{y\,x^{13}}{(x^2+y^2)^7} + \frac{13}{168}\,\frac{y\,x^{11}}{(x^2+y^2)^6} + \frac{143}{1680}\,\frac{y\,x^9}{(x^2+y^2)^5} + \frac{429}{4480}\,\frac{y\,x^7}{(x^2+y^2)^4}\right. \\
&\quad \left. + \frac{143}{1280}\,\frac{y\,x^5}{(x^2+y^2)^3} + \frac{143}{1024}\,\frac{y\,x^3}{(x^2+y^2)^2} + \frac{429}{2048}\frac{y\,x}{(x^2+y^2)} + \frac{429}{2048}\arctan\left(\frac{y}{x}\right)\right].
\end{aligned}
$$

$$
\begin{aligned}
J_8(x,y) &= \int_{\psi}^{\pi/2} \cos^{16}\psi' \,\mathrm{d}\psi', \\
&= \int_{-\pi/2}^{-\psi} \cos^{16}\psi' \,\mathrm{d}\psi', \\
&= \frac{6435}{32768}\cdot\frac{\pi}{2} - \left[\frac{1}{16}\,\frac{y\,x^{15}}{(x^2+y^2)^8} + \frac{15}{224}\,\frac{y\,x^{13}}{(x^2+y^2)^7} + \frac{65}{896}\,\frac{y\,x^{11}}{(x^2+y^2)^6} + \frac{143}{1792}\,\frac{y\,x^9}{(x^2+y^2)^5}\right. \\
&\quad + \frac{1287}{14336}\,\frac{y\,x^7}{(x^2+y^2)^4} + \frac{429}{4096}\,\frac{y\,x^5}{(x^2+y^2)^3} + \frac{2145}{16384}\,\frac{y\,x^3}{(x^2+y^2)^2} + \frac{6435}{32768}\frac{y\,x}{(x^2+y^2)} \\
&\quad \left. + \frac{6435}{32768}\arctan\left(\frac{y}{x}\right)\right].
\end{aligned}
$$

$$
\begin{aligned}
J_9(x,y) &= \int_{\psi}^{\pi/2} \cos^{18}\psi'\,\mathrm{d}\psi', \\
&= \int_{-\pi/2}^{-\psi} \cos^{18}\psi'\,\mathrm{d}\psi', \\
&= \frac{12155}{65536}\cdot\frac{\pi}{2} - \left[\frac{1}{18}\,\frac{y\,x^{17}}{(x^2+y^2)^9} + \frac{17}{288}\,\frac{y\,x^{15}}{(x^2+y^2)^8} + \frac{85}{1344}\,\frac{y\,x^{13}}{(x^2+y^2)^7} + \frac{1105}{16128}\,\frac{y\,x^{11}}{(x^2+y^2)^6}\right. \\
&\quad + \frac{2431}{32256}\,\frac{y\,x^9}{(x^2+y^2)^5} + \frac{2431}{28672}\,\frac{y\,x^7}{(x^2+y^2)^4} + \frac{2431}{24576}\,\frac{y\,x^5}{(x^2+y^2)^3} + \frac{12155}{98304}\,\frac{y\,x^3}{(x^2+y^2)^2} \\
&\quad \left. + \frac{12155}{65536}\frac{y\,x}{(x^2+y^2)} + \frac{12155}{65536}\arctan\left(\frac{y}{x}\right)\right].
\end{aligned}
$$

D.2. DEFINITE INTEGRAL EVALUATED AT ψ_1 AND ψ_2, H_N

Define the function $H_n(x,y;c)$ in terms of $I_n(x,y)$, where $\tan\psi_2 = (c+y)/x$ and $\tan\psi_1 = y/x$.

$$
H_n(x,y;c) = \int_{\psi_1}^{\psi_2} \cos^{2n}\psi'\,\mathrm{d}\psi' = I_n(x,c+y) - I_n(x,y). \tag{D.3}
$$

Forms of Equation (D.3) in the main chapter(s) are,

$$
H_2(x,y;c) = \int_{\psi_1}^{\psi_2} \cos^{4}\psi'\,\mathrm{d}\psi' = I_2(x,c+y) - I_2(x,y).
$$

$$
H_3(x,y;c) = \int_{\psi_1}^{\psi_2} \cos^{6}\psi'\,\mathrm{d}\psi' = I_3(x,c+y) - I_3(x,y).
$$

$$
H_5(x,y;c) = \int_{\psi_1}^{\psi_2} \cos^{10}\psi'\,\mathrm{d}\psi' = I_5(x,c+y) - I_5(x,y).
$$

$$
H_6(x,y;c) = \int_{\psi_1}^{\psi_2} \cos^{12}\psi'\,\mathrm{d}\psi' = I_6(x,c+y) - I_6(x,y).
$$

$$H_7(x,y;c) = \int_{\psi_1}^{\psi_2} \cos^{14}\psi' \,\mathrm{d}\psi' = I_7(x,c+y) - I_7(x,y).$$

$$H_8(x,y;c) = \int_{\psi_1}^{\psi_2} \cos^{16}\psi' \,\mathrm{d}\psi' = I_8(x,c+y) - I_8(x,y).$$

$$H_9(x,y;c) = \int_{\psi_1}^{\psi_2} \cos^{18}\psi' \,\mathrm{d}\psi' = I_9(x,c+y) - I_9(x,y).$$

APPENDIX E

EXPANSION OF AND DEFINITION FOR THE INDEFINITE INTEGRAL $\sin^{2m}\theta\cos^2\theta$

The indefinite integral for the trigonometric function $\sin^{2m}\theta\cos^2\theta$ is defined as follows,

$$G_m(x,y) = \int \sin^{2m}\theta\cos^2\theta \mathrm{d}\theta, \tag{E.1}$$

where $\tan\theta = y/x$, gives $\sin\theta = y/(x^2+y^2)^{1/2}$ and $\cos\theta = x/(x^2+y^2)^{1/2}$, and the constants of integration are ignored.

Forms of Equation (E.1) used in the main chapters (and Appendix C) are,

$$\begin{aligned} G_0(x,y) &= \int \cos^2\theta \mathrm{d}\theta \\ &= \frac{1}{2}\,\sin\theta\,\cos\theta + \frac{1}{2}\,\theta \\ &= \frac{1}{2}\,\frac{y\,x}{(x^2+y^2)} + \frac{1}{2}\arccos\left(\frac{x}{(x^2+y^2)^{1/2}}\right) \end{aligned}$$

$$\begin{aligned} G_1(x,y) &= \int \sin^2\theta\cos^2\theta \mathrm{d}\theta \\ &= -\frac{1}{4}\,\sin\theta\,\cos^3\theta + \frac{1}{8}\sin\theta\,\cos\theta + \frac{1}{8}\,\theta \\ &= -\frac{1}{4}\,\frac{y\,x^3}{(x^2+y^2)^2} + \frac{1}{8}\frac{y\,x}{(x^2+y^2)} + \frac{1}{8}\arccos\left(\frac{x}{(x^2+y^2)^{1/2}}\right) \end{aligned}$$

$$\begin{aligned} G_2(x,y) &= \int \sin^4\theta\cos^2\theta \mathrm{d}\theta \\ &= -\frac{1}{6}\,\sin^3\theta\,\cos^3\theta - \frac{1}{8}\,\sin\theta\,\cos^3\theta + \frac{1}{16}\sin\theta\,\cos\theta + \frac{1}{16}\,\theta \\ &= -\frac{1}{6}\,\frac{y^3\,x^3}{(x^2+y^2)^3} - \frac{1}{8}\,\frac{y\,x^3}{(x^2+y^2)^2} + \frac{1}{16}\frac{y\,x}{(x^2+y^2)} + \frac{1}{16}\arccos\left(\frac{x}{(x^2+y^2)^{1/2}}\right) \end{aligned}$$

$$
\begin{aligned}
G_3(x,y) &= \int \sin^6\theta\cos^2\theta \mathrm{d}\theta \\
&= -\frac{1}{8}\sin^5\theta\,\cos^3\theta - \frac{5}{48}\sin^3\theta\,\cos^3\theta - \frac{5}{64}\sin\theta\,\cos^3\theta + \frac{5}{128}\sin\theta\,\cos\theta \\
&\quad + \frac{5}{128}\theta \\
&= -\frac{1}{8}\frac{y^5\,x^3}{(x^2+y^2)^4} - \frac{5}{48}\frac{y^3\,x^3}{(x^2+y^2)^3} - \frac{5}{64}\frac{y\,x^3}{(x^2+y^2)^2} + \frac{5}{128}\frac{y\,x}{(x^2+y^2)} \\
&\quad + \frac{5}{128}\arccos\left(\frac{x}{(x^2+y^2)^{1/2}}\right)
\end{aligned}
$$

APPENDIX F

NUMERICAL ALGORITHM FOR DIMENSIONLESS ONE-DIMENSIONAL MODEL

The functions describing ferric ion concentration $c(t,x)$ and MOF occupancy $b(t)$ are discretised and the following definitions are used,

$$c(t_n, x_i) = c_i^n, \qquad c(t,0) = c_0^n, \qquad c(t, L/\ell) = c_I^n, \qquad b(t_n) = b^n.$$

First, the value of the MOF occupancy b^{n+1} is updated, so that the updated value is used to calculate the ferric ion concentration c_0^{n+1} at $x = 0$. A Runge-Kutta 4 scheme is used

$$\begin{aligned} f(y) &= s_2\, c_0^n(1-y) - s_2\, s_3 y, \\ k_1 &= \Delta t\, f(b^n), \qquad & k_2 &= \Delta t\, f\left(b^n + \frac{k_1}{2}\right), \\ k_3 &= \Delta t\, f\left(b^n + \frac{k_2}{2}\right), \qquad & k_4 &= \Delta t\, f(b^n + k_3). \end{aligned}$$

At time step $n+1$, the MOF occupancy is

$$b^{n+1} = b^n + \frac{1}{6}(k_1 + 2k_2 + 2k_3 + k_4),$$

where $b(0) = b^0 = 0$.

Next, the ferric ion concentration throughout the solution is updated using the Crank-Nicolson forwards-time, centred-space. The following difference formulas for the first and second derivatives were used

$$c(t,x) = \frac{1}{2}(c_i^n + c_i^{n+1}),$$
$$\frac{\partial}{\partial x}c(t,x) = \frac{1}{2}\left[\frac{c_{i+1}^n - c_{i-1}^n}{2\Delta x} + \frac{c_{i+1}^{n+1} - c_{i-1}^{n+1}}{2\Delta x}\right], \qquad \frac{\partial}{\partial t}c(t,x) = \frac{c_i^{n+1} - c_i^n}{\Delta t}$$
$$\frac{\partial^2}{\partial x^2}c(t,x) = \frac{1}{2}\left[\frac{c_{i+1}^n - 2c_i^n + c_{i-1}^n}{\Delta x^2} + \frac{c_{i+1}^{n+1} - 2c_i^{n+1} + c_{i-1}^{n+1}}{\Delta x^2}\right].$$

Substituting these formulas into the ferric ion diffusion equation gives

$$\frac{c_i^{n+1} - c_i^n}{\Delta t} = \frac{s_1}{2}\left[\frac{c_{i+1}^n - 2c_i^n + c_{i-1}^n}{\Delta x^2} + \frac{c_{i+1}^{n+1} - 2c_i^{n+1} + c_{i-1}^{n+1}}{\Delta x^2}\right].$$

Terms with time step $n+1$ are collected on the left and n on the right hand side of the equation, so that the general scheme is

$$-\alpha\, c_{i+1}^{n+1} + (2+2\alpha)c_i^{n+1} - \alpha\, c_{i-1}^{n+1} = \alpha\, c_{i+1}^n + (2-2\alpha)c_i^n + \alpha\, c_{i-1}^n,$$

where $\alpha = s_1\Delta t/\Delta x^2$. The boundary conditions concerning the ferric ion concentration need to be incorporated, and so the flux at the MOF-polymer boundary (equation (7.12)) becomes

$$s_1\left[c_1^n - c_{-1}^n + c_1^{n+1} - c_{-1}^{n+1}\right] = 2s_4s_2\Delta x(c_0^n + c_0^{n+1})(1 - b^{n+1}) - 4\Delta x s_4 s_2 s_3\, b^{n+1}.$$

Now, adjust the general scheme at and near the boundaries:

for $i = 0$, the MOF-polymer boundary,

$$-2\alpha\, c_1^{n+1} + [2 + 2\alpha + 2\alpha s_4 s_2 \Delta x(1 - b^{n+1})/s_1]c_0^{n+1}$$
$$= 2\alpha\, c_1^n + [2 - 2\alpha - 2\alpha s_4 s_2 \Delta x(1 - b^{n+1})/s_1]c_0^n + 4\Delta x s_2 s_3 s_4\, b^{n+1}/s_1,$$

for $i = I$, far field boundary (equation (7.13)),

$$c_I^n = 1, \quad \forall n,$$

for $i = I-1$,

$$(2+2\alpha)c_{I-1}^{n+1} - \alpha\, c_{I-2}^{n+1} = (2-2\alpha)c_{I-1}^{n} + \alpha\, c_{I-2}^{n} + 2\alpha.$$

The finite difference scheme can be written as a linear system,

$$L\underline{c}^{n+1} = R\underline{c}^{n} + A,$$

where

$$L = \begin{bmatrix} 2+2\alpha+2\alpha s_4 s_2 \Delta x(1-b^{n+1})/s_1 & -\alpha & 0 & 0 & \cdots & 0 & 0 & 0 & 0 \\ -\alpha & 2+2\alpha & -\alpha & 0 & \cdots & 0 & 0 & 0 & 0 \\ \ddots & \ddots & \ddots & & \cdots & 0 & 0 & 0 & 0 \\ 0 & 0 & 0 & 0 & \cdots & -\alpha & 2+2\alpha & -\alpha & 0 \\ 0 & 0 & 0 & 0 & \cdots & 0 & -\alpha & 2+2\alpha & 0 \\ 0 & 0 & 0 & 0 & \cdots & 0 & 0 & 0 & 1 \end{bmatrix},$$

$$R = \begin{bmatrix} 2-2\alpha-2\alpha s_4 s_2 \Delta x(1-b^{n+1})/s_1 & \alpha & 0 & 0 & \cdots & 0 & 0 & 0 & 0 \\ \alpha & 2-2\alpha & \alpha & 0 & \cdots & 0 & 0 & 0 & 0 \\ \ddots & \ddots & \ddots & & \cdots & 0 & 0 & 0 & 0 \\ 0 & 0 & 0 & 0 & \cdots & \alpha & 2-2\alpha & \alpha & 0 \\ 0 & 0 & 0 & 0 & \cdots & 0 & \alpha & 2-2\alpha & 0 \\ 0 & 0 & 0 & 0 & \cdots & 0 & 0 & 0 & 0 \end{bmatrix},$$

$$A = [4\Delta x s_2 s_3 s_4\, b^{n+1}/s_1, 0, \cdots, 0, 2\alpha, 1]^{\mathrm{T}},$$

and

$$\underline{c}^{n} = [c_0^n,\, c_1^n, c_2^n, \cdots, c_{I-2}^n, c_{I-1}^n, c_I^n]^{\mathrm{T}},$$

where L and R are real $(I+1)\times(I+1)$ matrices, and A and $\underline{c}^n$ are $(I+1)$-vectors.

The system describing the concentration of ferric ions through the solution can be evaluated as

$$\underline{c}^{n+1} = L^{-1}(R\underline{c}^{n} + A),$$

where $c(0,x) = c_i^0 = \underline{1}$. Table F.1 provides the numerical values for the graphs shown in the main text. Tests were performed for various timesteps and mesh sizes to ensure numerical accuracy.

Δt	Δx	L/ℓ
0.005	0.1	10

Table F.1: Numerical values for one-dimensional simulation.

APPENDIX G

NUMERICAL ALGORITHM FOR DIMENSIONLESS TWO-DIMENSIONAL MODEL

The functions describing ferric ion concentration $c(t, \mathbf{x})$ and MOF occupancy $b(t, x_1)$ are discretised and the following definitions are used,

$$c(t, x_1, x_2) = c(t_n, x_i, x_j) = c^n_{i\,j}, \qquad c(t, -L/\ell, x_2) = c^n_{0\,j}, \qquad c(t, L/\ell, x_2) = c^n_{I\,j},$$
$$c(t, -1, x_2) = c^n_{il\,j}, \qquad c(t, 1, x_2) = c^n_{ir\,j}, \qquad c(t, x_1, 0) = c^n_{i\,jm},$$
$$c(t, x_1, -h/\ell) = c^n_{i\,0}, \qquad c(t, x_1, L/\ell) = c^n_{i\,J}, \qquad b(t, x_1) = b(t_n, x_i) = b^n_i.$$

In the same way as the one-dimensional model was solved, the MOF occupancy is first updated for the next time step b^{n+1}_i and later used to update the ferric ion concentration $c^{n+1}_{i\,j}$ at $|x_1| \leq 1$ and $x_2 = 0$. A Runge-Kutta 4 scheme is used to discretise $b(t, x_1)$ at $|x_1| \leq 1$,

$$f(y) = s_2\, c^n_{i\,jm}(1 - y) - s_2\, s_3 y, \qquad \text{for } i = il, ..., rl,$$
$$k_1 = \Delta t\, f(b^n_i), \qquad k_2 = \Delta t\, f\left(b^n_i + \frac{k_1}{2}\right),$$
$$k_3 = \Delta t\, f\left(b^n_i + \frac{k_2}{2}\right), \qquad k_4 = \Delta t\, f(b^n_i + k_3).$$

At the next time step $n + 1$ for $i = il, ..., ir$, the MOF occupancy is

$$b^{n+1}_i = b^n_i + \frac{1}{6}(k_1 + 2k_2 + 2k_3 + k_4),$$

where $b^0_i = 0$.

The ferric ion concentration is updated and uses a forwards-time, two-dimensional centred-space scheme. The following difference formulas for the first and second derivatives were used

$$\frac{\partial}{\partial t}c(t,\mathbf{x}) = \frac{c_{i\,j}^{n+1} - c_{i\,j}^{n}}{\Delta t},$$
$$\frac{\partial}{\partial x_1}c(t,\mathbf{x}) = \frac{c_{i+1\,j}^{n} - c_{i-1\,j}^{n}}{2\Delta x_1}, \qquad \frac{\partial}{\partial x_2}c(t,\mathbf{x}) = \frac{c_{i\,j+1}^{n} - c_{i\,j-1}^{n}}{2\Delta x_2},$$
$$\nabla^2 c(t,\mathbf{x}) = \frac{c_{i+1\,j}^{n} - 2c_{i\,j}^{n} + c_{i-1\,j}^{n}}{\Delta x_1^2} + \frac{c_{i\,j+1}^{n} - 2c_{i\,j}^{n} + c_{i\,j-1}^{n}}{\Delta x_2^2}.$$

Substituting the formulas into the ferric ion diffusion equation in the solution for $x_2 \geq 0$ gives

$$\frac{c_{i\,j}^{n+1} - c_{i\,j}^{n}}{\Delta t} = s_1 \left[\frac{c_{i+1\,j}^{n} - 2c_{i\,j}^{n} + c_{i-1\,j}^{n}}{\Delta x_1^2} + \frac{c_{i\,j+1}^{n} - 2c_{i\,j}^{n} + c_{i\,j-1}^{n}}{\Delta x_2^2} \right].$$

Terms with time step $n+1$ are collected on the left and n on the right hand side of the equation, so that the general scheme $\forall i$ and $j = jm+1 : J-1$ is

$$c_{i\,j}^{n+1} = (1 - 2s_x - 2s_y)c_{i\,j}^{n} + s_x(c_{i+1\,j}^{n} + c_{i-1\,j}^{n}) + s_y(c_{i\,j+1}^{n} + c_{i\,j-1}^{n}).$$

Similarly, diffusion in the polymer $\forall i$ and $j = 1 : jm-1$ is

$$c_{i\,j}^{n+1} = (1 - 2s_x D - 2s_y D)c_{i\,j}^{n} + s_x D(c_{i+1\,j}^{n} + c_{i-1\,j}^{n}) + s_y D(c_{i\,j+1}^{n} + c_{i\,j-1}^{n}),$$

where $s_x = s_1\Delta t/\Delta x_1^2$ and $s_y = s_1\Delta t/\Delta x_2^2$. The boundary conditions of the system need to be accounted for to update the numerical scheme accordingly:

for $\forall i, n$ and $j = J$, far field boundary condition (Equation (7.4)) at $x_2 = L/\ell$,

$$c_{i\,J}^{n} = 1,$$

for $i = 0$ and $j = jm+1 : J-1$, no flux boundary condition (Equation (7.5)) for solution medium at $x_1 = -L/\ell$,

$$c_{0\,j}^{n+1} = (1 - 2s_x - 2s_y)c_{0\,j}^{n} + s_x(c_{1\,j}^{n} + c_{1\,j}^{n}) + s_y(c_{0\,j+1}^{n} + c_{0\,j-1}^{n}),$$

for $i = 0$ and $j = 1 : jm-1$, no flux boundary condition (Equation (7.5)) for polymer medium at

$x_1 = -L/\ell$,

$$c_{0\,j}^{n+1} = (1 - 2s_xD - 2s_yD)c_{0\,j}^n + s_xD(c_{1\,j}^n + c_{1\,j}^n) + s_yD(c_{0\,j+1}^n + c_{0\,j-1}^n),$$

for $i = I$ and $j = jm + 1 : J - 1$, no flux boundary condition (Equation (7.5)) for solution medium at $x_1 = L/\ell$,

$$c_{I\,j}^{n+1} = (1 - 2s_x - 2s_y)c_{I\,j}^n + s_x(c_{I-1\,j}^n + c_{I-1\,j}^n) + s_y(c_{I\,j+1}^n + c_{I\,j-1}^n),$$

for $i = I$ and $j = 1 : jm - 1$, no flux boundary condition (Equation (7.5)) for polymer medium at $x_1 = L/\ell$,

$$c_{I\,j}^{n+1} = (1 - 2s_xD - 2s_yD)c_{I\,j}^n + s_xD(c_{I-1\,j}^n + c_{I-1\,j}^n) + s_yD(c_{I\,j+1}^n + c_{I\,j-1}^n),$$

for $i = 1, ..., I - 1$ and $j = 0$, no flux boundary condition (Equation (7.5)) for polymer-optic fibre at $x_2 = -h/\ell$,

$$c_{i\,0}^{n+1} = (1 - 2s_xD - 2s_yD)c_{i\,0}^n + s_xD(c_{i+1\,0}^n + c_{i-1\,0}^n) + s_yD(c_{i\,1}^n + c_{i\,1}^n),$$

for $i = 0$ and $j = 0$, no flux boundary condition (Equation (7.5)) at $x_1 = -L/\ell$ and $x_2 = -h/\ell$,

$$c_{0\,0}^{n+1} = (1 - 2s_xD - 2s_yD)c_{0\,0}^n + s_xD(c_{1\,0}^n + c_{1\,0}^n) + s_yD(c_{0\,1}^n + c_{0\,1}^n),$$

for $i = I$ and $j = 0$, no flux boundary condition (Equation (7.5)) at $x_1 = L/\ell$ and $x_2 = -h/\ell$,

$$c_{I\,0}^{n+1} = (1 - 2s_xD - 2s_yD)c_{I\,0}^n + s_xD(c_{I-1\,0}^n + c_{I-1\,0}^n) + s_yD(c_{I\,1}^n + c_{I\,1}^n),$$

for $i = 1, ..., I - 1$ and $j = jm$, solution-polymer boundary continuity condition (Equation (7.3)) at

$x_2 = 0$,

$$\frac{\partial c}{\partial t} = s_1 \frac{\partial^2 c}{\partial x_1^2} + s_1 \frac{\partial}{\partial x_2}\left[D_i \frac{\partial c}{\partial x_2}\right] = s_1 \frac{\partial^2 c}{\partial x_1^2} + \frac{s_1}{\Delta x_2}\left[\frac{\partial c_+}{\partial x_2} - D\frac{\partial c_-}{\partial x_2}\right],$$

$$\frac{c_{i\,jm}^{n+1} - c_{i\,jm}^{n}}{\Delta t} = s_1\left[\frac{c_{i+1jm}^{n} - 2c_{i\,jm}^{n} + c_{i-1\,jm}^{n}}{\Delta x_1^2}\right] + \frac{s_1}{\Delta x_2}\left[\frac{c_{i\,jm+1}^{n} - c_{i\,jm}^{n}}{\Delta x_2}\right] - \frac{s_1 D}{\Delta x_2}\left[\frac{c_{i\,jm}^{n} - c_{i\,jm-1}^{n}}{\Delta x_2}\right],$$

$$c_{i\,jm}^{n+1} = (1 - 2s_x - s_y(1+D))c_{i\,jm}^{n} + s_x(c_{i+1\,jm}^{n} + c_{i-1\,jm}^{n}) + s_y c_{i\,jm+1}^{n} + s_y D c_{i\,jm-1}^{n},$$

for $i = 0$ and $j = jm$, solution-polymer boundary continuity condition (Equation (7.3)) and no flux boundary condition (Equation (7.5)) at $x_1 = -L/\ell$ and $x_2 = 0$,

$$c_{0\,jm}^{n+1} = (1 - 2s_x - s_y(1+D))c_{0\,jm}^{n} + s_x(c_{1\,jm}^{n} + c_{1\,jm}^{n}) + s_y c_{0\,jm+1}^{n} + s_y D c_{0\,jm-1}^{n},$$

for $i = I$ and $j = jm$, solution-polymer continuity condition (Equation (7.3)) and no flux boundary condition (Equation (7.5)) at $x_1 = L/\ell$ and $x_2 = 0$,

$$c_{I\,jm}^{n+1} = (1 - 2s_x - s_y(1+D))c_{I\,jm}^{n} + s_x(c_{I-1\,jm}^{n} + c_{I-1\,jm}^{n}) + s_y c_{I\,jm+1}^{n} + s_y D c_{I\,jm-1}^{n},$$

for $i = il - 1$ and $j = jm$, solution-polymer continuity condition (Equation (7.3)) and no flux boundary condition (Equation (7.7)) at $x_1 = -1_-$ and $x_2 = 0$,

$$c_{il-1\,jm}^{n+1} = (1 - 2s_x - s_y(1+D))c_{il-1\,jm}^{n} + s_x(c_{il-2\,jm}^{n} + c_{il-2\,jm}^{n}) + s_y c_{il-1\,jm+1}^{n} + s_y D c_{il-1\,jm-1}^{n},$$

for $i = ir + 1$ and $j = jm$, solution-polymer continuity condition solution-polymer continuity condition (Equation (7.3)) and no flux boundary condition (Equation (7.7)) at $x_1 = 1_+$ and $x_2 = 0$,

$$c_{ir+1\,jm}^{n+1} = (1 - 2s_x - s_y(1+D))c_{ir+1\,jm}^{n} + s_x(c_{ir+2\,jm}^{n} + c_{ir+2\,jm}^{n}) + s_y c_{ir+1\,jm+1}^{n} + s_y D c_{ir+1\,jm-1}^{n},$$

At the solution-MOF-polymer boundary, the continuity condition (Equation (7.3)) is used to find

$$c_{i\,jm-1}^{n} = \frac{-c_{i\,jm+1}^{n} + (1+D)c_{i\,jm}^{n}}{D}.$$

For $i = il, ..., ir$ and $j = jm$, MOF-solution flux condition (Equation (7.6)) at $|x_1| \leq 1$ and $x_2 = 0$

gives

$$s_1\left[\frac{c_{i\,jm+1}^{n+1}-c_{i\,jm-1}^{n+1}}{2\Delta x_2}\right]=s_4s_2(c_{i\,jm}^{n+1}(1-b_i^{n+1})-s_3b_i^{n+1}),$$

$$c_{i\,jm}^{n+1}=\frac{s_1(1+D)c_{i\,jm+1}^{n+1}+2\Delta x_2Ds_4s_2s_3b_i^{n+1}}{s_1(1+D)+2\Delta x_2Ds_4s_2(1-b_i^{n+1})}.$$

Table G.1 provides the numerical values for the graphs shown in the main text. Tests were performed for various time steps and mesh sizes to ensure numerical accuracy.

Δt	Δx_1	Δx_2	L/ℓ	h/ℓ	D
0.0005	0.1	0.1	10	10	0.5

Table G.1: Numerical values for two-dimensional simulation.

Unless otherwise stated, D takes the value found in Table G.1.

APPENDIX H

CODE

Note that all the code generated for this thesis is provided here.

H.1. PART I

Code here relates to Chapter 3, and adjustments can be made to generate the remainder of the plots in Part I.

H.1.1. Plots for interaction potential energy, force and kinetic energy: semi-infinite case

```
%function plot_shell_interaction_forces
% MATLAB version R2019b
% DATE: 28/08/2020
% EDITED: 21/03/2023
%
% DESCRIPTION: This code produces plots for the Lennard-Jones potential and
%   force interactions between a hydrated ferric ion and a semi-infinite
%   MOF pore. Also, a short summary for physical attributes of the system.
% INPUT:
%   SI_con_energy - convertion constant for energy i.e. 1kcal/mol = 4184 J/mol
%   SI_con_length - convertion constant for length i.e. 1 angstrom = 10^-10 m
%   m - scalar, number of cells
%   type - scalar, is set to 1 for semi-infinite case, 2 is for the finite case
%   section - character, to produce plots for a specific section, ie
%       IE - plots for interaction energy
%       IF - plots for interaction force
%       WA - plots for acceptance energy
%       W - plots for work done
%       ALL - all plots are prodoced
%   E_j_k - vector, the interaction energy betweem elements j and k
%   E_sum_j - vector,
%   E_tot - vector,
%   F_j_k - vector, the interaction force betweem elements j and k
%   F_sum_j - vector,
%   F_tot - vector,
%   W_a_j - vector,
```

```
27 %   W_a_tot_j - vector,
28 %   W_a_tot_X0 - vector,
29 % OUTPUT:
30 %   graphs - Interacting energy between the hydrated ferric ion and the MOF
31 %       pore.
32 %   graphs - Interacting force between the hydrated ferric ion and the MOF
33 %       pore.
34 %   graphs - Work need to be done by the hydrated ferric ion to be sucked
35 %       into the MOF pore and the total energy, with variation to MOF pore
36 %       radius.
37 %   summary text for semi-infinte sense checks.
38
39 %%
40 %%%%%%%%%%%%%%%%%%%%%%%%%%%%%%%%%%%%%%%%%%%%%%%%%%%%%%%%%%%%%%%%%%%%%%%
41 %                                                                       %
42 %             Input paramters - same atom type                          %
43 %                                                                       %
44 %%%%%%%%%%%%%%%%%%%%%%%%%%%%%%%%%%%%%%%%%%%%%%%%%%%%%%%%%%%%%%%%%%%%%%%
45
46 % clc
47 % clear all
48 % close all
49
50 % Convert: 1kcal/mol = 4184 J/mol, to be in line with SI base units.
51 SI_con_energy = 0.04336413;          % eV/particle
52
53 % Convert: 1 angstrom = 10^-10 m, to be in line with SI base units.
54 SI_con_length = 1;                   % angstrom
55
56 m=1;                                 % number of cells
57
58 Input_LJ_constants_Pore_parameters
59
60 IE_IF_W_related_funtions
61
62 section = 'ALL'; % 'ALL', 'IE', 'IF', 'W'
63
64 calculation_shell_interaction_forces
65
66 %%
```

```
%%%%%%%%%%%%%%%%%%%%%%%%%%%%%%%%%%%%%%%%%%%%%%%%%%%%%%%%%%%%%%%%%%%%%%%
%                                                                       %
%     Potential energy - Hydrated ferric ion to MOF pore                %
%                                                                       %
%%%%%%%%%%%%%%%%%%%%%%%%%%%%%%%%%%%%%%%%%%%%%%%%%%%%%%%%%%%%%%%%%%%%%%%

% Colour scheme
colour_Fe= [224 102 51]./255;
colour_Eu= [97 255 199]./255;
colour_sum = [103 166 169]./255;
colour_C = [110 110 110]./255;
colour_ash = [169 178 172]./255;

x_lim = [-20*SI_con_length 20*SI_con_length];
x_tick = (-20*SI_con_length:4*SI_con_length:20*SI_con_length);
x_label = join(["Position relative to pore's entrance, $X$",unit_length]);

if (strcmp(section,'ALL') || strcmp(section,'IE'))


% energy in eV
    y_lim_E_Fe = [-0.013 0.0005];
    y_tick_E_Fe = (-0.012:0.002:0);

    y_lim_E_HS = [-0.65 0.025];
    y_tick_E_HS = (-0.6:0.2:0);

    y_lim_E_OS = y_lim_E_HS;
    y_tick_E_OS = y_tick_E_HS;

    y_lim_E_tot = [-1.15 0.05];
    y_tick_E_tot = (-1:0.2:0);

    y_label_E_Fe = join(["Potential energy, $E_{\rm Fe}(X)$",unit_energy]);
    y_label_E_OS = join(["Potential energy, $E_{\rm OS}(X)$",unit_energy]);
    y_label_E_HS = join(["Potential energy, $E_{\rm HS}(X)$",unit_energy]);
    y_label_E_tot = join(["Potential energy, $E_{\rm tot}(X)$",unit_energy]);

%%%%%%%%%%%%%%%%%%%%%%%%%%%%%%%%%%%%%%%%%%%%%%%%%%%%%%%%%%%%%%%%%%%%%%%
%                     Ferric ion point                                  %
```

```
107 %%%%%%%%%%%%%%%%%%%%%%%%%%%%%%%%%%%%%%%%%%%%%%%%%%%%%%%%%%%%%%%%%%%%%%%
108
109     figure
110     hold on
111     set(gca,...
112     'xlim',x_lim,...
113     'xtick',x_tick,...
114     'ylim',y_lim_E_Fe,...
115     'ytick',y_tick_E_Fe,...
116     'fontname','helvetica',...
117     'fontsize',12)
118
119     plot(X,E_Fe_Eu,'color',colour_Eu,'linewidth',1.2);
120     plot(X,E_Fe_H,'k-- ','linewidth',1.2);
121     plot(X,E_Fe_O,'r','linewidth',1.2);
122     plot(X,E_Fe_C,'color',colour_C,'linewidth',1.2);
123     plot(X,E_sum_Fe,'-. ','color',colour_sum,'linewidth',1.2);
124
125     % To indicate pore's entrance
126     plot([0 0],y_lim_E_Fe,'color',colour_ash,'linewidth',0.7);
127
128     ax = gca;
129     ax.YAxis.Exponent = 0;
130
131     legend({'Fe(III) - Eu in pore','Fe(III) - H in pore','Fe(III) - O in pore', ...
132         'Fe(III) - C in pore','Total'},'Location','southwest','Interpreter','latex')
133
134     xlabel(x_label,'Interpreter','latex');
135     ylabel(y_label_E_Fe,'Interpreter','latex');
136     ytickformat('%.3f')
137     hold off
138
139 %%%%%%%%%%%%%%%%%%%%%%%%%%%%%%%%%%%%%%%%%%%%%%%%%%%%%%%%%%%%%%%%%%%%%%%
140 %                         Oxygen shell                                   %
141 %%%%%%%%%%%%%%%%%%%%%%%%%%%%%%%%%%%%%%%%%%%%%%%%%%%%%%%%%%%%%%%%%%%%%%%
142
143     figure
144     hold on
145     set(gca,...
146     'xlim',x_lim,...
```

```
147     'xtick',x_tick,...
148     'ylim',y_lim_E_OS,...
149     'ytick',y_tick_E_OS,...
150     'fontname','helvetica',...
151     'fontsize',12)
152 
153     plot(X,E_OS_Eu,'color',colour_Eu,'linewidth',1.2);
154     plot(X,E_OS_H,'k-- ','linewidth',1.2);
155     plot(X,E_OS_O,'r','linewidth',1.2);
156     plot(X,E_OS_C,'color',colour_C,'linewidth',1.2);
157     plot(X,E_sum_OS,'-- ','color',colour_sum,'linewidth',1.2);
158 
159     % To indicate pore's entrance
160     plot([0 0],y_lim_E_OS,'color',colour_ash,'linewidth',0.7);
161 
162     ax = gca;
163     ax.YAxis.Exponent = 0;
164 
165     legend({'O sphere - Eu in pore','O sphere - H in pore','O sphere - O in pore', ...
166         'O sphere - C in pore','Total'},'Location','southwest','Interpreter','latex')
167 
168     xlabel(x_label,'Interpreter','latex');
169     ylabel(y_label_E_OS,'Interpreter','latex');
170     ytickformat('%.1f')
171     hold off
172 
173 %%%%%%%%%%%%%%%%%%%%%%%%%%%%%%%%%%%%%%%%%%%%%%%%%%%%%%%%%%%%%%%%%%%%%%%
174 %                        Hydrogen shell                                  %
175 %%%%%%%%%%%%%%%%%%%%%%%%%%%%%%%%%%%%%%%%%%%%%%%%%%%%%%%%%%%%%%%%%%%%%%%
176 
177     figure
178     hold on
179     set(gca,...
180     'xlim',x_lim,...
181     'xtick',x_tick,...
182     'ylim',y_lim_E_HS,...
183     'ytick',y_tick_E_HS,...
184     'fontname','helvetica',...
185     'fontsize',12)
186 
```

```
187     plot(X,E_HS_Eu,'color',colour_Eu,'linewidth',1.2);
188     plot(X,E_HS_H,'k-- ','linewidth',1.2);
189     plot(X,E_HS_O,'r','linewidth',1.2);
190     plot(X,E_HS_C,'color',colour_C,'linewidth',1.2);
191     plot(X,E_sum_HS,'color',colour_sum,'linewidth',1.2);
192 
193     % To indicate pore's entrance
194     plot([0 0],y_lim_E_HS,'color',colour_ash,'linewidth',0.7);
195 
196     ax = gca;
197     ax.YAxis.Exponent = 0;
198 
199     legend({'H sphere - Eu in pore','H sphere - H in pore','H sphere - O in pore', ...
200         'H sphere - C in pore','Total'},'Location','southwest','Interpreter','latex')
201 
202     xlabel(x_label,'Interpreter','latex');
203     ylabel(y_label_E_HS,'Interpreter','latex');
204     ytickformat('%.1f')
205     hold off
206 
207 %%%%%%%%%%%%%%%%%%%%%%%%%%%%%%%%%%%%%%%%%%%%%%%%%%%%%%%%%%%%%%%%%%%%%%%
208 %                   Total potential energy                              %
209 %%%%%%%%%%%%%%%%%%%%%%%%%%%%%%%%%%%%%%%%%%%%%%%%%%%%%%%%%%%%%%%%%%%%%%%
210 
211     figure
212     hold on
213     set(gca,...
214     'xlim',x_lim,...
215     'xtick',x_tick,...
216     'ylim',y_lim_E_tot,...
217     'ytick',y_tick_E_tot,...
218     'fontname','helvetica',...
219     'fontsize',12)
220 
221     plot(X,E_sum_Fe,'-. ','color',colour_sum,'linewidth',1.2);
222     plot(X,E_sum_OS,'--','color',colour_sum,'linewidth',1.2);
223     plot(X,E_sum_HS,'color',colour_sum,'linewidth',1.2);
224     plot(X,E_tot,'k','linewidth',1.2);
225 
226     % To indicate pore's entrance
```

```
227     plot([0 0],y_lim_E_tot,'color',colour_ash,'linewidth',0.7);
228 
229     ax = gca;
230     ax.YAxis.Exponent = 0;
231 
232     legend('Fe(III) - MOF pore','O sphere - MOF pore','H sphere - MOF pore', ...
233         'Total','Location','southwest','Interpreter','latex')
234 
235     xlabel(x_label,'Interpreter','latex');
236     ylabel(y_label_E_tot,'Interpreter','latex');
237 
238     % title('Total potential energy')
239     ytickformat('%.1f')
240     hold off
241 end
242 
243 %%
244 %%%%%%%%%%%%%%%%%%%%%%%%%%%%%%%%%%%%%%%%%%%%%%%%%%%%%%%%%%%%%%%%%%%%%%%
245 %                                                                       %
246 %           Force - Hydrated ferric ion to MOF pore                     %
247 %                                                                       %
248 %%%%%%%%%%%%%%%%%%%%%%%%%%%%%%%%%%%%%%%%%%%%%%%%%%%%%%%%%%%%%%%%%%%%%%%
249 
250 if (strcmp(section,'ALL') || strcmp(section,'IF'))
251 
252 
253 % force in eV/AA
254     unit_force = '[eV/ \AA]';
255     y_lim_F_Fe = [-0.75e-4 0.0018];
256     y_tick_F_Fe = (0:3e-4:0.0018);
257 
258     y_lim_F_HS = [-0.005 0.1];
259     y_tick_F_HS = (0:0.02:0.1);
260 
261     y_lim_F_OS = y_lim_F_HS;
262     y_tick_F_OS = y_tick_F_HS;
263 
264     y_lim_F_tot = [-0.005 0.15];
265     y_tick_F_tot = (0:0.02:0.15);
266 
```

```
267     y_label_F_Fe = join(["Force, $F_{\rm Fe}(X)$",unit_force]);
268     y_label_F_OS = join(["Force, $F_{\rm OS}(X)$",unit_force]);
269     y_label_F_HS = join(["Force, $F_{\rm HS}(X)$",unit_force]);
270     y_label_F_tot = join(["Force, $F_{\rm tot}(X)$",unit_force]);
271
272
273 %%%%%%%%%%%%%%%%%%%%%%%%%%%%%%%%%%%%%%%%%%%%%%%%%%%%%%%%%%%%%%%%%%%%%%%
274 %                       Ferric ion point                                  %
275 %%%%%%%%%%%%%%%%%%%%%%%%%%%%%%%%%%%%%%%%%%%%%%%%%%%%%%%%%%%%%%%%%%%%%%%
276
277     figure
278     hold on
279     set(gca,...
280     'xlim',x_lim,...
281     'xtick',x_tick,...
282     'ylim',y_lim_F_Fe,...
283     'ytick',y_tick_F_Fe,...
284     'fontname','helvetica',...
285     'fontsize',12)
286
287     plot(X,F_sum_Fe,'-. ','color',colour_sum,'linewidth',1.2);
288     plot(X,F_Fe_C,'color',colour_C,'linewidth',1.2);
289     plot(X,F_Fe_O,'r','linewidth',1.2);
290     plot(X,F_Fe_H,'k-- ','linewidth',1.2);
291     plot(X,F_Fe_Eu,'color',colour_Eu,'linewidth',1.2);
292
293     % To indicate pore's entrance
294     plot([0 0],y_lim_F_Fe,'color',colour_ash,'linewidth',0.7);
295
296     ax = gca;
297     ax.YAxis.Exponent = 0;
298
299     legend({'Total','Fe(III) - C in pore','Fe(III) - O in pore', ...
300         'Fe(III) - H in pore','Fe(III) - Eu in pore'},'Location','northeast','
    Interpreter','latex')
301
302     xlabel(x_label,'Interpreter','latex');
303     ylabel(y_label_F_Fe,'Interpreter','latex');
304     ytickformat('%.4f')
305     hold off
```

```
306
307 %%%%%%%%%%%%%%%%%%%%%%%%%%%%%%%%%%%%%%%%%%%%%%%%%%%%%%%%%%%%%%%%%%%%%%%
308 %                          Oxygen shell                                  %
309 %%%%%%%%%%%%%%%%%%%%%%%%%%%%%%%%%%%%%%%%%%%%%%%%%%%%%%%%%%%%%%%%%%%%%%%
310
311     figure
312     hold on
313     set(gca,...
314     'xlim',x_lim,...
315     'xtick',x_tick,...
316     'ylim',y_lim_F_OS,...
317     'ytick',y_tick_F_OS,...
318     'fontname','helvetica',...
319     'fontsize',12)
320
321     plot(X,F_sum_OS,'-- ','color',colour_sum,'linewidth',1.2);
322     plot(X,F_OS_C,'color',colour_C,'linewidth',1.2);
323     plot(X,F_OS_O,'r','linewidth',1.2);
324     plot(X,F_OS_H,'k-- ','linewidth',1.2);
325     plot(X,F_OS_Eu,'color',colour_Eu,'linewidth',1.2);
326
327     % To indicate pore's entrance
328     plot([0 0],y_lim_F_OS,'color',colour_ash,'linewidth',0.7);
329
330     ax = gca;
331     ax.YAxis.Exponent = 0;
332
333     legend({'Total','O sphere - C in pore','O sphere - O in pore', ...
334         'O sphere - H in pore','O sphere - Eu in pore'},'Location','northeast','
    Interpreter','latex')
335
336     xlabel(x_label,'Interpreter','latex');
337     ylabel(y_label_F_OS,'Interpreter','latex');
338     ytickformat('%.2f')
339     hold off
340
341 %%%%%%%%%%%%%%%%%%%%%%%%%%%%%%%%%%%%%%%%%%%%%%%%%%%%%%%%%%%%%%%%%%%%%%%
342 %                         Hydrogen shell                                 %
343 %%%%%%%%%%%%%%%%%%%%%%%%%%%%%%%%%%%%%%%%%%%%%%%%%%%%%%%%%%%%%%%%%%%%%%%
344
```

```
345     figure
346     hold on
347     set(gca,...
348     'xlim',x_lim,...
349     'xtick',x_tick,...
350     'ylim',y_lim_F_HS,...
351     'ytick',y_tick_F_HS,...
352     'fontname','helvetica',...
353     'fontsize',12)
354
355     plot(X,F_sum_HS,'color',colour_sum,'linewidth',1.2);
356     plot(X,F_HS_C,'color',colour_C,'linewidth',1.2);
357     plot(X,F_HS_O,'r','linewidth',1.2);
358     plot(X,F_HS_H,'k--','linewidth',1.2);
359     plot(X,F_HS_Eu,'color',colour_Eu,'linewidth',1.2);
360
361     % To indicate pore's entrance
362     plot([0 0],y_lim_F_HS,'color',colour_ash,'linewidth',0.7);
363
364     ax = gca;
365     ax.YAxis.Exponent = 0;
366
367     legend({'Total','H sphere - H in pore','H sphere - C in pore','H sphere - H in pore
        ', ...
368         'H sphere - Eu in pore'},'Location','northeast','Interpreter','latex')
369
370     xlabel(x_label,'Interpreter','latex');
371     ylabel(y_label_F_HS,'Interpreter','latex');
372     ytickformat('%.2f')
373     hold off
374
375 %%%%%%%%%%%%%%%%%%%%%%%%%%%%%%%%%%%%%%%%%%%%%%%%%%%%%%%%%%%%%%%%%%%%%%%
376 %                          Total force                                    %
377 %%%%%%%%%%%%%%%%%%%%%%%%%%%%%%%%%%%%%%%%%%%%%%%%%%%%%%%%%%%%%%%%%%%%%%%
378
379     figure
380     hold on
381     set(gca,...
382     'xlim',x_lim,...
383     'xtick',x_tick,...
```

```
    'ylim',y_lim_F_tot,...
    'ytick',y_tick_F_tot,...
    'fontname','helvetica',...
    'fontsize',12)

    plot(X,F_tot,'k','linewidth',1.2);
    plot(X,F_sum_HS,'color',colour_sum,'linewidth',1.2);
    plot(X,F_sum_OS,'-- ','color',colour_sum,'linewidth',1.2);
    plot(X,F_sum_Fe,'-. ','color',colour_sum,'linewidth',1.2);

    % To indicate pore's entrance
    plot([0 0],y_lim_F_tot,'color',colour_ash,'linewidth',0.7);

    ax = gca;
    ax.YAxis.Exponent = 0;

    legend('Total', 'H sphere - MOF pore','O sphere - MOF pore', ...
        'Fe(III) - MOF pore','Location','northeast','Interpreter','latex')

    xlabel(x_label,'Interpreter','latex');
    ylabel(y_label_F_tot,'Interpreter','latex');
    ytickformat('%.2f')
    hold off
%%
%%%%%%%%%%%%%%%%%%%%%%%%%%%%%%%%%%%%%%%%%%%%%%%%%%%%%%%%%%%%%%%%%%%%%%%
%                                                                       %
%    Roots of Force function - Hydrated iron to MOF pore    %
%                                                                       %
%%%%%%%%%%%%%%%%%%%%%%%%%%%%%%%%%%%%%%%%%%%%%%%%%%%%%%%%%%%%%%%%%%%%%%%

% Graphing limits and tick markers
x0_lim_HS = [0 6*SI_con_length];
x0_tick_HS = (0:1*SI_con_length:6*SI_con_length);

x0_label = join(["MOF radius, $a$",unit_length]);

%%%%%%%%%%%%%%%%%%%%%%%%%%%%%%%%%%%%%%%%%%%%%%%%%%%%%%%%%%%%%%%%%%%%%%%
%                     Ferric ion point                                  %
%%%%%%%%%%%%%%%%%%%%%%%%%%%%%%%%%%%%%%%%%%%%%%%%%%%%%%%%%%%%%%%%%%%%%%%

```

```
424     figure
425     hold on
426     set(gca,...
427     'xlim',x0_lim_HS,...
428     'xtick',x0_tick_HS,...
429     'ylim',x0_lim_HS,...
430     'ytick',x0_tick_HS,...
431     'fontname','helvetica',...
432     'fontsize',12)
433
434     ax = gca;
435     ax.YAxis.Exponent = 0;
436
437     plot(a_Fe(1:n),X_0_Fe(1:n),'-. ','color',colour_sum,'linewidth',1.2);
438     plot(a,0,'k*', 'MarkerSize', 10);
439
440     % Create textbox
441     annotation('textbox',[0.25 0.25 0.15 0.07],'String',{'repulsion'},...
442     'fontname','helvetica','fontsize',12,'Interpreter','latex',...
443     'EdgeColor', 'none');
444
445     % Create textbox
446     annotation('textbox',[0.5 0.5 0.15 0.07],'String',{'attraction'},...
447     'fontname','helvetica','fontsize',12,'Interpreter','latex',...
448     'EdgeColor', 'none');
449
450     xlabel(x0_label,'Interpreter','latex');
451     ylabel(join(['Attraction limit, $X_{0}$ ',unit_length]),'Interpreter','latex');
452
453     hold off
454
455 %%%%%%%%%%%%%%%%%%%%%%%%%%%%%%%%%%%%%%%%%%%%%%%%%%%%%%%%%%%%%%%%%%%%%%%
456 %                          Oxygen shell                                  %
457 %%%%%%%%%%%%%%%%%%%%%%%%%%%%%%%%%%%%%%%%%%%%%%%%%%%%%%%%%%%%%%%%%%%%%%%
458
459     figure
460     hold on
461     set(gca,...
462     'xlim',x0_lim_HS,...
463     'xtick',x0_tick_HS,...
```

```
464     'ylim',x0_lim_HS,...
465     'ytick',x0_tick_HS,...
466     'fontname','helvetica',...
467     'fontsize',12)
468 
469     ax = gca;
470     ax.YAxis.Exponent = 0;
471 
472     plot(a_OS(1:n+1),X_0_OS(1:n+1),'-- ','color',colour_sum,'linewidth',1.2);
473     plot(a,0,'k*', 'MarkerSize', 10);
474 
475     xlabel(x0_label,'Interpreter','latex');
476     ylabel(join(['Attraction limit, $X_{0}$ ',unit_length]),'Interpreter','latex');
477     hold off
478 
479 %%%%%%%%%%%%%%%%%%%%%%%%%%%%%%%%%%%%%%%%%%%%%%%%%%%%%%%%%%%%%%%%%%%%%%%
480 %                         Hydrogen shell                                 %
481 %%%%%%%%%%%%%%%%%%%%%%%%%%%%%%%%%%%%%%%%%%%%%%%%%%%%%%%%%%%%%%%%%%%%%%%
482 
483     figure
484     hold on
485     set(gca,...
486     'xlim',x0_lim_HS,...
487     'xtick',x0_tick_HS,...
488     'ylim',x0_lim_HS,...
489     'ytick',x0_tick_HS,...
490     'fontname','helvetica',...
491     'fontsize',12)
492 
493     ax = gca;
494     ax.YAxis.Exponent = 0;
495 
496     plot(a_HS(1:n+1),X_0_HS(1:n+1),'color',colour_sum,'linewidth',1.2);
497     plot(a,0,'k*', 'MarkerSize', 10);
498 
499     xlabel(x0_label,'Interpreter','latex');
500     ylabel(join(['Attraction limit, $X_{0}$ ',unit_length]),'Interpreter','latex');
501     hold off
502 
503 %%%%%%%%%%%%%%%%%%%%%%%%%%%%%%%%%%%%%%%%%%%%%%%%%%%%%%%%%%%%%%%%%%%%%%%
```

```
504 %                       Hydrated ferric ion                          %
505 %%%%%%%%%%%%%%%%%%%%%%%%%%%%%%%%%%%%%%%%%%%%%%%%%%%%%%%%%%%%%%%%%%%
506
507     figure
508     hold on
509     set(gca,...
510     'xlim',x0_lim_HS,...
511     'xtick',x0_tick_HS,...
512     'ylim',x0_lim_HS,...
513     'ytick',x0_tick_HS,...
514     'fontname','helvetica',...
515     'fontsize',12)
516
517     ax = gca;
518     ax.YAxis.Exponent = 0;
519
520     plot(a_tot(1:n+1),X_0_tot(1:n+1),'k','linewidth',1.2);
521     plot(a_Fe(1:n),X_0_Fe(1:n),'-. ','color',colour_sum,'linewidth',1.2);
522     plot(a,0,'k*', 'MarkerSize', 10);
523
524     legend('Total','Fe(III)','Location','northeast','Interpreter','latex')
525
526     xlabel(x0_label,'Interpreter','latex');
527     ylabel(join(['Attraction limit, $X_{0}$ ',unit_length]),'Interpreter','latex');
528     hold off
529 end
530
531 %%
532 %%%%%%%%%%%%%%%%%%%%%%%%%%%%%%%%%%%%%%%%%%%%%%%%%%%%%%%%%%%%%%%%%%%%
533 %                                                                       %
534 %Acceptance energy and Work done - Hydrated iron to MOF pore%
535 %                                                                       %
536 %%%%%%%%%%%%%%%%%%%%%%%%%%%%%%%%%%%%%%%%%%%%%%%%%%%%%%%%%%%%%%%%%%%%
537
538 if (strcmp(section,'ALL') || strcmp(section,'W'))
539
540     x0_label = join(["MOF radius, $a$",unit_length]);
541
542 % energy in eV
543     y_lim_W_Fe = [-0.04 0.08];
```

```
544     y_tick_W_Fe = (-0.04:0.04:0.08);
545
546     y_lim_W_HS = [-0.04 0.64];
547     y_tick_W_HS = (0:0.2:0.6);
548
549     y_lim_W_OS = y_lim_W_HS;
550     y_tick_W_OS = y_tick_W_HS;
551
552     y_lim_W_tot = [-0.04 1.2];
553     y_tick_W_tot = (0:0.2:1.2);
554
555 %%%%%%%%%%%%%%%%%%%%%%%%%%%%%%%%%%%%%%%%%%%%%%%%%%%%%%%%%%%%%%%%%%%%%%%
556 %                       Ferric ion point                                 %
557 %%%%%%%%%%%%%%%%%%%%%%%%%%%%%%%%%%%%%%%%%%%%%%%%%%%%%%%%%%%%%%%%%%%%%%%
558
559     figure
560     hold on
561     set(gca,...
562     'xlim',[2*SI_con_length 10*SI_con_length],...
563     'xtick',(2*SI_con_length:2*SI_con_length:10*SI_con_length),...
564     'ylim',y_lim_W_Fe,...
565     'ytick',y_tick_W_Fe,...
566     'fontname','helvetica',...
567     'fontsize',12)
568
569     ax = gca;
570     ax.YAxis.Exponent = 0;
571
572     plot(a_Fe,W_Fe,'-. ','color',colour_sum,'linewidth',2);
573     plot(a_Fe,W_a_Fe,'-. ','color',colour_sum,'linewidth',1.2);
574     plot(a,W_a_sum_Fe,'k*', 'MarkerSize', 10);
575     plot(a,W_sum_Fe,'k*', 'MarkerSize', 10);
576
577     legend('$Ek_{\rm Fe}$','$Ea_{\rm Fe}$','Location','northeast','Interpreter','latex'
        )
578
579     xlabel(x0_label,'Interpreter','latex');
580     ylabel(join(['Kinetic energy, ',unit_energy]),'Interpreter','latex');
581     ytickformat('%.2f')
582     grid on
```

```
583     hold off
584
585 %%%%%%%%%%%%%%%%%%%%%%%%%%%%%%%%%%%%%%%%%%%%%%%%%%%%%%%%%%%%%%%%%%%%%%%
586 %                          Oxygen shell                                  %
587 %%%%%%%%%%%%%%%%%%%%%%%%%%%%%%%%%%%%%%%%%%%%%%%%%%%%%%%%%%%%%%%%%%%%%%%
588
589     figure
590     hold on
591     set(gca,...
592     'xlim',[2*SI_con_length 10*SI_con_length],...
593     'xtick',(2*SI_con_length:2*SI_con_length:10*SI_con_length),...
594     'ylim',y_lim_W_OS,...
595     'ytick',y_tick_W_OS,...
596     'fontname','helvetica',...
597     'fontsize',12)
598
599     ax = gca;
600     ax.YAxis.Exponent = 0;
601
602     plot(a_OS(con_OS:end),W_OS,'-- ','color',colour_sum,'linewidth',2);
603     plot(a_OS(con_OS:end),W_a_OS,'-- ','color',colour_sum,'linewidth',1.2);
604     plot(a,W_a_sum_OS,'k*', 'MarkerSize', 10);
605     plot(a,W_sum_OS,'k*', 'MarkerSize', 10);
606
607     legend('$Ek_{\rm OS}$','$Ea_{\rm OS}$','Location','northeast','Interpreter','latex'
        )
608
609     xlabel(x0_label,'Interpreter','latex');
610     ylabel(join(['Kinetic energy, ',unit_energy]),'Interpreter','latex');
611     ytickformat('%.1f')
612     grid on
613     hold off
614
615 %%%%%%%%%%%%%%%%%%%%%%%%%%%%%%%%%%%%%%%%%%%%%%%%%%%%%%%%%%%%%%%%%%%%%%%
616 %                         Hydrogen shell                                 %
617 %%%%%%%%%%%%%%%%%%%%%%%%%%%%%%%%%%%%%%%%%%%%%%%%%%%%%%%%%%%%%%%%%%%%%%%
618
619     figure
620     hold on
621     set(gca,...
```

```
    'xlim',[2*SI_con_length 10*SI_con_length],...
    'xtick',(2*SI_con_length:2*SI_con_length:10*SI_con_length),...
    'ylim',y_lim_W_HS,...
    'ytick',y_tick_W_HS,...
    'fontname','helvetica',...
    'fontsize',12)

    ax = gca;
    ax.YAxis.Exponent = 0;

    plot(a_HS(con_HS:end),W_HS,'color',colour_sum,'linewidth',2);
    plot(a_HS(con_HS:end),W_a_HS,'color',colour_sum,'linewidth',1.2);
    plot(a,W_a_sum_HS,'k*', 'MarkerSize', 10);
    plot(a,W_sum_HS,'k*', 'MarkerSize', 10);

    legend('$Ek_{\rm HS}$','$Ea_{\rm HS}$','Location','northeast','Interpreter','latex'
    )

    xlabel(x0_label,'Interpreter','latex');
    ylabel(join(['Kinetic energy, ',unit_energy]),'Interpreter','latex');
    ytickformat('%.1f')
    grid on
    hold off

%%%%%%%%%%%%%%%%%%%%%%%%%%%%%%%%%%%%%%%%%%%%%%%%%%%%%%%%%%%%%%%%%%%%%%%
%                   Total potential energy                              %
%%%%%%%%%%%%%%%%%%%%%%%%%%%%%%%%%%%%%%%%%%%%%%%%%%%%%%%%%%%%%%%%%%%%%%%

    figure
    hold on
    set(gca,...
    'xlim',[2*SI_con_length 10*SI_con_length],...
    'xtick',(2*SI_con_length:2*SI_con_length:10*SI_con_length),...
    'ylim',y_lim_W_tot,...
    'ytick',y_tick_W_tot,...
    'fontname','helvetica',...
    'fontsize',12)

    ax = gca;
    ax.YAxis.Exponent = 0;
```

```
661
662     plot(a_tot(con_tot:end),W_tot,'k','linewidth',2);
663     plot(a_tot(con_tot:end),W_a_tot,'k','linewidth',1.2);
664     plot(a_Fe,W_Fe,'-. ','color',colour_sum,'linewidth',2);
665     plot(a_Fe,W_a_Fe,'-. ','color',colour_sum,'linewidth',1.2);
666
667     plot(a,W_a_sum_tot,'k*', 'MarkerSize', 10);
668     plot(a,W_sum_tot,'k*', 'MarkerSize', 10);
669     plot(a,W_a_sum_Fe,'k*', 'MarkerSize', 10);
670     plot(a,W_sum_Fe,'k*', 'MarkerSize', 10);
671
672     legend('$Ek_{\rm tot}$','$Ea_{\rm tot}$','$Ek_{\rm Fe}$','$Ea_{\rm Fe}$', ...
673         'Location','northeast','Interpreter','latex')
674
675     xlabel(x0_label,'Interpreter','latex');
676     ylabel(join(['Kinetic energy, ',unit_energy]),'Interpreter','latex');
677     ytickformat('%.1f')
678     grid on
679     hold off
680
681 %%
682 %%%%%%%%%%%%%%%%%%%%%%%%%%%%%%%%%%%%%%%%%%%%%%%%%%%%%%%%%%%%%%%%%%%%%%%
683 %                                                                       %
684 %                           Comments                                    %
685 %                                                                       %
686 %%%%%%%%%%%%%%%%%%%%%%%%%%%%%%%%%%%%%%%%%%%%%%%%%%%%%%%%%%%%%%%%%%%%%%%
687
688     if (isreal(W_tot))
689         disp(join(["Good: total energy is real: ",num2str(W_sum_tot), unit_energy(2:end
    -1)]))
690         disp(join(["Good: total energy for Fe3+ is real: ",num2str(W_sum_Fe),
    unit_energy(2:end-1)]))
691         disp(join(["Good: total energy for oxygen sphere is real: ",num2str(W_sum_OS),
    unit_energy(2:end-1)]))
692         disp(join(["Good: total energy for hydrogen sphere is real: ",num2str(W_sum_HS)
    , unit_energy(2:end-1)]))
693     else
694         disp('Bad: total acceptance energy is not real.')
695     end
696
```

```
697     if (isreal(v_tot))
698         disp(['Good: velocity of ferric ion due to total suction energy is real: ',
        num2str(v_Fe), ' m s^-1'])
699         disp(['Good: velocity of hydrated ferric ion due to total suction energy is
        real: ',num2str(v_tot), ' m s^-1'])
700     else
701         disp('Bad: velocity due to total acceptance energy is not real.')
702     end
703
704 end
```

H.1.2. Lennard-Jones parameters and surface densities

```
1  % function Input_LJ_constants_Pore_parameters(SI_con_energy,SI_con_length,m)
2  % MATLAB version R2019b
3  % DATE: 23/09/2020
4  % EDITED: 05/12/2022
5  %
6  % DESCRIPTION: This code only provides the parameters used for the .
7  % INPUT:
8  %   SI_con_energy - convertion constant for energy i.e. 1kcal/mol = 4184 J/mol
9  %   SI_con_length - convertion constant for length i.e. 1 angstrom = 10^-10 m
10 %
11 %   m - the number of unit cells in a MOF pore
12 %
13 %   The Lennard jones constants are taken from a paper rappe1992uff,
14 %   LJ(rho) = -2*D_i*(x_i/rho)^6 + D_i*(x_i/rho)^12
15 %       x_H = 2.886 kcal/mol - the equilibrium distance for H-H
16 %       D_H = 0.044 angstrom - the well depth for H-H
17 %       x_C = 3.851 kcal/mol - the equilibrium distance for C-C
18 %       D_C = 0.105 angstrom - the well depth for C-C
19 %       x_O = 3.5 kcal/mol   - the equilibrium distance for O-O
20 %       D_O = 0.06 angstrom  - the well depth for O-O
21 %       x_Fe = 2.912 kcal/mol - the equilibrium distance for Fe3+ - Fe3+
22 %       D_Fe = 0.013 angstrom - the well depth for Fe3+ - Fe3+
23 %       x_Eu = 3.493 kcal/mol - the equilibrium distance for Eu-Eu
24 %       D_Eu = 0.008 angstrom - the well depth for Eu-Eu
25 %   a - the radius a unit cell in MOF crystal, m
26 %   h - height of a unit cell in MOF crystal, m
27 %   n_i*area_cylinder - the number of atom i in a unit cell, mol
28 %   mass_Fe - molar mass of iron atom, kg/mol
```

```
29
30 unit_length = '[\AA]';                    % distance in angstrom
31 unit_energy = '[eV]';                     % energy in eV
32
33 %%
34 %%%%%%%%%%%%%%%%%%%%%%%%%%%%%%%%%%%%%%%%%%%%%%%%%%%%%%%%%%%%%%%%%%%%%%%%
35 %                          Geometry                                       %
36 %              Input paramters - MOF pore                                 %
37 %                                                                         %
38 %%%%%%%%%%%%%%%%%%%%%%%%%%%%%%%%%%%%%%%%%%%%%%%%%%%%%%%%%%%%%%%%%%%%%%%%
39
40 % Pore parameters
41 m = 1 ;                                % number of unit cells for finite calc
42 a_axis = 11.5130*SI_con_length;         % a basis vector length
43 b_axis = 6.829*SI_con_length;           % b basis vector length
44 c_axis = 20.976*SI_con_length;          % c basis vector length
45
46 angle_ac_obtuse = (102.8)*pi/180;       % beta, the obtuse angle a-axis and c-axis
       intersect
47 angle_ac_acute = (180-102.8)*pi/180;    % 180 - beta
48
49 a = a_axis/2;                           % m;     pore radius
50 h = m*b_axis;                           % m; height for finite cell depth
51
52 area_cylinder = 2*pi*a*b_axis;          % m^2; area for unit cell
53
54 % Mean densities for pore
55 n_H = 52/area_cylinder;
56 n_C = 54/area_cylinder;
57 n_O = 38/area_cylinder;
58 n_Eu = 8/area_cylinder;
59
60 %%
61 %%%%%%%%%%%%%%%%%%%%%%%%%%%%%%%%%%%%%%%%%%%%%%%%%%%%%%%%%%%%%%%%%%%%%%%%
62 %                          Geometry                                       %
63 %              Input paramters - Hydrated ferric ion                      %
64 %                                                                         %
65 %%%%%%%%%%%%%%%%%%%%%%%%%%%%%%%%%%%%%%%%%%%%%%%%%%%%%%%%%%%%%%%%%%%%%%%%
66
67 % Surface area parameters for ferric ion molecule - Fe3+ and 6(H2O)
```

```
68 b_OS    = 2.039*SI_con_length;          % m
69 area_OS = 4*pi*b_OS^2;                  % m^2
70
71 b_OH = 0.982*SI_con_length;             % m; distance between O and H
72 angle_FeOH = (360-106.76)*pi/(2*180);   % radians; angle between Fe-O-H
73
74 b_HS    = sqrt(b_OH^2 + b_OS^2 - 2*b_OH*b_OS*cos(angle_FeOH));   % m
75 area_HS = 4*pi*b_HS^2;                                           % m^2
76
77 % Mean densities for ferric ion molecule - Fe3+ and 6(H2O)
78 num_O = 6;
79 num_H = 12;
80
81 n_OS = num_O/area_OS;
82 n_HS = num_H/area_HS;
83
84 % Mass of elements in ferric ion molecule - Fe3+ and 6(H2O)
85 mass_Fe = 55.845e-3;                    % kg/mol
86 mass_O  = 15.9994e-3;                   % kg/mol
87 mass_H  = 1.00794e-3;                   % kg/mol
88
89 %%
90 %%%%%%%%%%%%%%%%%%%%%%%%%%%%%%%%%%%%%%%%%%%%%%%%%%%%%%%%%%%%%%%%%%%%%%%%%%%%
91 %                  Lennard-Jones constants                                    %
92 %              Input paramters - same atom type                               %
93 %                                                                             %
94 %%%%%%%%%%%%%%%%%%%%%%%%%%%%%%%%%%%%%%%%%%%%%%%%%%%%%%%%%%%%%%%%%%%%%%%%%%%%
95
96 % From rappe1992uff
97 % Hydrogen
98 A_H = 2*(0.044*SI_con_energy)*(2.886*SI_con_length)^6;      % J/mol m^6;    A_H = 2*D_i
       *x_i^6
99 B_H = (0.044*SI_con_energy)*(2.886*SI_con_length)^12;       % J/mol m^12;   B_H = 2*D_i
       *x_i^12
100 sigma_H = (B_H/A_H)^(1/6);                                  % m;            r_min =
       2.886 = (2*B_H/A_H)^(1/6)
101 epsilon_H = A_H^2/(4*B_H);                                 % J/mol
102
103 % Carbon
104 A_C = 2*(0.105*SI_con_energy)*(3.851*SI_con_length)^6;      % J/mol m^6
```

```
105 B_C = (0.105*SI_con_energy)*(3.851*SI_con_length)^12;       % J/mol m^12
106 sigma_C = (B_C/A_C)^(1/6);                                  % m;            r_min =
      3.851 = (2*B_C/A_C)^(1/6);
107 epsilon_C = A_C^2/(4*B_C);                                  % J/mol
108
109 % Oxygen
110 A_O = 2*(0.06*SI_con_energy)*(3.5*SI_con_length)^6;         % J/mol m^6
111 B_O = (0.06*SI_con_energy)*(3.5*SI_con_length)^12;          % J/mol m^12
112 sigma_O = (B_O/A_O)^(1/6);                                  % m;            r_min = 3.5
       = (2*B_O/A_O)^(1/6);
113 epsilon_O = A_O^2/(4*B_O);                                  % eV
114
115 % Iron III - Ferric ion - Fe3+
116 A_Fe = 2*(0.013*SI_con_energy)*(2.912*SI_con_length)^6;     % J/mol m^6;
117 B_Fe = (0.013*SI_con_energy)*(2.912*SI_con_length)^12;      % J/mol m^12;
118 sigma_Fe = (B_Fe/A_Fe)^(1/6);                               % m;            r_min =
      2.912 = (2*B_Fe/A_Fe)^(1/6);
119 epsilon_Fe = A_Fe^2/(4*B_Fe);                               % J/mol
120
121 % Europium III - Eu3+
122 A_Eu = 2*(0.008*SI_con_energy)*(3.493*SI_con_length)^6;     % J/mol m^6;
123 B_Eu = (0.008*SI_con_energy)*(3.493*SI_con_length)^12;      % J/mol m^12;
124 sigma_Eu = (B_Eu/A_Eu)^(1/6);                               % m;            r_min =
      3.493 = (2*B_Eu/A_Eu)^(1/6);
125 epsilon_Eu = A_Eu^2/(4*B_Eu);                               % J/mol
126
127 %%
128 %%%%
```

```
sigma_Fe_C = mean([sigma_Fe, sigma_C]);
epsilon_Fe_C = sqrt(epsilon_Fe*epsilon_C);
A_Fe_C = 4*epsilon_Fe_C*sigma_Fe_C^6;
B_Fe_C = 4*epsilon_Fe_C*sigma_Fe_C^12;

% Iron III vs Oxygen
sigma_Fe_O = mean([sigma_Fe, sigma_O]);
epsilon_Fe_O = sqrt(epsilon_Fe*epsilon_O);
A_Fe_O = 4*epsilon_Fe_O*sigma_Fe_O^6;
B_Fe_O = 4*epsilon_Fe_O*sigma_Fe_O^12;

% Iron III vs Europium III
sigma_Fe_Eu = mean([sigma_Fe, sigma_Eu]);
epsilon_Fe_Eu = sqrt(epsilon_Fe*epsilon_Eu);
A_Fe_Eu = 4*epsilon_Fe_Eu*sigma_Fe_Eu^6;
B_Fe_Eu = 4*epsilon_Fe_Eu*sigma_Fe_Eu^12;

A_sum_Fe = n_H*A_Fe_H + n_C*A_Fe_C + n_O*A_Fe_O + n_Eu*A_Fe_Eu;
B_sum_Fe = n_H*B_Fe_H + n_C*B_Fe_C + n_O*B_Fe_O + n_Eu*B_Fe_Eu;

sigma_sum_Fe = (B_sum_Fe/A_sum_Fe)^(1/6);
epsilon_sum_Fe = A_sum_Fe^2/(4*B_sum_Fe);

%%
%%%%%%%%%%%%%%%%%%%%%%%%%%%%%%%%%%%%%%%%%%%%%%%%%%%%%%%%%%%%%%%%
%                  Lennard-Jones constants                      %
%            Input paramters - Oxygen vs atom type              %
%                                                               %
%%%%%%%%%%%%%%%%%%%%%%%%%%%%%%%%%%%%%%%%%%%%%%%%%%%%%%%%%%%%%%%%

% Oxygen vs Hydrogen
sigma_O_H = mean([sigma_O, sigma_H]);
epsilon_O_H = sqrt(epsilon_O*epsilon_H);
A_O_H = 4*epsilon_O_H*sigma_O_H^6;
B_O_H = 4*epsilon_O_H*sigma_O_H^12;

% Oxygen vs Carbon
sigma_O_C = mean([sigma_O, sigma_C]);
epsilon_O_C = sqrt(epsilon_O*epsilon_C);
A_O_C = 4*epsilon_O_C*sigma_O_C^6;
```

```
B_O_C = 4*epsilon_O_C*sigma_O_C^12;

% Oxygen vs Europium III
sigma_O_Eu = mean([sigma_O, sigma_Eu]);
epsilon_O_Eu = sqrt(epsilon_O*epsilon_Eu);
A_O_Eu = 4*epsilon_O_Eu*sigma_O_Eu^6;
B_O_Eu = 4*epsilon_O_Eu*sigma_O_Eu^12;

A_sum_OS = n_H*A_O_H + n_C*A_O_C + n_O*A_O + n_Eu*A_O_Eu;
B_sum_OS = n_H*B_O_H + n_C*B_O_C + n_O*B_O + n_Eu*B_O_Eu;

sigma_sum_OS = (B_sum_OS/A_sum_OS)^(1/6);
epsilon_sum_OS = A_sum_OS^2/(4*B_sum_OS);

%%
%%%%%%%%%%%%%%%%%%%%%%%%%%%%%%%%%%%%%%%%%%%%%%%%%%%%%%%%%%%%%%%%%%%%%%%%
%                                                                       %
%             Input paramters - Hydrogen vs atom type                   %
%                                                                       %
%%%%%%%%%%%%%%%%%%%%%%%%%%%%%%%%%%%%%%%%%%%%%%%%%%%%%%%%%%%%%%%%%%%%%%%%

% Hydrogen vs Carbon
sigma_H_C = mean([sigma_H, sigma_C]);
epsilon_H_C = sqrt(epsilon_H*epsilon_C);
A_H_C = 4*epsilon_H_C*sigma_H_C^6;
B_H_C = 4*epsilon_H_C*sigma_H_C^12;

% Hydrogen vs Europium III
sigma_H_Eu = mean([sigma_H, sigma_Eu]);
epsilon_H_Eu = sqrt(epsilon_H*epsilon_Eu);
A_H_Eu = 4*epsilon_H_Eu*sigma_H_Eu^6;
B_H_Eu = 4*epsilon_H_Eu*sigma_H_Eu^12;

A_sum_HS = n_H*A_H + n_C*A_H_C + n_O*A_O_H + n_Eu*A_H_Eu;
B_sum_HS = n_H*B_H + n_C*B_H_C + n_O*B_O_H + n_Eu*B_H_Eu;

sigma_sum_HS = (B_sum_HS/A_sum_HS)^(1/6);
epsilon_sum_HS = A_sum_HS^2/(4*B_sum_HS);
```

H.1.3. Interaction potential energy, force and kinetic energy functions

```
% function IE_IF_W_related_funtions
% MATLAB version R2019b
% EDITED: 09/08/2022

%%%%%%%%%%%%%%%%%%%%%%%%%%%%%%%%%%%%%%%%%%%%%%%%%%%%%%%%%%%%%%%%%%%%%%%%
%                                                                       %
%   Expandions of J_n = \int \cos(x)^2n dx                              %
%                                                                       %
%%%%%%%%%%%%%%%%%%%%%%%%%%%%%%%%%%%%%%%%%%%%%%%%%%%%%%%%%%%%%%%%%%%%%%%%

I0 = @(r,x) atan(x./r);

I1 = @(r,x) (atan(x./r)/2) + (r.*x)./(2*(r.^2 + x.^2));

I2 = @(r,x) ((3.*atan(x./r))/8) + (r.^3.*x)./(4*(r.^2 + x.^2).^2) ...
    + (3*r.*x)./(8*(r.^2 + x.^2));

I3 = @(r,x) (5*atan(x./r)/16) + (r.^5.*x)./(6*(r.^2 + x.^2).^3) ...
    + (5*r.^3.*x)./(24*(r.^2 + x.^2).^2) + (5*r.*x)./(16*(r.^2 + x.^2));

I4 = @(r,x) (35*atan(x./r)./128) + (r.^7.*x)./(8*(r.^2 + x.^2).^4) ...
    + (7*r.^5.*x)./(48*(r.^2 + x.^2).^3) + (35*r.^3.*x)./(192*(r.^2 + x.^2).^2) ...
    + (35*r.*x)./(128*(r.^2 + x.^2));

I5 = @(r,x) (63*atan(x./r)./256) + (r.^9.*x)./(10*(r.^2 + x.^2).^5) ...
    + (9*r.^7.*x)./(80*(r.^2 + x.^2).^4) + (21*r.^5.*x)./(160*(r.^2 + x.^2).^3) ...
    + (21*r.^3.*x)./(128*(r.^2 + x.^2).^2) + (63*r.*x)./(256*(r.^2 + x.^2));

I6 = @(r,x) (231*atan(x./r)/1024) + (r.^11.*x)./(12*(r.^2 + x.^2).^6) ...
    + (11*r.^9.*x)./(120*(r.^2 + x.^2).^5) + (33*r.^7.*x)./(320*(r.^2 + x.^2).^4) ...
    + (77*r.^5.*x)./(640*(r.^2 + x.^2).^3) + (77*r.^3.*x)./(512*(r.^2 + x.^2).^2) ...
    + (231*r.*x)./(1024*(r.^2 + x.^2));

I7 = @(r,x) (429*atan(x./r)/2048) + (r.^13.*x)./(14*(r.^2 + x.^2).^7) ...
    + (13*r.^11.*x)./(168*(r.^2 + x.^2).^6) + (143*r.^9.*x)./(1680*(r.^2 + x.^2).^5)
    ...
    + (429*r.^7.*x)./(4480*(r.^2 + x.^2).^4) + (143*r.^5.*x)./(1280*(r.^2 + x.^2).^3)
    ...
    + (143*r.^3.*x)./(1024*(r.^2 + x.^2).^2) + (429*r.*x)./(2048*(r.^2 + x.^2));

```

```
39 I8 = @(r,x) (6435*atan(x./r)/32768) + (r.^15.*x)./(16*(r.^2 + x.^2).^8) ...
40     + (15*r.^13.*x)./(224*(r.^2 + x.^2).^7) + (65*r.^11.*x)./(896*(r.^2 + x.^2).^6) ...
41     + (143*r.^9.*x)./(1792*(r.^2 + x.^2).^5) + (1287*r.^7.*x)./(14336*(r.^2 + x.^2).^4)
       ...
42     + (429*r.^5.*x)./(4096*(r.^2 + x.^2).^3) + (2145*r.^3.*x)./(16384*(r.^2 + x.^2).^2)
       ...
43     + (6435*r.*x)./(32768*(r.^2 + x.^2));
44
45 I9 = @(r,x) (12155*atan(x./r)/65536) + (r.^17.*x)./(18*(r.^2 + x.^2).^9) ...
46     + (17*r.^15.*x)./(288*(r.^2 + x.^2).^8) + (85*r.^13.*x)./(1344*(r.^2 + x.^2).^7)
       ...
47     + (1105*r.^11.*x)./(16128*(r.^2 + x.^2).^6) + (2431*r.^9.*x)./(32256*(r.^2 + x.^2)
       .^5) ...
48     + (2431*r.^7.*x)./(28672*(r.^2 + x.^2).^4)+ (2431*r.^5.*x)./(24576*(r.^2 + x.^2)
       .^3)...
49     + (12155*r.^3.*x)./(98304*(r.^2 + x.^2).^2) + (12155*r.*x)./(65536*(r.^2 + x.^2));
50
51 J0 = @(r,x) I0(0,1) - I0(r,x);
52
53 J1 = @(r,x) I1(0,1) - I1(r,x);
54
55 J2 = @(r,x) I2(0,1) - I2(r,x);
56
57 J3 = @(r,x) I3(0,1) - I3(r,x);
58
59 J4 = @(r,x) I4(0,1) - I4(r,x);
60
61 J5 = @(r,x) I5(0,1) - I5(r,x);
62
63 J6 = @(r,x) I6(0,1) - I6(r,x);
64
65 J7 = @(r,x) I7(0,1) - I7(r,x);
66
67 J8 = @(r,x) I8(0,1) - I8(r,x);
68
69 J9 = @(r,x) I9(0,1) - I9(r,x);
70
71 H2 = @(r,c,x) I2(r,c+x) - I2(r,x);
72
73 H3 = @(r,c,x) I3(r,c+x) - I3(r,x);
```

```
74
75 H5 = @(r,c,x) I5(r,c+x) - I5(r,x);
76
77 H6 = @(r,c,x) I6(r,c+x) - I6(r,x);
78
79 H7 = @(r,c,x) I7(r,c+x) - I7(r,x);
80
81 H8 = @(r,c,x) I8(r,c+x) - I8(r,x);
82
83 H9 = @(r,c,x) I9(r,c+x) - I9(r,x);
84
85 %%%%%%%%%%%%%%%%%%%%%%%%%%%%%%%%%%%%%%%%%%%%%%%%%%%%%%%%%%%%%%%%%%%%%%%
86 %                                                                       %
87 %                       Potential energy                                %
88 %                                                                       %
89 %%%%%%%%%%%%%%%%%%%%%%%%%%%%%%%%%%%%%%%%%%%%%%%%%%%%%%%%%%%%%%%%%%%%%%%
90
91     lambda = @(a,b) sqrt(a.^2 - b.^2);
92
93 %%%%%%%%%%%%%%%%%%%%%%%%%%%%%%%%%%%%%%%%%%%%%%%%%%%%%%%%%%%%%%%%%%%%%%%
94 %                       Point to cylinder                               %
95 %%%%%%%%%%%%%%%%%%%%%%%%%%%%%%%%%%%%%%%%%%%%%%%%%%%%%%%%%%%%%%%%%%%%%%%
96
97     E_point = @(a,A,B,x) (2*pi/a^4)*(-A*J2(a,x) + (B/a^6)*J5(a,x));
98
99 %%%%%%%%%%%%%%%%%%%%%%%%%%%%%%%%%%%%%%%%%%%%%%%%%%%%%%%%%%%%%%%%%%%%%%%
100 %                       Sphere to cylinder                              %
101 %%%%%%%%%%%%%%%%%%%%%%%%%%%%%%%%%%%%%%%%%%%%%%%%%%%%%%%%%%%%%%%%%%%%%%%
102
103     E_shell = @(a,b,n,A,B,x) (8*pi^2*a*b^2*n/lambda(a,b)^5)*(- A*(J2(lambda(a,b),x) ...
104         + 2*(b/lambda(a,b))^2*J3(lambda(a,b),x)) + (B/5)*(lambda(a,b)^(-6))*(5*J5(
    lambda(a,b),x)...
105         + 80*(b/lambda(a,b))^2*J6(lambda(a,b),x) + 336*(b/lambda(a,b))^4*J7(lambda(a,b)
    ,x)...
106         + 512*(b/lambda(a,b))^6*J8(lambda(a,b),x) + 256*(b/lambda(a,b))^8*J9(lambda(a,b
    ),x)));
107
108 %%%%%%%%%%%%%%%%%%%%%%%%%%%%%%%%%%%%%%%%%%%%%%%%%%%%%%%%%%%%%%%%%%%%%%%
109 %                                                                       %
110 %                             Force                                     %
```

```
111 %                                                                       %
112 %%%%%%%%%%%%%%%%%%%%%%%%%%%%%%%%%%%%%%%%%%%%%%%%%%%%%%%%%%%%%%%%%%%%
113
114 %%%%%%%%%%%%%%%%%%%%%%%%%%%%%%%%%%%%%%%%%%%%%%%%%%%%%%%%%%%%%%%%%%%%
115 %                       Point to cylinder                               %
116 %%%%%%%%%%%%%%%%%%%%%%%%%%%%%%%%%%%%%%%%%%%%%%%%%%%%%%%%%%%%%%%%%%%%
117
118     F_point = @(a,A,B,x) (2*pi*a).*(A./((a.^2 + x.^2).^3) - B./((a.^2 + x.^2).^6));
119
120 %%%%%%%%%%%%%%%%%%%%%%%%%%%%%%%%%%%%%%%%%%%%%%%%%%%%%%%%%%%%%%%%%%%%
121 %                       Sphere to cylinder                              %
122 %%%%%%%%%%%%%%%%%%%%%%%%%%%%%%%%%%%%%%%%%%%%%%%%%%%%%%%%%%%%%%%%%%%%
123
124     F_shell = @(a,b,n,A,B,x) (8*pi^2*a*b^2*n).*(A*((a.^2 - b^2 + x.^2).^-3 ...
125         + 2*b^2*(a.^2 - b^2 + x.^2).^-4) - (B/5)*(5*(a.^2 - b^2 + x.^2).^-6  ...
126         + 80*b^2*(a.^2 - b^2 + x.^2).^-7 + 336*b^4*(a.^2 - b^2 + x.^2).^-8 ...
127         + 512*b^6*(a.^2 - b^2 + x.^2).^-9 + 256*b^8*(a.^2 - b^2 + x.^2).^-10));
128
129
130 %%%%%%%%%%%%%%%%%%%%%%%%%%%%%%%%%%%%%%%%%%%%%%%%%%%%%%%%%%%%%%%%%%%%
131 %                                                                       %
132 %                 Acceptance/Kinetic Energy                           %
133 %                                                                       %
134 %%%%%%%%%%%%%%%%%%%%%%%%%%%%%%%%%%%%%%%%%%%%%%%%%%%%%%%%%%%%%%%%%%%%
135
136    lambda = @(a,b) sqrt(a.^2 - b.^2);
137
138 %%%%%%%%%%%%%%%%%%%%%%%%%%%%%%%%%%%%%%%%%%%%%%%%%%%%%%%%%%%%%%%%%%%%
139 %                       Point to cylinder                               %
140 %%%%%%%%%%%%%%%%%%%%%%%%%%%%%%%%%%%%%%%%%%%%%%%%%%%%%%%%%%%%%%%%%%%%
141
142     W_point = @(a,A,B,r,x) (2*pi./a.^4).*(A*J2(r,x) - (B*J5(r,x))./a.^6);
143
144 %%%%%%%%%%%%%%%%%%%%%%%%%%%%%%%%%%%%%%%%%%%%%%%%%%%%%%%%%%%%%%%%%%%%
145 %                       Sphere to cylinder                              %
146 %%%%%%%%%%%%%%%%%%%%%%%%%%%%%%%%%%%%%%%%%%%%%%%%%%%%%%%%%%%%%%%%%%%%
147
148     W_shell = @(a,b,n,A,B,r,x) (8*pi^2*a.*b^2.*(lambda(a,b).^(-5))*n).*(A*(J2(r,x) ...
149         + 2*(b./lambda(a,b)).^2.*J3(r,x)) - (B/5).*(lambda(a,b).^(-6)).*(5*J5(r,x)...
150         + 80*(b./lambda(a,b)).^2.*J6(r,x) + 336*(b./lambda(a,b)).^4.*J7(r,x)...
```

```
151         + 512*(b./lambda(a,b)).^6.*J8(r,x) + 256*(b./lambda(a,b)).^8.*J9(r,x)));
```

H.1.4. Calculating interaction potential energy, force and kinetic energy

```
1  %function calculation_shell_interaction_forces
2  % MATLAB version R2019b
3  % DATE: 28/08/2020
4  % EDITED: 17/04/2023
5  %
6  % DESCRIPTION: This code values to plot the Lennard-Jones potential and
7  %   force interactions between a hydrated ferric ion and a semi-infinite
8  %   MOF pore. Also, values for a short summary for physical attributes of
9  %   the system.
10 % INPUT:
11 %   The Lennard-Jones equation:
12 %   LJ(rho) = -A/(rho)^6 + B/(rho)^12
13 %       A_k - attractive constant for element k in (C, H, O, Fe, Eu)
14 %       B_k - repulsive constant for element k in (C, H, O, Fe, Eu)
15 %       n_k - the mean density for element k in (C, H, O, Eu, OS, HS)
16 %       A_sum_j - sum the attractive constants n_k*A_j_k for element
17 %           k in (C, H, O, Eu), elements found in the MOF pore, where j is
18 %           the respective elements found in the hydrated ferric ion, j in
19 %           (OS - oxygen sphere, HS - hydrogen sphere).
20 %       B_sum_j - sum the repulsive constants n_k*B_j_k for element
21 %           k in (C, H, O, Eu).
22 %   sigma_sum_Fe -
23 %   a - the radius a unit cell in MOF crystal, angstrom
24 %   b_OS - the radius of the oxygen sphere
25 %   b_HS - the radius of the hydrogen sphere
26 %   n_i - the number of atom i in a unit cell, mol
27 % OUTPUT:
28 %   E_j_k - the interaction energy betweem elements j and k
29 %   E_sum_j - the summation of interaction energies, E_j_k over k
30 %   E_tot - the summation of interaction energies, E_sum_j over j
31 %   F_j_k - the interaction force betweem elements j and k
32 %   F_sum_j - the summation of interaction forces, F_j_k over k
33 %   F_tot - the summation of interaction force, F_sum_j over j
34 %   a_j - varying MOF pore radius with unchanged MOF densities
35 %   X_0_j - attraction limit
36 %   W_a_sum_j - the acceptance energy gained by j due to interaction force
37 %       from "true" MOF
```

```
38 %   W_a_sum_tot - the summation of "true" acceptance energy, W_a_sum_j over
39 %       j
40 %   W_a_j - the acceptance energy gained by j due to interaction force from
41 %       "varying" MOF
42 %   W_a_tot - the summation of "varying" acceptance energy, W_a_sum_j over j
43 %   W_sum_j - the kinetic energy gained by j due to interaction force
44 %       from "true" MOF
45 %   W_sum_tot - the summation of "true" kinetic energy, W_sum_j over j
46 %   W_j - the kinetic energy gained by j due to interaction force from
47 %       "varying" MOF
48 %   W_tot - the summation of "varying" acceptance energy, W_j over j
49
50 X = linspace(-20*SI_con_length,20*SI_con_length,10000);
51
52 %%
53 %%%%%%%%%%%%%%%%%%%%%%%%%%%%%%%%%%%%%%%%%%%%%%%%%%%%%%%%%%%%%%%%%%%%%%%%
54 %                                                                       %
55 %    Potential energy - Hydrated ferric ion to MOF pore                 %
56 %                                                                       %
57 %%%%%%%%%%%%%%%%%%%%%%%%%%%%%%%%%%%%%%%%%%%%%%%%%%%%%%%%%%%%%%%%%%%%%%%%
58
59 if (strcmp(section,'ALL') || strcmp(section,'IE'))
60
61 %%%%%%%%%%%%%%%%%%%%%%%%%%%%%%%%%%%%%%%%%%%%%%%%%%%%%%%%%%%%%%%%%%%%%%%%
62 %                     Ferric ion point                                  %
63 %%%%%%%%%%%%%%%%%%%%%%%%%%%%%%%%%%%%%%%%%%%%%%%%%%%%%%%%%%%%%%%%%%%%%%%%
64
65     E_Fe_H = E_point(a,A_Fe_H,B_Fe_H,-X)*n_H;
66     E_Fe_C = E_point(a,A_Fe_C,B_Fe_C,-X)*n_C;
67     E_Fe_O = E_point(a,A_Fe_O,B_Fe_O,-X)*n_O;
68     E_Fe_Eu = E_point(a,A_Fe_Eu,B_Fe_Eu,-X)*n_Eu;
69
70     E_sum_Fe = E_point(a,A_sum_Fe,B_sum_Fe,-X);
71
72 %%%%%%%%%%%%%%%%%%%%%%%%%%%%%%%%%%%%%%%%%%%%%%%%%%%%%%%%%%%%%%%%%%%%%%%%
73 %                        Oxygen shell                                   %
74 %%%%%%%%%%%%%%%%%%%%%%%%%%%%%%%%%%%%%%%%%%%%%%%%%%%%%%%%%%%%%%%%%%%%%%%%
75
76     E_OS_H = E_shell(a,b_OS,n_OS,A_O_H,B_O_H,-X)*n_H;
77     E_OS_C = E_shell(a,b_OS,n_OS,A_O_C,B_O_C,-X)*n_C;
```

```
78      E_OS_O = E_shell(a,b_OS,n_OS,A_O,B_O,-X)*n_O;
79      E_OS_Eu = E_shell(a,b_OS,n_OS,A_O_Eu,B_O_Eu,-X)*n_Eu;
80
81      E_sum_OS = E_shell(a,b_OS,n_OS,A_sum_OS,B_sum_OS,-X);
82
83  %%%%%%%%%%%%%%%%%%%%%%%%%%%%%%%%%%%%%%%%%%%%%%%%%%%%%%%%%%%%%%%%%%%%%%%
84  %                          Hydrogen shell                                %
85  %%%%%%%%%%%%%%%%%%%%%%%%%%%%%%%%%%%%%%%%%%%%%%%%%%%%%%%%%%%%%%%%%%%%%%%
86
87      E_HS_H = E_shell(a,b_HS,n_HS,A_H,B_H,-X)*n_H;
88      E_HS_C = E_shell(a,b_HS,n_HS,A_H_C,B_H_C,-X)*n_C;
89      E_HS_O = E_shell(a,b_HS,n_HS,A_O_H,B_O_H,-X)*n_O;
90      E_HS_Eu = E_shell(a,b_HS,n_HS,A_H_Eu,B_H_Eu,-X)*n_Eu;
91
92      E_sum_HS = E_shell(a,b_HS,n_HS,A_sum_HS,B_sum_HS,-X);
93
94  %%%%%%%%%%%%%%%%%%%%%%%%%%%%%%%%%%%%%%%%%%%%%%%%%%%%%%%%%%%%%%%%%%%%%%%
95  %                     Total potential energy                             %
96  %%%%%%%%%%%%%%%%%%%%%%%%%%%%%%%%%%%%%%%%%%%%%%%%%%%%%%%%%%%%%%%%%%%%%%%
97
98      E_tot = E_sum_Fe + E_sum_OS + E_sum_HS;
99  end
100
101 %%
102 %%%%%%%%%%%%%%%%%%%%%%%%%%%%%%%%%%%%%%%%%%%%%%%%%%%%%%%%%%%%%%%%%%%%%%%
103 %                                                                        %
104 %           Force - Hydrated ferric ion to MOF pore                      %
105 %                                                                        %
106 %%%%%%%%%%%%%%%%%%%%%%%%%%%%%%%%%%%%%%%%%%%%%%%%%%%%%%%%%%%%%%%%%%%%%%%
107
108 if (strcmp(section,'ALL') || strcmp(section,'IF'))
109
110 %%%%%%%%%%%%%%%%%%%%%%%%%%%%%%%%%%%%%%%%%%%%%%%%%%%%%%%%%%%%%%%%%%%%%%%
111 %                       Ferric ion point                                 %
112 %%%%%%%%%%%%%%%%%%%%%%%%%%%%%%%%%%%%%%%%%%%%%%%%%%%%%%%%%%%%%%%%%%%%%%%
113
114     F_Fe_H = F_point(a,A_Fe_H,B_Fe_H,-X)*n_H;
115     F_Fe_C = F_point(a,A_Fe_C,B_Fe_C,-X)*n_C;
116     F_Fe_O = F_point(a,A_Fe_O,B_Fe_O,-X)*n_O;
117     F_Fe_Eu = F_point(a,A_Fe_Eu,B_Fe_Eu,-X)*n_Eu;
```

```
118
119     F_sum_Fe = F_point(a,A_sum_Fe,B_sum_Fe,-X);
120
121 %%%%%%%%%%%%%%%%%%%%%%%%%%%%%%%%%%%%%%%%%%%%%%%%%%%%%%%%%%%%%%%%%%%%
122 %                          Oxygen shell                                 %
123 %%%%%%%%%%%%%%%%%%%%%%%%%%%%%%%%%%%%%%%%%%%%%%%%%%%%%%%%%%%%%%%%%%%%
124
125     F_OS_H = F_shell(a,b_OS,n_OS,A_O_H,B_O_H,-X)*n_H;
126     F_OS_C = F_shell(a,b_OS,n_OS,A_O_C,B_O_C,-X)*n_C;
127     F_OS_O = F_shell(a,b_OS,n_OS,A_O,B_O,-X)*n_O;
128     F_OS_Eu = F_shell(a,b_OS,n_OS,A_O_Eu,B_O_Eu,-X)*n_Eu;
129
130     F_sum_OS = F_shell(a,b_OS,n_OS,A_sum_OS,B_sum_OS,-X);
131
132 %%%%%%%%%%%%%%%%%%%%%%%%%%%%%%%%%%%%%%%%%%%%%%%%%%%%%%%%%%%%%%%%%%%%
133 %                          Hydrogen shell                               %
134 %%%%%%%%%%%%%%%%%%%%%%%%%%%%%%%%%%%%%%%%%%%%%%%%%%%%%%%%%%%%%%%%%%%%
135
136     F_HS_H = F_shell(a,b_HS,n_HS,A_H,B_H,-X)*n_H;
137     F_HS_C = F_shell(a,b_HS,n_HS,A_H_C,B_H_C,-X)*n_C;
138     F_HS_O = F_shell(a,b_HS,n_HS,A_O_H,B_O_H,-X)*n_O;
139     F_HS_Eu = F_shell(a,b_HS,n_HS,A_H_Eu,B_H_Eu,-X)*n_Eu;
140
141     F_sum_HS = F_shell(a,b_HS,n_HS,A_sum_HS,B_sum_HS,-X);
142
143 %%%%%%%%%%%%%%%%%%%%%%%%%%%%%%%%%%%%%%%%%%%%%%%%%%%%%%%%%%%%%%%%%%%%
144 %                            Total force                                %
145 %%%%%%%%%%%%%%%%%%%%%%%%%%%%%%%%%%%%%%%%%%%%%%%%%%%%%%%%%%%%%%%%%%%%
146
147     F_tot = F_sum_Fe + F_sum_OS + F_sum_HS;
148 end
149
150 %%%%%%%%%%%%%%%%%%%%%%%%%%%%%%%%%%%%%%%%%%%%%%%%%%%%%%%%%%%%%%%%%%%%
151 %                                                                       %
152 % Roots of Force function - Hydrated ferric ion to MOF pore            %
153 %                                                                       %
154 %%%%%%%%%%%%%%%%%%%%%%%%%%%%%%%%%%%%%%%%%%%%%%%%%%%%%%%%%%%%%%%%%%%%
155
156 if (strcmp(section,'ALL') || strcmp(section,'IF') || strcmp(section,'W'))
157
```

```
%%%%%%%%%%%%%%%%%%%%%%%%%%%%%%%%%%%%%%%%%%%%%%%%%%%%%%%%%%%%%%%%%%%%%%%
%                       Ferric ion point                                %
%%%%%%%%%%%%%%%%%%%%%%%%%%%%%%%%%%%%%%%%%%%%%%%%%%%%%%%%%%%%%%%%%%%%%%%

n=10000;

a0_Fe = sigma_sum_Fe*SI_con_length;

a_Fe = [linspace(0,a0_Fe,n), linspace(a0_Fe, 10*SI_con_length,n)];

X_0_Fe = [sqrt(sigma_sum_Fe^2 - a_Fe(1:n).^2), zeros(1,n)];

%%%%%%%%%%%%%%%%%%%%%%%%%%%%%%%%%%%%%%%%%%%%%%%%%%%%%%%%%%%%%%%%%%%%%%%
%                          Oxygen shell                                 %
%%%%%%%%%%%%%%%%%%%%%%%%%%%%%%%%%%%%%%%%%%%%%%%%%%%%%%%%%%%%%%%%%%%%%%%

% a0_OS = 4.7841*SI_con_length;
% a0_OS = 1.5024*sigma_sum_OS*SI_con_length;
F_OS_a0 = @(a_test) F_shell(a_test,b_OS,n_OS,A_sum_OS,B_sum_OS,0);
a0_OS = fzero(F_OS_a0,4.78439*SI_con_length);

a_OS = [linspace(0,a0_OS,n), linspace(a0_OS, 10*SI_con_length,n)];

X_0_OS = zeros(1,2*n);

for i= 2:n

F_OS_X0 = @(x) F_shell(a_OS(i),b_OS,n_OS,A_sum_OS,B_sum_OS,x);

X_0_OS(i) = fzero(F_OS_X0,0);

end

X_0_OS = abs(X_0_OS);

X_0_OS(1) = X_0_OS(2);

%%%%%%%%%%%%%%%%%%%%%%%%%%%%%%%%%%%%%%%%%%%%%%%%%%%%%%%%%%%%%%%%%%%%%%%
%                         Hydrogen shell                                %
%%%%%%%%%%%%%%%%%%%%%%%%%%%%%%%%%%%%%%%%%%%%%%%%%%%%%%%%%%%%%%%%%%%%%%%
```

```
198
199 % a0_HS = 5.24*SI_con_length;
200 % a0_HS = 1.797*sigma_sum_HS*SI_con_length;
201 F_HS_a0 = @(a_test) F_shell(a_test,b_HS,n_HS,A_sum_HS,B_sum_HS,0);
202 a0_HS = fzero(F_HS_a0,5.24*SI_con_length);
203
204 a_HS = [linspace(0,a0_HS,n), linspace(a0_HS, 10*SI_con_length,n)];
205
206 X_0_HS = zeros(1,2*n);
207
208 for i= 2:n
209
210 F_HS_X0 = @(x) F_shell(a_HS(i),b_HS,n_HS,A_sum_HS,B_sum_HS,x);
211
212 X_0_HS(i) = fzero(F_HS_X0,0);
213
214 end
215
216 X_0_HS = abs(X_0_HS);
217
218 X_0_HS(1) = X_0_HS(2);
219
220 %%%%%%%%%%%%%%%%%%%%%%%%%%%%%%%%%%%%%%%%%%%%%%%%%%%%%%%%%%%%%%%%%%%%%%%
221 %                       Hydrated ferric ion                             %
222 %%%%%%%%%%%%%%%%%%%%%%%%%%%%%%%%%%%%%%%%%%%%%%%%%%%%%%%%%%%%%%%%%%%%%%%
223
224 % a0_tot = 5.15254*SI_con_length;
225 F_tot_a0 = @(a_test) F_point(a_test,A_sum_Fe,B_sum_Fe,0) ...
226     + F_shell(a_test,b_OS,n_OS,A_sum_OS,B_sum_OS,0)...
227     + F_shell(a_test,b_HS,n_HS,A_sum_HS,B_sum_HS,0);
228 a0_tot = fzero(F_tot_a0,5.152*SI_con_length);
229
230 a_tot = [linspace(0,a0_tot,n), linspace(a0_tot, 10*SI_con_length,n)];
231
232 X_0_tot = zeros(1,2*n);
233
234 for i= 2:n
235
236 F_tot_X0 = @(x)  F_point(a_tot(i),A_sum_Fe,B_sum_Fe,x) ...
237     + F_shell(a_tot(i),b_OS,n_OS,A_sum_OS,B_sum_OS,x)...
```

```
238     + F_shell(a_tot(i),b_HS,n_HS,A_sum_HS,B_sum_HS,x);
239
240 X_0_tot(i) = fzero(F_tot_X0,0);
241
242 end
243
244 X_0_tot = abs(X_0_tot);
245
246 X_0_tot(1) = X_0_tot(2);
247
248 end
249
250 %%
251 %%%%%%%%%%%%%%%%%%%%%%%%%%%%%%%%%%%%%%%%%%%%%%%%%%%%%%%%%%%%%%%%%%%%%%%
252 %                                                                       %
253 %            Acceptance energy - Hydrated iron to MOF pore              %
254 %                                                                       %
255 %%%%%%%%%%%%%%%%%%%%%%%%%%%%%%%%%%%%%%%%%%%%%%%%%%%%%%%%%%%%%%%%%%%%%%%
256 %                  Accepteance suction force                            %
257 %%%%%%%%%%%%%%%%%%%%%%%%%%%%%%%%%%%%%%%%%%%%%%%%%%%%%%%%%%%%%%%%%%%%%%%
258
259 if (strcmp(section,'ALL') || strcmp(section,'W'))
260
261 %%%%%%%%%%%%%%%%%%%%%%%%%%%%%%%%%%%%%%%%%%%%%%%%%%%%%%%%%%%%%%%%%%%%%%%
262 %                       Ferric ion point                                %
263 %%%%%%%%%%%%%%%%%%%%%%%%%%%%%%%%%%%%%%%%%%%%%%%%%%%%%%%%%%%%%%%%%%%%%%%
264     W_a_sum_Fe = W_point(a,A_sum_Fe,B_sum_Fe,h,0);
265
266     W_a_Fe = W_point(a_Fe,A_sum_Fe,B_sum_Fe,a_Fe,-X_0_Fe);
267
268 %%%%%%%%%%%%%%%%%%%%%%%%%%%%%%%%%%%%%%%%%%%%%%%%%%%%%%%%%%%%%%%%%%%%%%%
269 %                           Oxygen shell                                %
270 %%%%%%%%%%%%%%%%%%%%%%%%%%%%%%%%%%%%%%%%%%%%%%%%%%%%%%%%%%%%%%%%%%%%%%%
271     W_a_sum_OS = W_shell(a,b_OS,n_OS,A_sum_OS,B_sum_OS,h,0);
272
273     con_OS = find( a_OS > b_OS, 1 ); % condition where a_OS>b_OS, such that the Wa, W
      is not complex
274
275     W_a_OS = W_shell(a_OS(con_OS:end),b_OS,n_OS,A_sum_OS,B_sum_OS,lambda(a_OS(con_OS:
      end),b_OS),-X_0_OS(con_OS:end));
```

```
276
277 %%%%%%%%%%%%%%%%%%%%%%%%%%%%%%%%%%%%%%%%%%%%%%%%%%%%%%%%%%%%%%%%%%%%%%%
278 %                          Hydrogen shell                                 %
279 %%%%%%%%%%%%%%%%%%%%%%%%%%%%%%%%%%%%%%%%%%%%%%%%%%%%%%%%%%%%%%%%%%%%%%%
280     W_a_sum_HS = W_shell(a,b_HS,n_HS,A_sum_HS,B_sum_HS,h,0);
281
282     con_HS = find( a_HS > b_HS, 1 ); % condition where a_HS>b_HS, such that the Wa, W
        is not complex
283
284     W_a_HS = W_shell(a_HS(con_HS:end),b_HS,n_HS,A_sum_HS,B_sum_HS,lambda(a_HS(con_HS:
        end),b_HS),-X_0_HS(con_HS:end));
285
286 %%%%%%%%%%%%%%%%%%%%%%%%%%%%%%%%%%%%%%%%%%%%%%%%%%%%%%%%%%%%%%%%%%%%%%%
287 %                     Total potential energy                              %
288 %%%%%%%%%%%%%%%%%%%%%%%%%%%%%%%%%%%%%%%%%%%%%%%%%%%%%%%%%%%%%%%%%%%%%%%
289
290     W_a_sum_tot = W_a_sum_Fe + W_a_sum_OS + W_a_sum_HS;
291
292     con_tot = find( a_tot > b_HS, 1 ); % condition where a_HS>b_HS, such that the Wa, W
         is not complex
293
294     W_a_tot_Fe = W_point(a_tot(con_tot:end),A_sum_Fe,B_sum_Fe,a_tot(con_tot:end),-
        X_0_tot(con_tot:end));
295     W_a_tot_OS = W_shell(a_tot(con_tot:end),b_OS,n_OS,A_sum_OS,B_sum_OS,lambda(a_tot(
        con_tot:end),b_OS),-X_0_tot(con_tot:end));
296     W_a_tot_HS = W_shell(a_tot(con_tot:end),b_HS,n_HS,A_sum_HS,B_sum_HS,lambda(a_tot(
        con_tot:end),b_HS),-X_0_tot(con_tot:end));
297
298     W_a_tot = W_a_tot_Fe + W_a_tot_OS + W_a_tot_HS;
299 % end
300
301 %%
302 %%%%%%%%%%%%%%%%%%%%%%%%%%%%%%%%%%%%%%%%%%%%%%%%%%%%%%%%%%%%%%%%%%%%%%%
303 %                                                                         %
304 %            Kinetic energy - Hydrated iron to MOF pore                   %
305 %                                                                         %
306 %%%%%%%%%%%%%%%%%%%%%%%%%%%%%%%%%%%%%%%%%%%%%%%%%%%%%%%%%%%%%%%%%%%%%%%
307 %                      Total suction force                                %
308 %%%%%%%%%%%%%%%%%%%%%%%%%%%%%%%%%%%%%%%%%%%%%%%%%%%%%%%%%%%%%%%%%%%%%%%
309
```

```
% if (strcmp(section,'ALL') || strcmp(section,'W'))

%%%%%%%%%%%%%%%%%%%%%%%%%%%%%%%%%%%%%%%%%%%%%%%%%%%%%%%%%%%%%%%%%%%%%%%
%                      Ferric ion point                                 %
%%%%%%%%%%%%%%%%%%%%%%%%%%%%%%%%%%%%%%%%%%%%%%%%%%%%%%%%%%%%%%%%%%%%%%%

    W_sum_Fe = W_point(a,A_sum_Fe,B_sum_Fe,0,-1);

    W_Fe = W_point(a_Fe,A_sum_Fe,B_sum_Fe,0,-1);

%%%%%%%%%%%%%%%%%%%%%%%%%%%%%%%%%%%%%%%%%%%%%%%%%%%%%%%%%%%%%%%%%%%%%%%
%                         Oxygen shell                                  %
%%%%%%%%%%%%%%%%%%%%%%%%%%%%%%%%%%%%%%%%%%%%%%%%%%%%%%%%%%%%%%%%%%%%%%%

    W_sum_OS = W_shell(a,b_OS,n_OS,A_sum_OS,B_sum_OS,0,-1);

    W_OS = W_shell(a_OS(con_OS:end),b_OS,n_OS,A_sum_OS,B_sum_OS,0,-1);

%%%%%%%%%%%%%%%%%%%%%%%%%%%%%%%%%%%%%%%%%%%%%%%%%%%%%%%%%%%%%%%%%%%%%%%
%                        Hydrogen shell                                 %
%%%%%%%%%%%%%%%%%%%%%%%%%%%%%%%%%%%%%%%%%%%%%%%%%%%%%%%%%%%%%%%%%%%%%%%

    W_sum_HS = W_shell(a,b_HS,n_HS,A_sum_HS,B_sum_HS,0,-1);

    W_HS = W_shell(a_HS(con_HS:end),b_HS,n_HS,A_sum_HS,B_sum_HS,0,-1);

%%%%%%%%%%%%%%%%%%%%%%%%%%%%%%%%%%%%%%%%%%%%%%%%%%%%%%%%%%%%%%%%%%%%%%%
%                    Total potential energy                             %
%%%%%%%%%%%%%%%%%%%%%%%%%%%%%%%%%%%%%%%%%%%%%%%%%%%%%%%%%%%%%%%%%%%%%%%

    W_sum_tot = W_sum_Fe + W_sum_OS + W_sum_HS;

    W_tot_Fe = W_point(a_tot(con_tot:end),A_sum_Fe,B_sum_Fe,0,-1);
    W_tot_OS = W_shell(a_tot(con_tot:end),b_OS,n_OS,A_sum_OS,B_sum_OS,0,-1);
    W_tot_HS = W_shell(a_tot(con_tot:end),b_HS,n_HS,A_sum_HS,B_sum_HS,0,-1);

    W_tot = W_tot_Fe + W_tot_OS + W_tot_HS;


%%
```

```
350 %%%%%%%%%%%%%%%%%%%%%%%%%%%%%%%%%%%%%%%%%%%%%%%%%%%%%%%%%%%%%%%%%%%%%%%
351 %                                                                       %
352 %                            Comments                                   %
353 %                                                                       %
354 %%%%%%%%%%%%%%%%%%%%%%%%%%%%%%%%%%%%%%%%%%%%%%%%%%%%%%%%%%%%%%%%%%%%%%%
355
356     % To convert work done into J/mol to get the SI velocity.
357     W_tot_J = W_sum_tot*(4184/SI_con_energy);
358     W_sum_Fe_J = W_sum_Fe*(4184/SI_con_energy);
359
360     v_tot = sqrt(2*W_tot_J/(mass_Fe + num_O*mass_O + num_H*mass_H));
361     v_Fe = sqrt(2*W_sum_Fe_J/(mass_Fe));
362
363 end
```

H.2. PART II

Code here relates to Chapter 7, and adjustments can be made to generate the remainder of the plots for the one-dimensional numerical model.

H.2.1. Numerical scheme for nondimensional two-dimensional system

```
% function FDS_2D
% MATLAB version R2019b
% DATE: 17/11/2021
% EDITED: 04/04/2023

% DESCRIPTION: This code maps the classic diffusion equation,
%     c_t = D_i*(c_xx + c_yy). Using numerical methods to solve the
%     diffusion equation, the finite difference scheme is the chosen
%     numerical scheme. When y>0 the ferric ions are diffusing through the
%     analyte solution, when y<0 the ferric ions are diffusing through the
%     polymer.
%     This code only considers MOF cystals at the solution/polymer
%     boundary. At the boundary y=0, the flux is a system of equations,
%     including a psuedo ODE, b(t,x).
%     Runge-Kutta is used as the numerical solver for b(t,x).
%     Where c(t,x,y) is the concentration of ferric ions and b(t,x) is the
%     occupancy of the MOF crystal.
%     Note that CAPITALISATION means that variable/function is dimensional,
%     and where c(t,x,y), b(t,x) are the non-dimensional forms.
%       c - VECTOR, non-dimensional, concentration of ferric ions at time t
%       and cordinate (x,y), c range [0, 1]
%       b - VECTOR, non-dimentional, occupancy of MOF crystal at time t and
%       cordinate (x,0), b range [0 1]
%       t - VECTOR, non-dimensional time
%       x - VECTOR, non-dimension space
%       y - VECTOR, non-dimension space

% INPUT: Nondimensional parameters needed and time/spacial steps,
%   s_1 - SCALAR, nondinmensional diffusion coefficient
%   s_2 - SCALAR, effective association parameter
%   s_3 - SCALAR, effective dissociation parameter
%   s_4 - SCALAR, effective flux parameter
%   D   - SCALAR, relative diffusion coefficient
```

```
34 %   nT  - SCALAR, number of time steps
35 %   dt  - SCALAR, time step size
36 %   nX  - SCALAR, number of horizontal spacial steps
37 %   dx  - SCALAR, horivontal spacial step size
38 %   nY  - SCALAR, number of vertical spacial steps
39 %   dy  - SCALAR, vertical spacial step size
40 %   nM  - SCALAR, MOF length
41 %   yM  - SCALAR, x-cordinates of MOF on polymer/solution boundary
42 %   lM  - SCALAR, x-LHS position of MOF
43 %   rM  - SCALAR, x-RHS position of MOF
44
45 % OUTPUT: Produces plots for the ferric ion concentration c(t,x,y),
46 %    and the MOF occupancy b(t,x).
47
48 % close all;
49 % clear all;
50 % clc
51
52 %% Initialisation
53
54 dx = 0.1;
55 dy = 0.1;
56 dt = 0.0005;
57
58 xmax = 10;
59 xmin = -10;
60
61 ymax = 10;
62 ymin = -10;
63
64 tmax = 10;
65 tmin = 0;
66
67 x = (xmin:dx:xmax)';    nX = length(x);
68 y = (ymin:dy:ymax)';    nY = length(y);
69 t = (tmin:dt:tmax)';    nT = length(t);
70
71 %MOF details
72 xM = (-1:dx:1)';            % x-cordinates of MOF on polymer/solution boundary
73 nM = length(xM);            % MOF length
```

```
yM = find(y==0);            % x-cordinates of MOF on polymer/solution boundary
lM = find(x==-1);           % x-LHS position of MOF
rM = find(x==1);            % x-RHS position of MOF
xmM = find(x==0);           % x-mid position of MOF

[b_base,b_t_base,c_base] = Numerics_2D_FDS(1,1,1,1,0.5,nT,dt,nX,dx,nY,dy,nM,yM,lM,rM);

%%
s_1 = [0.1,1,5];

b_s1 = zeros(nT,3);

c_s1 = zeros(nT,3);

for i=1:3
    [b,~,c] = Numerics_2D_FDS(s_1(i),1,1,1,0.5,nT,dt,nX,dx,nY,dy,nM,yM,lM,rM);

    b_s1(:,i) = b(:,11);

    for j=1:nT
        c_s1(j,i) = c(yM,xmM,j);
    end
end

%%
s_2 = [0.1,1,10];

b_s2 = zeros(nT,3);

c_s2 = zeros(nT,3);

for i=1:3
    [b,~,c] = Numerics_2D_FDS(1,s_2(i),1,1,0.5,nT,dt,nX,dx,nY,dy,nM,yM,lM,rM);

    b_s2(:,i) = b(:,11);

    for j=1:nT
        c_s2(j,i) = c(yM,xmM,j);
    end
end
```

```
114
115 %%
116 s_3 = [0,0.1,1,10];
117
118 b_s3 = zeros(nT,4);
119
120 c_s3 = zeros(nT,4);
121
122 for i=1:4
123     [b,~,c] = Numerics_2D_FDS(1,1,s_3(i),1,0.5,nT,dt,nX,dx,nY,dy,nM,yM,lM,rM);
124
125     b_s3(:,i) = b(:,11);
126
127     for j=1:nT
128         c_s3(j,i) = c(yM,xmM,j);
129     end
130 end
131 %%
132 s_4 = [0.1,1,10];
133
134 b_s4 = zeros(nT,3);
135
136 c_s4 = zeros(nT,3);
137
138 for i=1:3
139     [b,~,c] = Numerics_2D_FDS(1,1,1,s_4(i),0.5,nT,dt,nX,dx,nY,dy,nM,yM,lM,rM);
140
141     b_s4(:,i) = b(:,11);
142
143     for j=1:nT
144         c_s4(j,i) = c(yM,xmM,j);
145     end
146 end
147
148 %%
149 D = [0.1,0.5,1];
150
151 b_D = zeros(nT,3);
152 % b_t_D = zeros(nT,3); % --- int b(t)
153
```

```
154 c_D = zeros(nY,3);
155 c_Dend = zeros(nY,3);
156
157 for i=1:3
158     [b,~,c] = Numerics_2D_FDS(1,1,1,1,D(i),nT,dt,nX,dx,nY,dy,nM,yM,lM,rM);
159 %     [b,b_t,c] = Numerics_2D_FDS(1,1,1,1,D,nT,dt,nX,dx,nY,dy,nM,yM,lM,rM);
160
161     b_D(:,i) = b(:,11);
162 %     b_t_D(:,i) = b_t;
163
164     c_D(:,i) = c(:,xmM,501);
165     c_Dend(:,i) = c(:,xmM,5001);
166
167 end
168
169 %% Plots
170
171 figure
172 surf(x,y,c_base(:,:,1001),'EdgeColor', 'interp')
173 xlabel('$x_1$ axis','fontsize',12,'Interpreter','latex')
174 ylabel('$x_2$ axis','fontsize',12,'Interpreter','latex')
175 xlim([-5 5])
176 ylim([-5 5])
177 zlim([0 1])
178 h = colorbar('ylim', [0 1], 'location', 'eastoutside');
179 h.Label.String = 'Ferric ion concntration';
180 h.Label.Interpreter = 'latex';
181 h.Label.FontSize = 12;
182
183 figure
184 surf(x,y,c_base(:,:,10001),'EdgeColor', 'interp')
185 xlabel('$x_1$ axis','fontsize',12,'Interpreter','latex')
186 ylabel('$x_2$ axis','fontsize',12,'Interpreter','latex')
187 xlim([-5 5])
188 ylim([-5 5])
189 zlim([0 1])
190 h = colorbar('ylim', [0 1], 'location', 'eastoutside');
191 h.Label.String = 'Ferric ion concntration';
192 h.Label.Interpreter = 'latex';
193 h.Label.FontSize = 12;
```

```
% h.tick.format = '%.1f';

%%%%%%%%%%%%%%%%%%%%%%%%%%%%%%%%%%%%%%%%%%%%%%%%%%%%%%%%%%%%%%%%%%%%%%%
figure
hold on
set(gca,...
'xlim',[xmin 5],...
'xtick',(-5:1:5),...
'ylim',[0 1],...
'ytick',(0:0.2:1),...
'fontname','helvetica',...
'fontsize',12)

    plot(y,c_base(:,xmM,1001),'k','linewidth',1.2)
    plot(y,c_base(:,xmM,2001),'k--','linewidth',1.2)
    plot(y,c_base(:,xmM,3001),'k-.','linewidth',1.2)
    plot(y,c_base(:,xmM,4001),'k.','linewidth',1.2)
    plot(y,c_base(:,xmM,10001),'k:','linewidth',1.2)

    % Create arrow
    annotation('arrow',[0.49 0.36],[0.16 0.38]);

    % Create arrow
    annotation('arrow',[0.55 0.67],[0.9 0.75]);

    polymer = fill([-5 -5 0 0], [0 1 1 0], [0.7529 0.5804 0],'EdgeColor', 'none');
    polymer.FaceAlpha = 0.3;

    solution = fill([0 0 5 5], [0 1 1 0], [0.7490 0.8314 0.7255],'EdgeColor', 'none');
    solution.FaceAlpha = 0.3;

axis([-5 5 0 1])
xlabel('Distance from solution-polymer boudary, $x_2$','Interpreter','latex')
ylabel('Concentration, $c(t, 0, x_2)$','Interpreter','latex')
ytickformat('%.1f')
hold off


figure
hold on
```

```
set(gca,...
'xlim',[tmin 5],...
'xtick',(0:1:5),...
'ylim',[0 1],...
'ytick',(0:0.2:1),...
'fontname','helvetica',...
'fontsize',12)

    plot(t,b_t_base,'k--','linewidth',1.2)
    plot(t,b_base(:,11),'k','linewidth',1.2)
    legend({'$b_{tot}(t)$','$b(t,0)$'} ,'Location','southeast','Interpreter','latex')

axis([tmin 5 0 1])
xlabel('Time, $t$','Interpreter','latex')
ylabel('MOF occupancy','Interpreter','latex')
ytickformat('%.1f')
hold off

%%%%%%%%%%%%%%%%%%%%%%%%%%%%%%%%%%%%%%%%%%%%%%%%%%%%%%%%%%%%%%%%%%%%%%%%%%%%%%%
figure
hold on
set(gca,...
'xlim',[tmin 5],...
'xtick',(0:1:5),...
'ylim',[0 1],...
'ytick',(0:0.2:1),...
'fontname','helvetica',...
'fontsize',12)

    plot(t,c_s1(:,1),'k','linewidth',1.2)
    plot(t,c_s1(:,2),'k','linewidth',1.2)
    plot(t,c_s1(:,3),'k','linewidth',1.2)

    % Create arrow
    annotation('arrow',[0.18 0.16],[0.83 0.39]);

axis([tmin 5 0 1])
xlabel('Time, $t$','Interpreter','latex')
ylabel('Concentration, $c(t, 0, 0)$','Interpreter','latex')
ytickformat('%.1f')
```

```
hold off

figure
hold on
set(gca,...
'xlim',[tmin 5],...
'xtick',(0:1:5),...
'ylim',[0 1],...
'ytick',(0:0.2:1),...
'fontname','helvetica',...
'fontsize',12)

    plot(t,b_s1(:,1),'k','linewidth',1.2)
    plot(t,b_s1(:,2),'k','linewidth',1.2)
    plot(t,b_s1(:,3),'k','linewidth',1.2)

    % Create arrow
    annotation('arrow',[0.29 0.2],[0.26 0.4]);

axis([tmin 5 0 1])
xlabel('Time, $t$','Interpreter','latex')
ylabel('MOF occupancy, $b(t, 0)$','Interpreter','latex')
ytickformat('%.1f')
hold off

%%%%%%%%%%%%%%%%%%%%%%%%%%%%%%%%%%%%%%%%%%%%%%%%%%%%%%%%%%%%%%%%%%%%%%%
figure
hold on
set(gca,...
'xlim',[tmin 5],...
'xtick',(0:1:5),...
'ylim',[0 1],...
'ytick',(0:0.2:1),...
'fontname','helvetica',...
'fontsize',12)

    plot(t,c_s2(:,1),'k','linewidth',1.2)
    plot(t,c_s2(:,2),'k','linewidth',1.2)
    plot(t,c_s2(:,3),'k','linewidth',1.2)

```

```
    % Create arrow
    annotation('arrow',[0.175 0.19],[0.91 0.5]);

axis([tmin 5 0 1])
xlabel('Time, $t$','Interpreter','latex')
ylabel('Concentration, $c(t, 0, 0)$','Interpreter','latex')
ytickformat('%.1f')
hold off

figure
hold on
set(gca,...
'xlim',[tmin 5],...
'xtick',(0:1:5),...
'ylim',[0 1],...
'ytick',(0:0.2:1),...
'fontname','helvetica',...
'fontsize',12)

    plot(t,b_s2(:,1),'k','linewidth',1.2)
    plot(t,b_s2(:,2),'k','linewidth',1.2)
    plot(t,b_s2(:,3),'k','linewidth',1.2)

    % Create arrow
    annotation('arrow',[0.5 0.38],[0.19 0.57]);

axis([tmin 5 0 1])
xlabel('Time, $t$','Interpreter','latex')
ylabel('MOF occupancy, $b(t, 0)$','Interpreter','latex')
ytickformat('%.1f')
hold off

%%%%%%%%%%%%%%%%%%%%%%%%%%%%%%%%%%%%%%%%%%%%%%%%%%%%%%%%%%%%%%%%%%%%%%%
figure
hold on
set(gca,...
'xlim',[tmin 5],...
'xtick',(0:1:5),...
'ylim',[0 1],...
'ytick',(0:0.2:1),...
```

```
'fontname','helvetica',...
'fontsize',12)

    plot(t,c_s3(:,1),'k','linewidth',1.2)
    plot(t,c_s3(:,2),'k','linewidth',1.2)
    plot(t,c_s3(:,3),'k','linewidth',1.2)
    plot(t,c_s3(:,4),'k','linewidth',1.2)

    % Create arrow
    annotation('arrow',[0.47 0.26],[0.52 0.92]);

axis([tmin 5 0 1])
xlabel('Time, $t$','Interpreter','latex')
ylabel('Concentration, $c(t, 0, 0)$','Interpreter','latex')
ytickformat('%.1f')
hold off

figure
hold on
set(gca,...
'xlim',[tmin 5],...
'xtick',(0:1:5),...
'ylim',[0 1],...
'ytick',(0:0.2:1),...
'fontname','helvetica',...
'fontsize',12)

    plot(t,b_s3(:,1),'k','linewidth',1.2)
    plot(t,b_s3(:,2),'k','linewidth',1.2)
    plot(t,b_s3(:,3),'k','linewidth',1.2)
    plot(t,b_s3(:,4),'k','linewidth',1.2)

    % Create arrow
    annotation('arrow',[0.36 0.5],[0.66 0.14]);

axis([tmin 5 0 1])
xlabel('Time, $t$','Interpreter','latex')
ylabel('MOF occupancy, $b(t, 0)$','Interpreter','latex')
ytickformat('%.1f')
hold off
```

```
394
395 %%%%%%%%%%%%%%%%%%%%%%%%%%%%%%%%%%%%%%%%%%%%%%%%%%%%%%%%%%%%%%%%%%%%%%%
396 figure
397 hold on
398 set(gca,...
399 'xlim',[tmin 10],...
400 'xtick',(0:1:10),...
401 'ylim',[0 1],...
402 'ytick',(0:0.2:1),...
403 'fontname','helvetica',...
404 'fontsize',12)
405
406     plot(t,c_s4(:,1),'k','linewidth',1.2)
407     plot(t,c_s4(:,2),'k','linewidth',1.2)
408     plot(t,c_s4(:,3),'k','linewidth',1.2)
409
410     % Create arrow
411     annotation('arrow',[0.23 0.4],[0.91 0.2]);
412
413 axis([tmin 10 0 1])
414 xlabel('Time, $t$','Interpreter','latex')
415 ylabel('Concentration, $c(t, 0, 0)$','Interpreter','latex')
416 ytickformat('%.1f')
417 hold off
418
419 figure
420 hold on
421 set(gca,...
422 'xlim',[tmin 5],...
423 'xtick',(0:1:5),...
424 'ylim',[0 1],...
425 'ytick',(0:0.2:1),...
426 'fontname','helvetica',...
427 'fontsize',12)
428
429     plot(t,b_s4(:,1),'k','linewidth',1.2)
430     plot(t,b_s4(:,2),'k','linewidth',1.2)
431     plot(t,b_s4(:,3),'k','linewidth',1.2)
432
433     % Create arrow
```

```
434     annotation('arrow',[0.39 0.49],[0.55 0.17]);
435
436 axis([tmin 5 0 1])
437 xlabel('Time, $t$','Interpreter','latex')
438 ylabel('MOF occupancy, $b(t, 0)$','Interpreter','latex')
439 ytickformat('%.1f')
440 hold off
441
442 %%%%%%%%%%%%%%%%%%%%%%%%%%%%%%%%%%%%%%%%%%%%%%%%%%%%%%%%%%%%%%%%%%%%%%%
443 figure
444 hold on
445 set(gca,...
446 'xlim',[tmin 5],...
447 'xtick',(-5:1:5),...
448 'ylim',[0 1],...
449 'ytick',(0:0.2:1),...
450 'fontname','helvetica',...
451 'fontsize',12)
452
453     plot(y,c_D(:,1),'k','linewidth',1)
454     plot(y,c_D(:,2),'k','linewidth',1)
455     plot(y,c_D(:,3),'k','linewidth',1)
456
457     % Create arrow
458     annotation('arrow',[0.5 0.4], [0.15 0.34]);
459
460     % Create arrow
461     annotation('arrow',[0.55 0.64], [0.92 0.78]);
462
463     polymer = fill([-5 -5 0 0], [0 1 1 0], [0.7529 0.5804 0],'EdgeColor', 'none');
464     polymer.FaceAlpha = 0.3;
465
466     solution = fill([0 0 5 5], [0 1 1 0], [0.7490 0.8314 0.7255],'EdgeColor', 'none');
467     solution.FaceAlpha = 0.3;
468
469 axis([-5 5 0 1])
470 xlabel('Distance from solution-polymer boudary, $x_2$','Interpreter','latex')
471 ylabel('Concentration, $c(0.5, 0, x_2)$','Interpreter','latex')
472 ytickformat('%.1f')
473 hold off
```

```
474
475 figure
476 hold on
477 set(gca,...
478 'xlim',[tmin 5],...
479 'xtick',(-5:1:5),...
480 'ylim',[0 1],...
481 'ytick',(0:0.2:1),...
482 'fontname','helvetica',...
483 'fontsize',12)
484
485     plot(y,c_Dend(:,1),'k','linewidth',1)
486     plot(y,c_Dend(:,2),'k','linewidth',1)
487     plot(y,c_Dend(:,3),'k','linewidth',1)
488
489     % Create arrow
490     annotation('arrow',[0.5 0.3], [0.15 0.45]);
491
492     % Create arrow
493     annotation('arrow',[0.58 0.69],[0.91 0.7]);
494
495     polymer = fill([-5 -5 0 0], [0 1 1 0], [0.7529 0.5804 0],'EdgeColor', 'none');
496     polymer.FaceAlpha = 0.3;
497
498     solution = fill([0 0 5 5], [0 1 1 0], [0.7490 0.8314 0.7255],'EdgeColor', 'none');
499     solution.FaceAlpha = 0.3;
500
501 axis([-5 5 0 1])
502 xlabel('Distance from solution-polymer boudary, $x_2$','Interpreter','latex')
503 ylabel('Concentration, $c(0.5, 0, x_2)$','Interpreter','latex')
504 ytickformat('%.1f')
505 hold off
506
507 figure
508 hold on
509 set(gca,...
510 'xlim',[tmin 5],...
511 'xtick',(0:1:5),...
512 'ylim',[0 1],...
513 'ytick',(0:0.2:1),...
```

```
'fontname','helvetica',...
'fontsize',12)

    plot(t,b_D(:,1),'k','linewidth',1)
    plot(t,b_D(:,2),'k','linewidth',1)
    plot(t,b_D(:,3),'k','linewidth',1)

    % Create arrow
    annotation('arrow',[0.37 0.5], [0.57 0.39]);

axis([tmin 5 0 1])
xlabel('Time, $t$','Interpreter','latex')
ylabel('MOF occupancy, $b(t, 0)$','Interpreter','latex')
ytickformat('%.1f')
hold off

function [b,b_t,c_store] = Numerics_2D_FDS(s_1,s_2,s_3,s_4,D,nT,dt,nX,dx,nY,dy,nM,yM,lM
    ,rM)
% DATE: 17/11/2021
% EDITED: 17/01/2022
% DESCRIPTION: This code maps the classic diffusion equation,
%     c_t = D_i*(c_xx + c_yy). Using numerical methods to solve the
%     diffusion equation, the finite difference scheme is the chosen
%     numerical scheme. When y>0 the ferric ions are diffusing through the
%     analyte solution, when y<0 the ferric ions are diffusing through the
%     polymer.
%     This code only considers MOF cystals at the solution/polymer
%     boundary. At the boundary y=0, the flux is a system of equations,
%     including a psuedo ODE, b(t,x).
%     Runge-Kutta is used as the numerical solver for b(t,x).
%     Where c(t,x,y) is the concentration of ferric ions and b(t,x) is the
%     occupancy of the MOF crystal.
%     Note that CAPITALISATION means that variable/function is dimensional,
%     and where c(t,x,y), b(t,x) are the non-dimensional forms.
%       c - VECTOR, non-dimensional, concentration of ferric ions at time t
%       and cordinate (x,y), c range [0, 1]
%       b - VECTOR, non-dimentional, occupancy of MOF crystal at time t and
%       cordinate (x,0), b range [0 1]
%       t - VECTOR, non-dimensional time
%       x - VECTOR, non-dimension space
```

```
553 %       y - VECTOR, non-dimension space
554
555 % INPUT: Nondimensional parameters needed and time/spacial steps,
556 %   s_1 - SCALAR, nondinmensional diffusion coefficient
557 %   s_2 - SCALAR, effective association parameter
558 %   s_3 - SCALAR, effective dissociation parameter
559 %   s_4 - SCALAR, effective flux parameter
560 %   D   - SCALAR, relative diffusion coefficient
561 %   nT  - SCALAR, number of time steps
562 %   dt  - SCALAR, time step size
563 %   nX  - SCALAR, number of horizontal spacial steps
564 %   dx  - SCALAR, horivontal spacial step size
565 %   nY  - SCALAR, number of vertical spacial steps
566 %   dy  - SCALAR, vertical spacial step size
567 %   nM  - SCALAR, MOF length
568 %   yM  - SCALAR, x-cordinates of MOF on polymer/solution boundary
569 %   lM  - SCALAR, x-LHS position of MOF
570 %   rM  - SCALAR, x-RHS position of MOF
571
572 % OUTPUT: Produces numerical values of the concentration of c(t,x,y),
573 %    and the density profile of b(t,x).
574
575 % close all;
576 % clear all;
577 % clc
578
579 %% Initialisation
580
581 % check = s_1*D*dt/(dx^2)
582
583 %% Building 2D and 3D matrices
584
585 % 3D matrix to save time data of the ferric ion concentration
586 c_store=zeros(nY,nX,nT);
587
588 % Initial condition
589 c_old=[zeros(yM-1,nX);
590     ones(nY-yM+1,nX)];
591
592 sx= s_1*dt/(dx^2);  %calcualting Sx
```

```
sy= s_1*dt/(dy^2);  %calcualting Sy

% 2D matrix to save time data of the MOF crystal occupancy
b = zeros(nT,nM);

%% Algorithm
% Non-dimensional

c=c_old;%taking the initial value
c_store(:,:,1) = c_old;

for n=2:nT

    % MOF
    f = @(y) s_2*c_old(yM,lM:rM).*(1-y) - s_2*s_3*y;

    k1 = dt*f(b(n-1,:));
    k2 = dt*f(b(n-1,:) + k1./2);
    k3 = dt*f(b(n-1,:) + k2./2);
    k4 = dt*f(b(n-1,:) + k3);

    b(n,:) = b(n-1,:) + (k1 + 2*k2 + 2*k3 + k4)./6;

    % Polymer
    c(2:yM-1,2:nX-1) = (1 - 2*D*sx - 2*D*sy)*c_old(2:yM-1,2:nX-1) + ...
        sx*D*c_old(2:yM-1,3:nX) + sx*D*c_old(2:yM-1,1:nX-2) + ...
        sy*D*c_old(3:yM,2:nX-1) + sy*D*c_old(1:yM-2,2:nX-1);

    % Solution
    c(yM+1:nY-1,2:nX-1) = (1 - 2*sx - 2*sy)*c_old(yM+1:nY-1,2:nX-1) + ...
        sx*c_old(yM+1:nY-1,3:nX) + sx*c_old(yM+1:nY-1,1:nX-2) + ...
        sy*c_old(yM+2:nY,2:nX-1) + sy*c_old(yM:nY-2,2:nX-1);

    % LHS Polymer/Solution boundary
    c(yM,2:lM-2) = (1 - 2*sx - (1+D)*sy)*c_old(yM,2:lM-2) + ...
        sx*c_old(yM,3:lM-1)   + sx*c_old(yM,1:lM-3) + ...
        sy*c_old(yM+1,2:lM-2) + sy*D*c_old(yM-1,2:lM-2);

    % lM-1 Polymer/Solution boundary
    c(yM,lM-1) = (1 -2*sx - (1+D)*sy)*c_old(yM,lM-1) + ...
```

```
633         sx*c_old(yM,lM-2)   + sx*c_old(yM,lM-2) + ...
634         sy*c_old(yM+1,lM-1) + sy*D*c_old(yM-1,lM-1);
635
636     % rM+1 Polymer/Solution boundary
637     c(yM,rM+1) = (1 -2*sx - (1+D)*sy)*c_old(yM,rM+1) + ...
638         sx*c_old(yM,rM+2)   + sx*c_old(yM,rM+2) + ...
639         sy*c_old(yM+1,rM+1) + sy*D*c_old(yM-1,rM+1);
640
641     % RHS Polymer/Solution boundary
642     c(yM,rM+2:nX-1) = (1 -2*sx -(1+D)*sy)*c_old(yM,rM+2:nX-1) + ...
643         sx*c_old(yM,rM+3:nX)     + sx*c_old(yM,rM+1:nX-2) + ...
644         sy*c_old(yM+1,rM+2:nX-1) + sy*D*c_old(yM-1,rM+2:nX-1);
645
646     % MOF/Polymer/Solution boundary
647     c(yM,lM:rM) = ( s_1*(1+D)*c(yM+1,lM:rM) + ...
648         2*dy*D*s_2*s_3*s_4*b(n,:))./(s_1*(1+D) + 2*dy*D*s_2*s_4*(1-b(n,:)));
649
650 %     c(yM,lM:rM) = ((1+D)*c(yM+1,lM:rM) + ...
651 %         2*dy*D*s_2*s_3*s_4*b(n,:)/s_1)./((1+D) + 2*dy*D*s_2*s_4*(1-b(n,:))/s_1);
652
653     % Polymer - Boundary condition at i=0
654     c(2:yM-1,1) = (1 -2*D*sx - 2*D*sy)*c_old(2:yM-1,1) + ...
655         D*sx*c_old(2:yM-1,2) + D*sx*c_old(2:yM-1,2) + ...
656         D*sy*c_old(3:yM,1)   + D*sy*c_old(1:yM-2,1);
657
658     % Solution/Polymer - Boundary condition at i=0, j = jm
659     c(yM,1) = (1 -2*sx - (1+D)*sy)*c_old(yM,1) + ...
660         sx*c_old(yM,2)   + sx*c_old(yM,2) + ...
661         sy*c_old(yM+1,1) + D*sy*c_old(yM-1,1);
662
663     % Solution - Boundary condition at i=0
664     c(yM+1:nY-1,1) = (1 - 2*sx - 2*sy)*c_old(yM+1:nY-1,1) + ...
665         sx*c_old(yM+1:nY-1,2) + sx*c_old(yM+1:nY-1,2) + ...
666         sy*c_old(yM+2:nY,1)   + sy*c_old(yM:nY-2,1);
667
668     % Polymer - Boundary condition at i=I
669     c(2:yM-1,nX) = (1 - 2*D*sx - 2*D*sy)*c_old(2:yM-1,nX) + ...
670         sx*D*c_old(2:yM-1,nX-1) + sx*D*c_old(2:yM-1,nX-1) + ...
671         sy*D*c_old(3:yM,nX)     + sy*D*c_old(1:yM-2,nX);
672
```

```
673     % Solution/Polymer - Boundary condition at i=I, j = jm
674     c(yM,nX) = (1 - 2*sx - (1+D)*sy)*c_old(yM,nX) + ...
675         sx*c_old(yM,nX-1) + sx*c_old(yM,nX-1) + ...
676         sy*c_old(yM+1,nX) + sy*D*c_old(yM-1,nX);
677
678     % Solution - Boundary condition at i=I
679     c(yM+1:nY-1,nX) = (1 - 2*sx - 2*sy)*c_old(yM+1:nY-1,nX) + ...
680         sx*c_old(yM+1:nY-1,nX-1) + sx*c_old(yM+1:nY-1,nX-1) + ...
681         sy*c_old(yM+2:nY,nX)     + sy*c_old(yM:nY-2,nX);
682
683     % Far field at j=J
684     c(nY,:)= 1;
685
686     % No flux at j=0
687     c(1,2:nX-1) = (1 - 2*sx - 2*sy)*c_old(1,2:nX-1) + ...
688         sx*c_old(1,3:nX)   + sx*c_old(1,1:nX-2) + ...
689         sy*c_old(2,2:nX-1) + sy*c_old(2,2:nX-1);
690
691     % No flux at j=0 and i=0
692     c(1,1) = (1 - 2*sx - 2*sy)*c_old(1,1) + ...
693         sx*c_old(1,2) + sx*c_old(1,2) + ...
694         sy*c_old(2,1) + sy*c_old(2,1);
695
696     % No flux at j=0 and i=I
697     c(1,nX) = (1 - 2*sx - 2*sy)*c_old(1,nX) + ...
698         sx*c_old(1,nX-1) + sx*c_old(1,nX-1) + ...
699         sy*c_old(2,nX)   + sy*c_old(2,nX);
700
701     %storing the values in 3D matrix
702     c_store(:,:,n)=c;
703
704     c_old = c;
705 end
706
707 b_t = trapz(b,2)*dx;
708 end
```

H.3. PART III

Code here relates to Chapter 11.

H.3.1. Calculating admitted Lie point symmetries for system of PDEs

```
load dimsym23;

%x(1)=t, x(2)=x, u(1)=c, u(2)=b

freeunknown(s1);
freeunknown(s2);
freeunknown(s3);

% modified PDE - Chapter 11, Section 1
% loaddeq( u(1,2,2) = (1 + s2/((u(1)+s2)**2))*u(1,1) );

% system of PDES with dissociation - Chapter 11, Section 2, Subsection 1
loaddeq( u(1,2,2) = u(1,1)/(s1) );
loaddeq( u(2,1) = s2*u(1)*(1 - u(2)) - s2*s3*u(2));

% system of PDES with no dissociation, s3=0 - Chapter 11, Section 2, Subsection 2
% loaddeq( u(1,2,2) = u(1,1)/(s1) );
% loaddeq( u(2,1) = s2*u(1)*(1 - u(2)));

mkdets(point);
showdets();
solvedets(std);
mkgens();
showdets();

end;
```

APPENDIX I

STATEMENTS OF AUTHORSHIP

University of South Australia

Statement of Authorship

Title of Paper	Interaction of ferric ions with europium metal organic framework and application to mineral processing sensing
Publication Status	☑ Published ☐ Accepted for Publication ☐ Submitted for Publication ☐ Unpublished and Unsubmitted work written in manuscript style
Publication Details Relevant reference details	Philosophical Magazine, 102(13): 1231-1246, 2022

PRINCIPAL AUTHOR

Name of Principal Author (Candidate)	K. I. Louw	
Contribution to the Paper Brief description of your work in this publication	Conceptualisation, investigation, methodology, software, visualisation, writing- original draft.	
Overall Percentage (%)	60%	
Certification	This paper reports on original research I conducted during the period of my Higher Degree by Research candidature and is not subject to any obligations or contractual agreements with a third party that would constrain its inclusion in this thesis. I am the primary author of this paper.	
Signature *Signatures will be redacted by the Library at the time of publication*	[redacted]	Date 4/5/23

CO-AUTHOR CONTRIBUTIONS

By signing the Statement of Authorship, each author certifies that:

I. the candidate's stated contribution to the publication is accurate (as detailed above);

II. permission is granted for the candidate in include the publication in the thesis; and

III. the sum of all co-author contribution is equal to 100% less the candidate's stated contribution.

Name of Co-Author 1	B. H. Bradshaw-Hajek	
% Contribution to the Paper	20%	
Signature *Signatures will be redacted by the Library at the time of publication*	[redacted]	Date 12 May 2023
Name of Co-Author 2	J. M. Hill	

University of South Australia

% Contribution to the Paper	20%	
Signature *Signatures will be redacted by the Library at the time of publication*	[redacted]	Date 13/05/23
Name of Co-Author 3		
% Contribution to the Paper		
Signature *Signatures will be redacted by the Library at the time of publication*		Date
Name of Co-Author 4		
% Contribution to the Paper		
Signature *Signatures will be redacted by the Library at the time of publication*		Date
Name of Co-Author 5		
% Contribution to the Paper		
Signature *Signatures will be redacted by the Library at the time of publication*		Date
Name of Co-Author 6		
% Contribution to the Paper		
Signature *Signatures will be redacted by the Library at the time of publication*		Date
Name of Co-Author 7		
% Contribution to the Paper		
Signature *Signatures will be redacted by the Library at the time of publication*		Date
Name of Co-Author 8		
% Contribution to the Paper		

University of South Australia

Statement of Authorship

Title of Paper	Ferric Ion Diffusion for MOF-Polymer Composite with Internal Boundary Sinks
Publication Status	☑ Published ☐ Accepted for Publication ☐ Submitted for Publication ☐ Unpublished and Unsubmitted work written in manuscript style
Publication Details Relevant reference details	Nanomaterials, 12(5): 887, 2022

PRINCIPAL AUTHOR

Name of Principal Author (Candidate)	K. I. Louw	
Contribution to the Paper Brief description of your work in this publication	Conceptualisation, investigation, methodology, software, visualisation, writing- original draft.	
Overall Percentage (%)	60%	
Certification	This paper reports on original research I conducted during the period of my Higher Degree by Research candidature and is not subject to any obligations or contractual agreements with a third party that would constrain its inclusion in this thesis. I am the primary author of this paper.	
Signature *Signatures will be redacted by the Library at the time of publication*	[redacted]	Date 4/5/23

CO-AUTHOR CONTRIBUTIONS

By signing the Statement of Authorship, each author certifies that:

I. the candidate's stated contribution to the publication is accurate (as detailed above);

II. permission is granted for the candidate in include the publication in the thesis; and

III. the sum of all co-author contribution is equal to 100% less the candidate's stated contribution.

Name of Co-Author 1	B. H. Bradshaw-Hajek	
% Contribution to the Paper	20%	
Signature *Signatures will be redacted by the Library at the time of publication*	[redacted]	Date 12 May 2023
Name of Co-Author 2	J. M. Hill	

University of South Australia

% Contribution to the Paper	20%	
Signature *Signatures will be redacted by the Library at the time of publication*	[redacted]	Date 13/05/23
Name of Co-Author 3		
% Contribution to the Paper		
Signature *Signatures will be redacted by the Library at the time of publication*		Date
Name of Co-Author 4		
% Contribution to the Paper		
Signature *Signatures will be redacted by the Library at the time of publication*		Date
Name of Co-Author 5		
% Contribution to the Paper		
Signature *Signatures will be redacted by the Library at the time of publication*		Date
Name of Co-Author 6		
% Contribution to the Paper		
Signature *Signatures will be redacted by the Library at the time of publication*		Date
Name of Co-Author 7		
% Contribution to the Paper		
Signature *Signatures will be redacted by the Library at the time of publication*		Date
Name of Co-Author 8		
% Contribution to the Paper		

University of South Australia

Statement of Authorship

Title of Paper	van der Waals interaction energies for ferric ion sensors using prismatic and cylindrical pore approximations for a MOF pore
Publication Status	☐ Published ☑ Accepted for Publication ☐ Submitted for Publication ☐ Unpublished and Unsubmitted work written in manuscript style
Publication Details Relevant reference details	Royal Society Open Science

PRINCIPAL AUTHOR

Name of Principal Author (Candidate)	K. I. Louw	
Contribution to the Paper Brief description of your work in this publication	Conceptualisation, investigation, methodology, software, visualisation, writing- original draft.	
Overall Percentage (%)	60%	
Certification	This paper reports on original research I conducted during the period of my Higher Degree by Research candidature and is not subject to any obligations or contractual agreements with a third party that would constrain its inclusion in this thesis. I am the primary author of this paper.	
Signature *Signatures will be redacted by the Library at the time of publication*	[redacted]	Date 4/5/23

CO-AUTHOR CONTRIBUTIONS

By signing the Statement of Authorship, each author certifies that:

I. the candidate's stated contribution to the publication is accurate (as detailed above);

II. permission is granted for the candidate in include the publication in the thesis; and

III. the sum of all co-author contribution is equal to 100% less the candidate's stated contribution.

Name of Co-Author 1	B. H. Bradshaw-Hajek	
% Contribution to the Paper	20%	
Signature *Signatures will be redacted by the Library at the time of publication*	[redacted]	Date 12 May 2023
Name of Co-Author 2	J. M. Hill	

University of South Australia

% Contribution to the Paper	20%	
Signature *Signatures will be redacted by the Library at the time of publication*	[redacted]	Date 13/05/23
Name of Co-Author 3		
% Contribution to the Paper		
Signature *Signatures will be redacted by the Library at the time of publication*		Date
Name of Co-Author 4		
% Contribution to the Paper		
Signature *Signatures will be redacted by the Library at the time of publication*		Date
Name of Co-Author 5		
% Contribution to the Paper		
Signature *Signatures will be redacted by the Library at the time of publication*		Date
Name of Co-Author 6		
% Contribution to the Paper		
Signature *Signatures will be redacted by the Library at the time of publication*		Date
Name of Co-Author 7		
% Contribution to the Paper		
Signature *Signatures will be redacted by the Library at the time of publication*		Date
Name of Co-Author 8		
% Contribution to the Paper		